

|

# Ultrasound Data Communication System for Bioelectronic Medicines



Banafsaj Jaafar Rasool

School of Engineering

Newcastle University

A thesis submitted for the degree of

*Doctor of Philosophy*

December 2020



## Abstract

The coming years may see the advent of distributed implantable devices to support bioelectronic medicinal treatments. Such treatments could be complementary and, in some cases, may even prove superior to pharmaceutical treatments for certain chronic disease conditions. Therefore, a significant research effort is being undertaken in the bioelectronics domain. Target conditions include diabetes, inflammatory bowel disease, lupus, and arthritis.

Modern active medical implantable devices require communications to transmit information to the outside world or other implantable sub-systems. This can include physiological data, diagnostics, and parameters to optimise the therapeutic protocol. However, the communication scheme can be very challenging especially for deeper devices. Challenges include absorption and scattering by tissue, and the need to ensure there are no undesirable heating effects. Wired connectivity is undesirable and tissue absorption of traditional radio frequency and optical methods mean that ultrasound communications have significant potential in this niche.

In this thesis, a reliable and efficient ultrasonic communication telemetry is presented. An omnidirectional transducer has been employed to implement intra body communication inside a model of the human body. A prototype has been implemented to evaluate the system performance in saline and up to 30 *cm* distance between the transmitter and receiver. Short pulses sequences with guard intervals have been employed to minimise the multipath effect that leads to an increase in the bit and thus packet error rates with distance. Error detection and correction code have been employed to improve communication at a low signal to noise ratio. The data rate is limited to 0.6 *kbps* due to the necessary guard intervals. Energy per bit and current consumption for the transmitter and receiver main parts are presented and discussed in terms of battery life. Transmission can be achieved at an energy cost of 642 *nJ* per bit data packet using on/off power cycling in the electronics.

## Acknowledgements

I would like to express my genuine appreciation and gratitude to my first supervisor, Professor Patrick Degenaar, for his support and guidance throughout this project. Without his limitless enthusiasm and patience, I doubt this thesis would ever have come to fruition. He continuously encouraged me through my research and never accepted less than my best efforts that enable me to know more new things.

Likewise, I would like to express my special thank of gratitude to my second supervisor, Mr Jeff Neasham, for sharing his vast experience in the field of ultrasound communication and giving me his precious time and kind feedback throughout my research. I would like to express my deepest appreciation to Dr Ahmed Soltan for his advice and scientific support.

I also gratefully acknowledge Newcastle University for funding my PhD, and the technical staff in the mechanical and electrical workshops for their expertise, assistance and their kindness patience concerning my many job requests.

I would like to thank all colleagues and staff within  $\mu$ Systems group and Intelligent Sensing and Communications at Newcastle University for their help and support to make my times here wonderful both socially and educationally. Special gratitude goes out to Dr Jun Luo, Dr Mohamed Abufalgha, Dr Israa Ali, Yu Liu and Dimitris Firfilionis.

Beyond the campus limits, I would like to thank my close friends Nicky Yaseri, Ehsan Al-Yasiri, and Ali Alqaisi for their support and encouragement to accomplish my mission successfully.

Most especially, I would like to thank my big family, my lovely mother, my sisters: Ansam, Ashjan, Raheeq, Dhifaf, my brother Ahmed and my small family, my wonderful husband Harith and my lovely son Ali, for their understanding and support. Words alone cannot express what I owe them for their encouragement and love that inspired me to complete this work.

# *Dedication*

*It is my genuine gratefulness that I dedicate this work to:*

*My life coach, my late father, and my mother: because I  
owe it all to you.*

*My lovely husband Harith and my son Ali.*

# List of Achievements

## List of Publications

### *Journal papers*

- Jaafar, Banafsaj, Junwen Luo, Dimitrios Firfilionis, Ahmed Soltan, Jeff Neasham, and Patrick Degenaar. "Ultrasound Intra Body Multi Node Communication System for Bioelectronic Medicine." *Sensors* 20, no. 1 (2020): 31.
- Jaafar, Banafsaj, Jeff Neasham and Patrick Degenaar. "What Ultrasound Can and Cannot Do in Implantable Medical Device Communications?." in *IEEE Reviews in Biomedical Engineering*, doi: 10.1109/RBME.2021.3080087.

### *International conference papers*

- Jaafar, Banafsaj, Jeffrey Neasham, Graeme Chester, and Patrick Degenaar. "Ultrasonic wireless powering link of visual cortical prosthesis implant." In 2017 IEEE Biomedical Circuits and Systems Conference (BioCAS), pp. 1-4. IEEE, 2017.
- Jaafar, Banafsaj, Ahmed Soltan, Jeff Neasham, and Patrick Degenaar. "Optical recording and stimulation of an injectable wireless medical implant." In 2018 IEEE British and Irish Conference on Optics and Photonics (BICOP), pp. 1-4. IEEE, 2018.
- Jaafar, Banafsaj, Ahmed Soltan, Jeff Neasham, and Patrick Degenaar. "Wireless Ultrasonic Communication for Biomedical Injectable Implantable Device." In 2019 41st Annual International Conference of the IEEE Engineering in Medicine and Biology Society (EMBC), pp. 4024-4027. IEEE, 2019. (Oral Presentation – 12 minutes).

### *Local Conferences*

- Won best poster presentation in Arm Research Summit, 2018, Cambridge. "Ultrasonic Wireless Implanted Pill for Fluorescence Sensing Using Ultra Low Power Microcontroller Based on Arm Cortex-M0+ Core".
- Won best poster presentation prize in Bioelectronic Medicines: Past, Present and Future, 2019, London. "Data Transmission of Ultrasound Omnidirectional Transducer for Bioelectronics Nodes".

## List of Acronyms

<i>AIMD</i>	Active Implantable Medical Device
<i>ASIC</i>	Application Specific Integrated Circuit Chip
<i>ASK</i>	Amplitude Shift Key
<i>AM</i>	Amplitude Modulation
<i>AFE</i>	Analog Front End
<i>ADC</i>	Analog to Digital Converter
<i>BeNs</i>	Bioelectronic Nodes
<i>BER</i>	Bit Error Rate
<i>BFSK</i>	Binary Frequency Shift Keying
<i>BPSK</i>	Binary Phase Shift Keying
<i>CMOS</i>	Complementary Metal-Oxide-Semiconductor
<i>CRC</i>	Cyclic Redundancy Check
<i>CPU</i>	Central Processing Unit
<i>DSP</i>	Digital Signal Processing
<i>DPPM</i>	Differential Pulse Position Modulation
<i>ECC</i>	Error Correction Code
<i>FDA</i>	Food and Drug Administration
<i>FCC</i>	Federal Communication Commission
<i>FSK</i>	Frequency Shift Keying
<i>FFT</i>	Fast Fourier Transform
<i>FEC</i>	Forward Error Correction
<i>GF</i>	Galois Field
<i>ISM</i>	Industrial Scientific and Medical
<i>IPG</i>	Implantable Pulse Generator
<i>I<sub>SPTA</sub></i>	Spectral Peak Temporal Average Intensity
<i>ISI</i>	Intersymbol Interference
<i>IoMT</i>	Internet of Medical Things
<i>IMD</i>	Implantable Medical Device
<i>LED</i>	Light Emitted Diode
<i>LQFP</i>	Low Profile Quad Flat Pack
<i>LDO</i>	Low Dropout Regulator
<i>MIMO</i>	Multiple-Input/Multiple-Output
<i>MCU</i>	Microcontroller Unit
<i>NDT</i>	Non-Destructive Testing

<i>NASA</i>	National Aeronautics and Space Administration
<i>OOK</i>	On-Off Keying
<i>Op – Amp</i>	Operation Amplifier
<i>OFDM</i>	Orthogonal Frequency Division Modulation
<i>PCB</i>	Printed Circuit Board
<i>PMUT</i>	Piezoelectric Micromachined Ultrasonic Transducers
<i>PPM</i>	Pulse Position Modulation
<i>PSK</i>	Phase Shift Keying
<i>PVDF</i>	Polyvinylidene Fluoride
<i>PMN</i>	Lead Meta-Niobate
<i>PZT</i>	Lead Zirconate Titanate
<i>PLL</i>	Phase-Locked Loop
<i>PER</i>	Packet Error Rate
<i>PU</i>	Polyurethane
<i>PMC</i>	Power Management Circuit
<i>QAM</i>	Quadrature Amplitude Modulation
<i>QPSK</i>	Quadrature Phase Shift Key
<i>QAM</i>	Quadrature Amplitude Modulation
<i>QPSK</i>	Quadrature Phase Shift Key
<i>RF</i>	Radio frequency
<i>RFID</i>	Radio Frequency Identification
<i>RS</i>	Reed Solomon
<i>RMS</i>	Roots Mean Square
<i>SNR</i>	Signal to Noise Ratio
<i>SEA</i>	Sensors, Electromagnetics and Acoustic
<i>TVR</i>	Transmitting Voltage Response
<i>VLPR</i>	Very Low Power Run
<i>VLPS</i>	Very Low Power Stop
<i>WSNs</i>	Wireless Sensor Networks

# Contents

<b>CHAPTER 1. INTRODUCTION .....</b>	<b>1</b>
1.1 INTRODUCTION .....	1
1.2 MOTIVATION AND CHALLENGES .....	2
1.3 THESIS CONTRIBUTION .....	4
1.4 THESIS SUMMARY .....	6
1.5 RESEARCH CONTRIBUTION .....	7
<b>CHAPTER 2. LITERATURE REVIEW .....</b>	<b>9</b>
2.1 INTRODUCTION .....	9
2.2 IMDs COMMUNICATION OVERVIEW .....	11
2.3 COMPARATIVE TRANSMISSION TECHNOLOGIES .....	15
2.3.1 <i>RF Transmission Link</i> .....	15
2.3.2 <i>Optical Transmission Link</i> .....	17
2.3.3 <i>Ultrasound Transmission Link</i> .....	17
2.4 ACTIVE VERSUS PASSIVE COMMUNICATION .....	19
2.5 COMPARISON OF THE STATE OF THE ART .....	19
2.5.1 <i>Transducer Form Factor Versus Data Rate</i> .....	23
2.5.2 <i>Transmission Distance Versus Transducer Size and Frequency</i> .....	24
2.5.3 <i>Data Rate Versus Frequency and Distance</i> .....	31
2.5.4 <i>Passive versus active modulation</i> .....	34
2.5.5 <i>Effect of Modulation Type</i> .....	35
2.6 PREVIOUS REPORTED WORK .....	36
2.6.1 <i>Directional Disc Transducer Form Factor</i> .....	36
2.6.2 <i>Directional Plate Transducer Form Factor</i> .....	39
2.6.3 <i>Directional Cube Transducer Form Factor</i> .....	40
2.6.4 <i>Directional PMUT Transducer Form Factor</i> .....	41
2.6.5 <i>Omnidirectional Sonomicrometry Transducer Form Factor</i> .....	41
2.7 CONCLUSION .....	43
<b>CHAPTER 3. WIRELESS COMMUNICATION SYSTEM .....</b>	<b>47</b>
3.1 INTRODUCTION .....	47
<b>3.2 FUNDAMENTALS OF ULTRASOUND .....</b>	<b>48</b>
3.2.1 <i>Operating Frequency</i> .....	48
3.2.2 <i>Speed of Propagation</i> .....	48
3.2.3 <i>Ultrasound Wave Types</i> .....	50
3.2.4 <i>Ultrasound Modes of Operation</i> .....	51
3.2.5 <i>Piezoelectric Materials</i> .....	53
3.2.6 <i>Ultrasound Attenuation in The Body</i> .....	54

3.2.7 Ultrasound Bandwidth .....	56
3.2.8 Ultrasound Transducer Beam Directivity.....	58
3.3 ULTRASOUND BIOPHYSICS .....	59
3.4 CHANNEL CHARACTERISTICS.....	60
3.4.1 Speed of propagation (described earlier in section 3.2.2).....	61
3.4.2 Path loss .....	61
3.4.3 Multipath Effect .....	61
3.5 MODULATION AND DEMODULATION .....	65
3.6 COMMON DIGITAL MODULATION TECHNIQUES .....	66
3.6.1 Phase Shift Keying .....	67
3.6.2 Frequency Shift Keying .....	68
3.6.3 Amplitude Shift Keying .....	69
3.6.4 Quadrature Amplitude Modulation.....	72
3.7 CHANNEL CAPACITY.....	73
3.8 EFFECT OF NOISE.....	74
3.8.1 Communication Crosstalk.....	77
3.9 SIGNAL TO NOISE RATIO .....	77
3.10 BIT ERROR RATE .....	78
3.10.1 BER Measurement Process.....	79
3.11 PACKET ERROR RATE .....	81
3.12 ERROR DETECTION AND CORRECTION .....	81
3.12.1 Block codes .....	82
3.12.2 Convolutional codes .....	83
3.13 BLOCK CODES VERSUS CONVOLUTIONAL CODES.....	84
3.14 REED SOLOMON CODE .....	85
3.14.1 RS Code Architecture .....	87
3.15 COMMUNICATION PROTOCOL.....	88
3.15.1 Communication Protocol for Intra Body Communication Network.....	89
3.15.2 The Proposed Communication Protocol .....	90
<b>CHAPTER 4. SYSTEM ARCHITECTURE.....</b>	<b>97</b>
4.1 INTRODUCTION .....	97
4.2 PIEZOCERAMIC TECHNOLOGY.....	98
4.2.1 Ultrasound Transduction.....	98
4.2.2 Wire Bonding.....	99
4.2.3 Encapsulation.....	103
4.2.4 Impedance Measurements.....	103
4.3 TRANSDUCER CALIBRATION.....	105
4.3.1 Calibration set-up.....	106
4.3.1 Calibration Results.....	107
4.4 ANALOG FRONT END.....	110

4.4.1 Broad Bandpass Filter Design (First Stage) .....	112
4.4.2 Multiple Feedback Filter Design (Second and Third Stages) .....	113
4.5 AFE SIMULATION DESIGN.....	114
4.5.1 Simulation Results the Three Stages Filtration and Amplification .....	116
4.6 EMBEDDED CONTROL UNIT.....	117
4.7 PHYSICAL IMPLEMENTATION.....	119
4.7.1 Ultrasound AFE PCB Design .....	119
4.7.2 System Prototype PCB Design .....	120
4.8 SOFTWARE ARCHITECTURE .....	122
<b>CHAPTER 5. SYSTEM LEVEL TESTING.....</b>	<b>125</b>
5.1 INTRODUCTION.....	125
5.2 TISSUE PHANTOM EXPERIMENTAL SETUP .....	125
5.2.1 AFE Frequency Response Results and Discussion.....	126
5.2.2 Channel Impulse Response.....	127
5.2.3 Signal to Noise Ratio Measurements.....	128
5.2.4 Latency Versus Distance .....	129
5.2.5 Transmission Loss Versus Distance .....	130
5.2.6 Electromagnetic Crosstalk .....	131
5.3 COMMUNICATION SYSTEM EVALUATION IN THE TISSUE PHANTOM.....	132
5.3.1 Timing and Multipath Analysis .....	133
5.3.2 Bandwidth and Received Signal Amplitude .....	136
5.3.3 Forward Error Correction Code .....	138
5.3.4 SNR, Latency and Data Throughput.....	139
5.3.5 BER and PER.....	143
5.3.6 Current Consumption and Energy Per Bit .....	146
<b>CHAPTER 6. CONCLUSION AND FUTURE WORK .....</b>	<b>151</b>
6.1 CONCLUSION .....	151
6.2 PERSONAL VIEW ON THE IMPACT OF THIS WORK IN THE BIOELECTRONIC MEDICINES FIELD..	151
6.3 PERSONAL WORK CRITICISM .....	152
6.4 FUTURE WORK.....	152
6.4.1 Hardware Improvement and Further Development .....	153
6.4.2 Communication Software Further Development .....	155
6.4.3 Experimental Testing and Investigation .....	160
<b>CHAPTER 7. APPENDIX A .....</b>	<b>161</b>
<b>REFERENCES.....</b>	<b>167</b>

# List of Figures

FIGURE 1-1: PER-CUTANEOUS AND INTRA-BODY COMMUNICATIONS. (A) SHALLOW SUB-CUTANEOUS AND SUB-MUSCULAR COMMUNICATIONS. (B) DEEP COMMUNICATIONS TO IN BODY IMPLANTS. (C) INTRA-BODY COMMUNICATIONS BETWEEN IMPLANTABLE NODES [12]. .....3

FIGURE 1-2: CONCEPT IMAGE OF HOW THE IMPLANTS CAN BE EMBEDDED INSIDE THE HUMAN BODY AND SCALE DOWN TO BE INJECTABLE, THE SLAVE SYSTEM IMPLANTS WILL BE CAPABLE OF COLLECTING THE SENSED DATA AND TRANSMIT THE INFORMATION TO THE CENTRAL UNIT (MASTER) THAT EMBEDDED INSIDE THE CHEST. THE LATTER WILL COMMUNICATE WITH THE EXTERNAL TRANSCEIVER. ....5

FIGURE 2-1: TYPES OF THE CURRENT IMPLANTABLE DEVICES: (A) DEEP BRAIN STIMULATION IMPLANT FROM MEDTRONIC; (B) HEART PACEMAKER (AZURE) FROM MEDTRONIC; (C) IMPLANTABLE INSULIN PUMP (SYNCHROMED) FROM MEDTRONIC; (D) SACRAL NERVE STIMULATOR FROM MEDTRONIC; (E) RETINAL IMPLANT (ARGUS II) FROM SECOND SIGHT MEDICAL PRODUCTS; (F) COCHLEAR IMPLANT FROM OTICON MEDICAL; (G) VAGUS NERVE STIMULATOR FROM CYBERONICS; (H) SPINAL CORD IMPLANT FROM ABBOTT.....11

FIGURE 2-2: ANIMAL RFID IMPLANTED CHIP: (A) GLASS TAGS ANIMAL IMPLANTED CHIPS WITH DIFFERENT DIMENSIONS FROM HID GLOBAL; (B) A MODEL OF THE ANIMAL IMPLANTED CHIP WITH THE INJECTION SYRINGE NEEDLE [46]; (C) 3D VIEW OF THE ANIMAL IMPLANTED TAG [47]. .....15

FIGURE 2-3: THE REPORTED TRANSDUCER SHAPES, MODULATION SCHEMES AND PROTOTYPES. (A) THE NUMBER OF PUBLICATIONS VERSUS PIEZOCERAMIC TYPES THAT HAVE BEEN USED FOR ULTRASOUND COMMUNICATION IN THE LAST 10 YEARS; (B) MODULATION SCHEMES THAT HAVE BEEN USED FOR ULTRASOUND COMMUNICATION; (C), (D) EXAMPLES OF ULTRASOUND TRANSDUCERS; (E) EXAMPLES OF TRANSDUCERS WITH ACTIVE CIRCUITRY, THE TRANSMITTER (LEFT) AND THE RECEIVER (RIGHT) OF THE SYSTEM USING OFF-CHIP SONOMICROMETRY PIEZOELECTRIC TRANSDUCER [66]; (F) PCB TRANSCEIVER FOR INTRABODY COMMUNICATION USING TUBE PIEZOELECTRIC TRANSDUCER [42]; (G) FULLY PACKAGED PCB IMPLANTED DEVICE FOR ULTRASOUND DATA COMMUNICATION USING PLATE PIEZOELECTRIC TRANSDUCERS [68]; (H) FULLY PACKAGED IMPLANTED NEURAL DUST, CUBE PIEZOELECTRIC TRANSDUCER IS EMPLOYED [82]. .....22

FIGURE 2-4: THE ACHIEVED DATA RATE OF THE REPORTED TRANSDUCERS VERSUS THE PUBLICATION YEAR, RED COLOUR DEVICES ARE INDICATING THE OMNIDIRECTIONAL TRANSMISSION (I.E., IN MANY DIRECTIONS) AND BLUE DEVICES INDICATE THE DIRECTIONAL TRANSMISSION. PRIOR TO 2017, ALL RESEARCH WAS DONE WITH DISC SHAPED TRANSDUCERS. SUBSEQUENTLY, THERE HAVE BEEN A VARIETY OF FORM FACTORS.....24

FIGURE 2-5: A COMPARISON OF PENETRATION DEPTH AND ANTENNA AREA FOR (A) ULTRASOUND (B) *RF* COMMUNICATIONS. AN ARBITRARY TRANSDUCER SIZE LIMIT WAS SET OF  $100\text{ mm}^2$  ( $10 \times 10\text{ mm}$ ) TO ALLOW PROPER COMPARISON. AN EXAMPLE FROM THIS FIGURE IS REFERENCE [68] WHICH DEMONSTRATED AN ULTRASONIC DEVICE WITH  $1.48\text{ mm}^2$  ANTENNA AREA AND  $2.5\text{ MHz}$  OPERATION FREQUENCY CAN COMMUNICATE AT  $85\text{ mm}$  DISTANCE IN CASTOR OIL. .26

FIGURE 2-6: A COMPARISON BETWEEN THE ULTRASOUND AND *RF* DEVICES. (A) EXPLORES THE TRANSMISSION DISTANCE VERSUS THE CARRIER FREQUENCY FOR THE PUBLISHED EXPERIMENTAL SETUP DATA. TO PROVIDE CONTEXT, THE RESULTS ARE COMPARED WITH SOME REPORTED INDUCTIVE *RF* LINKS. TWO DOMAINS ARE HIGHLIGHTED: IN RED IS THE TRANSMISSION DISTANCE PROVIDED BY *RF* WITHIN THE  $100\text{ mm}^2$  ARBITRARY SIZE LIMIT. IN BLUE IS THE TRANSMISSION DISTANCE PROVIDED BY ULTRASOUND WITHIN A DEFINED SIZE LIMIT. IT CAN BE CONCLUDED THAT FOR SHORT TRANSMISSION DISTANCES, AND WITHIN THE  $< 10\text{ MHz}$  OPERATING FREQUENCY, ULTRASOUND PROVIDES A NICHE BEYOND A FEW

TENS OF MILLIMETRES; (B) SHOWS ULTRASOUND AND *RF* ANTENNA AREA RANGE FOR DIFFERENT FORM FACTORS; (C) ULTRASOUND PUBLISHED DATA 3D REPRESENTATION THAT COMPARES ANTENNA AREA, DATA RATE AND PENETRATION FOR THE REPORTED EXPERIMENTAL DATA AT OPERATING FREQUENCY  $< 2.5\text{MHz}$ ; (D) ULTRASOUND PUBLISHED DATA 3D REPRESENTATION THAT COMPARES ANTENNA AREA, DATA RATE AND PENETRATION FOR THE REPORTED EXPERIMENTAL DATA AT OPERATING FREQUENCY  $> 2.5\text{MHz}$ ; (E) *RF* PUBLISHED DATA 3D REPRESENTATION THAT COMPARES ANTENNA AREA, DATA RATE AND PENETRATION. IT IS IMPORTANT TO HIGHLIGHT THAT THE PRESENTED *RF* DATA IS FOR OPERATING FREQUENCY  $< 10\text{MHz}$ , *RF* ANTENNAS CAN OPERATE UP TO *GHz* FREQUENCIES. .... 30

FIGURE 2-7: KEY DATA RATE AND ERROR RATE OF ULTRASOUND COMMUNICATIONS: (A) UNCORRECTED DATA RATE (I.E. INCLUDING ERROR), EXCLUDING REFERENCE [42], VERSUS THE OPERATING RESONANCE FREQUENCY OF THE REPORTED DEVICES, THE DOTTED LINE REPRESENTS THE LIMIT FROM THE PUBLISHED DATA TO DATE; (B) EXPLORES BOTH THE DATA RATE (LEFT Y-AXIS, BLUE CIRCLES) AND *BER*, (RIGHT Y-AXIS, RED TRIANGLES) VERSUS TRANSMISSION DISTANCE. BLUE HIGHLIGHT IS FOR WHERE ULTRASOUND SHOWS SUPERIOR PROPERTIES OVER *RF* COMMUNICATIONS UNCORRECTED DATA RATE AND BIT ERROR RATE, EXCLUDING REFERENCE [42], AS A FUNCTION OF DISTANCE INTO THE TISSUE. IT CAN BE SEEN THAT FOR SHORT DISTANCES BELOW  $40\text{mm}$ , IT IS GENERALLY BETTER TO USE OPTICAL OR *RF* METHODS. .... 33

FIGURE 2-8: THE EFFECT OF MODULATION TYPE ON THE DATA RATE AND BIT ERROR RATE WITH DISTANCE. MODULATION TYPES: *OOK, QAM, QPSK, PPM, ASK* – AMPLITUDE SHIFT KEY, *OFDM*. .... 36

FIGURE 3-1: ULTRASONIC DIGITAL TRANSMISSION BLOCK DIAGRAM, ILLUSTRATES THE MAIN BUILDING BLOCKS OF THE SYSTEM. .... 47

FIGURE 3-2: ULTRASOUND PROPAGATION TWO MODES: (A) LONGITUDINAL WAVES PROPAGATION TYPE WHICH CAN BE TRAVEL THROUGH DIFFERENT MATERIALS SUCH AS SOLID, GASES AND WATER; (B) SHEAR WAVE PROPAGATION TYPE, THE SHEAR WAVES CAN PROPAGATE IN SOLID MATERIALS ONLY; (C) SINUSOIDAL WAVES REPRESENTATION. .... 51

FIGURE 3-3: RESONANCE MODES OF THE PIEZOELECTRIC CRYSTAL; (A) THICKNESS EXTENSION MODE; (B) RADIAL EXTENSION MODE; (C) LENGTH EXTENSION MODE; (D) THICKNESS SHEAR MODE; (E) TRANSVERSE LENGTH MODE, IN THIS MODE THE WAVE MOTION DIRECTION IS VERTICAL TO THE OSCILLATION DIRECTION. THE BLUE SIDE INDICATES THE ELECTRODE POSITION IN THE TOP AND BOTTOM OF EACH GEOMETRY. SEVERAL TYPES OF RESONANCE CAN BE EXISTING IN THE SAME GEOMETRY AS CAN BE SEEN IN DISC SHAPE CRYSTAL (B) WHICH HAVE BOTH THICKNESS AND RADIAL EXTENSION MODES. .... 53

FIGURE 3-4: THE FREQUENCY RESPONSE OF TWO TRANSDUCERS THAT HAVE THE SAME CENTRE FREQUENCY. IT IS OBVIOUS THE DIFFERENCE BETWEEN THE DAMPED AND UNDAMPED TRANSDUCER, THE UNDAMPED TRANSDUCER PROVIDES HIGH AMPLITUDE OVER A NARROW BANDWIDTH WHEREAS THE DAMPED TRANSDUCER PROVIDES A LOWER AMPLITUDE OVER A BROADER BANDWIDTH [102]. .... 57

FIGURE 3-5: HUMAN BODY MODEL THAT SHOWS THE DIGESTIVE AND RESPIRATORY SYSTEMS. AIR FILLED CAVITIES AND BUBBLES ARE LOCATED MAINLY IN THE LUNGS AND INTESTINE WHICH MAKE THE ULTRASOUND SIGNAL SUFFERS FROM HIGH ATTENUATION. .... 60

FIGURE 3-6: SHOWS THE MULTIPATH PROPAGATION PHENOMENON WHICH IS ONE OF THE MAJOR ISSUES THAT INFLUENCE THE ULTRASOUND COMMUNICATION LINK, THE MULTIPATH EFFECT PRODUCES ATTENUATED REPLICAS OF THE ORIGINAL PRIMARY SIGNAL SPACED IN TIME. A FINITE MULTIPATH DELAY SPREAD WILL APPEAR AS SPARSE TRAINS OF DISCRETE ARRIVALS ECHOES THAT NEED TO CONSIDER IN THE RECEIVER DESIGN. .... 63

FIGURE 3-7: FADING CHANNEL CLASSIFIED INTO TWO MAIN TYPES: LARGE AND SMALL SCALE FADING. THE SMALL SCALE FADING INCLUDES MULTIPATH FADING THAT CHARACTERISED BY EITHER FLAT FADING OR FREQUENCY SELECTIVE FADING. .... 65

FIGURE 3-8: PHASE SHIFT KEYING DIGITAL MODULATION THAT MODULATES THE DATA BITSTREAM WITH THE CARRIER SIGNAL, THE CARRIER SIGNAL ILLUSTRATES HOW THE BINARY 0s AND 1s CAN BE ENCODED.....68

FIGURE 3-9: FREQUENCY SHIFT KEYING DIGITAL MODULATION THAT MODULATES THE DATA BIT STREAM (TOP) WITH THE CARRIER SIGNAL (BOTTOM), THE CARRIER SIGNAL ILLUSTRATES HOW THE BINARY 0s AND 1s CAN BE ENCODED BY ASSIGNING THE HIGH-FREQUENCY COMPONENTS TO THE BINARY BIT 1 AND THE LOW-FREQUENCY COMPONENTS TO THE BINARY BIT 0. ....69

FIGURE 3-10: AMPLITUDE SHIFT KEYING DIGITAL MODULATION THAT MODULATES THE DATA BIT STREAM (TOP) WITH THE CARRIER SIGNAL (BOTTOM), THE CARRIER SIGNAL ILLUSTRATES HOW THE BINARY 0s AND 1s CAN BE ENCODED AND FORM THE CARRIER-ENVELOPE THAT HELPS THE RECEIVER TO DEMODULATE THE SIGNAL. ....70

FIGURE 3-11: ON-OFF KEYING DIGITAL MODULATION THAT MODULATES THE DATA BITSTREAM WITH THE CARRIER SIGNAL, THE CARRIER SIGNAL ILLUSTRATES HOW THE BINARY 0s AND 1s CAN BE ENCODED. ....71

FIGURE 3-12: CARRIER SIGNALS TO MODULATE THE DATA AND CREATE *QAM* SYMBOLS FOR TRANSMISSION. THE TWO CARRIER SIGNALS IN PHASE (COSINE) AND QUADRATURE (SINE) ARE SHIFTED IN PHASE BY  $90^\circ$  PHASE SHIFT DIFFERENCE.....72

FIGURE 3-13: CONSTELLATION MAPPING POINTS OF THE 16-QAM THAT SHOW THE GRAY MAPPING OF THE IN PHASE AND QUADRATURE POINT, EACH POINT REPRESENTS ONE COMPLEX SYMBOL WITH POSSIBLE VALUES FOR  $A_q$  AND  $B_i$  TO BE  $(- + 1, - + 3, \dots)$ . ....73

FIGURE 3-14: NOISE SOURCES THAT AFFECT THE ANALOGUE AND DIGITAL COMMUNICATION SYSTEMS, THE NOISE SOURCE IS CLASSIFIED INTO TWO MAIN TYPES INTERNAL AND EXTERNAL. THE INTERNAL NOISE CAN BE REDUCED BY CAREFUL DESIGN OF THE SYSTEM CIRCUIT. CROSSTALK (HIGHLIGHTED) IS ONE OF THE EXTERNAL NOISE SOURCES THAT EXPLAINED IN DETAIL IN THE NEXT SECTION. ....76

FIGURE 3-15: TAXONOMY OF ERROR DETECTION AND CORRECTION CODES, IT DIVIDED INTO TWO MAIN TYPES: ERROR DETECTION CODES AND ERROR DETECTION AND CORRECTION CODES [143]. ....82

FIGURE 3-16: SYSTEMATIC BLOCK CODE STRUCTURE. THE REDUNDANT BITS CAN BE APPENDED TO THE FRONT OR BACK OF THE MESSAGE BITS.....83

FIGURE 3-17: ERROR CORRECTION CAPABILITY AND PARITY BITS OF THE *RS* CODE, THE PARITY BITS WILL BE ADDED TO THE PAYLOAD AT THE BEGINNING OF THE END OF THE PACKET (SYSTEMATIC). THE CORRECTION CAPABILITY SHOWS THE MAXIMUM NUMBER OF BITS THAT CAN BE CORRECTED FOR GIVEN PARITY BITS.....86

FIGURE 3-18: THE TIMING DIAGRAM FOR THE SYSTEM THAT INCLUDES TWO PHASES (A) THE SENSOR ACQUIRING DATA PROCESS THAT STARTING BY REQUESTING THE DATA FROM THE SENSOR UNIT, THE DATA WILL BE PROCESSED AND STORED TO BE TRANSMITTED LATER; (B) REPRESENTS THE ULTRASOUND COMMUNICATION LINK BETWEEN THE MASTER AND SLAVE SYSTEMS OR VICE VERSA. POWER CYCLING IS EMPLOYED TO REDUCE THE CURRENT CONSUMPTION BY SWITCHING BETWEEN THE NORMAL RUN AND VERY LOW POWER MODES. ....90

FIGURE 3-19: (A) PACKET STRUCTURE FOR THE ULTRASOUND DATA TRANSMISSION WHERE EACH NODE RECEIVES ITS PACKET SEPARATELY. THE PACKET INCLUDES THREE MAIN PARTS: HEADER, PAYLOAD, AND THE ERROR CORRECTION CODE. THE DOWNLINK TERM REPRESENTS THE MESSAGING FROM THE CENTRAL UNIT TOWARD THE BIOELECTRONIC NODES; (B) THE REVERSED DIRECTION IS REFERRED TO BY THE UPLINK TERM.....91

FIGURE 3-20: STATE TRANSITION DIAGRAM FOR THE COMMUNICATION MODE BETWEEN THE CENTRAL UNIT AND BIOELECTRONIC NODE, THIS MODE TRIGGERED BY SENDING A COMMAND BY THE CENTRAL UNIT TO THE TARGETED BIOELECTRONIC NODE WHICH REPLIES BY SENDING THE DATA STORED IN ITS MEMORY. THE RESPONSE TIME OF EACH NODE IS SEPARATED FROM

OTHER NODES BY THE SEPARATION TIME ( $T_s$ ) DEDICATED THE SYNCHRONIZATION MODE TO PREVENT ANY POSSIBLE INTERFERENCE.....	93
FIGURE 3-21: STATE TRANSITION DIAGRAM FOR THE REPORTING MODE: (A) DEPICTS REPORTING MODE INITIALIZATION, WHERE A COMMAND SENT BY THE CENTRAL UNIT TO DEDICATE T VALUE WHICH INDICATES THE REPETITION FREQUENCY. THIS VALUE IS STORED IN THE LOCAL TIMER; (B) DEPICTS THE REPORTING MODE WHERE THE LOCAL TIMER WAKES UP THE BIOELECTRONIC NODE EVERY T TIMES. ONCE IT WAKES, THE NODE COLLECTS DATA, STORE IT AND SEND IT BACK TO THE CENTRAL UNIT. ....	95
FIGURE 4-1: BLOCK DIAGRAM OF THE WHOLE SYSTEM SHOWING THE THREE MAIN PARTS OF THE IMPLANT, THE ONE-DIRECTIONAL ULTRASOUND COMMUNICATION LINK THAT OPERATES AT 320 KHZ RESONANCE FREQUENCY AND DRIVEN BY THE ANALOG FRONT END ELECTRONICS WHICH INCLUDES THREE STAGES FILTERS AND AMPLIFIER, THE EMBEDDED CONTROL SYSTEM WHICH DIGITIZES AND PROCESS THE DATA, AND THE SENSORS UNIT.....	97
FIGURE 4-2: THE OMNIDIRECTIONAL ULTRASOUND TRANSDUCER (A) RADIAL MODE VIBRATION OF THE ACTIVE ELEMENT, DIMENSIONS: $w_1 = 2.5\text{ mm}$ , $w_2 = 3.5\text{ mm}$ (B) STEPS THAT USED TO IMPLEMENT AND ENCAPSULATE THE TRANSDUCER, ASSEMBLY THE ACTIVE ELEMENTS ON THE CNC MACHINED METAL MOLD. THEN, THE ACTIVE ELEMENT ALIGNED IN THE CENTRE OF THE MOLD WITH A 1MM GAP AND THE SET IS FILLED WITH POLYURETHANE; (C) BARE PIEZOELECTRIC CRYSTAL OF HEIGHT $h = 3\text{ mm}$ AFTER THE SCRAPPING WITH EMERY PAPER; (D) WIRE BONDING THE INNER AND OUTER DIAMETER ELECTRODE; (E) THE TRANSDUCER FINAL SHAPE AFTER CURING. ....	99
FIGURE 4-3: SIDE VIEW OF THE PIEZOELECTRIC CRYSTAL THAT SHOWS THE WIRE BONDING IN THE INNER AND OUTER DIAMETERS IN THE TOP EDGES. ....	101
FIGURE 4-4: (A) THE SOLDER DOT OF THE OUTER DIAMETER OF THE CRYSTAL, THE MAXIMUM SOLDERING HEIGHT IS $1.2\text{ mm}$ ; (B) THE HEIGHT AND WIDTH OF THE SOLDERING AREA OF THE POINT HIGHLIGHTED IN (A); (C) MEASUREMENTS OF THE SOLDERING AREA THAT HIGHLIGHTED IN RED, THE VOLUME, SURFACE AREA AND CROSS-SECTION AREA WERE MEASURED. THE RATIO BETWEEN THE SOLDERING AREA AND THE CRYSTAL IS % 0.65.....	102
FIGURE 4-5: TRANSDUCER IMPEDANCE MEASUREMENTS BEFORE ENCAPSULATION: (A) THE IMPEDANCE MAGNITUDE MEASUREMENTS VERSUS FREQUENCY SWEEP FOR AN UNDAMPED (UNLOADED) TRANSDUCER IN THE AIR; (B) THE IMPEDANCE PHASE MEASUREMENTS VERSUS FREQUENCY OF UNDAMPED TRANSDUCER IN AIR. ....	104
FIGURE 4-6: (A) ENCAPSULATED TRANSDUCER IMPEDANCE MAGNITUDE BEHAVIOUR VERSUS FREQUENCY IN AIR AND WATER; (B) ENCAPSULATED TRANSDUCER PHASE RESPONSE VERSUS FREQUENCY IN AIR AND WATER.....	105
FIGURE 4-7: CALIBRATION SETUP FOR THE DESIGNED ULTRASOUND TRANSDUCER. THE TRANSDUCER AND THE HYDROPHONE WERE IMMersed IN A WATER TANK WITH A $0.5\text{ m}$ DISTANCE IN BETWEEN. SIGNAL CONDITIONING WAS USED FOR THE HYDROPHONE RECEIVED SIGNAL TO REDUCE THE OUTSIDE OF THE DESIRED FREQUENCY RANGE. ....	107
FIGURE 4-8: THE CONDITIONED HYDROPHONE RECEIVED SIGNAL, THE SIGNAL HAS $2.7\text{ V}$ AMPLITUDE AND THE RESULT SHOW THE FIRST PATH SIGNAL THEN FOLLOWED BY THE MULTIPATH 'ECHOES'. ....	109
FIGURE 4-9: FREQUENCY SPECTRUM OF THE HYDROPHONE RECEIVED SIGNAL. IT CAN BE SEEN THAT THE MAXIMUM FREQUENCY PEAK AT $320\text{ kHz}$ , THE SPECTRUM SHOWS THE DAMPED TRANSIENT PARTS AROUND THE RESONANCE FREQUENCY.....	110
FIGURE 4-10: THE DESIGNED AFE CIRCUIT SCHEMATIC THAT REQUIRED AT THE RECEIVER SIDE, THE TRANSDUCER IN THE RECEIVING OPERATION DRIVEN BY THREE STAGES FILTERS AND AMPLIFIER, THE FIRST STAGE IS BROADBAND BANDPASS FILTER AND THE SECOND AND THIRD STAGES ARE MULTIPLE FEEDBACK FILTERS DESIGNED TO ACHIEVE THE REQUIRED GAIN AT THE GIVEN CENTRE FREQUENCY.....	112

FIGURE 4-11: SIMULATED MAGNITUDE AND PHASE RESPONSES OF THE FIRST STAGE BANDPASS FILTER, THE ACHIEVED GAIN WAS 19 dB AND THE PASSBAND WAS 590 KHZ.....	115
FIGURE 4-12: AC RESPONSE SIMULATION RESULTS OF THE MULTIPLE FEEDBACK FILTERS: (A) THE MAGNITUDE RESPONSE OF THE TWO BANDPASS FILTERS, STAGGER TUNED TECHNIQUE HAS BEEN EMPLOYED TO ACHIEVE THE REQUIRED CENTRE FREQUENCY AND GAIN; (B) PHASE RESPONSE OF THE BANDPASS FILTERS.....	116
FIGURE 4-13: FREQUENCY RESPONSE SIMULATION OF THE THREE STAGES AMPLIFICATION AND FILTRATION, THE ACHIEVED GAIN IS 40 dB AT FREQUENCY OF 320 kHz AND 50 kHz BANDWIDTH.....	117
FIGURE 4-14: BLOCK DIAGRAM OF THE WHOLE SYSTEM FOCUSING ON THE EMBEDDED CONTROL UNIT WHICH CAN COLLECT THE RECORDED NEURAL DATA FROM THE RECORDING CHIP, THEN DIGITIZES AND PROCESS THE DATA FOR THE ULTRASOUND COMMUNICATION LINK. THE PMC SUPPLIES THE SYSTEM WITH THE REQUIRES POWER USING 3.7 V RECHARGEABLE BATTERY.....	119
FIGURE 4-15: ULTRASONIC AFE PCB DESIGN WITH AN AREA OF 351.67 mm <sup>2</sup> , THE PCB IMPLEMENTED FOR EXAMINING THE AC AND TRANSIENT RESPONSE OF THE FILTER AND AMPLIFIERS AND TO EXAMINE THE CHANNEL CHARACTERISTICS.....	120
FIGURE 4-16: THE DESIGNED PCB FOR THE OVERALL SYSTEM WITH (40 × 50 × 1.55) mm DIMENSIONS, THE SYSTEM PROTOTYPE HAS BEEN DESIGNED TO EXAMINE THE SYSTEM PERFORMANCE IN TERMS OF ULTRASOUND COMMUNICATION, ENERGY AND CHANNEL EFFECT.....	121
FIGURE 4-17: (A) AND (B) THE DESIGNED PCB FOR THE OVERALL SYSTEM WITH (50 × 40) MM DIMENSIONS. THE ULTRASOUND TRANSDUCER WIRE BONDING SHOWN IN (A) AND ENCAPSULATIONS OF THE ULTRASOUND AFE SHOWN IN (B).....	121
FIGURE 4-18: ULTRASOUND COMMUNICATION SOFTWARE ALGORITHM FOR BOTH THE TRANSMITTER AND RECEIVER.....	123
FIGURE 5-1: SIMULATED AND MEASURED FREQUENCY RESPONSE OF THE DESIGNED AMPLIFIER AND MULTIPLE FEEDBACK BANDPASS FILTER, THE GAIN IS 36 dB AT 320 kHz AND THE BANDWIDTH IS 50 kHz.....	127
FIGURE 5-2: CHANNEL IMPULSE RESPONSE OF THE EXPERIMENT SETUP. THE FIRST CHANNEL SHOWS THE TRANSMITTED SIGNAL OF 320 kHz FREQUENCY AND 1.8 V AMPLITUDE. THE SECOND CHANNEL SHOWS THE RECEIVED ACOUSTIC SIGNAL AND THE MULTIPATH, THE RESULTS WERE CAPTURED WITH THE AID OF AVERAGING.....	128
FIGURE 5-3: SIGNAL TO NOISE RATIO AGAINST THE DISTANCE FOR DIFFERENT TRANSMISSION VOLTAGES 1.8, 3.3 and 20V. IT CAN BE SEEN THAT A SLIGHT DECAYING IN THE SNR AS THE DISTANCE INCREASES.....	129
FIGURE 5-4: THE TIME CONSUMED FOR THE 5 CYCLES TRANSMITTED BURST TO ARRIVE AT THE RECEIVER AS A FUNCTION OF DISTANCE. IT CAN BE SEEN THAT FOR DIFFERENT TRANSMISSION VOLTAGES (1.8, 3.3 and 20) V THE TIME FOR THE TRANSMITTED SIGNAL IS SIMILAR. THE TIME CONSUMED FOR THE SIGNAL TO TRAVEL TO THE RECEIVER INCREASES AS THE DISTANCE INCREASE.....	130
FIGURE 5-5: TRANSMISSION LOSS THROUGH THE CHANNEL DURING THE TRANSMISSION AS A FUNCTION OF THE DISTANCE BETWEEN TX AND RX, IT CAN BE SEEN THAT THE POWER LOSS INCREASES AS THE DISTANCE BETWEEN THE TRANSMITTER AND RECEIVER INCREASES.....	131
FIGURE 5-6: TRANSIENT RESPONSE OF THE FIRST EXPERIMENT SETUP IN SALINE, 5 CYCLES OF SINE WAVE BURST ARE TRANSMITTED AT 320 kHz AND 3.3 V AMPLITUDE, THE RECEIVED SIGNAL SHOWS THE ELECTROMAGNETIC CROSSTALK THAT APPEARED EXACTLY IN THE SAME TIME OF THE TRANSMISSION, THEN FOLLOWED BY THE ULTRASOUND TRAINS OF SIGNALS. SIGNAL CAPTURED WITH THE HELP OF AVERAGING.....	132

FIGURE 5-7: (A) BLOCK DIAGRAM OF THE EXPERIMENTAL SET-UP FOR THE ULTRASOUND COMMUNICATION LINK, MEASURED RESULTS WERE RECORDED AS A FUNCTION OF THE DISTANCE BETWEEN THE TX AND RX; (B) THE EXPERIMENTAL SET-UP OF THE COMMUNICATION LINK AND THE TANK OF DIMENSIONS (50 x 30 x 25) cm WAS UTILISED FOR MIMICKING THE HUMAN TISSUE ENVIRONMENT. BOTH THE TRANSMITTER AND RECEIVER WERE GROUNDED WITH THE SALINE IN ORDER TO PREVENT ANY CHANCE OF THE ELECTROMAGNETIC CROSSTALK. .... 133

FIGURE 5-8: (A) OPERATION TRANSIENT RESULTS OF THE PROPOSED SYSTEM, TRACE 1 REPRESENTS THE TRANSMITTED PULSES AT 320 kHz, TRACE 2 IS THE RECEIVED SIGNAL AFTER FILTERING THE OUT OF OPERATION BAND NOISE AND AMPLIFICATION AND SHOWS THE MULTIPATH EFFECT, TRACE 3 IS THE OUTPUT OF THE COMPARATOR AND THE TRACE 4 SHOWS THE RECEIVED 16 bits; (B) PRESENTS THE DIRECT PATH AND MULTIPATH SIGNALS, A GUARD INTERVAL OF 1 ms INSERTED AT THE RECEIVER TO MITIGATE THE MULTIPATH EFFECT..... 135

FIGURE 5-9: ULTRASOUND SIGNAL TRANSMISSION EXEMPLAR THROUGH TISSUE PHANTOM FOR TWO DIFFERENT TRANSMISSION PULSES; (A) ONE PULSE GENERATED AT THE TRANSMITTER; (B) SIX PULSES TRANSMITTED THROUGH THE CHANNEL. IT CAN BE SEEN THAT THE SIGNAL AMPLITUDE HIGHER WHEN SIX PULSES WERE TRANSMITTED. .... 137

FIGURE 5-10: MAXIMUM AMPLITUDE AT THE RECEIVER FOR THE PRIMARY PATH AND THE FIRST MULTIPATH SIGNALS AS A FUNCTION OF NUMBER OF PULSE CYCLES AT THE TRANSMITTER. SIX PULSE CYCLES WERE EMPLOYED IN THE TRANSMITTER AS IT ACHIEVES HIGH AMPLITUDE AT THE RECEIVER..... 138

FIGURE 5-11: (A) SNR AS A FUNCTION OF DISTANCE, A GRADUAL DECREASE IN SNR PERFORMANCE CAN BE NOTICED AS THE DISTANCE BETWEEN THE TX AND RX INCREASES; (B) LATENCY OF THE ULTRASOUND SIGNAL WHEN GENERATED BY THE TX AND AFTER IT RECEIVED BY THE RX THROUGH THE CHANNEL AS A FUNCTION OF DISTANCE..... 141

FIGURE 5-12: DATA THROUGHPUT VERSUS THE DISTANCE BETWEEN THE TRANSMITTER AND RECEIVER FOR DIFFERENT PAYLOAD BYTES SIZE. .... 143

FIGURE 5-13: (A) MEASURED BER PERFORMANCE OF THE ULTRASOUND COMMUNICATION LINK VERSUS THE SNR FOR UP TO 30 cm DISTANCE IN MULTIPATH CHANNEL, RESULTS PRESENTED WITH AND WITHOUT RS CODE; (B) MEASURED PER VERSUS THE SNR FOR UP TO 30 cm DISTANCE IN MULTIPATH CHANNEL, RESULTS PRESENTED WITH AND WITHOUT RS CODE..... 145

FIGURE 5-14: (A) MEASURED BER PERFORMANCE OF THE ULTRASOUND COMMUNICATION LINK VERSUS THE NORMALISED Eb/N0 IN MULTIPATH CHANNEL, RESULTS PRESENTED WITH AND WITHOUT RS CODE; (B) MEASURED PER VERSUS THE NORMALISED Eb/N0 IN MULTIPATH CHANNEL, RESULTS PRESENTED WITH AND WITHOUT RS CODE. .... 146

FIGURE 5-15: (A) CURRENT CONSUMPTION OF BOTH THE TRANSMITTER AND RECEIVER, THE ASIC UNIT CONSUMES 35 µA, THE US ELECTRONICS AT THE RECEIVER ONLY CONSUME 250 µA, THE MICROCONTROLLER OPERATES IN THREE POWER MODES TO SAVE THE ENERGY IT CONSUMES 15 mA, 500 µA IN TX ONLY AND 3.5 µA FOR THE RUN, LISTEN AND STANDBY MODES RESPECTIVELY; (B) ENERGY PER BIT FOR THE TRANSMITTER AND RECEIVER, THE MICROCONTROLLER CONSUMES (482 and 232) nJ PER BIT AS A TRANSMITTER AND RECEIVER RESPECTIVELY, THE TRANSDUCER ENERGY IS 160 nJ PER BIT AND FINALLY THE RECEIVER US ELECTRONICS ENERGY PER BIT 412 nJ. .... 149

FIGURE 6-1: (A) SIDE VIEW WITH MM DIMENSIONS OF THE MINIATURISED SYSTEM; (B) TOP VIEW 3D MODEL OF THE SYSTEM BEFORE THE PASSIVATION THAT SHOWS THE MAIN UTILISED COMPONENTS AND HOW IT CAN BE MINIATURIZED TO BE INJECTABLE..... 153

FIGURE 6-2: THE KEY DIFFERENCE BETWEEN THE PPM AND DPPM, IT CAN BE SEEN THE DPPM REMOVE THE OFF PERIOD THAT FOLLOWED AFTER THE ON THE PULSE. Tm REPRESENTS THE MAPPING DURATION. .... 156

FIGURE 6-3: BIT ENCODING OF THE *DPPM*, TRACE 1 SHOWS THE TRANSMITTER PULSES STARTED BY THE SYNCH PERIOD, TRACE 2 SHOWS THE RECEIVER *AFE* AND TRACE 3 SHOWS THE DETECTED PULSES AT THE RECEIVER. .... 158

## List of Tables

TABLE 1-1: TABLE OF CONTRIBUTION. ....	7
TABLE 2-1: OVERVIEW OF MEDICAL COMMUNICATIONS IMPLANTS. ....	13
TABLE 2-2: EXPLAIN THE PROS AND CONS OF OPTICAL, <i>RF</i> AND ULTRASOUND COMMUNICATION LINKS.....	18
TABLE 2-3: SUMMARY OF ALL REPORTED ULTRASONIC TRANSDUCERS THAT HAVE BEEN EMPLOYED FOR COMMUNICATION LINKS. ....	21
TABLE 3-1: ULTRASOUND PROPERTIES IN DIFFERENT TISSUE TYPES [103]. ....	49
TABLE 3-2: PIEZO TRANSDUCER OPERATIONAL MODES. ....	52
TABLE 3-3: ULTRASOUND ATTENUATION COEFFICIENTS, TAKEN FROM [103, 115]. ....	55
TABLE 3-4: COMPARISON BETWEEN BLOCK CODES AND CONVOLUTIONAL CODES.....	85
TABLE 4-1: THE TUNED RESISTORS AND CAPACITORS VALUES OF THE <i>AFE</i> . ....	112
TABLE 4-2: OP-AMP KEY SPECIFICATION EMPLOYED FOR THE <i>AFE</i> DESIGN. ....	114
TABLE 5-1: SYSTEM PROTOTYPE MAIN SPECIFICATIONS. ....	125
TABLE 5-2: MICROCONTROLLER CURRENT CONSUMPTION IN THREE OPERATION MODES. ....	147
TABLE 6-1: ENCAPSULATION MATERIALS AND THEIR ACOUSTIC IMPEDANCE.....	154
TABLE 6-2: 2-DPPM BIT MAPPING.....	157
TABLE 6-3: MEASURED CURRENT CONSUMPTION OF THE MKL02Z32VFK4 MICROCONTROLLER. ....	159





# Chapter 1. Introduction

## 1.1 Introduction

Bioelectronic medicine is potentially a significant new therapeutic contribution to the treatment of chronic disease. The basic concept (also sometimes referred to as electroceuticals) is to stimulate the body's organs via the autonomic nervous system to modulate the body's biochemistry and thus treat diseases. If the modulation can be closer to the required biochemistry and better match the body's rhythms, then it might prove superior to pharmaceutical treatments for certain chronic disease conditions [1]. Therefore, a significant research effort is being undertaken in the bioelectronics domain. The key target is for those with chronic conditions such as diabetes [2], inflammatory bowel disease [3], lupus [4] and arthritis [5] and other age-related conditions. In the longer term, bioelectronic therapies may help with healthy ageing, even in relatively athletically active individuals [6].

The vagus (or 10<sup>th</sup> cranial) nerve has been proposed as the primary stimulus point for bioelectronic medicine. The vagus nerve controls a significant proportion of the parasympathetic nervous system. Stimulation of this nerve can, therefore, result in modulating the activity of downstream organs to achieve therapy. However, an important development is to progress from open-loop, pacemaker type, stimuli to closed-loop control methodologies which modify therapeutic stimuli according to need. Such systems will therefore also need sensors from perhaps downstream organs which can provide physiological information. Examples include blood oxygen and glucose levels, heart rate, chemical sensing, mechanical motion, and bioelectronic activity [7, 8].

Short term percutaneous power and data cabling can be acceptable for implantable systems that are utilised for days or perhaps a few weeks. However, a break in the skin barrier for longer than that presents an infection risk. As such, the most common form of transcutaneous communication—i.e., between outside and inside the body is via radio frequency (*RF*) methods. Such communication must adhere to MedRadio/Industrial Scientific and Medical (ISM) bands such as (402–405 MHz), (902–928 MHz) and 2.4 GHz. However, the body's absorption of radio waves increases with frequency [9, 10]. At lower frequencies in the kHz range, such as that

used in sacral stimulators, deep penetration can be used. However, efficient antennae scale inversely with frequency and can be very large in the cm-scale in the *kHz* range [11]. This is not desirable for long term mm size bioelectronic implants. Furthermore, for an arrangement as per Figure 1-1 (c), intrabody communication is required between a master system and bioelectronics nodes. Transmission distances between these devices can be in the tens of centimetres, making optical and near field *RF* methods unsuitable.

## 1.2 Motivation and Challenges

The main Bioelectronic therapies would need to comprise an Active Implantable Medical Device (*AIMD*) which can gather information, perform processing, and determine stimulus. The architecture of *AIMDs* typically consists of a hermetic implantable pulse generator (*IPG*) unit with leads to a neural stimulator (or recorder) that is implanted into the target tissue. The configurations vary according to the application.

The concept of bioelectronic medicine is, therefore, to apply therapeutic protocols to the peripheral nervous system to bring the body back to an ideal state. In its simplest form, this involves an implant similar to the *IPG* described above with electrodes stimulating the vagus nerve. However, to tune such systems, it can be desirable to monitor the effects on downstream organs and the body's chemistry. An architectural variation could, therefore, be to have a distributed system of devices communicating with a central host. In such a scenario, it would be undesirable to have internal wiring across the body. Therefore, it can be envisaged that such systems could communicate over an intrabody network.

The different approaches to *AIMD* communications can be seen in Figure 1-1. In the first instance (a) some systems may have subcutaneous, or sub-muscular transducers which allow for per-cutaneous communications between the implant and external devices. Examples include retinal prosthetics where an antenna is typically placed in a thin subcutaneous region behind the ear or pacemaker *IPGs* which are implanted in the chest. The second instance (b) is similar to the first, but the device may be much deeper. Examples include spinal stimulators for pain relief and bladder incontinence implants. The last case (c) is still conceptual. However, in this case, implants in one part of the

body may periodically transmit data to a central device that collates data and determines therapeutic intervention.

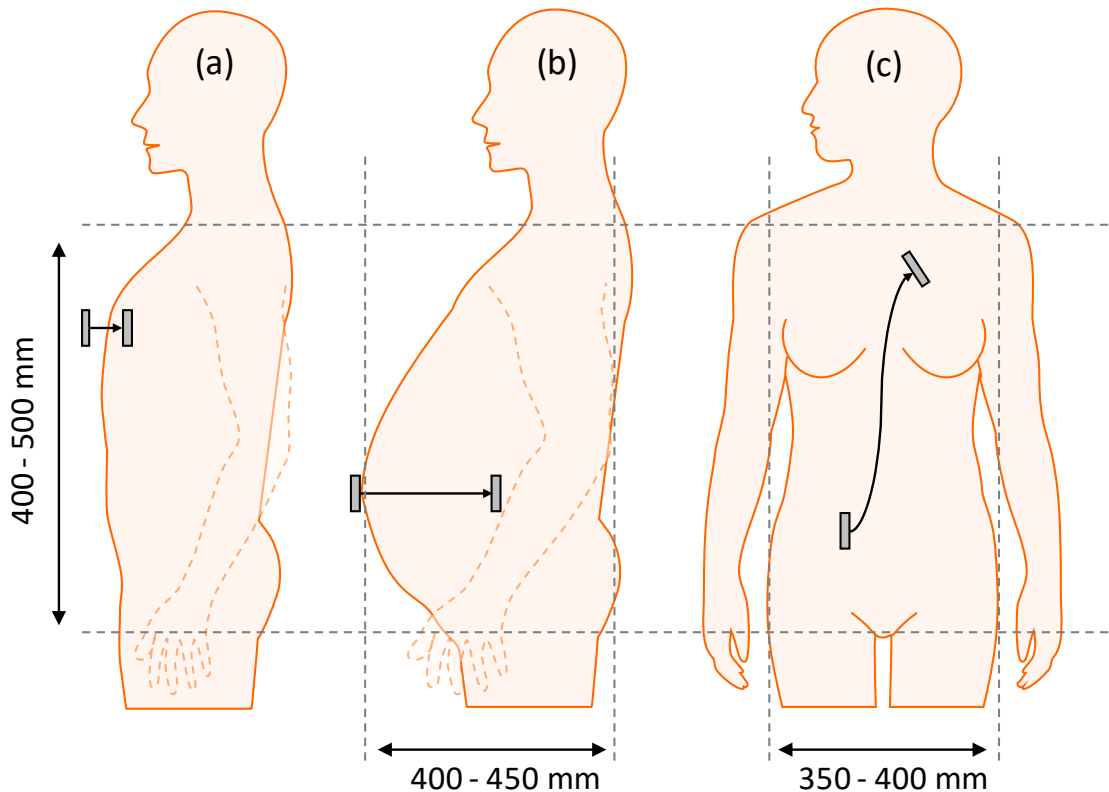


**Figure 1-1: Per-cutaneous and intra-body communications. (a) Shallow sub-cutaneous and sub-muscular communications. (b) Deep communications to in body implants. (c) Intra-body communications between implantable nodes [12].**

In the literature, 27 devices used in tissue phantom experimental setup were explored since 2010, those devices are implemented as a benchtop or Printed Circuit Board (*PCB*) or Application Specific Integrated Circuit Chip (*ASIC*). There are further analysis and graphical comparison for those devices in the next chapter. Most of the reported devices, however, did not consider the following points and challenges:

1. From these past efforts, directional piezoelectric transducers (i.e. plate and disc shapes) are more efficient for point to point data communication over short distances. However, over longer distances, if the plates become directionally misaligned, then the communication would become problematic especially for intra body communication scenario (see Figure 1-1 (c)). In such instances, non-

directional transmitters and receivers would be a more efficient method to achieve error-free data.

2. Most of the researchers used transducers that operate at *MHz* range operating frequency (i.e. *1 MHz* operating frequency). Hence, the high operating frequency is more prominent to attenuation over long transmission depth. Moreover, most of the proposed transducers form factor are disc form as these were readily available and employed for ultrasound imaging efforts.
3. The researchers transmitted raw data that does not include issues such as error correction/detection overhead, synchronisation overhead and packet losses. As such, further improvements need to be made to the error detection and correction protocols either on application-specific circuits or programmable digital logic such as microcontrollers. There is also significant development to be made in the core ultrasound communications before it can be considered for medical devices. In particular, although errors can be acceptable in collected data, the transmission of intervention protocols needs to be error-free – e.g. whether to release or not release a drug, or the stimulus intensity. As such, further improvements need to be made to the error detection and correction protocols either on application-specific circuits or programmable digital logic such as microcontrollers.

### **1.3 Thesis Contribution**

As downstream organs are geographically separated by tens of centimetres, a possible architecture is for a central implant unit together with satellite units called bioelectronic nodes (*BeNs*) which provide sensing and perhaps stimulation. This configuration can be seen in Figure 1-2. Ideally, such bioelectronic nodes would be injected to their target locations rather than be surgically inserted. As such, the devices would need to be in the mm size range. Such devices would have small batteries and thus be limited in operation. i.e., duty cycles would be for a few milliseconds each hour or day. However, such operation is sufficient for bioelectronic therapies which only need to infrequently monitor physiological responses.

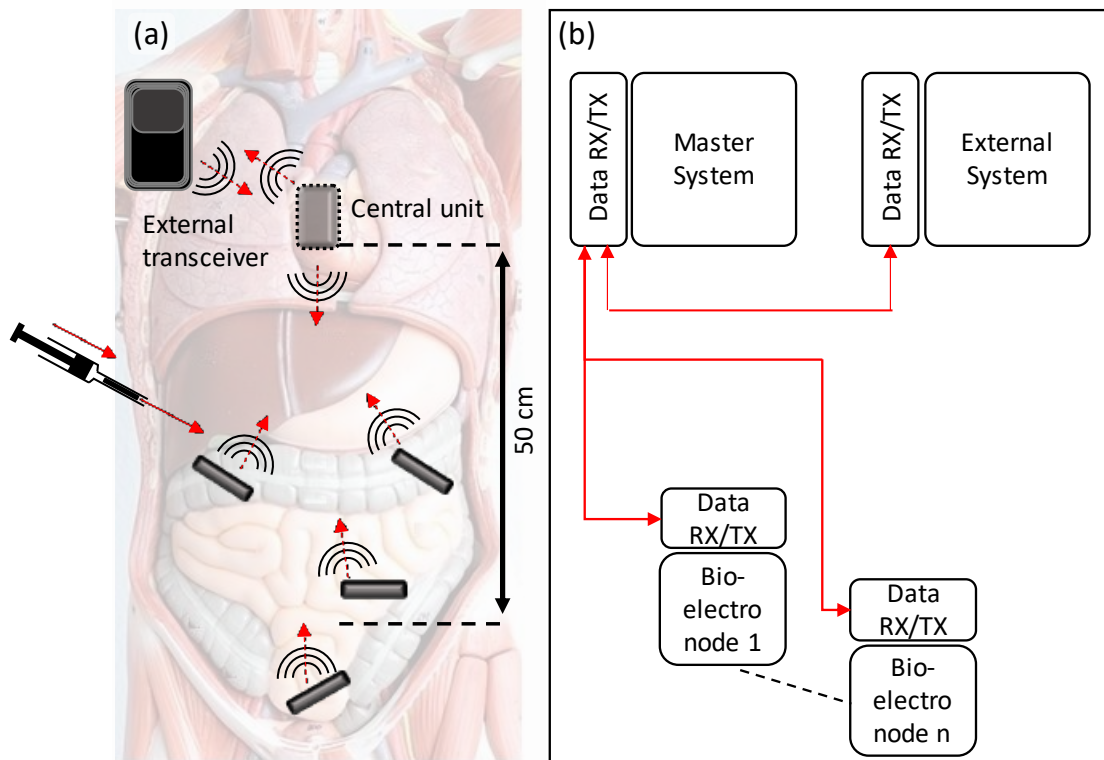


**Figure 1-2: Concept image of how the implants can be embedded inside the human body and scale down to be injectable, the slave system implants will be capable of collecting the sensed data and transmit the information to the central unit (master) that embedded inside the chest. The latter will communicate with the external transceiver.**

This thesis presents the following main contributions and key hypothesis:

1. Design and testing of a reliable and efficient ultrasonic communication telemetry. Miniaturised piezoelectric tube form transducers were employed with dimensions of  $(3 \times 3.5 \times 2.5) \text{ mm}$ , the selected transducers operate at  $320 \text{ kHz}$  frequency to reduce the attenuation effect that appears at high operating frequency range ( $\text{MHz}$  range). In terms of the directivity aspect, since the main target is to implement intra body network inside the human body via distributing *BeNs*, the device shape selected carefully to adapt to the human body environment. In particular, the small dimensions and arbitrary orientation of the *BeNs* mean that the directivity cannot be exploited in either the transmitter or the receiver. Therefore, an omnidirectional transducer was employed. As such, the *BeNs* could communicate even when they are distributed over a large distance and arbitrary orientation inside the body.

2. To counter an increasing bit, and thus packet, error rate with distance, error correction encoding scheme has incorporated. Thus, effective and error-free data was demonstrated even at low signal to noise ratio (*SNR*) transmission.
3. Employed a method, using low duty cycle transmission pulse sequences with relaxation intervals, to overcome the multi-propagation path effect that influences the ultrasound communication link and slow down the data rate.
4. The main drivers for the prototype design were the minimisation of hardware complexity and power consumption. At the transmitter, a low duty cycle transmission was employed. As such, the radiated energy per transmission bit is a low proportion of the overall energy per bit (energy efficient). At the receiver circuitry, the chosen modulation was a scheme that could be received with minimal energy and circuit area whilst also being tolerant of the multipath distortions. Additionally, the prototype demonstrates scalability towards low power consumption.

## 1.4 Thesis Summary

The thesis is structured as follows:

- Chapter 2 (Literature Review)  
In this chapter, the devices that have been reported in the literature since 2010 were explored. An empirical review of the state of the art technology and communication protocols is presented, as well as comparing the implications in terms of transmission distance, implant size, and data rate.
- Chapter 3 (Ultrasound Communication System)  
This chapter provides an in-depth analysis of the fundamentals of ultrasound transducers, also the background theory of the ultrasound communication systems.
- Chapter 4 (System Architecture)  
In this chapter, the piezoelectric transducer is implemented and tested in terms of impedance measurements and how it affected by the encapsulation of the transducer. The ultrasound electronics design and simulation results are presented. Moreover, the system *PCB* design and software architecture are presented.

- Chapter 5 (System Level Testing)

In this chapter, the transducer calibration test is performed, also a tissue phantom experimental test is implemented to evaluate the system performance in terms of packet and bit error rate, energy consumption and energy per bit.

- Chapter 6 (Conclusion and Future Work)

This chapter concludes the key contributions of the preceding chapters and highlights the findings of this work. The author also addresses some aspects of future work and highlight some areas where further contribution can be made for this work.

### 1.5 Research Contribution

This research project has taken place in the Electrical and Electronic Engineering Department at the School of Engineering. Two main experimental rigs are implemented for this project, the tissue phantom experiment has taken place in the Neuroprosthesis Lab, and the ultrasound transducer implementation and calibration have taken place in the Sensors, Electromagnetics and Acoustic (SEA) lab. Table 1-1 shows the main team members collaboration.

**Table 1-1: Table of contribution.**

	<b>Banafsaj (Violet) Jaafar (primary)</b>	<b>Others(secondary)</b>
Ultrasound transducers	Design and fabrication	
Transducer electronics	Design, simulation and PCB.	
Experimental setup	Designed and performed the experiments.	
Embedded control unit	The embedded control unit and ultrasound communication link integration.	Embedded control unit utilised from Jun Luo.
Software programming	Software development for the communication link.	
RS code	Implemented MATLAB code.	Reed Solomon- C programming code utilised from Jeff Neasham and then adapted for my system.



## Chapter 2. Literature Review

### 2.1 Introduction

Implantable devices have substantial therapeutic potentials such as providing long-term monitoring and accurate measurement, controlling of living organ or tissue, and a replacement or support of biological organ functionality. Several proposals are developed to be nowadays applications that are used by millions due to their vitality in facilitating a patient's daily life.

Over the past four decades, there has been an increase in the development and utilisation of Implantable Medical Devices. An example of these implanted devices is shown in Figure 2-1:

1. **Deep brain pacemakers** became available in the 1990s [13], and have been used by over 160,000 [14] patients to treat several conditions such as Parkinson's [15], dystonia [16] and epilepsy [17]. The device includes implanting electrodes that placed in a certain area of the brain for stimulation. The electrodes are connected by leads to the *IPG* unit which is powered by a battery [14], see Figure 2-1 (a).
2. **Pacemaker**: The first battery-powered cardiac pacemaker became available in 1969 [18], nowadays pacemaker is a live-saving for many individuals with certain heart conditions and disorders, it consists of a hermetic *IPG* unit with leads to a neural stimulator into the heart tissue, see Figure 2-1 (b).
3. **Implantable insulin pump**: The first implantable insulin pump human trial was in 1980 [19], it includes a battery-powered implanted device that mimics the pancreas by providing the required insulin to the diabetic human, see Figure 2-1 (c).
4. **The sacral nerve stimulator** controls the patient's bladder, bowel, and pelvic functions by electrically stimulating the sacral nerve. Hence, the sensation of bladder fullness will be perceived. The device implanted in the lower side under the skin of the patient's back [20], see Figure 2-1 (d).
5. **Retinal prosthesis** first approved by the food and drug administration (*FDA*) in 2013 [21], retinal implant utilised to restore a limited sight for patients who lost

their vision due to retinitis pigmentosa or age-related macular degeneration. The implant includes eyeglasses that hold a camera, video processing unit and a transmitter, electrode array implanted on the back of the eye to stimulate the retina cells, See Figure 2-1 (e).

6. **Cochlear neuroprosthetics** became available in the 1970s [22] to help patients that suffering from sensorineural hearing loss, it consist of two parts, see Figure 2-1 (f): the first part is external processor unit that sits behind the ear, and the second part is the implanted unit that sends the electrical signals to the cochlea.
7. **Vagus nerve stimulator** first human trial performed in 1988 [23], similar to the pacemaker, it includes *IPG* unit with electrodes connected to the left vagus nerve in the human neck, See Figure 2-1 (g), the *IPG* unit sends mild electrical signals to inhibit the abnormal brain activity such as the epileptic seizures.
8. **Spinal cord stimulators** became available in 1967 [24] for relieving chronic pain by masking the pain signals before they arriving the brain, it consists of *IPG* unit that generates a moderate electric current signal to stimulate the spinal cord, see Figure 2-1 (h).

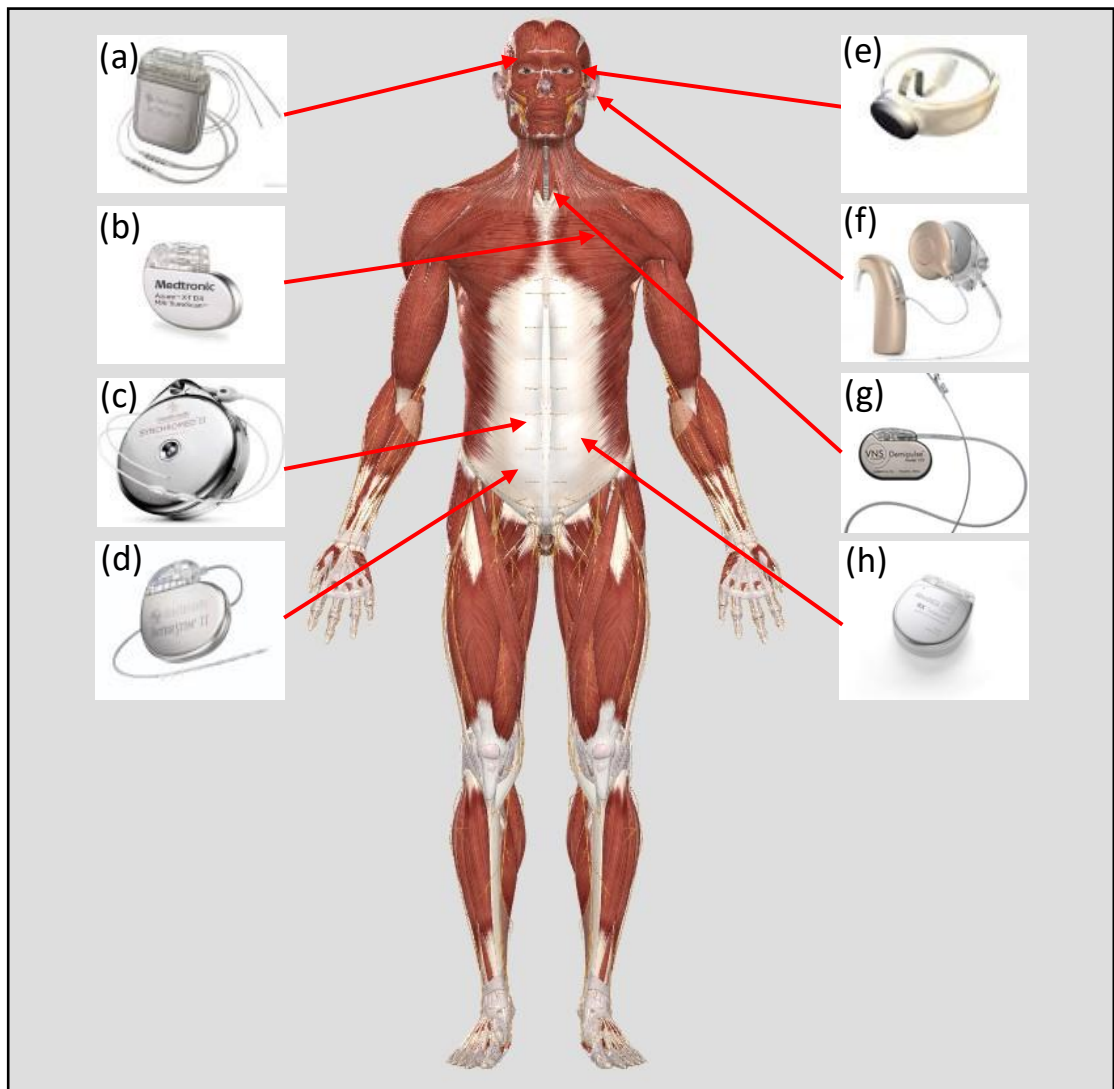


**Figure 2-1: Types of the current implantable devices: (a) Deep brain stimulation implant from Medtronic; (b) Heart pacemaker (Azure) from Medtronic; (c) Implantable insulin pump (Synchromed) from Medtronic; (d) Sacral nerve stimulator from Medtronic; (e) Retinal implant (Argus II) from Second Sight Medical Products; (f) Cochlear implant from Oticon medical; (g) Vagus nerve stimulator from Cyberonics; (h) Spinal cord implant from Abbott.**

## 2.2 IMDs Communication Overview

The architecture of *AIMDs* typically consists of a hermetic *IPG* with leads to a neural stimulator (or recorder) that is implanted into the target tissue. The configurations vary according to the application. For example, Sensory prosthetics require a continuous stream of visual [25] or auditory information [26]. Relatively passive systems such as bladder and bowel incontinence implants [27] require some level of external user

control. Even pacemaker type devices are increasingly requiring sophisticated communication schemes. For instance, pulse generators for conditions such as epilepsy [28] require considerable tuning to the individual. This is best performed after the analysis of significant amounts of the patient's individual brain data. Therefore, such devices transmit significant patient data to online medical clouds on a regular basis. For each of these examples, the current communication protocol is typically *RF*, although, in one of the cases of retinal prosthetics, optical communication is used [29].

A further interesting domain is the relatively new field of 'bioelectronic medicine' [30]. Despite advances in pharmaceuticals, treatments for chronic conditions such as lupus [4], inflammatory diseases [3] and arthritis [31] remain problematic. Such chronic conditions typically occur at later stages in the individual's life and correspond to changes in the body's chemistry and inflammatory systems.

Table 2-1 provides examples of some existing implanted devices, the telemetry distance, and the required communication rate. In nearly all these cases, telemetry is performed via *RF* transmission. *RF* has some significant advantages in moderate to high data rates and has lots of architecture already in place [32]. At lower frequencies, it is possible to penetrate further, albeit at lower data rates. At frequencies less than 1 *GHz*, the transmission is almost always in the near field, which means there are some directional sensitivity and antenna alignment required. Also, operational frequencies are generally limited to those within the MedRadio and *ISM* bands.

Optical transmission is currently clinically limited to one architectural form of the visual prosthesis [29], with transmission through the (transparent) eye. Optical communication in the near infrared is the basis for much of the world's communication architecture and can reach very high data rates. Though in practice power limitations on the implantable side, and challenges in connecting highly collimated beams will reduce the data rates to considerably less than the *Gbits/s* transmission rates that can be achieved in optic fibre networks.

**Table 2-1: Overview of medical communications implants.**

Medical devices	Distance (mm)	Data rate	Comm type	Source
<i>RF communications</i>				
Heart pacemakers	20 – 30	1 <i>Mbps</i>	Percutaneous	[33, 34]
Cochlear prostheses	9	400 <i>kbps</i> 600 <i>kbps</i>	Percutaneous	[35-37]
Implantable pain controllers	10 – 12	-	Percutaneous	[37, 38]
Sacral neuromodulation implant	20	-	Percutaneous	[39]
Retinal prosthesis	20 – 50	2.5 <i>Mbps</i>	Percutaneous	[37, 40]
Neural recording implant	20	3 <i>Mbps</i>	Percutaneous	[41]
<i>Optical communications</i>				
Retinal prosthetics		> 1 <i>Mbps</i>	Per-ocular	[25, 29]
<i>Ultrasonic communications (currently conceptual)</i>				
Bioelectronic multi-devices	150	1 <i>kbps</i>	Intrabody	[42]

The required data rate for a given *AIMD* can vary widely, depending on the application. Furthermore, the temporal requirement for data rate can be very different. Sensory prosthetics such as vision and cochlear prostheses need a continuous data stream. Other systems, such as pacemakers and pain controllers will typically operate independently, but then transmit stored at specific timepoints. In this case, processing may occur through some form of relay system to a medical cloud for processing. Thus, the data transfer rate may depend on how long an individual is prepared to be stationary to allow reliable transfer to a relay device that transfers data to the cloud.

A further consideration is component size. As bioelectronic interventions increase, there is a desire for simpler, less invasive surgery. As such, it is desirable for devices to be able to be inserted via keyhole surgery or through a simple injection. Such devices need to be similar to the animal radio frequency identification (*RFID*) tags in the shape and size to be inserted with the minor operation, Figure 2-2 presents a model of the animal tags chips. Much of that miniaturisation relates to the battery and power requirements of the device. But as implantable systems become smaller, antenna size becomes increasingly important. Furthermore, implant size has implications for the type of transmission that possible. i.e., small globular implants are more suited to

omnidirectional or semi-directional transmission rather than transmitting all information in a narrow optimal direction.

*RF* transmission is expected to remain the dominant form of per-cutaneous communications – as it has a very strong mixture of high data rate, tolerance to antenna misalignment, and a long history of development. Optical systems may also play a future role in very high data rate transmissions. However, for deeper transmissions, both optical and high frequency *RF* are subject to severe scattering and absorption losses. Low frequency *RF* requires an increasingly large antenna which is not desirable for injectable devices. There should, therefore, be niche domains in which ultrasound may be an attractive alternative. At the current time, there are no clinical systems that utilise ultrasound as a communication method. However, it is widely used for in-body imaging [43], obstetrical ultrasound to monitor the fetus development during pregnancy as well as the mother's uterus and ovaries [44], and finally in some forms of therapeutic intervention such as kidney stone removal [45]. Its physiological effects are well understood, and thus clinical utilisation, especially for monitoring the women and babies during pregnancy, has no inherent regulatory barriers and no known harmful effects on humans.

As such, the objective of this chapter is to take an empirical review of the state of the art to explore which domains ultrasonic communications may be the optimum solution.

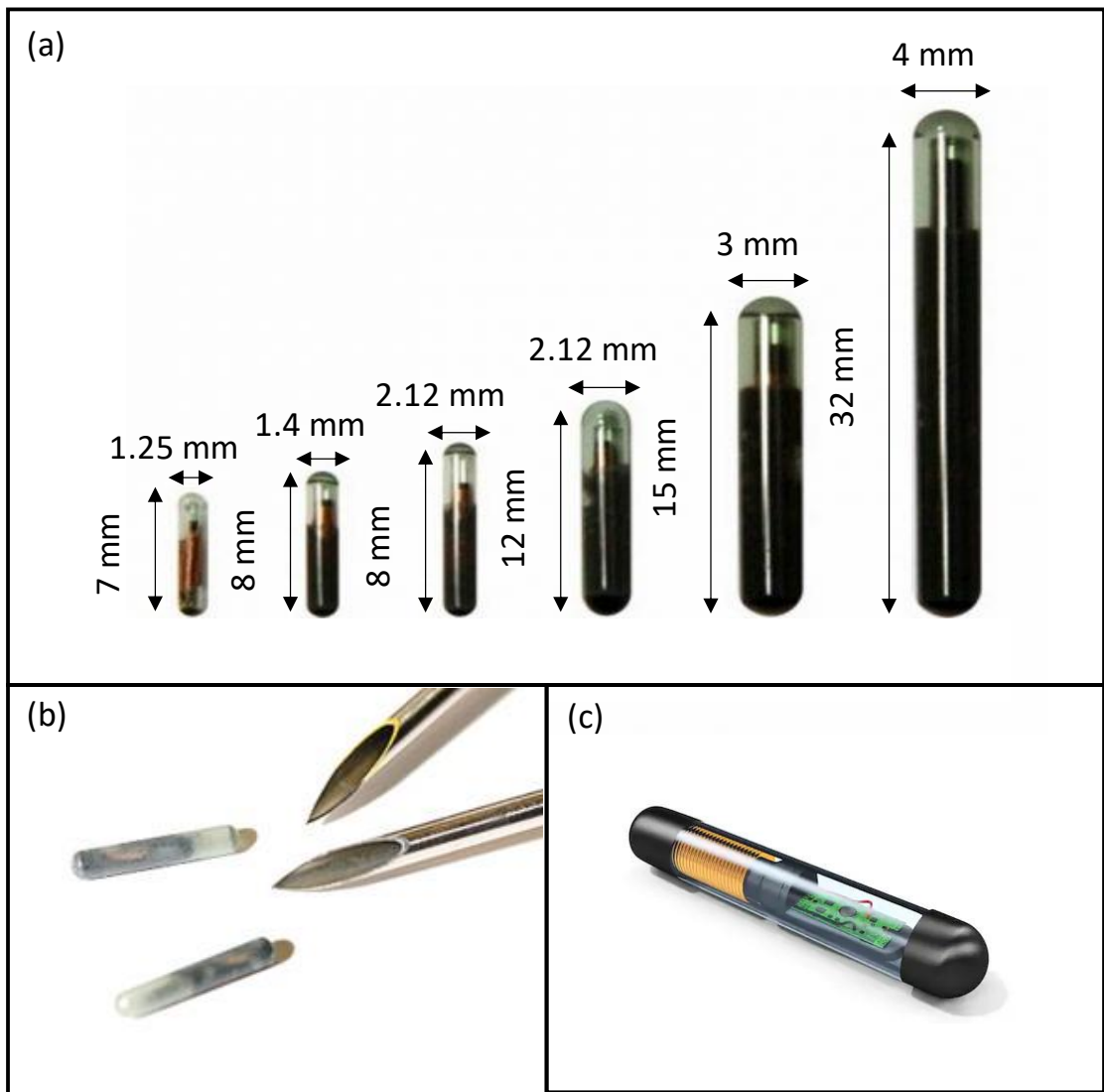


**Figure 2-2: Animal RFID implanted chip: (a) Glass tags animal implanted chips with different dimensions from Hid Global; (b) A model of the animal implanted chip with the injection syringe needle [46]; (c) 3D view of the animal implanted tag [47].**

## 2.3 Comparative Transmission Technologies

There are three primary methods suitable for percutaneous and intra-body communications: Electromagnetic signal transmission in the *RF* domain, optical transmission in the red/near infra-red spectral domain, and ultrasonic transmission.

### 2.3.1 RF Transmission Link

In general, most current medical devices utilise RF methods. RF occupies the frequency range from 3 *kHz* to 300 *GHz* of the spectrum [48].

However, frequencies above 3 GHz are problematic due to absorption in the tissue. Within these frequencies, there are two applicable standards current ISM (6.78, 13.56, 27.12, 40.68, 433.92, 915, 2450, 5725) MHz of channel bandwidth (0.03, 0.014, 0.326, 0.04, 1.74, 26, 100, and 150) MHz respectively and MedRadio (403, 416, 429, 441, 454, + 3) MHz bands, the channel bandwidth of MedRadio bands is ranging between 100 kHz to 6 MHz and is permitted only to the Federal Communication Commission (FCC) authorised health care providers [49, 50].

The wavelengths of the RF in these bands vary between 10 cm (2.4 GHz) and 44 m (6.78 MHz). In general, the antenna is much smaller than these wavelengths. As such, transmission distances can be defined into 3 bands: Where transmission distance  $d \ll \lambda$ , then we define it to be in the (non-radiating) near-field. If  $d \gg \lambda$ , then it is in the (radiating) far-field, and in between is the mid-field [51, 52]. Thus, for almost all cases described in Table 2-1, the 'transmission mode' is in the near field or mid-field.

Near field approaches are used for different applications such as RFID and biomedical applications such as cochlear implants. It should be noted that the energy spreading loss with distance in the near field is  $\frac{1}{r^3}$  compared to  $\frac{1}{r^2}$  for a non-directional beam. So, it operates best over shorter distances. An example of this transmission is from Catrysse et al. who presented an inductive bi-directional data transmission link using 700 kHz operation frequency. The coil's diameters were 60 mm and 20 mm for the primary and secondary respectively. The nominal transmission distance was 30 mm, the achieved data rate is 60 kbps [53]. These dimensions are suitable for larger implants but are more difficult for injectable devices. Jiang et al. [54], presented a Passive Phase Shift Keying (PPSK) modulator for biomedical implants using an inductive link that operates at 13.56 MHz. The coil's diameters were 16 mm for the primary and 25 mm for the secondary to overcome the possible misalignment. They achieved a data rate and bit error rate of 1.35 Mbps and  $10^{-8}$  respectively at 9 mm distance through pork skin. Kiani et al. [55], achieved a higher data rate of 13.56 Mbps with a bit error rate  $10^{-7}$  at carrier frequency 50 MHz by employing a Pulse Delay Modulation (PDM) technique and dual-band inductive link. The downlink communication results were measured at 10 mm distance between the inductive link. The size of the coils for the communication link were (10 × 10) mm and (30 × 30) mm.

The mid-field is the transition between the far-field and near field. Poon et al. [56] explored this domain in the low gigahertz frequency range for both wireless power transfer and data communication. Operating in this frequency range allows miniature millimetre implant size and wider bandwidth (thus higher data rate). Similarly, Yakovlev et al. [57] presented the experiment results in a 3.5 *cm* porcine heart. They achieved 4 to 20 *Mbps* at 1.32 *GHz* operation frequency. However, high tissue attenuation and misalignment are still major challenges in this region [58].

### 2.3.2 Optical Transmission Link

An alternative form of communication is a direct optical link. Optical communications are widely used in the telecoms industry, and 800 – 1300 *nm* optical communications wavelengths match the optimum transmission band in tissue [59]. As such, Liu et al. have demonstrated a peak transmission at 50 *Mbps* up to 4 *mm* depth of tissue [60]. However, this can only be achieved with precise alignment. Such alignment can become increasingly difficult with depth, especially in cases where the implant may undergo some rotation. Non-collimated light emitting diodes (*LEDs*) in comparison typically provide a Lambertian emission sphere, which reduces alignment constraints. But in return, the signal degrades with the square of the depth before tissue scattering effects are considered. As such, significant amplification may be required or else *SNR* can be poor. Given power limits inside the body, this means that the transmission rate will also decay with depth. As such, it is currently being clinically used in a particular form of transmission for retinal prosthetics where infrared pulses act as both power and data through the transparent eye.

### 2.3.3 Ultrasound Transmission Link

The final modality is ultrasound. Ultrasonic imaging is already in widespread clinical use, and its safe operational domains are well characterised, the *FDA* limits the spectral peak temporal average intensity ( $I_{SPTA}$ ) to be 720 *mW/cm<sup>2</sup>* and the mechanical index to 1.9 maximum for safety concerns [61]. To date, there has been some limited exploration of ultrasound for communications [62]. The primary domain for ultrasonic communications has been in the control, monitoring and positioning of underwater instruments and vehicles. This is the case because such waves experience vastly reduced

absorption loss compared to electromagnetic waves at typical *RF* communication frequencies (especially in seawater due to its high conductivity) and optical communication is also severely limited in range due to scattering by suspended particles [63]. AS such, acoustic waves at frequencies below 100 kHz have been used to carry data. Since human tissue is largely composed of water, and highly conductive, acoustic waves in the ultrasound region are also potentially the most efficient means of communication with deeper implants Figure 1-1 (b) and inter implant Figure 1-1 (c) communication. Table 2-2 presents the advantages and disadvantages of optical, *RF* and ultrasound communication technologies.

**Table 2-2: Explain the pros and cons of optical, *RF* and ultrasound communication links.**

	<b>Optical</b>	<b><i>RF</i></b>	<b>Ultrasound</b>
<b>Mechanism</b>	Electromagnetic	Electromagnetic	Mechanical
<b>Wavelengths</b>	800 -1300 nm	0.1 – 44 m (2450 – 6.78 MHz)	15 – 0.75 mm (100 – 2000 kHz)
<b>Safe limit</b>	360 mW/cm <sup>2</sup> [64]	1.6 W/Kg	720 mW/cm <sup>2</sup> [61]
<b>Advantages</b>	<ul style="list-style-type: none"> <li>• Very high bandwidth and data rate (if collimated)</li> <li>• Provides a miniaturised antenna.</li> </ul>	<ul style="list-style-type: none"> <li>• Regulatory regime well understood.</li> <li>• Existing incumbent technology base.</li> <li>• High data rates.</li> </ul>	<ul style="list-style-type: none"> <li>• Can achieve much deeper penetration.</li> <li>• Transceivers can be very small.</li> <li>• Immunity to the electromagnetic interference of other devices.</li> <li>• Cause minimal tissue heating when operating at low frequencies.</li> </ul>
<b>Disadvantages</b>	<ul style="list-style-type: none"> <li>• High tissue scattering.</li> <li>• Limited effective penetration depth.</li> <li>• Alignment challenges with</li> </ul>	<ul style="list-style-type: none"> <li>• High absorption loss in human tissue.</li> <li>• Supra GHz bands limited by tissue heating effects.</li> <li>• Common ISM frequency bands are susceptible to interference with other <i>ISM</i> devices.</li> </ul>	<ul style="list-style-type: none"> <li>• For longer distances, high tissue scattering.</li> </ul>

	collimated communications.	<ul style="list-style-type: none"> <li>• Leakage of signals in/out the body gives the potential for eavesdropping, spoofing and denial of service attacks.</li> </ul>	
--	----------------------------	---	--

## 2.4 Active Versus Passive Communication

The carrier transmission for data transfer in a biomedical implant is a significant burden in terms of power consumption. Therefore, based on the application and the power budget, passive or active data telemetry can be utilised.

Active communication systems include a power source that can independently transmit the carrier signal at each node. This approach provides robust communication depending on the power expended by the transmission amplifier. As such, optimisation needs to be performed especially on implantable nodes to trade the requirement for low power, with the requirement for an acceptable signal to noise ratio. Furthermore, it means that either sufficient power is being provided to an energy scavenger, and/or a battery needs to be used – adding to implant size.

An alternative approach is to use scavenged energy to modify the properties of a transceiver such that signals are backscattered. If modulated correctly, all the power can be provided from an external transmitter. Thus, the implant can become considerably smaller. This is a significant advantage, leading to ultra-small implants. Nevertheless, there are some disadvantages, such as the backscatter temporal jitter effect that directly influences the retrieval of data. Also, in order to operate effectively, there must be an efficient power-coupling between the external device and an internal device which limits the transmission distance achieved with the passive data telemetry [65]. Therefore, it can only be used for shallow sub-cutaneous and sub-muscular communications scenarios, see Figure 1-1 (a).

## 2.5 Comparison of The State of The Art

27 devices have been explored in the literature since 2010 to understand and inform readers as to the direction of future research. The references [42, 66-90] for these papers have been summarised in Table 2-3 according to their form factor. There is a

further analysis with comparison tables (A-1 to A-6) provided in Appendix A. As such, the data from these tables have been compared in more detail and graphically in the next sections.

Also, the reported ultrasound devices have been compared with some of the reported *RF* inductive devices in references [53, 91-96] which operate up to 10 *MHz*.

Figure 2-3 shows the breakdown of the published papers according to their primary architectural considerations – the transducer form factor and the modulation type. Figure 2-3 (a) shows the breakdown of the number of papers according to the form factor that includes seven different types. As will be discussed, until recently, the most available transducer type was the disc form. Hence, the majority of papers have utilised this transducer form factor.

Figure 2-3 (b) presents the modulation schemes that been used. It should be noted that backscattering is not strictly a modulation type, rather it is a form of transmission (passive rather than active) onto which other modulation can be implemented. But it has been included as only 5 papers have been published in this domain. On-Off Keying (*OOK*) is the most commonly used modulation because it does not require sophisticated hardware to implement. More complex reported schemes include Quadrature Amplitude Modulation (*QAM*), Quadrature Phase Shift Key (*QPSK*), and Orthogonal Frequency Division Modulation (*OFDM*) modulations. These advanced schemes have been employed to increase the data rate. However, more complex hardware and software are required to implement them (particularly the receiver) which in turn can consume more power. An example of omnidirectional transducers that have been employed for ultrasound communication is sonomicrometry and tube shape, which are vibrating under the radial extension mode Figure 2-3 (c,d). Sonomicrometry transducers have been integrated on active Printed Circuit Board (PCB) circuitry Figure 2-3 (e). Similarly, Tube piezoelectric transducer has been integrated with active PCB circuitry for intrabody communication Figure 2-3 (f). Another example is the plate piezoelectric transducers that employed for ultrasound wireless power and data communication and integrated with passive circuitry Figure 2-3 (g). Similarly, cube piezoelectric transducers have been employed for neural dust. In the later case, a backscattering communication approach was adopted Figure 2-3 (h).

**Table 2-3: Summary of all reported ultrasonic transducers that have been employed for communication links.**

Transducer type	Size (mm)	Resonance frequency (MHz)	Modulation	Data rate (kbps)	Transmission distance (mm)	References
Directional disc	Diameter (1.1 – 19)	0.5 – 5	ASK, FSK, PSK, OOK-OFDM, QAM, PPM, OOK – PM, Backscattering.	0.5 – 30,000	10 – 180	[70, 74-81, 83-85]
Directional plate	W(0.55 – 1.44) x L(0.5 – 1.08) x H(0.9 – 1.08)	1 – 2.5	OOK, QPSK	25 – 250	30 – 85	[68, 69, 86]
Directional cube	W(0.75-1.44) x L(0.75-1.44) x H(0.75-1.44)	1 – 1.85	OOK, backscattering	500	8.9 – 60	[71, 82, 87, 90]
Directional PMUT	W(0.5) x L(3) x H(3)	0.6	BPSK, QPSK	298 – 596	50	[72]
Omnidirectional sonometry	1 – 2 (diameter)	1.2 – 1.3	OOK, QAM, OFDM	200 – 1000	30 – 100	[66, 67, 88, 97]
Omnidirectional tube	W(2.5) x L(3.5) x H(3)	0.32	OOK	1 – 70	10 – 360	[42, 73]

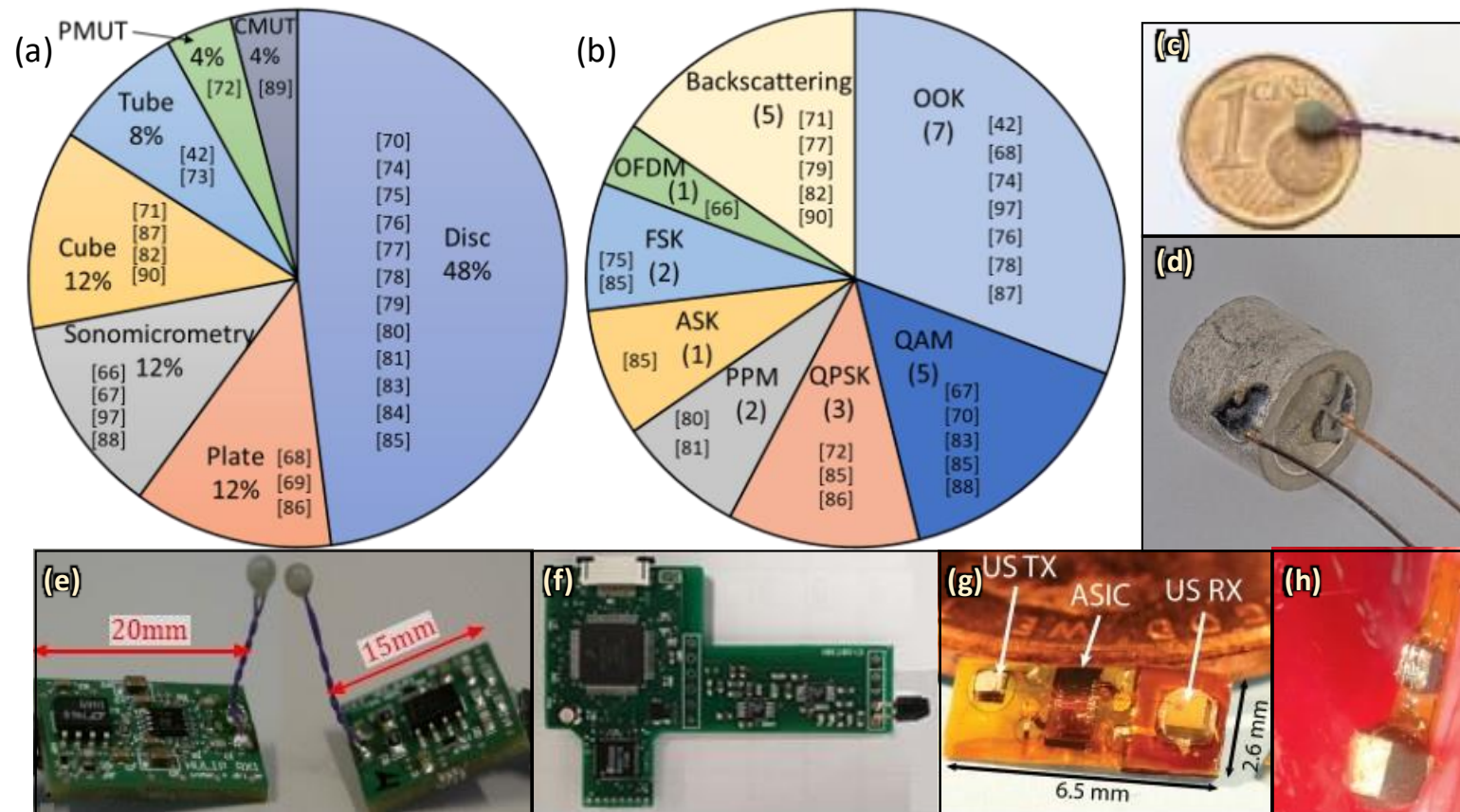


Figure 2-3: The reported transducer shapes, modulation schemes and prototypes. (a) The number of publications versus piezoceramic types that have been used for ultrasound communication in the last 10 years; (b) Modulation schemes that have been used for ultrasound communication; (c), (d) Examples of ultrasound transducers; (e) Examples of transducers with active circuitry, The transmitter (left) and the receiver (right) of the system using off-chip sonomicrometry piezoelectric transducer [66]; (f) PCB transceiver for intrabody communication using tube piezoelectric transducer [42]; (g) Fully packaged PCB implanted device for ultrasound data communication using plate piezoelectric transducers [68]; (h) Fully packaged implanted neural dust, cube piezoelectric transducer is employed [82].

### 2.5.1 Transducer Form Factor Versus Data Rate

A key requirement for any communication system is its data rate. Higher is almost always better for two reasons – (i) it allows more data within a given transmission time limit and (ii) for a given quantity of data, the transmission time is shorter, reducing the transmitter on-time, and thus power consumption.

The first exploration of the ultrasonic communication method for implantable medical devices was in the 2011 publication by Tsai et al. [85]. In that work, and up until 2016, research was performed with directional disc transducers as these were readily available from ultrasound imaging efforts. Since then, several other device form factors have been explored. Figure 2-4 presents the achieved data rate for the reported work in the last ten years. The directivity of the transducers is highlighted in the legend, with blue shapes indicating directional and red indicating omnidirectional.

Over this accumulated effort, the data rate has varied widely between 0.5 to 30000 *kbps*. It is interesting to note that the graph does not show a steadily improving data rate with the publication year. There are a number of interesting reasons for this.

Considering the channel capacity of a communication system is proportion to the bandwidth (which in turn scales with operating frequency) and *SNR*. In the subsequent sections, frequency and bandwidth will be explored, but it should be noted that the signal strength (and thus *SNR*) is determined by how the signal propagates. i.e. if the communication is directional, then there will be more energy received over a defined distance than if it was omnidirectional. As such, the highest data rates have been achieved with (directional) form factors (disc, plate and Piezoelectric Micromachined Ultrasonic Transducers (*PMUT*)). However, it should be further note that it is not just the form factor that determines directionality. Placement of electrodes and the presence of any lensing or reflecting materials will also play a part.

There are also three further confounding factors that will be discussed in more detail:

1. Longer transmission depth and increased operating frequency both reduce the signal due to attenuation.

2. Over longer distances and lower frequencies, there is an increasing probability of multipath effects which causes dispersion in the received pulses (Intersymbol interference (*ISI*)), which will be explained in the next chapter.
3. The data rate quoted on many papers is a raw rate that does not include issues such as error correction/detection overhead, synchronisation overhead and packet losses. Thus, the data throughput in real applications is likely to be substantially lower.

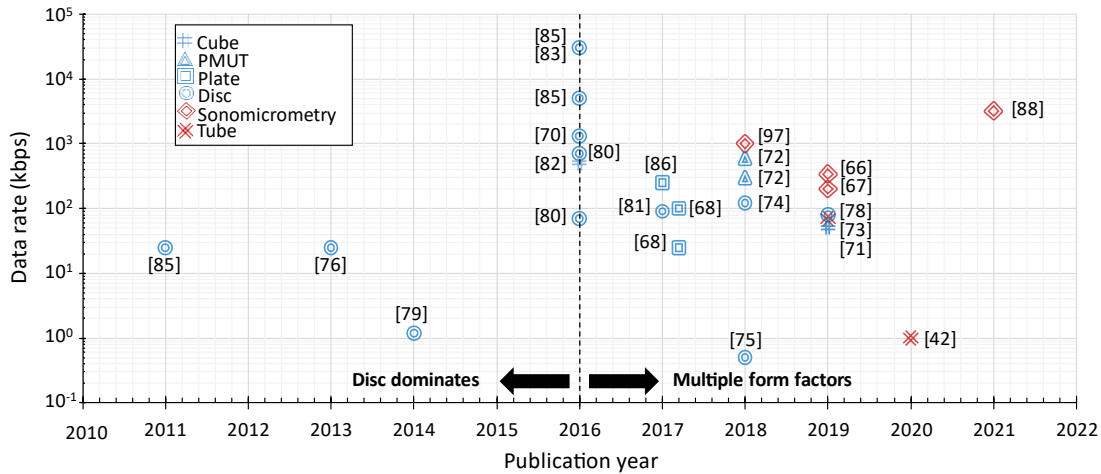


**Figure 2-4: The achieved data rate of the reported transducers versus the publication year, red colour devices are indicating the omnidirectional transmission (i.e., in many directions) and blue devices indicate the directional transmission. Prior to 2017, all research was done with disc shaped transducers. Subsequently, there have been a variety of form factors.**

### 2.5.2 Transmission Distance Versus Transducer Size and Frequency

As per Shannon-Hartley theorem, which will be explained in detail in section 3.7, the data rate of a transmission system depends on bandwidth, which in turn is a function of operating frequency. But when considering frequency, to make a fair comparison, the transmission depth and the transducer size need also to be considered. It is also useful to contrast ultrasound communication links with what is possible with *RF*.

Figure 2-5 shows the relationship between transmission distance (left y-axis, blue circles), Antenna area (right y-axis, red triangles), and operating frequency (x-axis). This is from the published record, so it does not necessarily show minimum limits. However, a graph of the general expected relationship has derived between transmission distance

and operating frequency, and the maximum values from the literature. Also, for comparison, Figure 2-5 (a) shows ultrasound devices, and Figure 2-5 (b) shows some published *RF* devices. An example from this figure is reference [68] which demonstrated an ultrasonic device with  $1.48 \text{ mm}^2$  antenna area and  $2.5 \text{ MHz}$  operation frequency can communicate at  $85 \text{ mm}$  distance in castor oil. An important caveat is that the reported transmission distance does not necessarily represent the transmission limit. In some cases, it was simply the distance at which the experiment was measured. In others, it was whatever distance the authors arbitrarily determined provided an acceptable signal. There is no consistent definition of how to determine the maximum transmission distance in these papers. For an implantable device, an arbitrary transducer (piezoelectric or antenna) was placed with a maximum area of  $100 \text{ mm}^2$  as a guide. Triangles above this line indicate large transducers and those below demonstrate smaller ones.

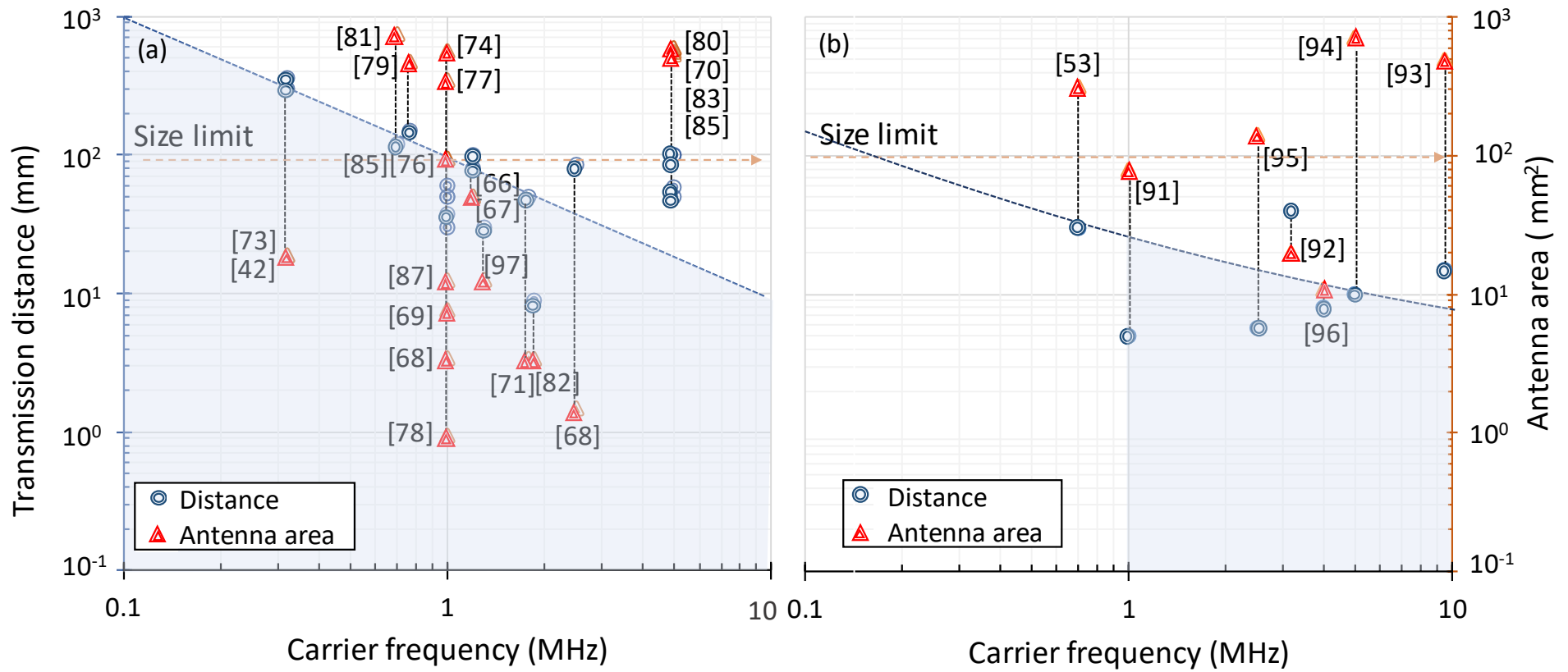


Figure 2-5: A comparison of penetration depth and antenna area for (a) Ultrasound (b) RF communications. An arbitrary transducer size limit was set of  $100 \text{ mm}^2$  ( $10 \times 10 \text{ mm}$ ) to allow proper comparison. An example from this figure is reference [68] which demonstrated an ultrasonic device with  $1.48 \text{ mm}^2$  antenna area and  $2.5 \text{ MHz}$  operation frequency can communicate at  $85 \text{ mm}$  distance in castor oil.

As per equation **3-1**, which will be explained in the next chapter, the absorption of an ultrasonic beam in soft tissue is a function of frequency, with  $\sim 1 \text{ dB per cm}$  for  $1 \text{ MHz}$ . For emitters with dispersive profiles, there is an additional effect of the power being divided by the dispersal surface at a given distance (e.g. for a spherical emission:  $1 / (4\pi r^2)$ ). So, for deeper implants, the power of the transmitter needs to be increased and/or the gain of the receiving amplifier. As such, an analysis of depth is multifunction with power, frequency, and beam shape. However, none of the efforts to date have presented an optimised microelectronic implementation of ultrasonic transceiver electronics, so it is not possible to provide a fair comparison. Therefore, a comparison of what data is available in terms of transmission distance versus frequency is presented in Figure 2-6 (a).

An important caveat for Figure 2-6 (a) is that the reported transmission distance does not necessarily represent the transmission limit. In some cases, it was simply the distance at which the experiment was measured. In others, it was whatever distance the authors arbitrarily determined provided an acceptable signal such as the transducer natural focus. There is no consistent definition of how to determine the maximum transmission distance (independent of signal strength) in these papers. For example, the Beer-Lambert law suggests a definition of penetration depth where the intensity reaches  $1/e$  ( $-4.3 \text{ dB}$ ) of its original intensity. However, perhaps a more useful definition might be:

$$UPD = -10dB \qquad \qquad \qquad \mathbf{2-1}$$

Where UPD is the ultrasonic penetration depth and  $-10 \text{ dB}$  represents a 90% loss of intensity. This would equate to  $\sim 10 \text{ cm}$  penetration of soft tissue with  $1 \text{ MHz}$  or  $20 \text{ cm}$  penetration at  $500 \text{ kHz}$ , which is broadly in line with what can be seen in Figure 2-6 (a). A relationship for this limit has been sketched in blue. Chang et al. [68] are above the curve, but they used a compound phantom where a kidney ( $2 \text{ dB/cm}$ ) was embedded in a larger much lower attenuating medium ( $0.1 \text{ dB/cm}$ ). The body will likewise have varying attenuation for different tissues, so we should view a  $-10 \text{ dB}$  limit as a guide rather than a fixed boundary.

Although the increasing attenuation can broadly be seen as a negative to the signal to noise ratio and thus the data rate, it has an important secondary effect. Multipath will be longer than the primary path. As such, for higher frequencies, these multipath will attenuate more and, for some systems (certainly shorter distance systems), will significantly reduce the effect. As such, mitigations such as guard intervals can be significantly reduced, thus significantly increasing the data rate.

For comparison, some *RF* references in these frequencies are included. Normally *ISM/MedRadio* operate at much higher frequencies around 400 MHz – 2.4 GHz. But these references provide an empirical view for the crossover between relative penetration depth for ultrasound and *RF*.

Figure 2-6 (b) provides the area of the largest side of the ultrasonic transducers to date (blue circles). For comparison, the sizes of some *RF* antennae (red circles) have also been provided. As there are only a few references for *PMUT* and tube-shaped transducers, these data points have augmented with additional values available from transducer suppliers Meggitt Ferroperm. As can be seen, the minimum area of the antenna tends to around 10 mm<sup>2</sup>. Ultrasound, in contrast, tends to around 1 mm<sup>2</sup>.

There is, however, a caveat for small area ultrasound transducers, which can be seen in equation 3-4 (will be explained in detail in section 3.2.8). If the frequency is 1 MHz ( $\lambda = 1.5\text{ mm}$ ), then for a 1 mm<sup>2</sup> area, the focus is  $\ll 1\text{ mm}$ . i.e. the emission will be dispersive. That will reduce the intensity for a given distance but will also make the implant less dependent on transducer angle.

For a final comparison of the published data, two broad ultrasound scenarios are presented in Figure 2-6 (c,d) along with *RF* Figure 2-6 (e). The lines represent the published data, whereas the yellow regions represent what believe to be the general operating range for each category assuming optimisation. *RF* presents a generally good methodology for all categories. the data rate has extended up to the Mb/s range as this is technically feasible for some of the higher frequency MedRadio bands whilst still being able to penetrate some mm into tissue.

The first ultrasonic domain is presented in Figure 2-6 (c), which can be utilised for deep implants Figure 1-1 (b) and intrabody communication Figure 1-1 (c). Given the longer

distances, lower frequencies between  $0.1 - 2.5 \text{ MHz}$  can be used. The implanted device can thus be very small and penetration depths long. However, in this domain, data rates will likely be low once multipath effects are taken into account.

The first ultrasonic domain is presented in Figure 2-6 (d), which can be utilised for shallow implants Figure 1-1 (a). Given the shorter distances, frequencies  $> 2.5 \text{ MHz}$  can be used, leading to much higher data rates, with a much reduced multipath effect. The implanted device can be small, though the external device is likely to be long to provide a focused beam. If optimised correctly, this domain could realistically compete with *RF*, although the latter is a much more mature technology.

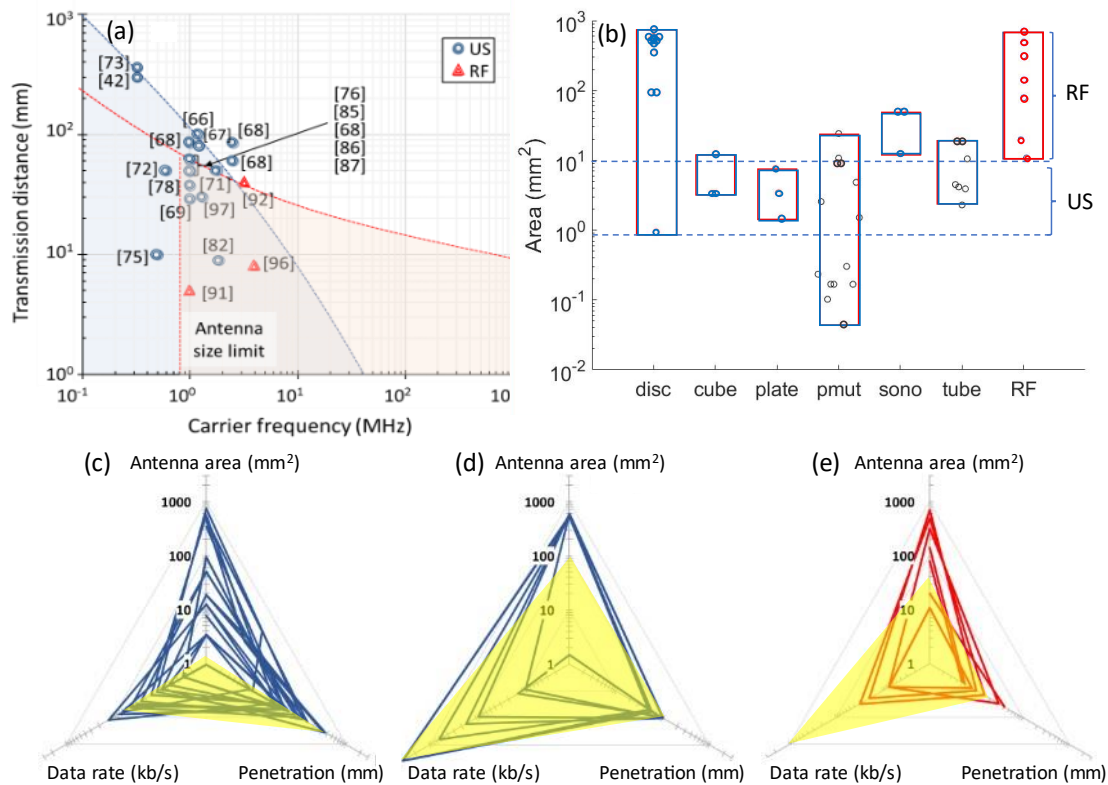


**Figure 2-6: A comparison between the ultrasound and RF devices. (a) Explores the transmission distance versus the carrier frequency for the published experimental setup data. To provide context, the results are compared with some reported inductive *RF* links. two domains are highlighted: In red is the transmission distance provided by *RF* within the  $100 \text{ mm}^2$  arbitrary size limit. In blue is the transmission distance provided by ultrasound within a defined size limit. It can be concluded that for short transmission distances, and within the  $< 10 \text{ MHz}$  operating frequency, ultrasound provides a niche beyond a few tens of millimetres; (b) Shows ultrasound and *RF* antenna area range for different form factors; (c) Ultrasound published data 3D representation that compares antenna area, data rate and penetration for the reported experimental data at operating frequency  $< 2.5 \text{ MHz}$ ; (d) Ultrasound published data 3D representation that compares antenna area, data rate and penetration for the reported experimental data at operating frequency  $> 2.5 \text{ MHz}$ ; (e) *RF* published data 3D representation that compares antenna area, data rate and penetration. It is important to highlight that the presented *RF* data is for operating frequency  $< 10 \text{ MHz}$ , *RF* antennas can operate up to *GHz* frequencies.**

### 2.5.3 Data Rate Versus Frequency and Distance

The other key parameter from equation 3-13, which will be explained in detail in section 3.7, is the bandwidth which scales with the carrier frequency. The literature published to date follows this trend, albeit with wide variation. Figure 2-7 (a) provides a plot of data rate vs carrier frequency for each of the published papers. A boundary line is sketched through the highest reported values to provide a trend.

There are a number of reasons for the large variation in the data. Not all authors have focused on optimising the data rate. More fundamentally, although bandwidth can increase with operating frequency, in practice, there are also other parameters. High Q-factor transducers will provide a greater output signal, but lower transmission bandwidth. Conversely, the opposite is true. Hence, data rate and distance penetration/power are not independent.

A further issue is that with longer distances, there will be increased absorption and dispersion of the beam. Thus, for a given power budget, the *SNR* will be reduced and thus the bit/packet error rate will worsen, thus reducing the effective data rate. The published data points for achieved data rate and bit error rate vs transmission distance can be seen in Figure 2-7 (b). Again, an expected trend line is presented going through the maximum achieved value.

What can be seen from the data is that the correlation between data rate and distance is actually very weak. The reason for this can partially be explained by equation 3-4 which will be discussed in more detail in section 3.2.8. i.e. most of the systems to date have utilised disc type transmitters that can focus ultrasound several *cm* into the tissue. In this case, the losses due to dispersion are relatively low, and thus other factors affecting the data rate are dominant. However, for non-directional approaches and for backscattering, the correlations should be much stronger.

There are also two further considerations with distance:

- i. higher frequencies will attenuate faster with transmission depth compared to lower frequencies.

- ii. over longer distances there is an increasing probability of multipath effects (described below).

Finally, it should be noted that the data rate quoted on many papers is a raw rate that does not include issues such as error correction/detection overhead, synchronisation overhead and packet losses. Thus, the data throughput in real applications is likely to be substantially lower.

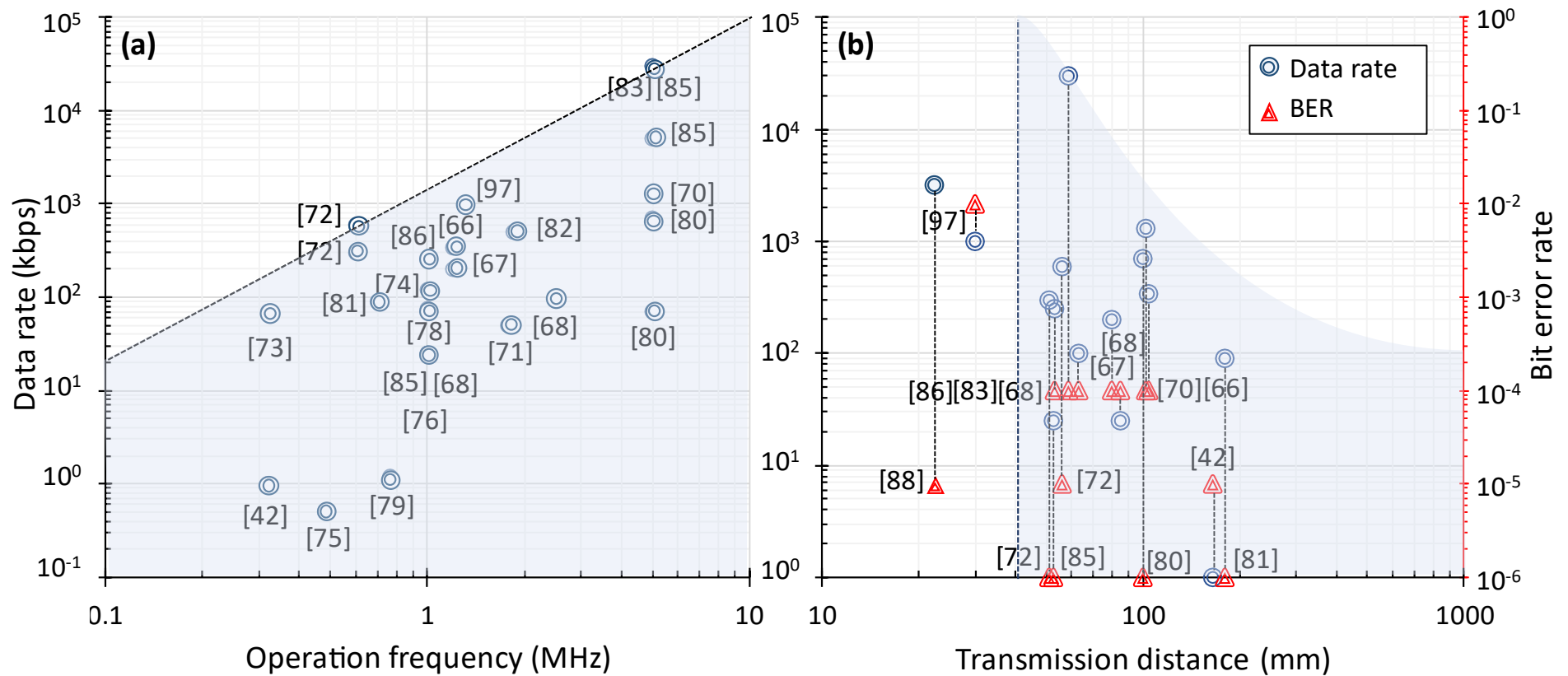


Figure 2-7: Key data rate and error rate of ultrasound communications: (a) Uncorrected data rate (i.e. including error), excluding reference [42], versus the operating resonance frequency of the reported devices, the dotted line represents the limit from the published data to date; (b) Explores both the data rate (left y-axis, blue circles) and *BER*, (right y-axis, red triangles) versus transmission distance. Blue highlight is for where ultrasound shows superior properties over *RF* communications. Uncorrected data rate and bit error rate, excluding reference [42], as a function of distance into the tissue. It can be seen that for short distances below  $40\text{mm}$ , it is generally better to use optical or *RF* methods.

The required data rate for the implanted devices can be determined by the application and not all will require data rates that are as high as those with radio links. Achieving high data rate ultrasonic communication requires a sophisticated modulation scheme that employs multi-carrier transmission and/or channel equalisation which is more challenging in terms of implanted devices due to the high design complexity and energy demand. Conversely, a simple implant system with very low energy requirements and acceptable data rates for many applications can be achieved by adopting schemes with very simple demodulation, such as *OOK* or pulse position modulation (*PPM*), combined with time gating approaches to mitigate multipath effects.

#### **2.5.4 Passive versus active modulation**

Three possible scenarios for ultrasonic communication have presented in Figure 1-1: (i) shallow percutaneous communication (Figure 1-1 (a)) (ii) Deep percutaneous (Figure 1-1 (b)) and (iii) intrabody communications (Figure 1-1 (c)). For the latter active communications are required i.e. both nodes on the communication link need to transmit their signals via amplifiers. However, for the first scenario and potentially the second (depending on depth and optimisation), there is the possibility of using a passive backscattering approach.

Mazzilli et al. [77] presented such a technique. They used a microprocessor to modulate the transducer stiffness, allowing passive data transmission of “1” or “0”. Ozeri et al. [79] used impedance mismatch to modulate the data by increasing the load resistance of the system by nine per cent which results in an increase in the acoustic reflection coefficients by twelve per cent. Finally, a fully passive wireless ultrasonic neural dust for peripheral nervous system recording was presented by Seo et al. [82], in this case, a series of  $6 \times 540 \text{ ns}$  was transmitted every  $100 \mu\text{s}$  by the external transducer and reflected pulse intensities recorded by the external transceiver.

Backscattering is also utilised in the *RF* space, notably with *RFID*. But as per section 2.5.2, the advantage with ultrasonic approaches is that for longer distances ( $>$  a few  $10$ 's of mm) a smaller transducer can be achieved for a similar transmission distance and data rate. However, A further consideration for such approaches is that implant degradation tends to occur due to electrolytic effects under the influence of electric

fields. As such, if implants are not continuously powered, but passively await periodic signals, then their lifetime is effectively extended considerably. Or alternatively, the encapsulation requirements can be significantly relaxed.

### 2.5.5 Effect of Modulation Type

An analysis has provided in Figure 2-8 for *BER* performance (*BER*, left y-axis, red triangles) and data rate (right y-axis, blue circles) as a function of reported distance (x-axis). It is hard to draw direct conclusions from the *BER* data. There is no consistent relationship between published data for *BER* and distance or for transmission type. The relatively consistent *BER* range of  $10^{-6}$  to  $10^{-4}$  indicates that various authors have designed their systems to operate in this range which is a reasonable target for a useful communication link. However, it should be noted that a *BER* of  $10^{-4}$ , though small, represents a 2.5% packet error rate if data was transmitted in 32-byte packets for example. Hence error detection or correction methodologies will certainly need to be included as per [42], especially if the cost of packet retransmissions is to be minimised within the energy budget of a given system.

To summarise, multiple schemes have been used - *OOK*, *ASK* – Amplitude Shift key, and *PPM* – Pulse Position Modulation. Additionally, some more complex symbol schemes have been used: *QAM*, *QPSK*. Unsurprisingly those that used the latter functions achieved higher data rates. With advanced modulation methods, data rates in excess of 10 *Mbits/s* have been achieved. However, there is a question mark as to the energy cost of demodulation for an implant. Programmable digital logic units typically used for prototyping can be very power-hungry, whereas optimised microelectronics much less so. Furthermore, if data transmission can occur over a short time, then wake-up cycles can be much shorter and sleep cycles longer, thus conserving power. Such optimisation analysis has not yet been performed.

A further issue to consider is that in most of the literature to date is that the phantoms used are: (i) relatively homogeneous and (ii) relatively small compared to the man torso. As such, the real world multipath scattering effects may be quite different. Thus, for longer transmission distances and transmission through less homogeneous tissue, these

effects may make the more complex modulation types much more difficult. i.e., bit error rates will increase and thus, effective data rates will decrease.

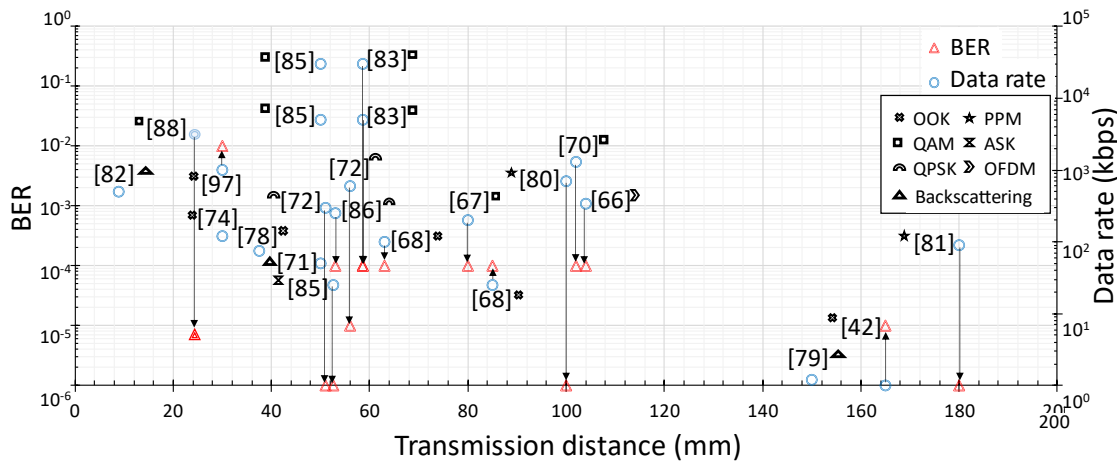


**Figure 2-8: The effect of modulation type on the data rate and bit error rate with distance. Modulation types: *OOK*, *QAM*, *QPSK*, *PPM*, *ASK* – Amplitude Shift key, *OFDM*.**

## 2.6 Previous Reported Work

### 2.6.1 Directional Disc Transducer Form Factor

Most of the reported work has employed the disc shape crystal because multiple off the shelf commercial transducers are available. The disc also allows for directional ultrasound communications. Further summary for the reported devices can be seen in Appendix A (Table A-1).

Tsai et al. [85] demonstrated a prototype that includes ultrasonic data communication and ultrasonic power for neural stimulation application. They used a piezopolymer (*PVDF*) transducer with a 6 mm diameter and 1 MHz operation frequency. An experimental set up presented to examine the prototype using a 5 cm tissue phantom, the achieved data rate for the commands signals was 25 kbps and the BER was  $10^{-6}$ . However, only when the SNR ratio higher than 10 dB and the modulation scheme that they employed based on a fixed time interval which means take into account the off period after one or two sine wave pulses transmitted, in this period the receiver implant

will be on and hence that influence the power consumption. The focus of this paper was to assess the *BER* performance for different coding schemes.

Another study carried out by Keramatzadeh et al. [74] to improve the data rate of multiple data streams for implanted microsystems, taking advantage of the frequency division multiplexing technique. The input serial data bitstream is de-multiplexed into parallel concurrent sub-streams. These concurrent sub-streams are modulated using several subcarriers that were located within the bandwidth of the link. They used a single element commercial transducer *TL1000KA* operate at *1 MHz* resonance frequency. An experiment set up conducted in saline to examine the designed link, the transducers immersed in saline at a distance of *3 cm*. *OOK* modulated is employed to encode the bit streams, eight concurrent bitstreams are transmitted through the ultrasonic link. The achieved data rate per channel was *15 kbps* for each subcarrier. Power consumption study, however, is not reported for this system.

Li et al. [75] presented a study to examine the feasibility of using the ultrasound link for body sensor network, they used two different commercial transducers operated at *500 kHz* and *40 kHz* and examined the communication using *ASK*, *FSK* and *PSK* modulation schemes in both air and water at distance of *10 mm*. They found that *BFSK* achieves better *BER* performance.

Another study performed by Singer et al. [84] presented an *Mbps* data rate of an ultrasonic link which is sufficient for a high definition video stream. *QAM* is employed for the data link, and the resonance frequency of the transducer is *5 MHz*, the transducers placed in a degassed water tank at distance: *5.86 cm*, which is similar to the natural focus of the transducers. Tissue samples of beef liver and pork loin placed between the transducers, the transmitted signal followed by *1 ms* guard interval to overcome the multipath propagation. At the receiver end, the received signal from the transducer was filtered and amplified, then saved for offline computer processing. The achieved data rate was *5 Mbps* and up to *30 Mbps* depends on the modulation order, centre frequency, and symbol rate for both tissue samples. The same research group in [83] implemented the same experiment set up to examine the bit error rate performance. The achieved *BER* was less than  $10^{-4}$  at *5.86 cm* distance. However, for *64-QAM* the *SNR* was not sufficient to perform bit error rate measurement. Also, the

same group presented a method for high bandwidth acoustic communication and power transfer in a patent [98].

High data rate system for wireless intrabody network proposed by Demirors et al. [70], they implemented a software testbed and hardware for the transmitter and receiver, they used frequency division multiplexing signalling scheme and grey-coded modulation schemes to increase the data rate. Their system includes a transducer, switch (switching between the transmitter and receiver), a power amplifier/preamplifier, field-programmable gate array (for the digital signal processing), and PC Matlab processing. They employed a commercial immersion transducer with 5 MHz centre frequency and 9.5 mm diameter. They used human kidney phantom for ultrasound communication link evaluation performed at 10 cm distance. The observed data rate was 28.12 Mbps but on the price of the BER which was  $10^{-1}$  for 128 – QAM, and at  $10^{-4}$  the data rate can be up to 1.3 Mbps for 8 – QAM modulation.

Meng et al. [78] presented a concept design of a gastric seed to treat gastroparesis and functional dyspepsia disorders, they designed ultrasound wireless power and data that includes power management unit and two disc shapes transducers for data and powering that operates at 1 MHz, and they employed time multiplex technique to avoid the interference between the data and power link. The prototype examined in water at 37.5 mm distance. The achieved data rate was 75 kbps at 1 MHz frequency using OOK modulation.

Santagati et al. [80] presented a software-defined testbed architecture for intra-body area network application, they employed ultrasound wideband and medium access control protocols to overcome the multipath and interference. They implement a field-programmable gate array-based system to be used for ultrasound wideband and medium access control protocols implementation. They used human kidney phantom to evaluate the system, the phantom, and coupling gel sandwiched between the transducers that operate at 5 MHz resonance frequency at 10 cm distance. They demonstrated that a high data rate of 700 kbps and a BER of  $10^{-6}$  can be achieved at 40 μW transmit power and 16 dB SNR, or a lower data rate of 70 kbps achieved at a lower transmit power of 8 μW and 9 dB SNR. Also, the same group presented a

reconfigurable implantable medical system for both ultrasonic power control and telemetry in a patent [99].

Low power ultrasonic transmission platform for internet of medical things (*IoMT*) proposed by Santagati et al. in a research paper [81] and a patent [100], they presented a system that includes an implantable device called *IoMT*-mote and a wearable device called *IoMT*- patch, the implanted devices communicate with the wearable device using ultrasonic intra-body communication at 700 kHz resonance frequency. The propagation loss was examined using porcine meat and compared with *RF* 2.4 GHz and 403.5 MHz attenuation losses, the obtained attenuation for ultrasound link was 25 dB at 10 cm distance which is lower than *RF* 2.4 GHz attenuation by 70 dB and *RF* 403.5 MHz *MICS* by 30 dB. Bit error rate performance was examined using thoracic phantom at 18 cm distance for different code length and input power, the achieved bit error rate was  $10^{-6}$  and the data rate was 90 kbps at code length of 1 and input power of 0.1 mW. The packet error rate of *IoMT*- mote is examined for different transmit power and using 12 cm porcine meat, the achieved packet error rate was  $10^{-3}$  at  $-20$  dB input power and for code length and frame of 1.

Ultrasonic data and power link presented by Luo et al. [76], they designed and fabricated in 0.35  $\mu\text{m}$  complementary metal-oxide-semiconductor (*CMOS*) chip that for deep tissue stimulation application. Pulsed *OOK* was adapted to modulate the data, a bit "1" represented by two pulses and a bit "0" represented by one pulse both have a fixed period for the bit which is 40  $\mu\text{s}$ . 1 MHz ultrasound transducer of 6 mm diameters and 2.55 mm thickness employed for the experiment set up. The transducer implanted inside the rat tissue at the focal distance of the transducer 5 cm, the achieved data rate was 25 kbps. However, the authors highlighted that the device could operate at the focal distance only and may not receive the data correctly if the distances vary.

### **2.6.2 Directional Plate Transducer Form Factor**

Further summary for the reported devices can be seen in Appendix A (Table A-2). Jayant et al. [69] presented bi-direction transmission of millimetre size implantable device, they employed ultrasound communication for the downlink data only as it can be used for commands or control signals and they used the *RF* ultra-wideband (loop antenna) for

the data uplink transmission which can be utilised for transmitting sensor data. They employed lead zirconate titanate (*PZT*) transducer that resonates at 1 *MHz* frequency. An experimental set up demonstrated for a fully packaged implant of (4 × 7.8) *mm* size, the implant embedded in 3 *cm* distance of chicken breast, however, no evaluation for the ultrasound communication link in terms of bit error rate, packet error rate and *SNR* was presented.

A fully packaged printed circuit board implant device is presented by Chang et al. [68], they used ultrasound link for wireless data and powering, two piezoelectric transducers employed for bi-directional data link and powering. They utilised two piezoelectric transducers to achieve full duplex. The receiver piezo ceramic transducer operates at 0.95 *MHz* resonance frequency, the transmitter piezo ceramic operates at a higher resonance frequency of 2.5 *MHz*. A fully packaged implant is evaluated in castor oil at 8.5 *cm* depth, the achieved bit error rate was less than  $10^{-4}$  at 15 *dB* signal to interface ratio, which is the same bit error rate achieved at 3.5 *cm* distance and 27.4 *dB* signal to interface ratio.

An acoustic multiple-input/multiple-output (*MIMO*) system proposed by Wang et al. [86], they employed the *MIMO* to increase the data rate for intra-body communication implanted systems, they demonstrated their system in mineral oil at 5 *cm* distance between the transmitter and receiver, they used *PZT* operates in length expander mode and resonate at 1 *MHz* frequency. Two channels of the data stream are modulated with *QPSK* and transmitted through the mineral oil, each channel has a data rate of 125 *kbps* which in total produce 250 *kbps*, the measured *BER* was below  $10^{-4}$ .

### **2.6.3 Directional Cube Transducer Form Factor**

Wang et al. [87] designed an ultrasonic array that of 32 transducer elements to interface wirelessly with miniaturised active implanted devices for data and power exchange, the implant's transducer size is 1.44 *mm*<sup>3</sup> that resonates at 1 *MHz* frequency, they demonstrated the communication link in castor oil at 6 *cm* distance, the data is presented using two modulation scheme *OOK* and *ASK*, the *ASK* demonstrated by disabling elements in the transducer array. Further summary for the reported devices can be seen in Appendix A (Table A-3).

#### 2.6.4 Directional PMUT Transducer Form Factor

Herrera et al. [72] presented high data rate ultrasound communication link using aluminium nitride *PMUT* which can be employed for intrabody networks, they demonstrated real-time video streaming using two *PMUTs* as transmitter and receiver through 5 cm tissue phantom, they compared the *PMUT* with *PZT* transducer (700 kHz centre frequency) in terms of bandwidth and data rate, results showed that *PMUT* provides higher bandwidth by two orders of magnitude than *PZT* transducer. Two different modulation scheme employed to compare between the *PMUT* and *PZT* transducer, the *PMUT* operation frequency was 600 kHz, results show that the data rate was the same for *PZT* and *PMUT* which are 298 kbps and 596 kbps for the binary phase shift keying (*BPSK*) and *QPSK* at the same bandwidth for both 500 kHz, the *PMUT* transmission link, however, achieved *BER* for *BPSK* and *QPSK* was  $10^{-6}$  and  $10^{-5}$  at 35 dB SNR. Further summary for the reported device can be seen in Appendix A (Table A-4).

#### 2.6.5 Omnidirectional Sonomicrometry Transducer Form Factor

Kondapalli et al. [97] proposed a technique to establish a reliable multiple implants communication using sonomicrometry crystals of 1 mm diameter, they employed on-off keying modulation and the transmitted signal at 1.3 MHz frequency, and they present single-crystal communication using chicken breast tissue at 3 cm to 10 cm distance. In addition, they demonstrate multi-access communication telemetry using three transmitters and one receiver, a 16 – bit Walsh- Hadamard orthogonal code employed for data encoding. The *BER*, however, was  $10^{-2}$  at 12 dB SNR, and 800 kbps data rate at 3 cm distance.

*QAM* communication link presented by Bos et al. [67], the proposed system for in-body communication application, they employed omnidirectional transducers that resonates at 1.2 MHz, an experimental set up implemented to examine the communication using gelatine bone phantom at 8 cm distance. The achieved data rate was 200 kbps using 4 – *QAM* modulation, the achieved *BER* was less than  $10^{-4}$ , the results compared with simulated results and the finite impulsive response channel models is characterised.

The same group in [66] employed *OFDM* modulation and designed transmitter and receiver *PCBs*, the transmitter *PCB* includes an amplifier of 11.9 *dB* gain and off *PCB* transducer, in the receiver *PCB* includes amplifier of 40 *dB* gain and 4<sup>th</sup> order Butterworth filter. The system examined using beef liver, the distance between the transmitter and receiver was 10 *cm*, the achieved data rate was higher 340 *kbps* and the *BER* was  $10^{-4}$  at (17 – 19) *dB* energy per bit to the spectral noise (*E<sub>b</sub>/N<sub>0</sub>*). Further summary for the reported devices can be seen in Appendix A (Table A-5).

## 2.7 Conclusion

*RF* communications are currently the accepted standard in medical devices. Given that it takes decades to get new devices to market. It is worth mentioning that any new technology must demonstrate significantly superior capabilities in a given application to be accepted. As such, it is important to try to draw some strong conclusions based on what has been achieved to date. Based on the three presented scenarios for data transmission (regardless of communication type): (i) shallow percutaneous (Figure 1-1 (a)) (ii) Deep percutaneous (Figure 1-1 (b)) and (iii) intrabody communications (Figure 1-1 (c)). Current *RF* operates largely in scheme (i) but also in scheme (ii). The only clinical scheme currently operating for optical communication is in a niche domain directly through a transparent window – i.e. the eye. But it is feasible to use that approach in domain (i). In comparison, ultrasound can operate in any of the domains, but will likely have a significant niche in the latter two.

- For percutaneous transmissions, ultrasound penetrates deeper with lower loss than for comparable *RF* methods. The transceiver can be smaller and if the multipath problem can be sufficiently negated, data rates comparable or even exceeding that of *RF* can be achieved. Furthermore, if operating in a backscattering mode, batteries can be negative, resulting in an implant that can be sufficiently small to be injectable. Seo et al. [82] has therefore developed the concept of neural dust. Backscattered, externally powered implants could also be produced via *RF* methods. Finally, an interesting clinical advantage over existing *RF* is that each device will have a specific ultrasonic signature. This can aid location and extraction (should that be necessary).
- For intrabody transmissions, ultrasound has a unique capability to transmit over tens of cm between implantable nodes with a very small energy budget. This is not realistically achievable with optical or *RF* transmission and thus forms a key niche area for the ultrasound.

There is also significant development to be made in the core of ultrasound communications before it can be considered for medical devices. Real world testing in human showing the real world attenuation and multipath effects has yet to be presented. Once this is understood, more sophisticated modulation schemes with

*PSK/QAM, OFDM* etc need to be explored as to which can be used within realistic energy budgets. In particular, these also need to be considered in terms of data integrity. Errors can be acceptable in collected data. However, the transmission of intervention protocols needs to be error-free – e.g. whether to release or not release a drug, or the stimulus intensity. As such, further improvements need to be made to the error detection and correction protocols.

The final aspect of the development is the optimisation of microelectronics systems, including application-specific circuits and microcontrollers. Whether operating in active or backscattered form, more advanced interventions per node will only be possible if the energy budget for information transmission and active intervention (recording, processing, stimulation) is reduced to a minimum.

The interplay between transmission energy budget, device dimensions, operating frequency, data rate and range is complex. Therefore, based on the literature the main characteristics of the designed device was concluded in the following points:

1. Though it is desirable to keep the frequency as low as possible to minimise absorption loss and receiver circuit power, ideally the frequency range between 100 *kHz* up to 1 *MHz*. As such, in this project, the transducers operate at 320 *kHz* frequency to reduce the attenuation effect that can be presented at a high operating frequency range.
2. Errors can be acceptable in the collected data. However, the transmission of intervention protocols needs to be error free – e.g. whether to release or not release a drug, or the stimulus intensity. As such, in this project, error correction encoding scheme has incorporated. Thus, effective and error free data was demonstrated even at low *SNR* transmission which is sufficient for bioelectronic medicine applications.
3. More sophisticated modulation schemes with *PSK/QAM, OFDM* etc can be employed but such schemes require more complicated hardware and software and the receiver energy budget is equally as important as the transmit energy budget for implantable devices. Therefore, the designed prototype is driven by low energy consumption and less hardware complexity using low duty cycle

transmission pulse sequences with relaxation intervals, to overcome the multi-propagation path effect.

4. The main target is to implement intra body communication network inside the human body via distributing *BeNs* to be either used for recoding and/or drug delivery or stimulus. The device shape needs to be selected carefully to fulfil the requirements and adapts to the human body environment. Therefore, in this project, an omnidirectional tube shape piezoelectric transducers with dimensions of  $(3 \times 3.5 \times 2.5) \text{ mm}$  are employed. As such, the *BeNs* could communicate even when they are distributed over a large distance and arbitrary orientation inside the body.



## Chapter 3. Wireless Communication System

### 3.1 Introduction

Wireless communication is one of the fascinating fields targeted by researchers throughout recorded history. The advancement in the wireless communication field is extensively supporting the medical implant applications field. It is important to understand the ultrasound communication system by introducing and analysing each main building block of the system. This chapter provides an in-depth analysis of the fundamentals of ultrasound transducers, background theory of the ultrasound communication systems and finally clarify in the main sections why the designed system adapted, based on the communication channel characteristics, this specific modulation, error correction technique and the proposed communication protocol (modes of operations). This chapter is splinted into two distinct main sections to explain the main building blocks shown in Figure 3-1:

- I. The physical mechanism of ultrasound communications: this section introduces and discuss the fundamentals of ultrasound signals in details.
- II. Communication strategies for the ultrasound: this section describes the main communication system blocks.

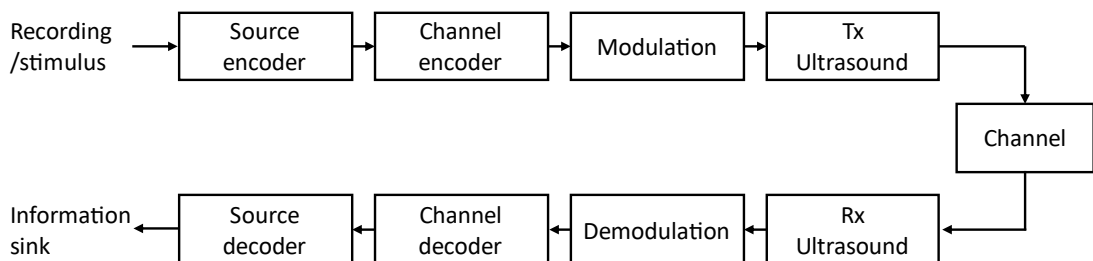


**Figure 3-1: Ultrasonic digital transmission block diagram, illustrates the main building blocks of the system.**

## I. The physical Mechanism of Ultrasound Communications

### 3.2 Fundamentals of Ultrasound

To fully understand the ultrasound waves, the main ultrasound concepts are presented in the following sections:

#### 3.2.1 Operating Frequency

Human hearing is typically between  $20\text{ Hz}$  to  $20\text{ kHz}$  (as a teenager). As such, ultrasound refers to the frequencies above this range and is inaudible to humans, although some animals such as bats and marine mammals can detect up to  $200\text{ kHz}$ . Perhaps the first practical use of artificial ultrasound was in 1915 by Paul Langevin who built the first sonar systems to locate submarines. Later, its first medical use was in the obstetric imaging of pre-nates in 1958 [101]. Currently, the main frequencies in clinical operation are between  $1 - 30\text{ MHz}$  [102], but for the purposes of communication inside the body, frequencies greater than  $100\text{ kHz}$  can be considered (since lower frequencies would require impractically large transducers for implantable devices). Higher frequencies allow for smaller transducers (described in more detail in the following section) but suffer from greater attenuation.

#### 3.2.2 Speed of Propagation

The speed of propagation of the ultrasound waves is determined by the medium's mechanical properties. In solid materials, the speed of sound for the shear-type waves depends on the shear modulus and the medium density. Same for the longitudinal type waves but adding the compressibility (bulk modulus) as another factor. In liquid material, only longitudinal waves are able to propagate. Therefore, the speed of sound depends only on the medium's density and compressibility. In ideal gases, the speed of sound depends only on the temperature of the gas since the molecular composition is fixed. For example, the average speed of sound in air (low-density medium) is slow ( $331\text{ m/sec}$ ). In contrast, the average speed of sound in water is  $1497\text{ m/sec}$  [103]. Table 3-1 below provides a full range of velocities for different tissue types. Air is included, as it fills the lungs and gas bubbles commonly form in the digestive tract. As

can be seen, the velocity varies from 331 – 3605  $m/s$  and at 1  $MHz$ , this equates to wavelengths in the range of 0.3 – 3.6  $mm$  respectively. As such, for most instances, the ultrasound will be a propagating rather than a standing wave. As a result, in addition to the primary signal, there can be secondary “echos” as the signals reflect off other structures (due to the difference in density and thus acoustic impedance). This is known as the multipath effect.

**Table 3-1: Ultrasound properties in different tissue types [103].**

Medium	Speed of sound (m/s)	Density ( $kg/m^3$ )	Acoustic Impedance ( $10^6$ )( $\frac{kg}{m^2 \cdot s}$ )	Attenuation coefficient (dB/cm) at 1 MHz
Air	331	1.3	429	12
Water	1497	1000	1.49	0.002-0.0022
Blood	1574	1060	1.63	0.18
Fat	1467	925	1.36	0.68
Muscle	1600	1075	1.69	1 – 2
Bone(varies)	3605	1400 – 1900	6.53	20
Soft tissue	1540	1058	1.63	0.9
Lung	–	–	–	40
Breast	1642	–	–	–
Liver	1589	1038	1.65	0.9
Kidney	1560.5	1038	1.62	1

The propagation speed of sound in a medium like water is about six orders of magnitude less than the speed of electromagnetic waves in air. Therefore, the delay time associated with the ultrasound wave while travelling in a medium that contains 60 % of water (e.g. human body) is significant especially when the distance increases [104]. Moreover, the speed of sound propagation is proportional to both the medium density and the local sound pressure. Basically, in the human body, the medium temperature and salinity associated with the density and the ultrasound waves travelling depth associated with the pressure. As presented in Table 3-1, The speed of propagation profile and the density of multiple human organs and parts.

### 3.2.3 Ultrasound Wave Types

Ultrasound waves require a material medium to propagate by inducing a local modification in the medium density, pressure, and temperature. Ultrasound waves classified into two different kinds based on the motion type induced in the medium:

1. The first type of waves is called longitudinal waves also termed as compression waves, this wave occurs if the medium particles move back and forth relative to the ultrasonic energy wave direction that is moving horizontally as well (ultrasound waves travelling in the same direction of particle motion). The longitudinal waves can be propagated through all different types of materials such as gases, solids, and liquids as well as the human tissues.
2. The second type is the shear waves also termed transverse waves, the shear wave propagates if the medium particles moving up and down (vertically) while the ultrasonic energy wave is travelling horizontally (ultrasound waves are perpendicular to the particle motion). Shear wave can propagate only in solid materials, hence is cannot travel through the human soft tissues, however, they can propagate in bone (solid tissues) [105]. Figure 3-2 shows the two different types of ultrasound waves propagation modes.

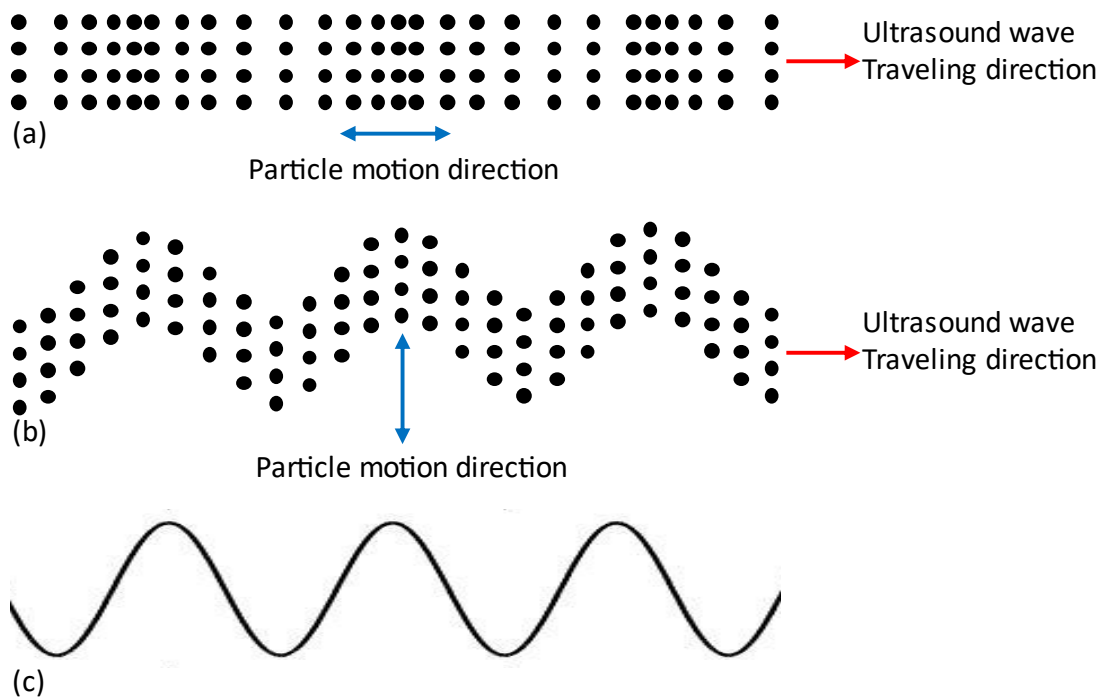


**Figure 3-2: Ultrasound propagation two modes: (a) Longitudinal waves propagation type which can travel through different materials such as solid, gases and water; (b) Shear wave propagation type, the shear waves can propagate in solid materials only; (c) Sinusoidal waves representation.**

### 3.2.4 Ultrasound Modes of Operation

The main ultrasound transducers convert electrical energy into propagating (ultrasonic) mechanical waves and vice versa. The main components of an ultrasound transducer are the piezoelectric crystal, electrode contacts, damping material, matching layer and an insulating layer. There are different shapes of the transducers available depending on piezoelectric crystal shape, application, directivity and operating frequency [106]. The output voltage generated from a receiving ultrasonic transducer due to the applied stresses or forces is typically low. Therefore, a signal conditioning circuit (preamplifier and filter) is invariably needed to obtain an effective output signal.

Piezoelectric crystals have five main modes of vibration (resonance) as shown in Table 3-2 below and described visually in Figure 3-3.

**Table 3-2: Piezo transducer operational modes.**

#	Mode	Operation
1	<b>Thickness extension mode:</b>	The piezoelectric crystal vibrates in the direction of its thickness. This kind of operation mode used widely in non-destructive testing and therapeutic applications, as shown in Figure 3-3 (a). Resonance frequency inversely proportional to the crystal thickness as shown in the following formula: $f_r = \frac{N_t}{t}$ , where $f_r$ is the resonance frequency, $N_t$ is the piezoelectric frequency constant and $t$ is the thickness of the crystal.
2	<b>Radial extension mode:</b>	This mode achieved when the vibration moves from the centre of the crystal toward its edges. This mode used for underwater communication applications and others [107], as shown in Figure 3-3 (b).
3	<b>Length mode</b>	this mode occurs when a long thin crystal has an electrode on the top and bottom of its small faces and the applied electric field in a similar direction to the longitudinal waves. This mode used for material stress sensors, energy harvesting applications, and others, as shown in Figure 3-3 (c) [108].
4	<b>Thickness shear mode</b>	This mode excited when the electrode placed on the longest thickness dimension of the crystal, and the electric field applied in the orthogonal direction of the crystal polarisation, as shown in Figure 3-3 (d).
5	<b>Transverse length mode</b>	This mode excited when the electric field applied in the same direction of the crystal polarisation and the displacement occurs orthogonally to the applied electric field, as shown in Figure 3-3 (a) [109].

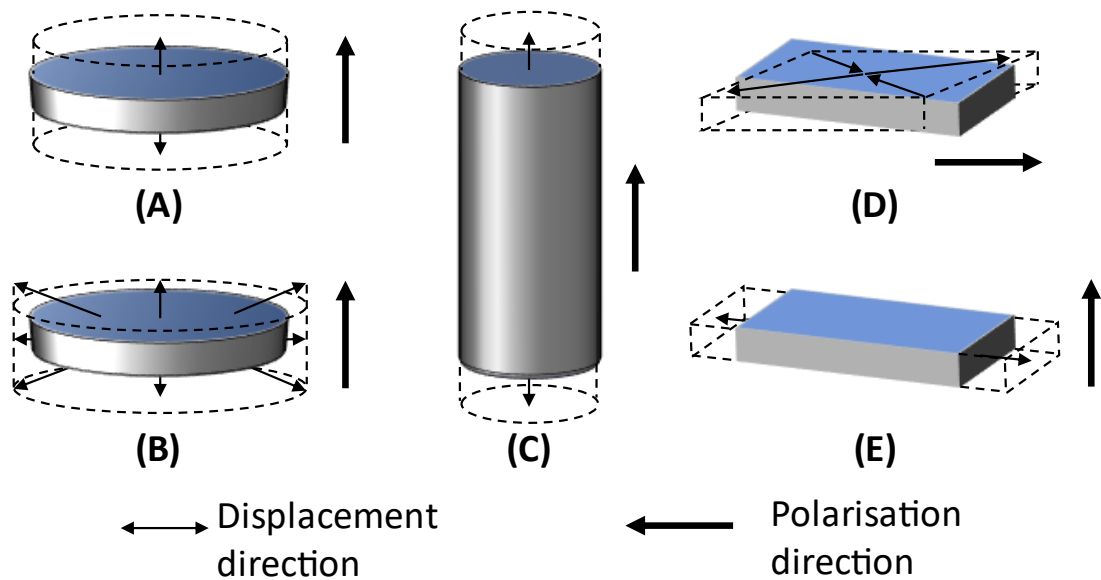


Figure 3-3: Resonance modes of the piezoelectric crystal; (a) Thickness extension mode; (b) Radial extension mode; (c) Length extension mode; (d) Thickness shear mode; (e) Transverse length mode, in this mode the wave motion direction is vertical to the oscillation direction. The blue side indicates the electrode position in the top and bottom of each geometry. Several types of resonance can be existing in the same geometry as can be seen in disc shape crystal (b) which have both thickness and radial extension modes.

### 3.2.5 Piezoelectric Materials

In 1880 the piezoelectric effect discovered by the French physicists Pierre and Jacques Curie. This effect occurs when the piezo material exposed to a deformation that results from a movement in the positive charges relative to the negative charges. Hence this will develop a dipole moment symmetric to the applied strain [102]. Piezoelectric materials divide into two types: piezo polymers and piezo ceramics.

1. **Piezo polymers** commonly employ nontoxic material (lead-free) such as polyvinylidene fluoride (*PVDF*), this material shows improvement in terms of biocompatibility, flexibility, low cost and power consumption. However, this material suffers from low electrical to mechanical conversion (order of magnitude lower than piezoceramics) and this leads to relatively poor transmit efficiency [102, 110].

2. **Piezo ceramics** are the most commonly used for ultrasonic medical applications and there are many types of piezoceramic material such as barium titanate ( $BaTiO_3$ ) [111], bismuth titanate ( $Bi_4Ti_3O_{12}$ ) [112], lead meta-niobate ( $PMN$ ) and  $PZT$ .  $PZT$  is the most popular material in use. It can be divided into two classes: 'soft' and 'hard'  $PZT$ . Soft  $PZT$  has higher electromechanical coupling factors, piezoelectric constants, permittivity and dielectric constants. However, the dielectric losses and linearity are poor compared to hard  $PZT$ , which limits its use in high power systems [106].

It should be noted that both Barium ( $BaTiO_3$ ) and Lead ( $PZT$ ) are highly cytotoxic, and barium is also genotoxic. Bismuth is somewhat less toxic. As such, in each of these cases, use in-vivo would need encapsulation and demonstration that failure would not lead to adverse effects. Alternatively, the field needs to develop less toxic piezoelectric materials for in-vivo application.

### 3.2.6 Ultrasound Attenuation in The Body

Ultrasonic waves will undergo different types of attenuation such as scattering, reflection, refraction and absorption as it traverses through tissue. Attenuation type can vary depending on the object size, shape and surface compared to the ultrasound signal wavelength. For example, diffuse scattering occurs if the object size smaller than the ultrasound wavelength, which will cause the ultrasound signal to scatter in different directions, diffuse scattering is common with red blood cells. If the object size is large (relatively has a smooth surface e.g., bone) in comparison with the ultrasound wavelength, the specular reflection will occur. Specular reflection is common with organs and other tissues boundaries that are different in their acoustic impedance. As such, it has the effect of both reducing the amplitude of transmission at a given distance as well as causing increased dispersion. Furthermore, the wave will be absorbed by the tissue, being converted to thermal energy. The thermal conversion becomes the ultimate limit in transmission power as there can be significant discomfort for the patient if the tissue temperature rises above  $38.5^{\circ}C$  [113].

The combination of these effects can provide an attenuation factor  $\alpha$  - equivalent to extinction in optics. For a collimated beam, the amplitude  $A$  at a given depth  $x$  can be given by:

$$A(x) = A_0 e^{-\alpha x} \quad \mathbf{3-1}$$

Where  $A_0$  is the amplitude and  $\alpha$  is the attenuation coefficient. It should be noted that both scattering and absorption increase with frequency. Table 3-3 provides some attenuation coefficients as a function of frequency for different tissues. Generally, the variance in attenuation with frequency can be given by the following relation [114], where  $f$  is the operating frequency and  $n$  is material-dependent:

$$\alpha = \alpha_0 f^n \quad \mathbf{3-2}$$

**Table 3-3: Ultrasound attenuation coefficients, taken from [103, 115].**

Medium	Attenuation coefficients		
	100 kHz	1 MHz	10 MHz
Water	-	0.002	0.5
Liver	0.3	0.8	10
Breast	-	1.5	10.5
Skin	-	3	-
Muscle	1.1	1.4	30
Skull bone	-	8	-

The final consideration is reflection. Reflections are generated when the ultrasonic wave encounters the boundary between materials of differing acoustic impedance ( $Z$ ). The ratio of the reflected pressure amplitude to the incident pressure amplitude can be expressed as follows:

$$R = \left( \frac{Z_2 - Z_1}{Z_2 + Z_1} \right)^2 \quad \mathbf{3-3}$$

Where  $Z_2$  and  $Z_1$  are the acoustic impedances of the mediums. As per Table 3-1, strong reflections can be expected at the skin-air interface, the tissue–lung cavity interface and when waves hit trapped gasses in the stomach and intestines. As a result, in addition to the primary signal, there can be secondary “echos” as the signals reflect off various structures with different acoustic impedance. This is known as the multipath effect [103]. This multipath will turn the pulse into a more complex waveform which can be harder to determine more complex characteristics such as phase without considerable (and power-hungry) processing.

Lower the reflection coefficient implies a good transmission and vice versa. To calculate the reflection coefficient of the air-water boundary, based on Table 3-1, air and water acoustic impedances are  $429 \text{ kg m}^{-2}\text{s}^{-1}$  and  $1.49 \times 10^6 \text{ kg m}^{-2}\text{s}^{-1}$  respectively which resulting in a 0.99 reflection coefficient. Whereas, for the water-fat boundary, the fat acoustic impedance is  $1.36 \times 10^6 \text{ kg m}^{-2}\text{s}^{-1}$  which results in a lower reflection coefficient of 0.002.

### **3.2.7 Ultrasound Bandwidth**

The ultrasound transducers are able to emit a broad range of frequencies with a strong emission at the centre frequency. The ultrasound frequency bandwidth represents the emission frequencies range that usually looks like a bell shape curve. The frequency bandwidth is inversely proportional to the pulse duration for a given resonance frequency, the longer the pulse duration results in narrower bandwidth. One of the main measures of the frequency bandwidth is related to the quality factor ( $Q$ ),  $Q$  is a description of the damping level of a resonator which represented by the ratio between the transducer resonance frequency to its bandwidth [116]. The frequency bandwidth is reversely proportional to the  $Q$  for a given resonance frequency. The broader the bandwidth the smaller the  $Q$  and vice versa, Figure 3-4 shows the frequency response of two different transducers in terms of damping.

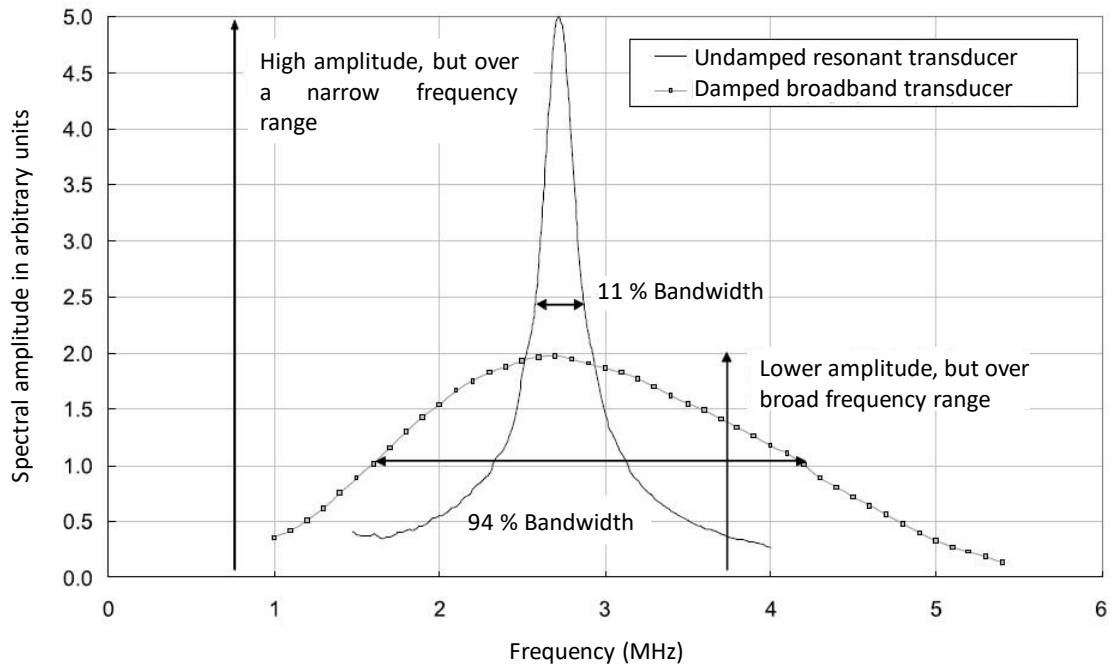


**Figure 3-4: The frequency response of two transducers that have the same centre frequency. It is obvious the difference between the damped and undamped transducer, the undamped transducer provides high amplitude over a narrow bandwidth whereas the damped transducer provides a lower amplitude over a broader bandwidth [102].**

Based on the transducer frequency response, the bandwidth can be calculated. Firstly, the frequency response peak needs to be addressed then relative to this peak, the half power points, (e.g.  $-3\text{ dB}$  or  $-6\text{ dB}$ ), where the frequency response curve crosses the points the lower ( $f_1$ ) and upper ( $f_2$ ) cut off frequencies can be assigned. The bandwidth represents the differences between those frequencies ( $f_2 - f_1$ ) [102].

All the ultrasound transducers are inherently resonant devices that maximally sensitive to a particular frequency. However, their output can be modified by the effect of mechanical damping. Undamped transducers provide a higher output signal but only with a narrower frequency bandwidth range (high  $Q$ ). Therefore, the undamped transducer used widely for ultrasonic heating, cleaning, and powering. In contrast, highly damped transducers are producing lower output signal but over a broader frequency range therefore their common applications are diagnostic ultrasonic imaging, non-destructive testing (*NDT*), and ultrasonic communication. Damped transducers

have broader bandwidth response corresponds to a short pulse length at the output in contrast with the undamped transducers.

### 3.2.8 Ultrasound Transducer Beam Directivity

The transducer emits ultrasound signals that are not only generated from one point but instead emitted from a collection of point sources along the transducer surface. For percutaneous transmission, the most efficient method is to direct a beam from external to a known location of an implant and vice versa. To achieve this, planar transducers are used. The single transducer pressure field is divided into two zones: the near field and far field. In the near field, or sometimes referred to as the Fresnel zone, for cylindrical shape transmitter transducer diffraction effects occur as the point sources interfere, creating constructive and destructive wave interference, which results in a fluctuation in the pressure intensity in that field. Therefore, it is difficult and unpredictable to examine the flaws using amplitude based measurements in the near field [103].

In the far field, the transmitted beam begins to diverge and the pressure waves spread spherically. In the far field, the pressure waves start to decay when distance increased. However, in the far field the pressure waves become smoother and more uniform than in the near field. The transition between the near and far field point is called natural focus or the focal point where the pressure field converges. The distance to the natural focus called the near field length ( $L$ ) which depends on the transducer diameter ( $d$ ) and the wavelength ( $\lambda$ ), can be expressed as:

$$L = \frac{d^2}{4\lambda} \quad \mathbf{3-4}$$

Hence, the larger diameter of the transducer radiating surface will result in a narrower sound directivity beam.

The wavelength,  $\lambda$ , is determined by the frequency ( $f$ ) and acoustic velocity ( $v$ ) as below:

$$\lambda = \frac{v}{f} \quad \mathbf{3-5}$$

The resonance frequency of the transducer is defined by the crystal thickness, as shown in Table 3-2, the thinner the crystal results a higher resonance frequency and vice versa. The thickness represents the dimension of the crystal alongside the ultrasound wave axis. To achieve an efficient operation of the crystal, the crystal thickness ( $t$ ) equal to half of the ultrasound wavelength,  $\lambda$ , and can be expressed as:

$$t = \frac{\lambda}{2} \quad \text{3-6}$$

### 3.3 Ultrasound Biophysics

The term ultrasound biophysics is generally meant by how the ultrasound and biological tissue or material interact together. When the ultrasound signal travels through a biological medium, it can affect the biological medium and those induced bioeffects can be classed into two different mechanisms thermal and non-thermal [105].

The thermal mechanism occurs, normally in continuous ultrasound waves exposure, when a portion of the ultrasound wave is converted into heat due to the absorption effect. Moreover, scattering is another effect that occurs when a portion of the ultrasound wave changes its direction, both effects are explained in more detail in the earlier section 3.2.6.

The non-thermal mechanism is represented by the induced bubble activity that generated ultrasonically in a biological tissue medium that already contains gaseous inclusions, this effect is attributed to acoustic cavitation [105]. The non-thermal mechanism usually associated with the pulsed ultrasound wave exposure. For ultrasound transmission scenarios, in the realistic situation, it is best to consider the non-thermal ultrasound effect is always accompanied by thermal ultrasound effect, since there is an interaction between the biological tissue and ultrasound waves, however, pulsing the ultrasound waves can reduce the thermal effect to a sufficient level and reduce the tissue injuries that might occur due to temperature rise [117, 118]. As shown in Figure 3-5, extra care that needs to be taken when passing the ultrasound waves in air-filled cavities such as lungs [119] and intestine [120] since the gas bubbles are problematic for the ultrasound signals and can suffer from attenuation due to the high reflection coefficient and multipath effect as explained earlier in 3.2.6.

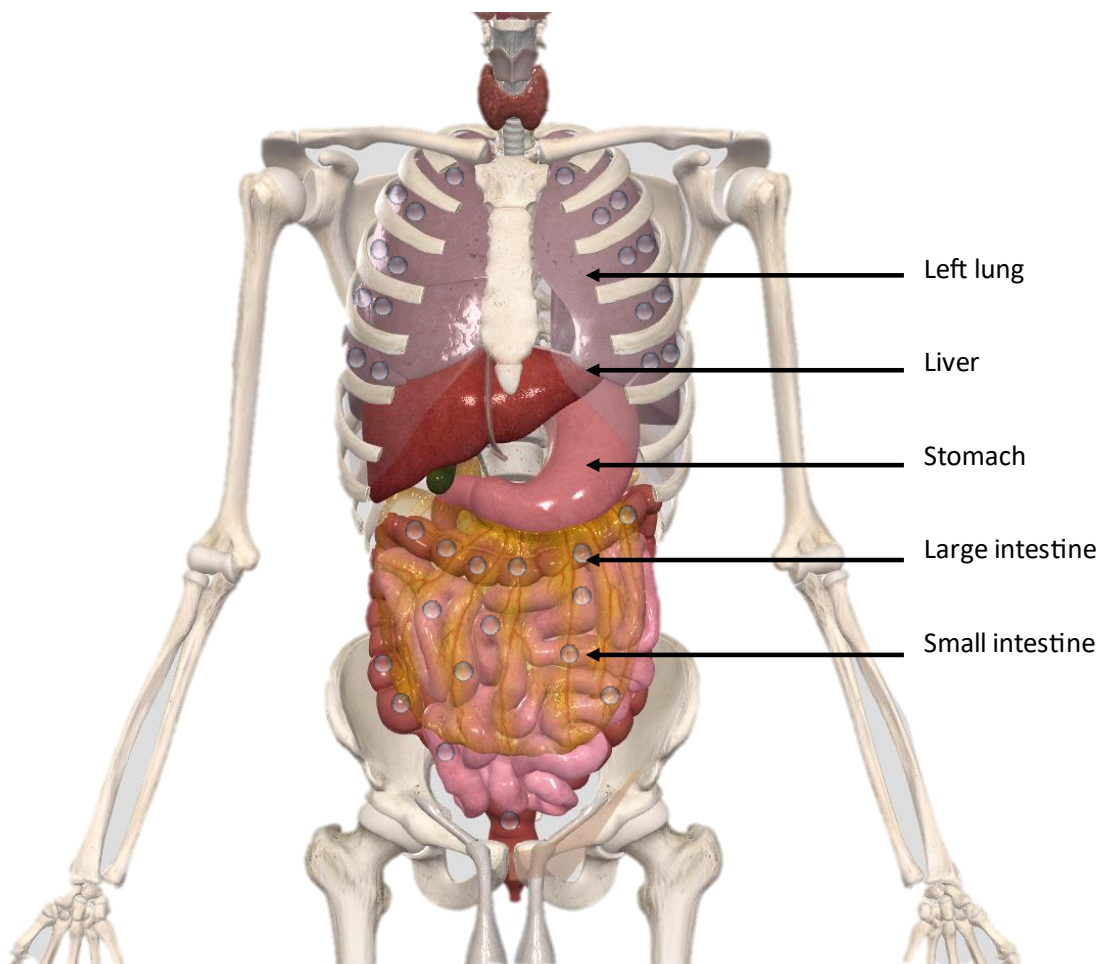


**Figure 3-5: Human body model that shows the digestive and respiratory systems. Air filled cavities and bubbles are located mainly in the lungs and intestine which make the ultrasound signal suffers from high attenuation.**

### **3.4 Channel Characteristics**

The communication channel is a representation of the physical medium or the connection used by the ultrasound wave to travel from the transmitter towards the receiver. There are two different types of physical channels: the first type is the wire channel which includes two twisted pairs of wires (e.g. coaxial cable and optical fibres), and the second type is the wireless channel such as air, sea, and vacuum. The channel characteristics are determined by three main factors: the speed of propagation, path loss, and multipath effect. These factors will be explained in the coming section.

### 3.4.1 Speed of propagation (described earlier in section 3.2.2)

### 3.4.2 Path loss

During the travelling of ultrasound signal through the channel towards the receiver, the transmitted signal suffers from one or more channel impairments such as noise, fading, distortion, and attenuation. Path loss resulting from the signal dissipated power as the propagation distance increases. Typically, the ultrasound unfocused wave emission will induce spreading loss and attenuation in the signal power. The logarithmic (*dB*) scale path loss ( $P_L$ ), neglects the variation due to multipath channel effects, is the ratio between the power of the transmitted signal ( $P_t$ ) to the power of the received signal ( $P_r$ ) as shown by the following equation [121]:

$$P_L = 10 \log_{10} \left( \frac{P_t}{P_r} \right) \quad 3-7$$

For a known distance linear path loss can be calculated using Friis equation for free space environment given as:

$$P_r = \frac{P_t G_t G_r \lambda^2}{(4\pi)^2 d^2} \quad 3-8$$

Where:  $d$  is the transmission distance,  $\lambda$  is the carrier signal wavelength,  $G_t$  and  $G_r$  are the transmitter and receiver antenna gain, respectively. From Friis equation and based on equation 3-7, the free space path loss can easily be derived. It is obvious that path loss is proportional to the square of signal travelling distance and square of the operating frequency [122].

### 3.4.3 Multipath Effect

Ultrasound propagation is severely influenced by the multipath effect that results from the inhomogeneity of the medium. The receiver system can be influenced by a random superposition of ultrasound signal copies that arrive over various propagation paths termed as multipath fading as shown in Figure 3-6, the multipath signal replicas can be added together to form a constructive or destructive interference depending on the phase. The multipath effect will result in a time domain dispersion, commonly referred to as multipath delay spread, to the ultrasound signal. Therefore, that will result in two direct consequences: firstly, that will create a sparse time support difference between

the transmitted signal (shortest) and received signal (largest). Secondly, the received signal power will be distributed along with the delay spread and according to the propagation channel response. Each signal replica that coming from different propagation paths will introduce a unique amplitude scaling to the transmitted signal [121]. Henceforth, that will lead to a difference in the received signal power for each corresponding propagation path. The power of the received signal  $P_{r(i)}$  for each corresponding path  $i$ th can be expressed as:

$$P_{r(i)} = f(\alpha_i^2) \quad \mathbf{3-9}$$

Where  $\alpha$  is the amplitude scaling factor and  $i = 1, 2, \dots, N$ .

As a result, the signals are reflected off other structures or particles as per equation **3-3**. Acoustic properties in tissue are different, there is a 20% variation between the highest impedance soft tissue structures (Liver, Muscle) and the lowest (fat, blood) (given in Table 3-1). This will cause some modest dispersion of the transmitted waves, but reflections are largest for bone and for air/gas. The latter case is not simply the air/tissue interface, but also the lungs, and gas pockets in the gut and intestines.

*ISI* is another consequence that has a significant effect on the transmitted signal at the receiver side. It is worth to mention the term symbol in digital communication is represents the signal that used to transmit one bit or multiple bits of information at a fixed period of time. *ISI* is introduced when the time support and power spread of the received ultrasound signal are large comparing to the symbol period. Thus, the former transmitted ultrasound symbols will interfere with the later symbols.

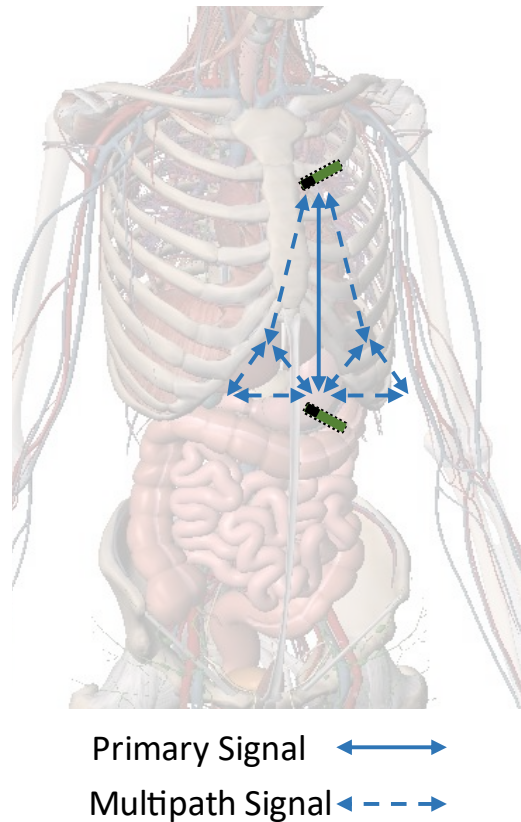


**Figure 3-6: Shows the multipath propagation phenomenon which is one of the major issues that influence the ultrasound communication link, the multipath effect produces attenuated replicas of the original primary signal spaced in time. A finite multipath delay spread will appear as sparse trains of discrete arrivals echoes that need to consider in the receiver design.**

The multipath effect can cause two different types of fading as shown in Figure 3-7 and explained as:

1. **Large scale fading:** this kind of fading occurs in large distances communication such as mobile cell phones on the move. It's induced due to the path loss of signal which is proportional to distance and also shadowing effect [123].
  - a. **Shadowing:** this effect experienced in the ultrasound imaging of the human body, the ultrasound signal absorbed or reflected when propagates through a solid obstacle such as bone or stone [124].
  - b. **Path loss:** the ultrasound signal power dispersed as the propagation path increases.

2. **Small scale fading:** this kind of fading occurs at short distances, small scale fading results from a rapid fluctuation in the signal amplitude and phase over time and cause constructive and destructive interference of multipath signals.
- a. **Multipath fading:** (Explained in section 3.4.3).
    - I. **Flat fading:** This fading occurs when the transmitted symbol period is greater than the delay spread, therefore, the effect of delay spread will be insignificant. As a result, the signal will propagate over the channel flat response [121].
    - II. **Frequency selective fading:** This kind of fading occurs when the transmitted symbol period is smaller than the delay spread. Therefore, as a result, the signal will be exposed to filtering effect due to the significant delay spread and will leads to a severe *ISI*, while travelling through the channel.
  - b. **Doppler spread:** this effect occurs when the channel impulse response varying with time and includes two types of fading:
    - I. **Fast fading:** This type of fading occurs when the symbol period is greater than the channel coherence time. The channel coherence time represents the duration of time over which the channel response stays correlated [121].
    - II. **Slow fading:** This fading appears when the symbol period is small comparing to the coherence time of the channel.

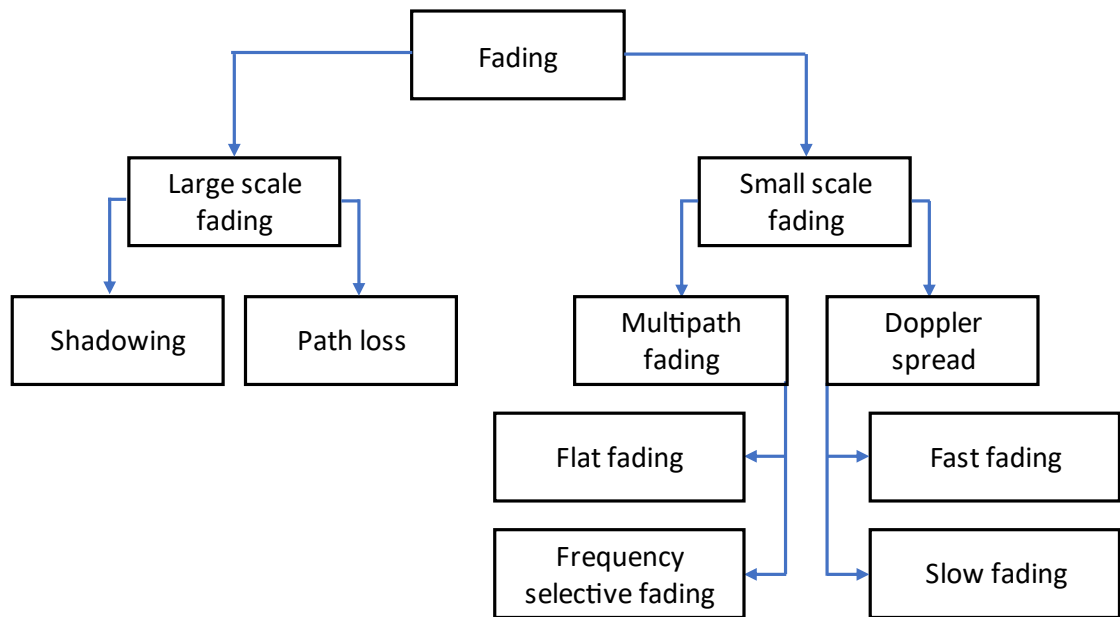


**Figure 3-7: Fading channel classified into two main types: large and small scale fading. The small scale fading includes multipath fading that characterised by either flat fading or frequency selective fading.**

### 3.5 Modulation and Demodulation

The communication systems are employed for transmitting the information carrying signals that refer to message signals over the required distances. In general, most of the message signals are so-called baseband signals which normally are low pass signals that occupying low frequency range from zero to the bandwidth of the signal [125]. Modulation is the representation of digital data in terms of analog signals to be eligible for transmission over the physical communication channel. The digital information might be formed as binary bits of 0s and 1s, which can be mapped into symbols (e.g. the bit “1” translated to 1 and the bit “0” translated to  $-1$ ) to be ready for mixing with the analog carrier waveform (bandpass signal) which normally have a higher frequency. High frequency of the bandpass signal is essential for long distance communication where the baseband transmission suffers from serious overlapping spectra [126].

At the receiver side, the demodulation process occurs to retrieve the transmitted information. However, the received signal is a noisy and distorted version of the transmitted one, Therefore, the key tasks of the demodulator are summarised as shown below [126]:

1. Discriminate the incoming signals from the transmitter and reduces the probability of error to the lowest acceptable level possible.
2. Minimize the channel effect that influences the transmitted signals by producing phase, frequency, and time shifts and this will lead to synchronisation problems at the receiver.
3. Compensate the induced *ISI* due to the dispersive channel effect.

The ultimate purpose of the demodulator is to provide a temporal decision on the incoming signals then to be prepared to feed them to the channel decoder. There are two different types of decisions, the first type called hard decision which achieved when the binary bits produced by the decision block, the decision block predicts whether the particular bit being “0” or “1”. The hard decision boundaries (upper and lower bounds) on maximum likelihood decoding are calculated by employing information on the cost weight leader distribution [127].

Hard decision decoding is less sophisticated, however, it is beset with some limitations such as the noise variance has a serious influence on the hard decision decoding, higher the noise variance results in unreliable decision, and the hard decision demodulator does not provide extra information on how reliable the decision was.

The second type is a soft decision that achieved when the demodulator gives an analog estimation for the likelihood of a specific bit being “0” or “1”. The decision boundaries of soft decision decoding can be calculated using the weight distribution of the codes [127]. Soft decision demodulator provides extra information besides the decision, this extra information is a measure of how confident the decision was. Soft decision demodulator is more powerful, However, more complicated in terms of design and implementation.

### **3.6 Common Digital Modulation Techniques**

Digital modulation is a process of mapping digital information sequence to the carrier signal for transmission over the channel. Parameters of the carrier signal can be varied or modulated. Usually, the carrier signal is a high frequency sinusoid that is transmitted with one or more of the three main parameters (phase, frequency, and amplitude) that

conveying the message signal. In the following subsections, the three major digital modulation techniques are demonstrated.

### 3.6.1 Phase Shift Keying

*PSK* is a digital phase modulation that modulates the serial bit stream of the message to the phase of the power transmission carrier, making sure that both the amplitude and frequency of the carrier signal are constant. Each phase transition in *PSK* is corresponding to one logic bit, the constellation of 2 – *PSK* or binary *PSK* (*BPSK*) is 180° out of phase. The *PSK* modulated signal can be represented in the time domain as shown in the following equation:

$$S_{PSK} = \left( \sum_n a_n g(t - nTs) \right) \cdot A \cos(2 \pi f_c)t \quad \mathbf{3-10}$$

Given that:

$$a_n = \begin{cases} 1, & \text{with probability } P \\ -1, & \text{with probability of } 1 - P \end{cases}$$

Where  $a_n$  is the binary digits amplitude,  $g(t)$  is the baseband signal,  $Ts$  in the interval of the signal and  $A$  and  $f_c$  is the amplitude and frequency of the carrier signal.

*PSK* is capable of transmitting at higher data rates per unit wireless bandwidth (High spectral efficiency) in comparison with the other techniques, by employing a smaller phase shift more than one bit for each phase transition can be transmitted as shown in Figure 3-8. For instance, quadrature *PSK* is able to transmit four symbols (i.e. two bits each phase) by employing four different phases with 90° in between [128].

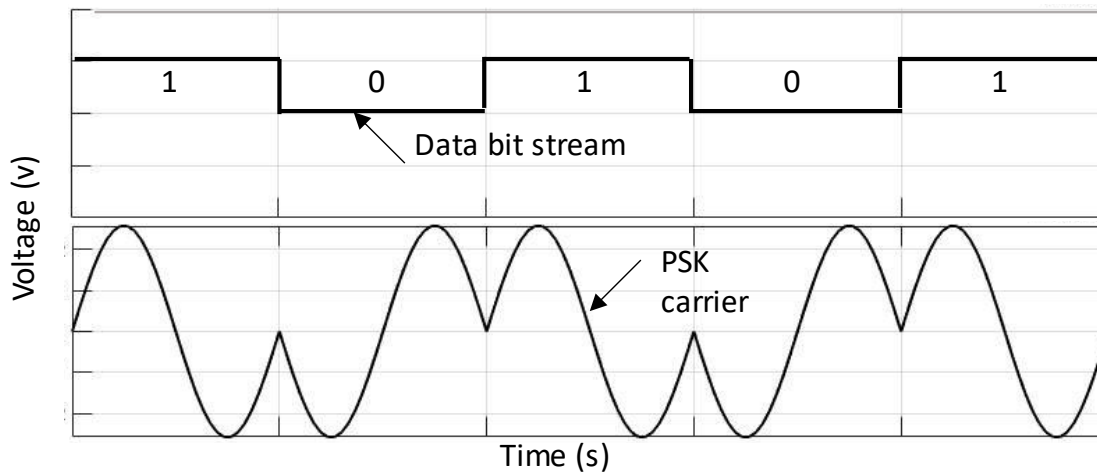


**Figure 3-8: Phase shift keying digital modulation that modulates the data bitstream with the carrier signal, the carrier signal illustrates how the binary 0s and 1s can be encoded.**

### 3.6.2 Frequency Shift Keying

*FSK* is a digital frequency modulation that widely used in high fidelity audio transmission, the data bit stream in *FSK* is modulated in the frequency of the power transmission carrier, making sure that both amplitude and phase of the carrier signal are constant [128]. The binary bits “0” and “1” are corresponding to  $f_0$  and  $f_1$  respectively of the transmitted carrier signals as shown in Figure 3-9. As such, the power of the carrier remains constant unrelatedly to the data. Another advantage to the *FSK* modulation is the immunity against the noise and interference; however, it suffers from the phase noise that influences the *FSK* modulator stability, and the bandwidth of the *FSK* frequency spectrum is wider in comparison to the *ASK* at the same data transmission rate. As a result, the quality factor of both the transmitter and receiver *FSK* circuits should be reduced to deliver a satisfactory bandwidth that enough for the carrier signal to pass. However, reducing the quality factor will reduce the power transmission efficiency, and based on Carlson’s rule to include 98 % of the total power of the frequency modulation signal the bandwidth ( $BW$ ) is expressed as [129]:

$$BW \approx 2(\delta_{MAX} + f_{MAX}) \quad \mathbf{3-11}$$

Where  $\delta_{MAX}$  represents the maximum frequency shift that results from the *FSK* modulation, and  $f_{MAX}$  is the maximum frequency contents of the *FSK* modulated signal.

To generate the *FSK* transmission signal, the input of the power amplifier can include two oscillators each one generates  $f_0$  and  $f_1$  signals respectively based on the digital data, or use voltage controlled oscillator which able to generates two different oscillation frequency by varying the oscillator time constant. The phase-locked loop (*PLL*) is often employed to stabilise the voltage controlled oscillator, *PLL* is implemented by referencing the voltage controlled oscillator to a low phase noise local oscillator [128].

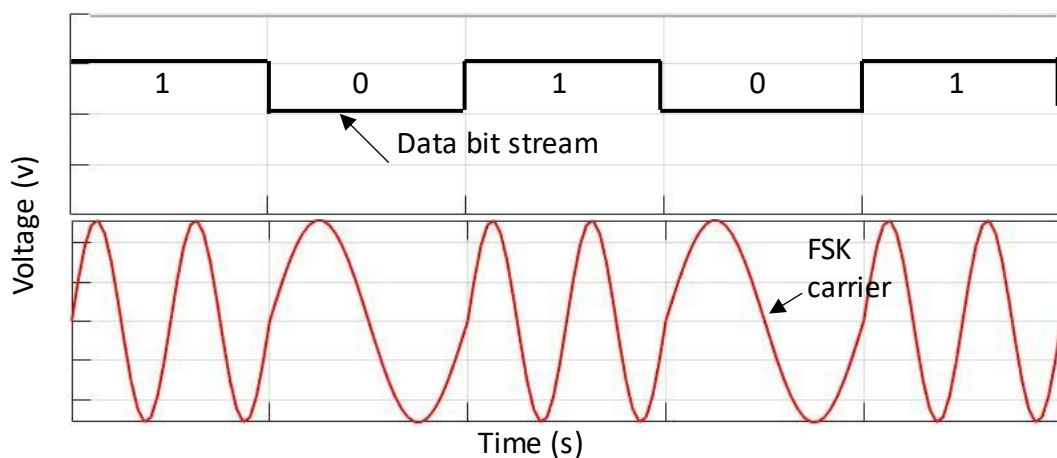


**Figure 3-9: Frequency shift keying digital modulation that modulates the data bit stream (top) with the carrier signal (bottom), the carrier signal illustrates how the binary 0s and 1s can be encoded by assigning the high-frequency components to the binary bit 1 and the low-frequency components to the binary bit 0.**

### 3.6.3 Amplitude Shift Keying

*ASK* modulates the digital serial data to the amplitude of the transmission carrier signal. The *ASK* signal can be generated by varying the supply voltage as shown in Figure 3-10 which will result in an output swing of the power amplifier at the transmitter side.

At the receiver side, the demodulator recovers the received data by using the envelope detector, the received signal is fed to a low pass filter that has a cutoff frequency ranging between the data bandwidth and the frequency of the carrier signal, in this case, the

high frequency carrier components will be rejected which leaving only the low frequency components, bypassing the low frequency signal to a high pass filter and decision comparator the serial digital data can be recovered back [130].

*ASK* has been used widely in biomedical implanted devices application especially for the forward data telemetry for several reasons such as the transmitter and receiver design simplicity, noise immunity and the transmission signal occupy smaller bandwidth comparing to the *FSK*.

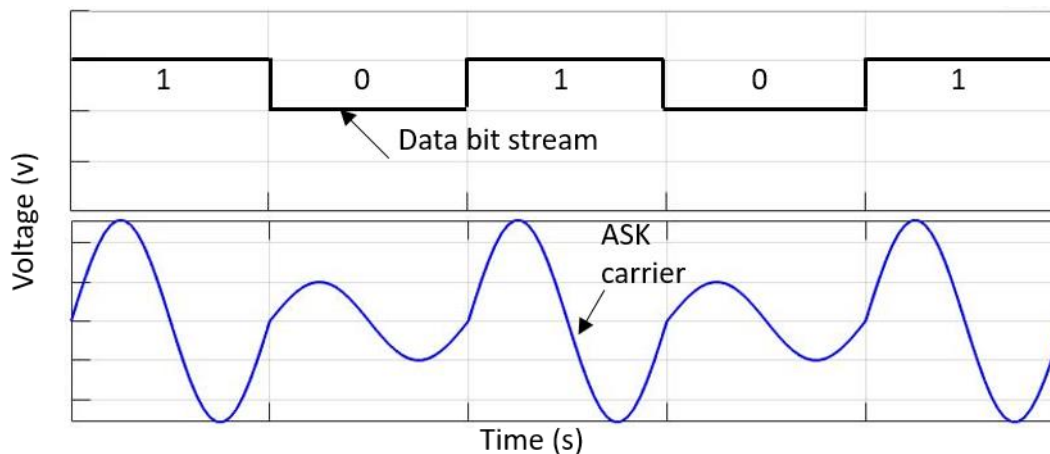


**Figure 3-10: Amplitude shift keying digital modulation that modulates the data bit stream (top) with the carrier signal (bottom), the carrier signal illustrates how the binary 0s and 1s can be encoded and form the carrier-envelope that helps the receiver to demodulate the signal.**

### ***ON-OFF Shift Keying***

*OOK* is the simplest form of *ASK* modulation technique, it encodes the binary bits “0” and “1” in the absence and presence of the carrier signal as shown in Figure 3-11, respectively. The unique difference between *OOK* and *ASK* is that the latter transmits a carrier signal for both transmissions of binary “0” and “1”, however, the transmission of bit “0” represented with a reduced carrier amplitude. Hence, this gives an advantage to the *OOK* modulation as the difference in the carrier amplitude signal when transmitting the bits “0” and “1” is higher than *ASK*, and in term of the receiver, it will be easier to distinguish between the two bit amplitude level.

The *OOK* transmission signal can be represented as:

$$S_{ook}(t) = a_n \cdot A \cos(2\pi f_c t) \quad \text{3-12}$$

Given 
$$a_n = \begin{cases} 1, & \text{with probability } P \\ 0, & \text{with probability of } 1 - P \end{cases}$$

Where  $a_n$  is the digits amplitude,  $A$  represents the carrier signal amplitude and  $f_c$  is the carrier signal frequency.

In this research project *OOK* modulation technique has been adapted for the below reasons:

1. *OOK* modulation technique is less complex, and the required implementation cost is low contrasting the *FSK* modulation that requires more sophisticated design implementation and high cost.
2. *OOK* modulation transmitter switch to the idle state when transmitting binary "0" bit, unlike the *ASK* that remains the carrier on when transmitting for both bits "0" and "1", which allow the transmitter to save power.
3. *OOK* is more deterrent to co-channel interference and requires lower bandwidth comparing to *FSK* [131].

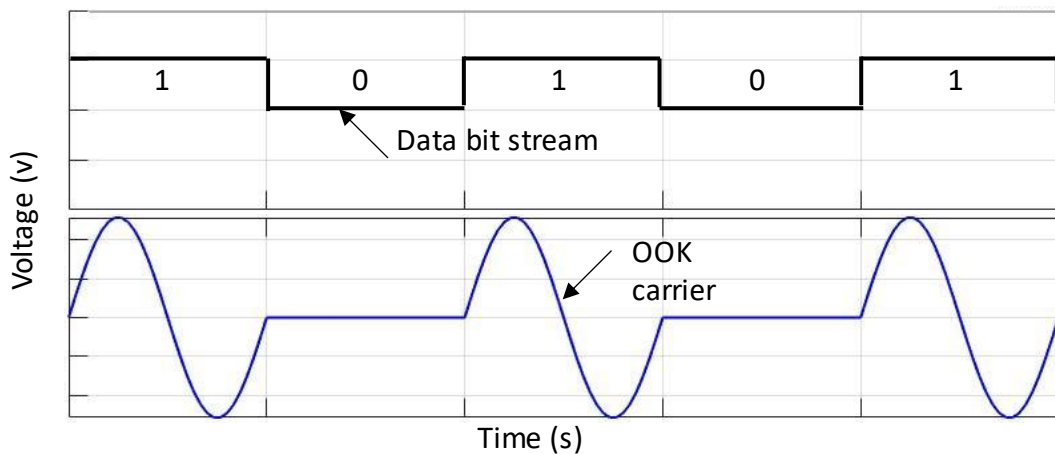


**Figure 3-11: On-Off Keying digital modulation that modulates the data bitstream with the carrier signal, the carrier signal illustrates how the binary 0s and 1s can be encoded.**

### 3.6.4 Quadrature Amplitude Modulation

*QAM* is widely used in modern telecommunications, and in particular employed in the communication systems that operated in a limited channel bandwidth to improve their spectral efficiency. *QAM* is implemented by changing both the amplitude, using analog amplitude modulation (*AM*) or digital using *ASK*, and phase components of carriers in such a way to make the two carriers have the same frequency but  $90^\circ$  out of phase with each other which is known as orthogonality, as shown in Figure 3-12.

Figure 3-13 shows the 16 – *QAM* constellation mapping for one of the most common forms of *QAM*. Higher constellation order can be employed, such as 64 – *QAM* and 256 – *QAM*, which give chance to transmit more bits per symbol hence improve the spectral efficiency. However, the very dense constellation will become more susceptible to noise as the constellation point become closer. Hence, any low noise level will be able to affect the data recovery decision at the receiver side [132].

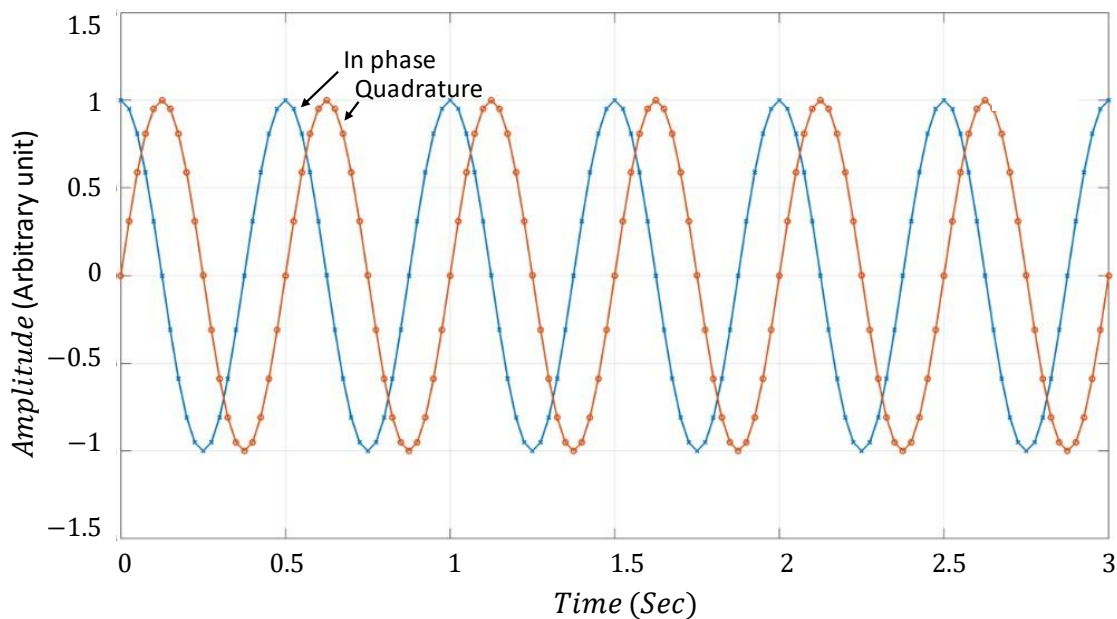


**Figure 3-12: Carrier signals to modulate the data and create *QAM* symbols for transmission. The two carrier signals in phase (cosine) and quadrature (sine) are shifted in phase by  $90^\circ$  phase shift difference.**

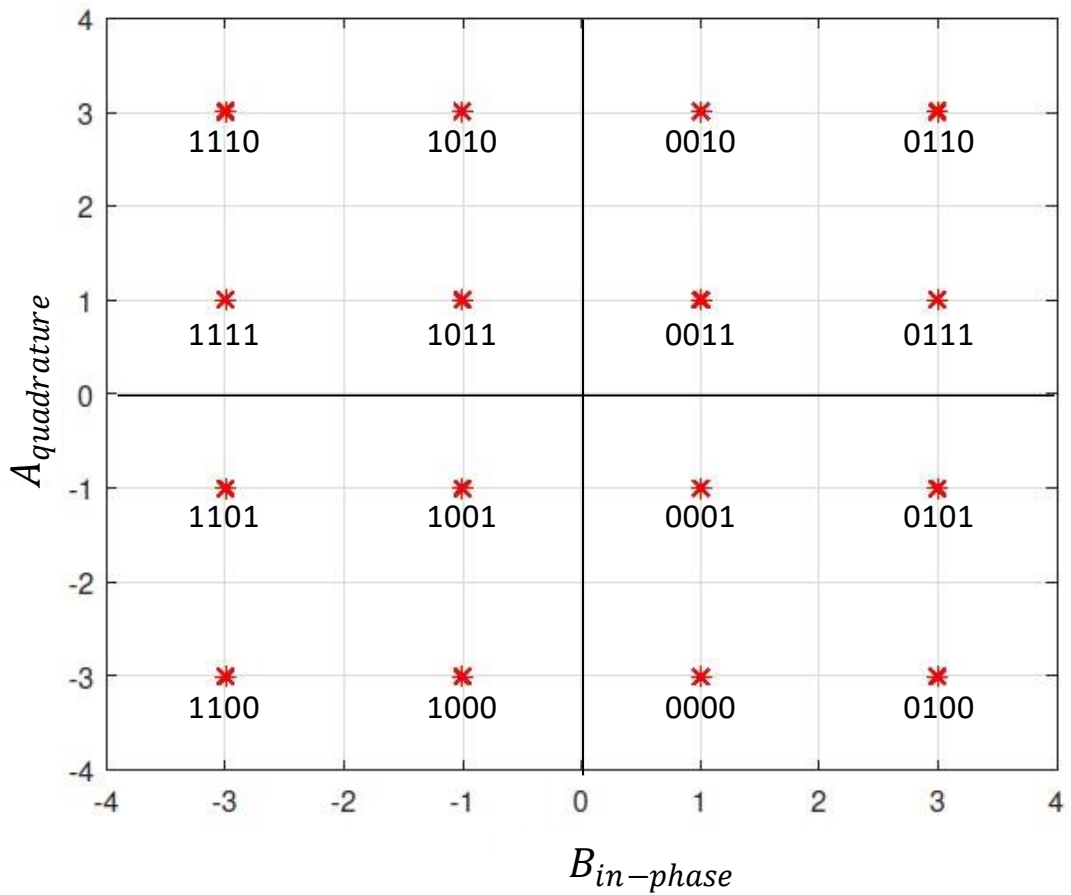


Figure 3-13: Constellation mapping points of the 16-QAM that show the Gray mapping of the in phase and quadrature point, each point represents one complex symbol with possible values for  $A_q$  and  $B_i$  to be ( $\pm 1, \pm 3, \dots$ etc).

## II. Communication Strategies for Ultrasound

### 3.7 Channel Capacity

The communication systems performance is evaluated by the transmitted information quality which is determined by two main factors: the first factor is channel bandwidth, and in order to transmit the information with reasonable fidelity a bandwidth is required to carry the information, the more information to transmit requires more bandwidth which is one of the communication system constraint [125]. The second factor is the  $SNR$  (details of the  $SNR$  is presented in section 3.9) since the noise is not avoidable in communication systems, the noise power is measured and compared relative to the

transmitted signal power, the larger the  $SNR$  ratio employ longer communication distance range.

In the view of the aforementioned factors, a logarithmic measure is stated by Claude Shannon in 1948 for the transmitter information contents, he defined the channel capacity (Shannon-Hartley theorem) to achieve a reliable transmission of information, the data rate channel capacity ( $C$ ) is a function of bandwidth and  $SNR$  defined as [132]:

$$C = B \log_2 \left( 1 + \frac{S}{N} \right) \quad \mathbf{3-13}$$

Where:  $B$  is the channel bandwidth,  $S$  is the signal power and  $N$  is the noise power. From the Shannon-Hartley theorem, the channel capacity rate represents the upper limit or maximum rate which can be the main target to achieve in the communication system design [125].

### **3.8 Effect of Noise**

Noise plays a vital role in the communication system as this unwanted energy can influence the signal transmission and impact the signal recovery at the receiver. Noise can be classified into two different types as shown in Figure 3-14 and explained below:

1. **Internal noise**, the transmitted signal commonly suffers from additive noise or thermal noise when travel through the communication channel, this type of noise is generated internally by the thermal agitation of electrons inside a conducting medium in the system components such as resistors. Internal noise cannot be completely avoided, however, it can be reduced by paying more attention to the circuit design, layout, and selection of the components [133]. The internal noise can be classified into two noise types. First, system or equipment noise. Second, system components noise can appear due to the following:
  - a) **Contact noise**: this noise is created due to a lack in the relay and switches adjustment of the system, this noise can affect the data transmission circuits and cause signal attenuation and thermal noise. Therefore, maintaining clean contact is necessary to overcome this kind of noise.

- b)  $\frac{1}{f}$  **noise**: this type of noise is negligible above the 10 kHz, it is sourced from the semiconductor materials that have fluctuations in their conductivity, this noise is inversely proportional to the frequency hence the name.
  - c) **Thermal noise**: this noise results from the collision that occurs between the electrons and ions due to their random movements.
  - d) **Shot noise**: this noise is the consequence of the statistical random fluctuations of the holes and electrons across the PN junctions. This type of noise is unavoidable as the free electrons responsible for the current flowing, electrons arrived at the anode at a discrete time which creates this noise.
  - e) **Electrostatic and electromagnetic coupling noise**: this noise created due to the inadequate circuit board layout, the electrostatic appears as parasitic capacitance effects and the electromagnetic appears as a transformer effect between the circuit tracks and the parallel conductors.
  - f) **Partition noise**: This type of noise occurs in the transistors when the current flows from the emitter to the base. During crossing the barrier, the current divided between the base and collector which cause a fluctuation in the base terminal.
2. **External noise** is the noise that occurs outside the communication system while the signal travel over the communication channel, this noise cannot be controlled because it comes from medium or channel external sources that are uncontrollable, however, instead it needs to be taken into consideration when designing the receiver to eliminate the effect and recover the desirable signal back [133]. Five main external noise types are listed as follow:
- (a) **Crosstalk** (adjacent pairs interference): electromagnetic crosstalk noise can be found during the experimental setup due to a lack of grounding or wiring.
  - (b) **Static interference**: this type of noise is unlikely to be found inside the human body. It can be generated from storm clouds and dust or sandstorms.
  - (c) **Mains induction**: this type of noise occurs due to the adjacent power routes interference when high voltage transmission lines induce voltage that

influences the neighbouring channels. It is unlikely to occur inside the human body.

(d) **Voltaic interference:** this type of noise is unlikely to be found inside the human body since it can be generated from volcanic activity.

(e) **Radiation:** this type of noise is unlikely to be found inside the human body. it can be induced from sunspot activity, cosmic or space radiations etc.

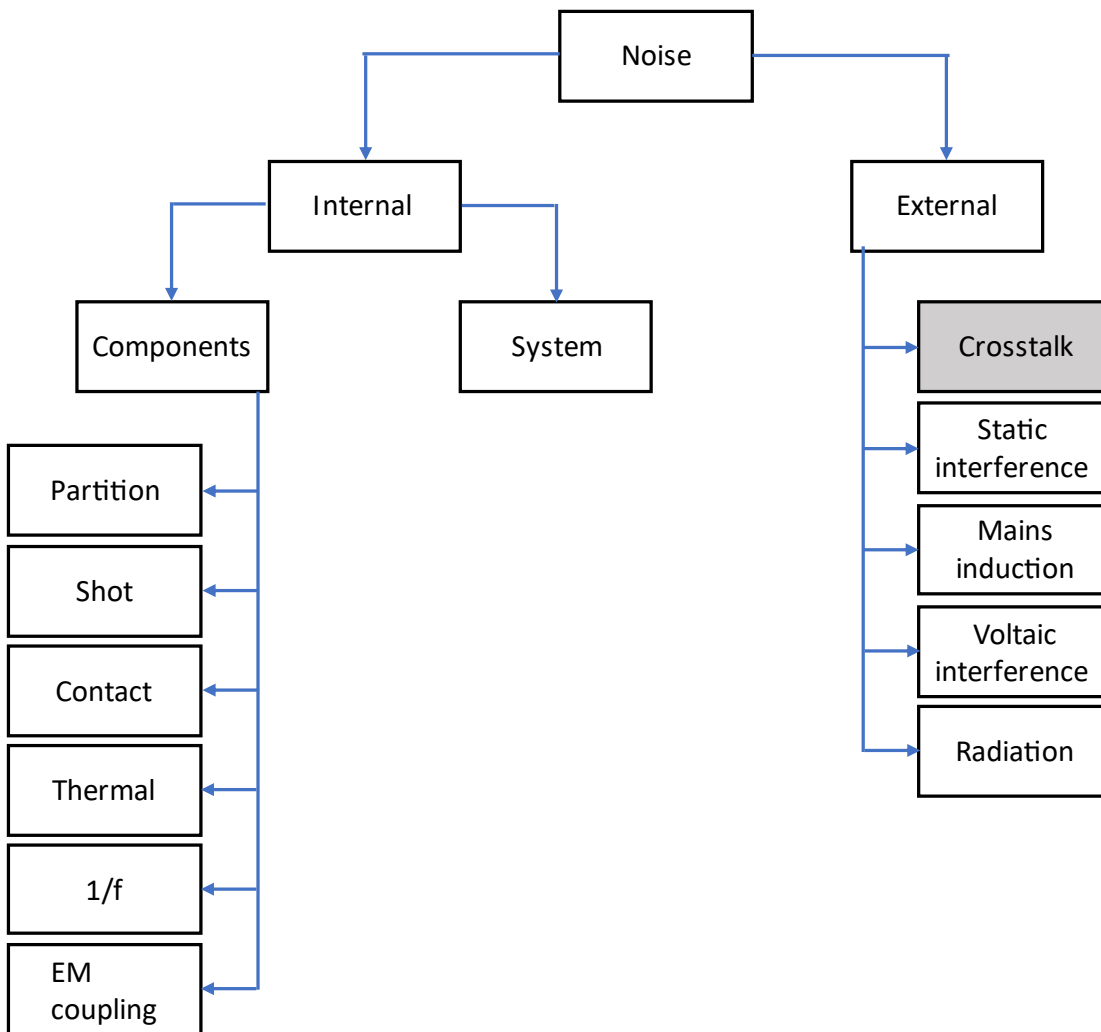


**Figure 3-14: Noise sources that affect the analogue and digital communication systems, the noise source is classified into two main types internal and external. The internal noise can be reduced by careful design of the system circuit. Crosstalk (highlighted) is one of the external noise sources that explained in detail in the next section.**

### 3.8.1 Communication Crosstalk

Crosstalk is one of the external noise effects that occur outside the communication system when the transmitted signal interferes with other signals that share the same channel; hence the noise will appear as it shares the same frequency of the desired signal. The occurrence of this erroneous signal can result from a deficiency in the mechanical or electrical isolation of the active element or the system [134]. The crosstalk effect can be a critical issue for some applications such as mobile robots that employ ultrasound range sensors to acquire environmental information [135, 136], and often happen in the ultrasound transducer array systems [137].

Ultrasound communication crosstalk appears as a relatively small amplitude signal arriving before the primary ultrasound signal on the receiver side. Typically, this crosstalk signal appears concurrently in time with the transmitted ultrasound signal which is not an ultrasound signal because the speed of ultrasound propagation generally in all the medium is slow. Therefore, this signal must be an electromagnetic crosstalk signal.

### 3.9 Signal to Noise Ratio

*SNR* is one of the main factors that determined the fidelity of the communication system and if adequate communication is taking place. *SNR* of any communication system depends on several factors such as the power of the transmitted signal, the gains, and losses of both transmitter and receiver antennas, the modulation scheme and coding techniques of the transmitted signal, external interference from other transmitters and the antennas path loss [138]. *SNR* is generically defined as the ratio between the signal power and noise power, *SNR* is commonly expressed in logarithmic scale since the absolute value of both the signal and noise are expressed in *dBm*. For instance, consider the signal power (*S*) is  $-103 \text{ dBm}$  and the noise power (*N*) is  $-113 \text{ dBm}$ , the *SNR* will be  $10 \text{ dB}$  difference in power between the signal and noise level [133]. *SNR* is defined in *dB* as:

$$SNR = 10 \log_{10} \left( \frac{S}{N} \right) \quad 3-14$$

In real world, the transmitted signal at the transmitter side has a minimum noise effect or noise-free, however, as the signal propagates through the channel a certain amount of noise and distortion will influence the desired signal and it becomes much worse from what it was at the transmitter side. In fact, as the signal power increases at the transmitter the effect of noise in the channel will be reduced, however, on the price of power budget especially in the implanted devices where the power is one of the main system constraints. As demonstrated in sections 3.7, both  $B$  and  $SNR$  are Interrelated, and to reduce the requirement of high  $SNR$ , the  $B$  need to increase. Nevertheless,  $B$  is one of the limitations in communication systems that operate at low frequency, especially ultrasonic transducers [75].

A reliable communication link is the main target in any communication system especially in the biomedical implanted devices as that directly reflected on the patient life and safety. Increasing the  $SNR$  by increasing the transmission signal power might reduce the chance of erroneous data at the receiver. However, it has several disadvantages such as reduce the battery life as the energy per bit increases, more complex and costly electronics required, and health hazards increases as the radiation of the transmit antenna become higher [102]. Therefore, in our design, only a certain minimum required  $SNR$  will be used to achieve a reliable communication.

$SNR$  is represented using the normalised expression  $\frac{Eb}{N_0}$ , especially in the digital communication system, when presented against the  $BER$ .  $Eb$  represents the product of the power of the signal with the bit period, and  $N_0$  is the noise power density ratio. In general,  $\frac{Eb}{N_0}$  is determines the achieved  $SNR$  if the received signal fed through an optimum matched filter for the selected modulation scheme [139].  $SNR$  can be calculated using the following formula:

$$\frac{Eb}{N_0} = SNR + 10 \log_{10}(R) \quad \mathbf{3-15}$$

Where:  $R$  is the code rate which explained in detail in section 3.12.1.

### **3.10 Bit Error Rate**

To evaluate the demodulation performance at the receiver a measurement of the probability of error ( $P_e$ ) or  $BER$  needs to be examined. Moreover, the  $P_e$  is employed to

estimate the link budget in terms of the reported error and the required *SNR* to determine at what distance can work and quantifies the reliability of the entire system. The *BER* is determined by adding up the number of received erroneous bits and dividing by the total number of the transmitted bit, *BER* can also be termed as a bit error ratio as it is not related to time as related to a ratio [122]. *BER* can be expressed as follows:

$$BER = \frac{Err}{TNBs} \quad \mathbf{3-16}$$

Where: *Err* is the number of erroneous bits and *TNBs* is the total number of the transmitted bits.

If the signal power is high and the signal channel is unperturbed, the *BER* becomes an insignificant issue. However, it becomes a significant issue if the *SNR* needs to be sufficient enough to maintain good communication quality in the presence of inadequate transmission due to electronic design circuitry or channel impairment.

As referred to in section 3.8, noise is one of the *BER* enemy that has direct effect on its performance. In fact, the internal noise (system circuitry noise) is described with the Gaussian probability density function. Whereas the external noise source (signal propagation noise) is described with the Rayleigh probability density function [140].

Besides, the system performance can be predicted using the  $P_e$  which can be determined for a given modulation type by estimating the  $E_b/N_0$ . The  $P_e$  is different for each modulation scheme since the error function (*erf*) is different, the average probability of getting zero at receiver whereas one is actually transmitted, and vice versa is expressed as:

$$P_e = 0.5 \operatorname{erfc}(E_b/N_0)^{0.5} \quad \mathbf{3-17}$$

Where *erfc* is a complementary error function,  $\operatorname{erfc} = 1 - \operatorname{erf}$ ,  $E_b$  is the energy per bit and  $N_0$  is the power spectral density of the noise.

### 3.10.1 BER Measurement Process

While the *BER* measurement concept is simple, the measurement process and execution of *BER* is not trivial. Assuming that a data source  $M_1(k)$ , at the transmitter,

is encoded and modulated then transmitted through the channel. The channel will affect the signal  $M_1(k)$  by adding noise, interference, and fade. At the receiver side, the received signal will be demodulated and that create the received data stream  $M_2(k)$  which considers being the same as the transmitted data source. The  $BER$  measurement process is established by comparing the data bit by bit between the transmitted and recovered data stream [141].  $BER$  measurement algorithm can be done by using  $XOR$  logical operation as shown below:

$$R(k) = M_1(k) \oplus M_2(k) \quad \mathbf{3-18}$$

Hence, the estimate of  $BER$  ( $BER''$ ) can be calculated for an  $N$  bit as:

$$BER'' = \sum_{k=0}^{N-1} R(k)/N \quad \mathbf{3-19}$$

Assuming the data transmission as a random process, in this case calculating the  $BER$  will take forever to accomplish. Therefore, it is important to address how big  $N$  should be to obtain an accurate  $BER$  measurement. As the above  $BER''$  expression is a statistical quantity if  $N$  was 12 the  $BER$  results will be 12 different answers due to the noise and channel effects, which express the meaning of  $BER$  estimation. For each trial or iteration of calculating the  $BER$ , that will produce a one with probability ( $p$ ) of true  $BER$ , and zero with the probability of  $(1 - p)$ . Hence, the mean ( $\mu$ ) and standard deviation ( $\sigma$ ) of the  $N$  average such a variable (i.e.,  $BER''$ ) is expressed as:

$$Ex(BER'') = \mu = p = BER \quad \mathbf{3-20}$$

$$std(BER'') = \sigma = p(1 - p)/N \quad \mathbf{3-21}$$

As a result, the calculated  $BER''$  can be a true Measurement of  $BER$  in the limit of large  $N$  and when  $\sigma$  of the  $BER''$  goes to zero.

### 3.11 Packet Error Rate

Packet error rate (*PER*) plays a vital role to evaluate the system reliability and throughput estimation. *PER* is the ratio of erroneously received packets divided by the total number of the data received packets. The received packet is declared incorrect if a single bit error or burst error occurs [142]. The *PER* expectation value is termed as packet error probability ( $P_p$ ) for  $N$  bits data packet can be expressed as:

$$P_p = 1 - (1 - P_e)^N \quad \mathbf{3-22}$$

### 3.12 Error Detection and Correction

In the data transmission link, the main goal is to deliver error free data between the nodes and achieve a reliable transmission. Most likely in the human body channel (noisy channel) especially for the *BeNs* is that the *SNR* insufficient to prevent data error from occurring. Therefore, it is essential to employ coding techniques to negate erroneous data which has a direct threat to the patient's life.

when the channel coding is employed for a system, it will add extra overhead bits to the transmitted information. Hence, that will significantly reduce the channel capacity of the system and slow the rate, which is a trade-off in the design. The coding techniques are commonly used today in different applications in our life such as wire and wireless communications techniques, digital television and radio, modems (e.g. Dial-up, DSL), satellite, optical data storage (e.g. CDs, DVDs, hard drive, Blu-Ray) and bar codes...etc.

Many channel coding techniques are employed in the transceiver design for either error detection or error detection and correction, Figure 3-15 presents the codes. In the error detection method, the receiver will be informed that the received message from the transmitter is not valid, in this case, the receiver can drop the erroneous message and send a request to the transmitter to resend the information packet again.

There are three main error detection codes that commonly used in digital communication and they are a simple class of block code: checksum, parity, and cyclic redundancy check (*CRC*) [122]. Repetition in the message transmission is insufficient in

terms of power consumption especially in the systems that have the power is one of the designs constrain. Also, if the error occurs with every transmitted message, then the retransmission method will be not feasible. Therefore, error detection and correction codes or termed as forward error correction (*FEC*) can be employed, as such the receiver will be able to recover the message if contains error bits up to the code capability limit without the need for the transmitter to resend the message again every time it contains an error. There are two different kinds of *FEC*: block codes and convolutional codes.

Automatic repeat request (ARQ)		Forward error correction code (FECC)			
Stop and wait	Continuous ARQ		Block codes		Convolutional codes
	Go back	Selective Repeat	Non-linear	Linear	
			Non cyclic	Cyclic	
				Golay	Bose–Chaudhuri–Hocquenghem (BCH)
				Non-binary RS	Binary BCH

**Figure 3-15: Taxonomy of error detection and correction codes, it divided into two main types: error detection codes and error detection and correction codes [143].**

### 3.12.1 Block codes

Block codes are a memoryless code that does not rely on previous events and usually used with hard decision decoding. The block coding is presenting the message in the binary format of  $k$  number of bits that comprising a set of  $2^k$ , the message is grouped into blocks of  $k$  binary sequence, and the encoder maps them into a longer block called codeword  $n$  by adding the redundancy or parity bits, the block code is characterised by the two code parameters  $(n, k)$  which help to evaluate the encoding efficiency and the error detection and correction capabilities. The parity bits  $(n - k)$  are the bits added by the encoder to the message as shown in Figure 3-16. The codeword will be transmitted at code rate  $R = k/n$  given that  $0 < R < 1$  when  $R$  is close or equal to 1 which implied a less or no redundancy [132].

The encoder output block is a sequence of  $n$  binary symbols, will be transmitted over the channel after applying one of the modulation schemes. These redundant bits will be used by the decoder at the receiver to decode the message by applying the inverse operation that applied in the encoder [144].

Linear block codes are more favourable for use than long block codes since they do not require large memory space for the code words, they only occupy memory space for the generator matrix which will be used to perform a linear combination (modulo-2) with the data word. Block codes are systematic codes that can be easy to append the parity bits to the message which can be either before or after the message bits. An example of block code is the hamming code, cyclic code, and Reed Solomon (*RS*) codes.

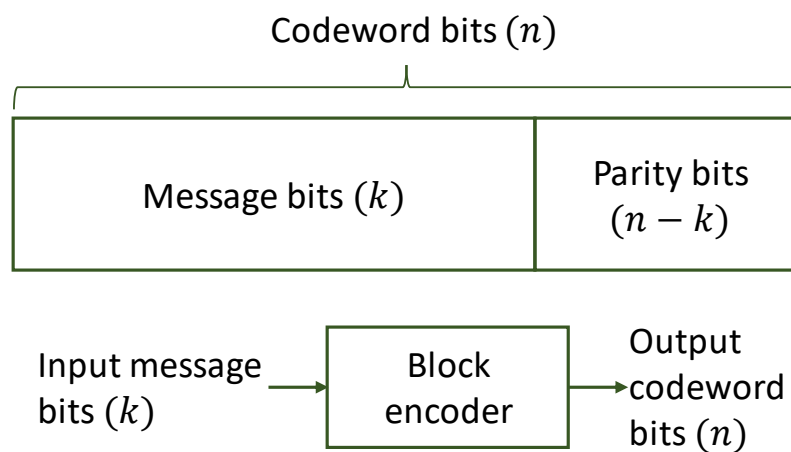


**Figure 3-16: Systematic block code structure. The redundant bits can be appended to the front or back of the message bits.**

### 3.12.2 Convolutional codes

Convolutional code is the second-class coding technique that contains memory and used usually with soft decision decoder. The convolutional code encoder output is, Unlike the block codes, an encoded sequence that generated from the (possibly all) previous and present data inputs sequence. Therefore, each message sequence at the transmitter will generate a unique encoded sequence. At the receiver, the decoder will utilise the encoded sequence redundancy to infer the data message sequence by performing an error correction process [144]. Also, the decoding process can employ an efficient

decoding algorithm (e.g., Viterbi algorithm) that utilise soft-input values from the demodulator. Hence, that will improve the performance of the code gain compared with the hard input decoding. The binary convolutional code is represented by three main code parameters  $(n, k, m)$  where  $m$  represents the number of memory elements, and the code rate is determined same as the block code by the ratio  $R = k/n$  [145].

### 3.13 Block Codes Versus Convolutional Codes

For any system design, the selection between the block and convolutional codes is mainly dependent on the application and system requirements. In general, the block codes theory resources are considerably richer than their counterparts. However, the literature argues that in almost all cases that convolutional codes are outperforming block codes which are not always the case as it is more application dependent [146].

For block codes design, multiple finite field concepts and mathematical structure concepts employed to implement efficient decoding and correcting algorithms. As a practical example of block codes, *RS* is one of the powerful codes in the block codes family that used widely in digital communication. For example, the National Aeronautics and Space Administration (*NASA*) employed Berlekamp's bit-serial *RS* encoders (*Ber82*) as a standard encoder for deep-space communication. Additionally, *RS* codes have a significant advantage for correcting burst errors such as the errors that occur in the second memories (e.g. disks, tapes) [132, 146].

Convolutional code in combination with the Viterbi decoding algorithm achieves good performance when the noise type is Gaussian and white. Viterbi decoding algorithm has the capability of exploiting the full soft decision information at the decoder input. On the other hand, *RS* code capability is limited in soft decision information. Moreover, code synchronization is easier in the convolutional codes (contain memory) than block codes (memoryless) [146]. The following Table 3-4 presents a comparison between the block and convolutional code.

**Table 3-4: Comparison between block codes and convolutional codes.**

	<b>Block codes</b>	<b>Convolutional Codes</b>
Decoding type	Hard decision decoding	Soft decision decoding
Processing	Memoryless	Require memory
Code type	Binary/non-binary	Binary/non-binary
Codeword type	Systematic (linear)	Systematic/ non-systematic
Decoding	Easy	Difficult
Decoding type	Hard decision decoding	Soft decision decoding

### 3.14 Reed Solomon Code

*RS* code is one of the oldest error control algorithms that nowadays commonly adapted in computer memories and compact disc players. *RS* code named for Irving Reed and Gustave Solomon, who published the code in 1960. *RS* code is a linear cyclic error correcting code that classified as a linear systematic non- binary block code, it combines the parity bits and the generator polynomials over finite fields known as Galois field (*GF*) to form the error detection and correction process [147].

*RS* code is characterized by three main parameters  $n$ ,  $k$ , and  $t$ , where  $n$  is the number of symbols and each symbol includes  $m$  number of bits,  $m$  bits length can vary depending on the application. However, usually, it is more convenient to represent  $m$  on a byte ( $m = 8$ ). Thus, each symbol will be a byte, and the *RS* code will process symbols rather than bits like any other cyclic codes.  $k$  is representing the payload symbols and  $t$  is the error-correcting capability which expressed in the following equation and presented in Figure 3-17 :

$$t = (n - k)/2$$

**3-23**

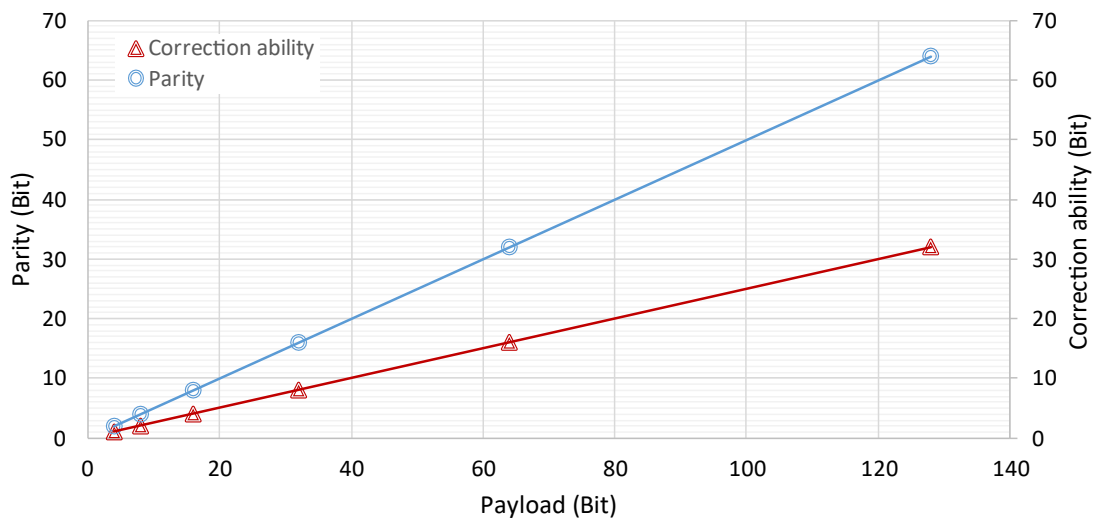


**Figure 3-17: Error correction capability and parity bits of the *RS* code, the parity bits will be added to the payload at the beginning of the end of the packet (systematic). The correction capability shows the maximum number of bits that can be corrected for given parity bits.**

If we consider the most popular *RS* code which is  $(n, k) = (255, 247)$ , this code over  $GF(2^8)$ , and has an error correction capability of up to 4 symbols in a block of 255 symbols no matter if one bit per symbol is an error or more than one. In the worst case scenario, when the errors are distributed on the block symbols, this code is able to correct *up to* 4 symbols. Alternatively, if a burst error occurs the code can correct 4 short bursts of errors ( $4 \times 8 = 32$  erroneous bits) [132].

*RS* code was adapted to negate transmission errors for the following reasons:

1. *RS* is capable of correcting burst errors since the correction occurs at the symbol level, rather than bit level, regardless of whether a single bit or multiple bits in the symbol are in error.
2. *RS* can be efficiently implemented in software on a microcontroller which saves the need for any additional hardware (i.e. low complexity).
3. *RS* is a hard decision decoder being suitable for a low power processor, its ability to operate with non-binary symbols and it has no error floor effect, so it eliminates the need for any additional error checking.

### 3.14.1 RS Code Architecture

As mentioned earlier, RS code uses a special mathematical field called  $GF$  to produce the generator polynomial. The  $GF$  arithmetic operations, such as (subtraction, addition, division, ...etc), on field elements have always a result in  $GF$ . Both the  $RS$  encoder and decoder require to implement software functions or special hardware to run those arithmetic operations [148].

The  $RS$  generator polynomial has a unique property that all the codewords are exactly divisible by the generator polynomial, the generator polynomial  $g(x)$  can be expressed as:

$$g(x) = (x - \alpha^i) (x - \alpha^{i+1}) (x - \alpha^{i+2}) \dots (x - \alpha^{i+2t_{ec}}) \quad \mathbf{3-24}$$

Where  $\alpha$  is a primitive element of the  $GF$ .

The codeword polynomial  $c(x)$  of the  $RS$  code is produced by multiplying the  $g(x)$  by the message polynomial  $m(x)$  as shown below:

$$c(x) = g(x)m(x) \quad \mathbf{3-25}$$

#### 1. RS Code Encoder

The encoding process is achieved by appending the parity symbols to the beginning or the end of the message vector, since it is systematic code, to form the codeword. The parity symbols  $p(x)$  are obtained by dividing the  $m(x)$  by the  $g(x)$  using the  $GF$  algebra [148]. The final codeword expression is shown below:

$$c(x) = m(x).x^{n-k} + p(x) \quad \mathbf{3-26}$$

The  $g(x)$  number of registers are corresponding to the  $n - k$ .

## 2. RS Code Decoder

At the receiver, the received polynomial  $r(x)$  represents the codeword and might include some errors due to the channel effect and noise, the  $r(x)$  expressed as:

$$r(x) = c(x) + e(x) \quad 3-27$$

The decoding process will pass through four main steps:

- 1) From the  $r(x)$ , the syndromes  $S_i$  need to be computed in a similar way of calculating the  $p(x)$  polynomial. Calculating the syndrome help to check if there is an error in the  $r(x)$ . The number of syndromes is corresponding to  $2t$  of the  $RS$  code, which depends mainly on the errors, not the entire codeword. The  $S_i$  can be expressed as [148]:

$$S_i = r(\alpha^i), \quad i = 1, 2, \dots, 2t \quad 3-28$$

Where  $\alpha^i$  represents the roots of  $g(x)$ .

- 2) Calculate error location polynomial  $A(x)$  and error magnitude polynomial by adapting Berlekamp- Massey algorithm.
- 3) Allocate the position of the errors by finding the inverse roots of the  $A(x)$ , then computing the error polynomial  $e(x)$  which can be expressed as:

$$e(x) = e_{j_1} x^{j_1} + e_{j_2} x^{j_2} + \dots + e_{j_n} x^{j_n} \quad 3-29$$

Where  $n$  index represents the number of errors,  $x^{j_n}$  represents the error positions.

- 4) The final step is to correct the errors of the  $r(x)$  by subtracting the  $e(x)$  from  $r(x)$ .

### 3.15 Communication Protocol

One of the main communication system aspects is the protocol that allows two or more *BeNs* to establish an adequate communication link. Moreover, the system communication protocol can be designed by either hardware or software or maybe both to identify the communication synchronisation, rules, and operation modes. For each

particular situation, the *BeNs* use a range of various well-defined messages format that can be exchanged between them to elicit the required response which can be information to stimulate or record for the biological tissue. Those messages can be defined as operation modes or protocols, addressing those modes are important to achieve reliable communication with realistic minimum power consumption. Several operating modes are widely demonstrated in the field of Wireless Sensor Networks (*WSNs*) such as active mode, routing mode, sensing mode, and sleeping mode [149].

### **3.15.1 Communication Protocol for Intra Body Communication Network**

Figure 3-18 illustrates two distinct timing diagrams, the sensing process of Implantable Medical Device (*IMD*) and the ultrasound communication process, respectively. The implant control system wakes up periodically to perform the sensing process. During this period, the control system initiates the sensing process. Consequently, the sensor unit starts the action. Thereafter, the control system unit implements the remaining three processes: data recording, data processing, and data storing. On the other hand, the master device sends an interrupt to wake up the implant for transmitting the stored data. Thereafter, the control system prepares the data to be transmitted by appending the overhead bits and the error correction code (*ECC*) to the payload. Then, the master device unit starts receiving the data which consists of three parts: header, payload, and parity bits.

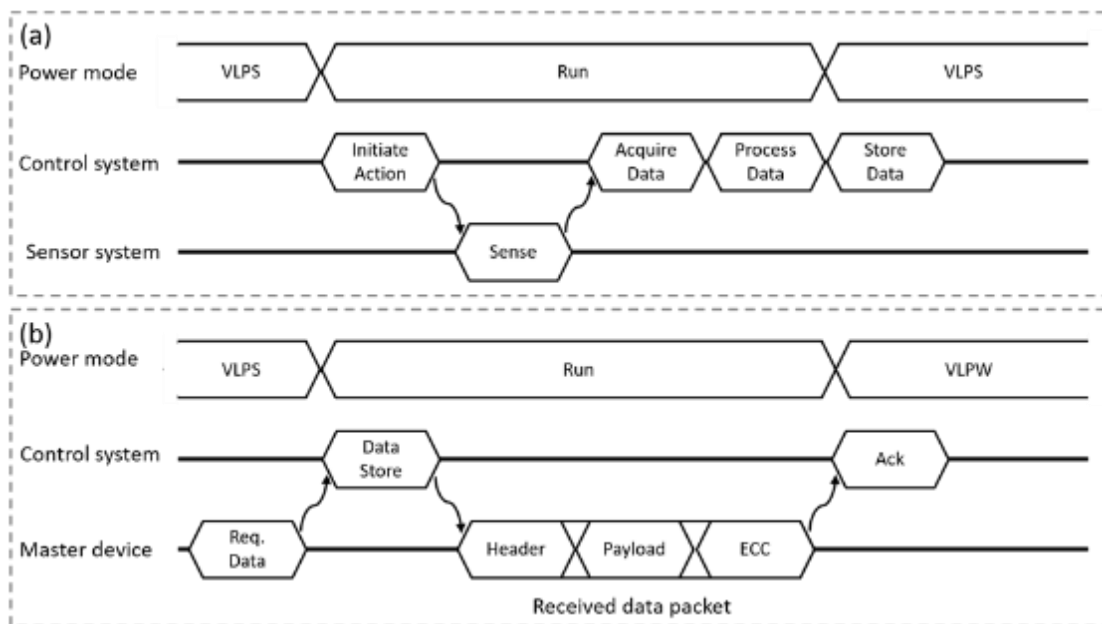


**Figure 3-18: The timing diagram for the system that includes two phases (a) The sensor acquiring data process that starting by requesting the data from the sensor unit, the data will be processed and stored to be transmitted later; (b) represents the ultrasound communication link between the master and slave systems or vice versa. Power cycling is employed to reduce the current consumption by switching between the normal run and very low power modes.**

### 3.15.2 The Proposed Communication Protocol

Seeking feasibility and a balance between the design constraints and the requirements, the proposed system is a network of four bioelectronic devices nodes that are implanted inside a human body. The main function of this network is to monitor the symptoms of a particular biomarker or any other indication of any possible disorder. In addition, this network is connected to a central unit which is fixed inside the chest. The main functionalities of this unit are controlling the process of synchronization, data communication with other bioelectronic nodes.

Due to the harsh operating environment and the limited powering resources of the systems, there is a necessity of sketching a plan to handle the operation of messaging inside the network during its normal operation and in the emergency cases such as a sudden drop in battery level or when a test is required to check the network health status. Therefore, the system proposed to work by either of five modes: synchronization

mode, test mode, communication mode, reporting mode, and emergency charging mode.

Figure 3-19 shows the general packet structure, downlink, and uplink, for any type of communication mode. Both destination address and source address are referring to the network entity (bioelectronic node or the base station) unique address which is an ID of 4-bit length uploaded prior to their implantation. Moreover, the operation mode is a 4-bit field that refers to one of five modes of operations mentioned previously. Furthermore, the payload structure of each mode has its unique structure as will be described in the next section for each mode: main purpose, functionality, and a brief description.

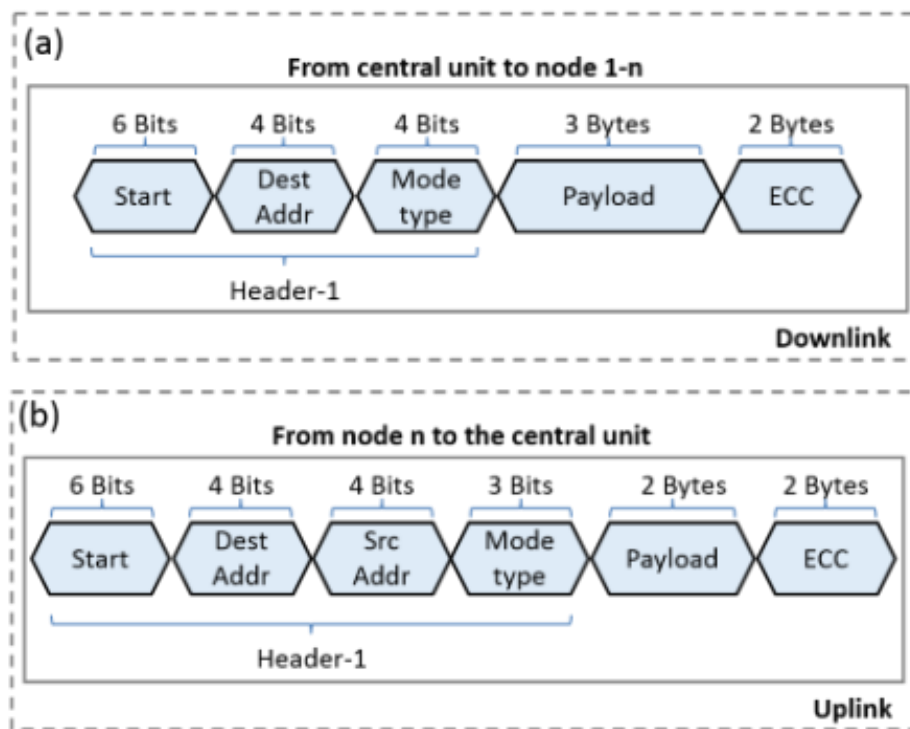


**Figure 3-19: (a) Packet structure for the ultrasound data transmission where each node receives its packet separately. The packet includes three main parts: header, payload, and the error correction code. The downlink term represents the messaging from the central unit toward the bioelectronic nodes; (b) The reversed direction is referred to by the uplink term.**

## 1. Synchronization Mode

A synchronization scheme is essential to maintain the accuracy of data dissemination and to secure a particular time slot for each node to implement its functions. In order to prioritise the set of devices, during this mode, the central unit follows a specific procedure to announce the timeslot dedicated to each bioelectronic node. The proposed procedure is launched by the central unit via sending four messages, each one for a particular bioelectronic node in the network. As depicted in Figure 3-19, the message contains the address of the targeted bioelectronic node, the mode of operation, and the payload which is consisting of three parts.

The first part of the payload has a length of 3 bits and indicates the number of bioelectronic nodes in the network ( $n = 4$ ). The second part is a 2 bytes length that contains the addresses of the  $n$  bioelectronic nodes ordered in the same order of their priorities inside the network. Finally, the third part is a set of 5 bits indicating the duration of time, hereafter known as separation time ( $T_s \leq 31 s$ ) that are separating the window of operation of any two bioelectronic nodes has consecutive priority. In order to acknowledge the setup, a check procedure is implemented by the central unit via launching test mode as illustrated in the following section.

## 2. Test Mode

During test mode, all devices are requested by the central unit to send a certain HELLO message after a specific duration  $T$ . Therefore, the payload field will contain two subfields:  $T$  and Hello message. Once a response is received, the central unit checks whether 4 HELLO messages separated by  $T_s$  are arrived. Consequently, synchronization of the network is acknowledged and both communication and reporting mode is ready to be launched.

## 3. Communication Mode

In this mode, each implant will communicate with other network entities. Such a mode is suitable to be used in the case of examining the response of the biological organ, where the node is bioelectronic, to a specific treatment or stimulation. There are two types of messages in this protocol, uplink, and downlink. In the first type, a message is generated by the central

unit as a request to the targeted bioelectronic node. Therefore, it consists of a destination address, operation mode and the request which is included in the payload part. As a response, an uplink message is sent from the mentioned bioelectronic node toward the requester entity. Figure 3-20 shows the state transition diagram for the communication mode. The utilisation of intra bioelectronic nodes communication is beneficial to increases the possibility of expanding the communication coverage area by facilitating some near bioelectronic nodes to function as hops between a faraway bioelectronic node and the central unit [150]. Such a scheme requires less power consumption in comparison to expanding the coverage by increasing transmitter power.

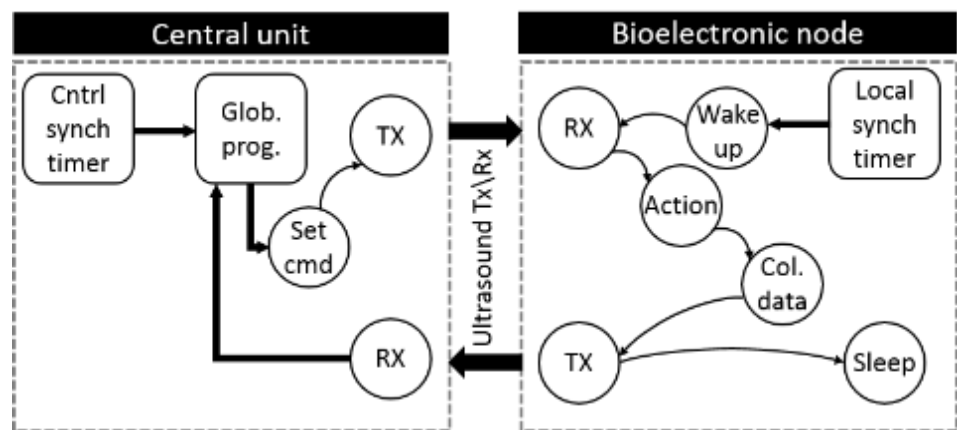


**Figure 3-20: State transition diagram for the communication mode between the central unit and bioelectronic node, this mode triggered by sending a command by the central unit to the targeted bioelectronic node which replies by sending the data stored in its memory. The response time of each node is separated from other nodes by the separation time ( $T_s$ ) dedicated the synchronization mode to prevent any possible interference.**

#### 4. Reporting Mode

This mode is utilised when the bioelectronic nodes are used to collect a specific type of data frequently and send the collected data at each time. Such an operation is one of the common topologies which are governing the nowadays *IMD* applications such as continuous monitoring to a particular biological marker. Working in this mode does not require request generation by the central unit where data are collected and sent by the

bioelectronic nodes automatically. Doing so leads to a significant reduction in power consumption where the power required to receive a request packet is saved. Launching this mode requires a presence of mode initialisation as shown in Figure 3-21 a. In this part, a downlink message is generated by the central unit and sent to the bioelectronic node in order to request continuous reporting after a specific duration of time  $T_{RS}$  dedicated by the first byte of the payload. In addition, the rest 20 bits of the payload are dedicated to identifying the repetition period ( $\tau$ ) which is the separating time between any two generations of the mentioned report. The bioelectronic node response, as depicted in Figure 3-19, is a normal communication uplink message that contains both addresses of the node and the central unit are generated by the bioelectronic nodes at a frequency of  $f = \tau^{-1}$ . Figure 3-21 b shows the second phase of operation, the local timer will wake up the node for aggregation of data.

## 5. Emergency Charging Mode

In the case of wireless powering node, emergency charging mode can be employed. Due to several circumstances, a particular device might experience a sudden depletion in battery charging which is out of the design specifications and life expectancy of each battery. In such an occasion, the device launches an emergency mode by stopping all sensing operations and dedicate communication functionality to be used only to recharge its battery by using wireless acoustic signals in order to make use of the harvested power to charge its battery.

The above-mentioned protocol has been proposed to be implemented in the project to facilitate the process of data communication between intra body communication network. Practically, However, it has been implemented using only two entities while the whole system is suggested to be implemented as a future work as mentioned in chapter 6.

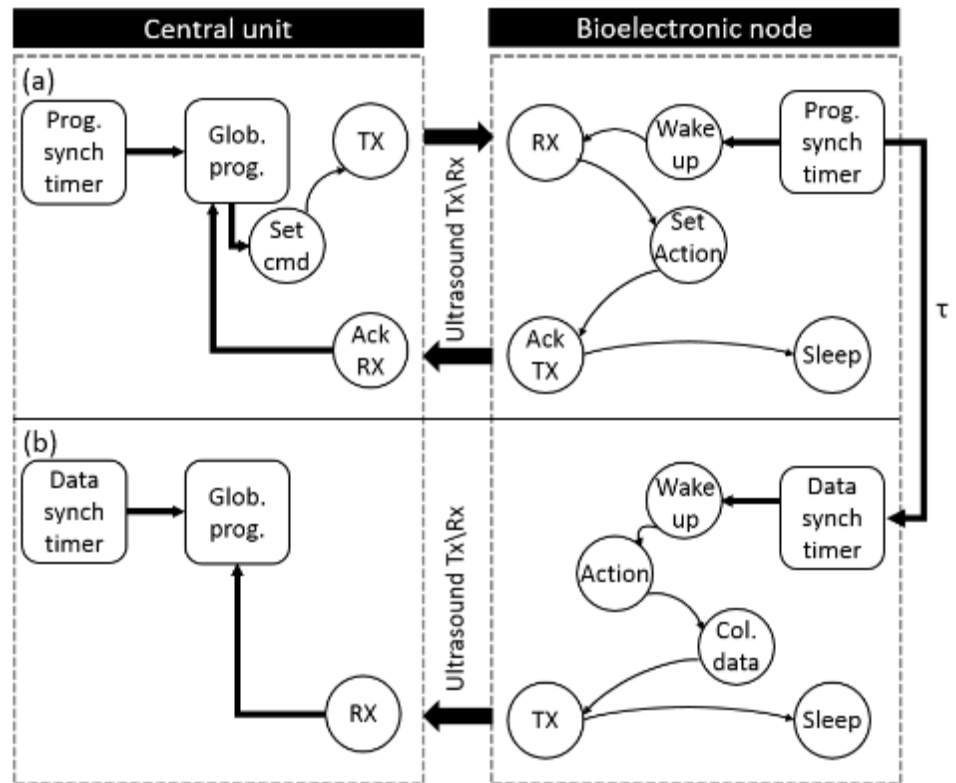


**Figure 3-21: State transition diagram for the reporting mode: (a) depicts reporting mode initialization, where a command sent by the central unit to dedicate  $\tau$  value which indicates the repetition frequency. This value is stored in the local timer; (b) depicts the reporting mode where the local timer wakes up the bioelectronic node every  $\tau$  times. Once it wakes, the node collects data, store it and send it back to the central unit.**



## Chapter 4. System Architecture

### 4.1 Introduction

The design, analysis and implementation of the proposed system prototype are presented in depth in this chapter. Additionally, the developed prototype system, which is invented to explore the proposed communication architecture, is presented. As illustrated in Figure 4-1, the proposed prototype system comprises three main units:

1. **The ultrasound communication link** comprises two units: the *PZT* transducer and the analog front end (*AFE*) unit which are described in detail in both section 4.2 and section 4.3 respectively.
2. **The embedded control unit** which is consisting of three main parts: comparator, switch, and the central processing unit (*CPU*). The functionality of this unit is illustrated in section 4.5.
3. **The sensor unit**, which is utilised to sense the medical parameters that are monitored based on the application. More details about this unit are depicted in section 4.6.

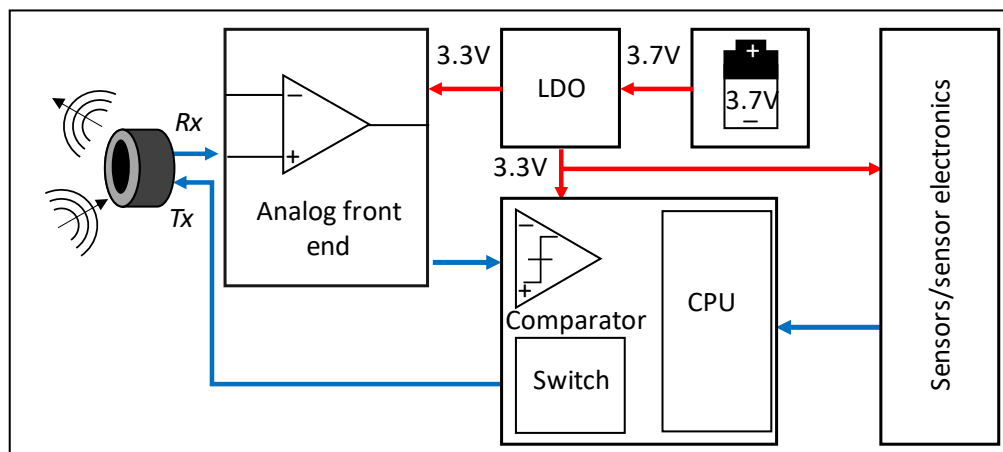


**Figure 4-1: Block diagram of the whole system showing the three main parts of the implant, the one-directional ultrasound communication link that operates at 320 kHz resonance frequency and driven by the analog front end electronics which includes three stages filters and amplifier, the embedded control system which digitizes and process the data, and the sensors unit.**

## 4.2 Piezoceramic Technology

Ultrasonic Based on the literature, transducers are considered the cornerstone in ultrasonic communication. They are utilised to perform the function of converting electrical signals into pressure waves. Ultrasound transducers have previously been manufactured in different shapes, such as discs [151], plates [152], and tubes [153], based on the application and operation mode. The first two types of *PZT* shapes, disc and plate, have a property of providing directional beams. Therefore, the manufactured *PZT* in both shapes performs a significant efficiency at the point to point transmission. However, in some instances, the line of sight may not always be possible. Furthermore, over time, implanted devices might experience some types of movement and rotation. As a result, directional shapes are proved to be inefficient for communication between bioelectronic implant devices [154]. Therefore, as an alternative, it is proved that the utilisation of inherently omnidirectional transducers which are functioning by emitting a pressure wave equally in all directions.

An alternative is to use *PZT*, piezo transducers in a tube architecture. These have been shown to have the most efficient piezoelectrical properties in terms of sensitivity. However, it should be noted that although *PZT* is currently the most efficient of the current batch of piezo transducers, 60% of the material is lead oxide, which is a toxic heavy metal, particularly to the nervous system. Nevertheless, *PZT* utilised the material as it is currently best in class, and the primarily focuses on the communication system as a whole.

### 4.2.1 Ultrasound Transduction

The tube-shaped *PZT* can be operated efficiently in the omnidirectional mode [106], as per Figure 4-2 (a). As a result, it is more suitable for the multipoint ultrasonic communication scheme system presented in Figure 1-2. In the proposed system, an off-chip piezoelectric tube transducer was utilised, as shown in Figure 4-2 (a, c). The utilised bare piezo crystals, which is constructed using the soft *Pz27 (Navy II)* material, are purchased from Meggitt A/S (Denmark) with the following specifications:

1. Good coupling factors ( $K_p$ ) of 0.59.
2. High charge coefficients ( $d_{33}$ ) of 440  $pC/N$ .

3. High Curie temperature of 350 °C.
4. Has dimensions of ( $h = 3 \text{ mm}$ ,  $w_1 = 2.5 \text{ mm}$  and  $w_2 = 3.5 \text{ mm}$ )
5. Manufactured to be operated at a resonance frequency  $f_r \cong 290 \text{ kHz}$ , which is determined based on the following equation:

$$f_r = \frac{2 \times N_{md}}{w_1 + w_2} \quad \mathbf{4-1}$$

where  $N_{md}$  is the speed of the sound of *Pz27* (medium diameter speed), which is 880 m/s [76].  $w_1$  and  $w_2$  are the outer and inner diameters, respectively.

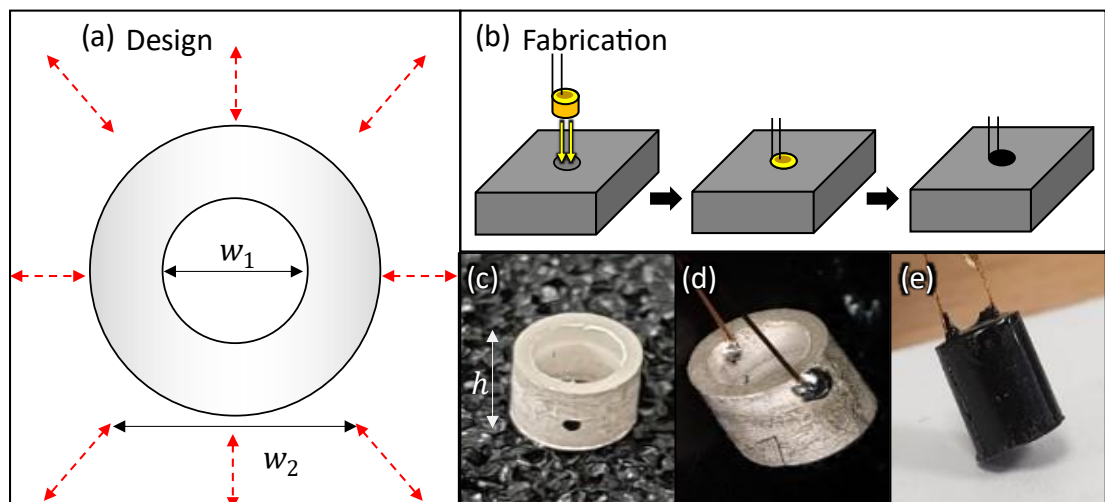


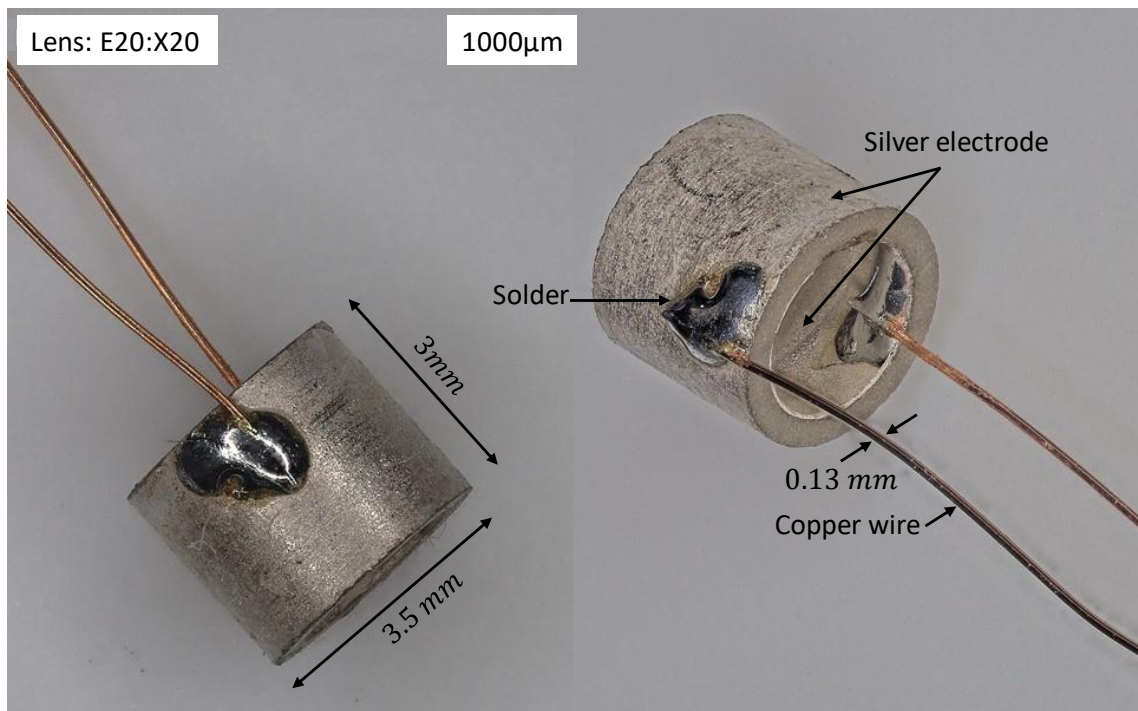
**Figure 4-2: The omnidirectional ultrasound transducer (a) Radial mode vibration of the active element, dimensions:  $w_1 = 2.5 \text{ mm}$ ,  $w_2 = 3.5 \text{ mm}$  (b) Steps that used to implement and encapsulate the transducer, Assembly the active elements on the *CNC* machined metal mold. Then, the active element aligned in the centre of the mold with a 1mm gap and the set is filled with polyurethane; (c) Bare piezoelectric crystal of height  $h = 3 \text{ mm}$  after the scraping with emery paper; (d) Wire bonding the inner and outer diameter electrode; (e) The transducer final shape after curing.**

#### 4.2.2 Wire Bonding

To prepare the *PZT* crystal for wire bonding, the surface of the crystal was scraped with emery paper, in order to remove the layer of silver oxide. Thereby attained a bright and flat surface of the electrode, Figure 4-2 (c) shows the tube shape bare *PZT* crystal after the scraping with silver electrodes on the curved flat surfaces where the single black dot is indicating the *PZT* polarisation. Afterward, the surface of the electrode was

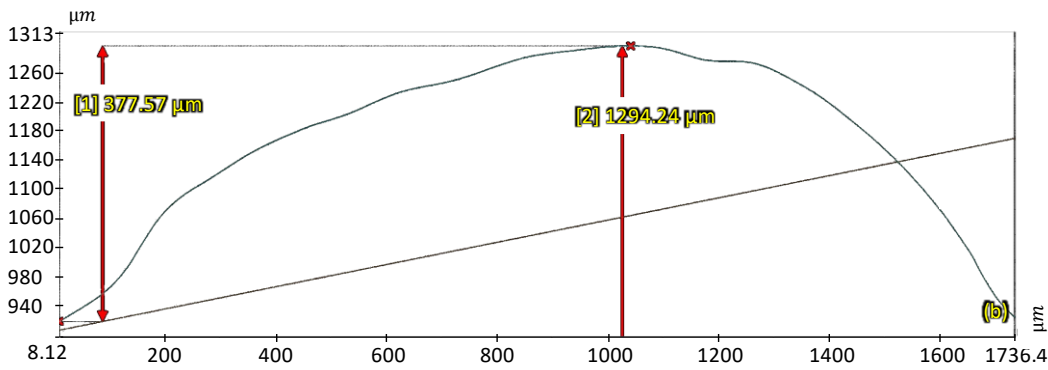
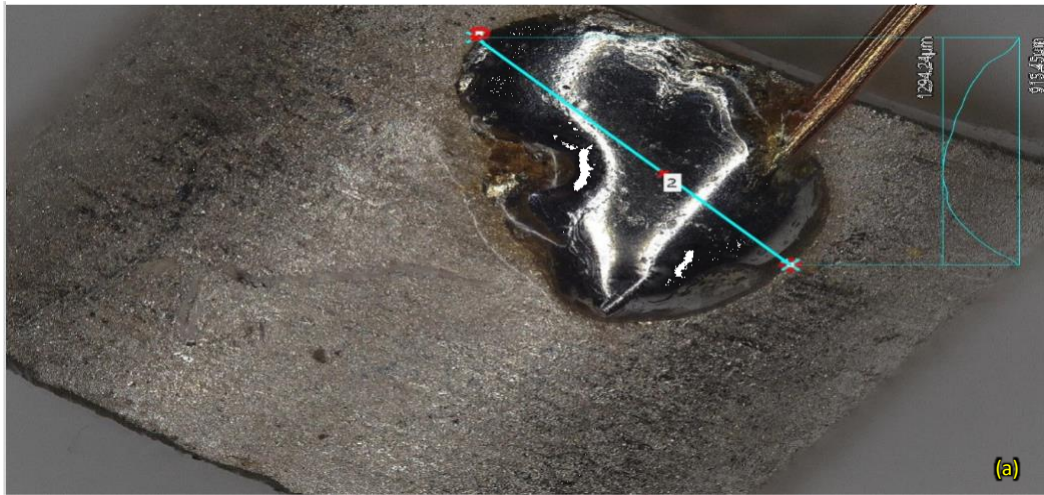
prepared by swabbing the surface with isopropyl alcohol (*IPA*) to remove any grease or dust. Low melting temperature solder 180 °C from Henkel technologies and 0.46 mm thickness was utilised in order to avoid the chance of excessive heating that may damage the silver electrode. A small amount of solder was applied in the desired location (near the edge of inner and outer diameters of the *PZT* crystal), then Unistrand Enamel ultrafine copper wire of diameter 0.13 mm from Rapid is connected to the crystal taking into account not moving the wire prior cool down the joint, Figure 4-1 (d) illustrates the *PZT* crystal with electrical leads connected.

Figure 4-3 shows the complete *PZT* crystals, captured under the microscope, after the wire bonding with a scale and dimensions. Care must be taken when attaching the wire leads since it is important for measuring the electrical generated signal. The insulation material of the thin copper wire is removed only at the connection point of the wire with the crystal, the removed length from the wire end was about (0.5 – 1) mm, and the insulation material must be kept especially near the edge of the wire bonding to avoid any electrical shorting that can affect the response of the crystal. Multiple wire bonding methods have been considered in this project (e.g. Commercial techniques). However, those solutions were not effective and limited due to the crystal miniaturised size. Therefore, low-temperature soldering and conductive epoxy approaches were employed. Wire soldering of the crystal inner diameter can be challenging due to the small size of the tube *PZT* crystal. Therefore, a fair amount of practice was essential to perform this task successfully.



**Figure 4-3: Side view of the piezoelectric crystal that shows the wire bonding in the inner and outer diameters in the top edges.**

Both the size and location of the solder dot has a significant impact on the damping effect of the transducer response. Therefore, a microscope is necessary to have a closer look in order to fit the solder dot in its optimum size and location, Figure 4-4 (a) demonstrates the solder dot of the outer crystal diameter under the microscope. Measurements of the inner solder can be challenging due to the small size of the tube *PZT* crystal. Therefore, the focus was on the outer diameter wire bonding connection. Figure 4-4 (b) shows the maximum and minimum soldering heights and the width of the solder as highlighted in Figure 4-4 (a). Figure 4-4 (c) shows the highlighted soldering area and the below table presents the measurements of the dimensions of the soldering area. The ratio between the soldering area to the tube shape crystal is determined to be % 0.65, which is small enough to provide a minimal damping effect on the transducer response.



No. 1	Volume ( $\mu m^3$ )	Surface Area ( $\mu m^2$ )	Cross section Area ( $\mu m^2$ )
Average	368495725.7825	1805296.83	1559646.73
Maximum	368495725.782	1805296.83	1559646.73
Minimum	368495725.783	1805296.83	1559646.73
Total	368495725.782	1805296.83	1559646.73

**Figure 4-4: (a) The solder dot of the outer diameter of the crystal, the maximum soldering height is 1.2 mm; (b) The height and width of the soldering area of the point highlighted in (a); (c) Measurements of the soldering area that highlighted in red, the volume, surface area and cross-section area were measured. The ratio between the soldering area and the crystal is % 0.65.**

### 4.2.3 Encapsulation

Encapsulation of transducers and electronics is important in order to insulate them from the surrounding environment (saline/tissue), achieve mechanical robustness and achieve wide communication bandwidth. Polyurethane (*PU*) was utilised as a coating material as its acoustic impedance is  $1.8 \text{ MRayls}$  which is close to that of water ( $1.5 \text{ MRayls}$ ). Such impedance matching is important in minimising possible reflections at the interface. Also, *PU* has excellent water resistance and has already been used in the pacemaker leads from a Medtronic model *P1501DR* [113], indicating biocompatibility. Therefore, a black polyurethane resin (*UR5041*) from Electrolube was utilised for the encapsulating the transducer. The target encapsulation layer thickness is  $0.5 \text{ mm}$  for the surrounded diameter and fully inserted into the inner diameter. Therefore, a custom mold was designed to fulfil the aforementioned requirement. The ultrasound transducer was fixed inside the mold after spraying a non-stick silicone coating into the mold, making sure it was centred and  $0.5 \text{ mm}$  space between the mold and outer diameter. After injecting the *PU* to the mold, the encapsulated transducer was baked in the oven for  $24 \text{ h}$  at  $40 \text{ }^\circ\text{C}$  to achieve a better solder connection to the electrode surface as depicted in Figure 4-2 (b). The final encapsulated transducer is shown in Figure 4-2 (e).

### 4.2.4 Impedance Measurements

A 500 kHz MFIA impedance analyser from Zurich Instruments was used to characterise the piezoelectric transducers. Figure 4-5 presents the real and imaginary parts of the impedance versus the frequency of the bare transducer in air. In Figure 4-5 (a) the bare transducer shows a high  $Q$  factor since the transducer is undamped, the impedance exhibits the highest value at the anti-resonance ( $f_a$ ) frequency. Whereas the impedance is approximately the minimum at the resonance frequency ( $f_r$ ). Figure 4-5 (b) shows the phase of the impedance. It is noticeable here that there is a slight difference between the theoretically calculated resonance frequency of the transducer using equation 4-1 and the below measured one. This difference can be explained as a result of three impacts: solder mass effect, wire bonding, and the effect of the mechanical losses resistance of the transducer that cannot be ignored in the practical measurements.

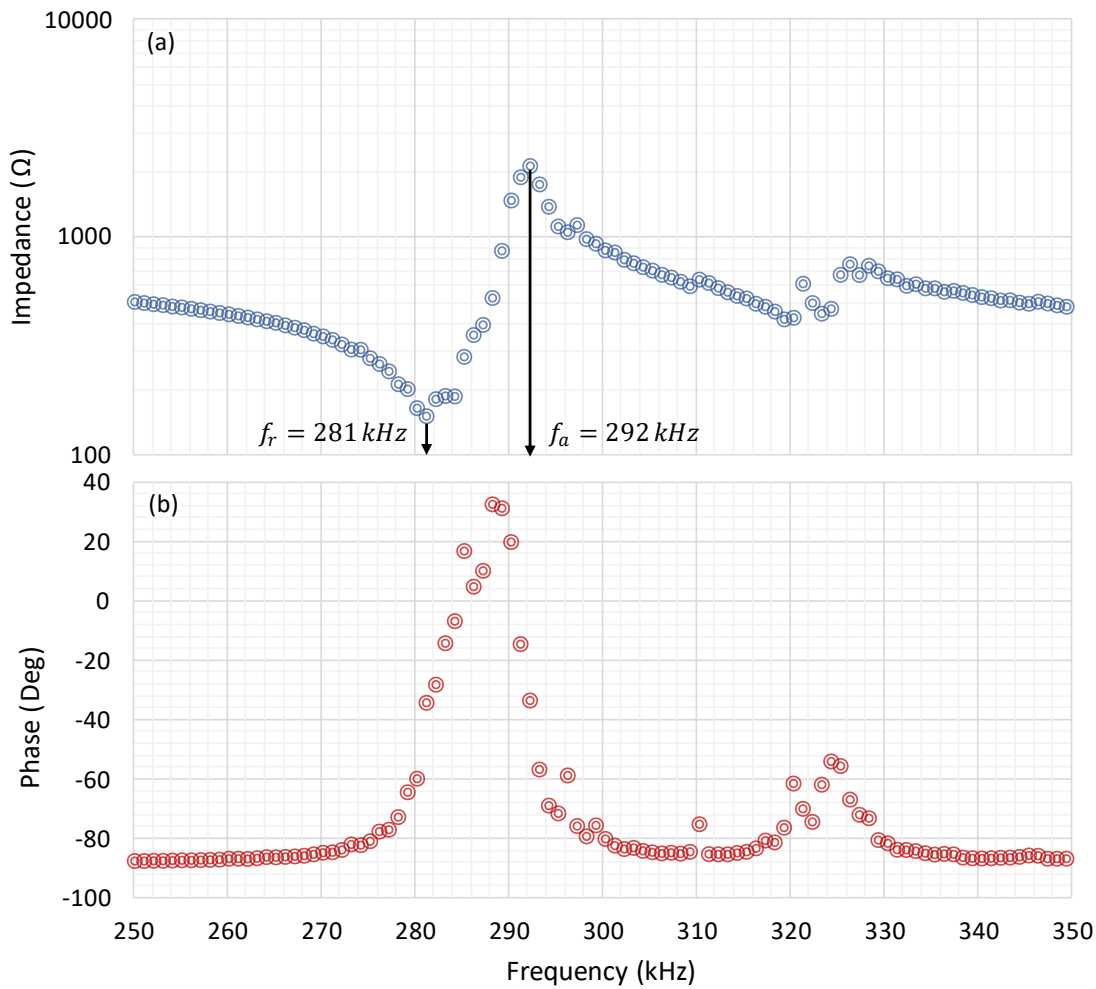


**Figure 4-5: Transducer impedance measurements before encapsulation: (a) The impedance magnitude measurements versus frequency sweep for an undamped (unloaded) transducer in the air; (b) The Impedance phase measurements versus frequency of undamped transducer in air.**

Figure 4-6 (a, b) illustrate the measured impedance of the encapsulated or damped transducer in air and water respectively which provides more broadband or flat response and can run across a wide frequency range. It can be seen the real impedance value variation when changing the medium which gives an indication of a good fabrication and wire bonding process. Hence, the acoustic signal is not trapped in the *PU* encapsulation wall.

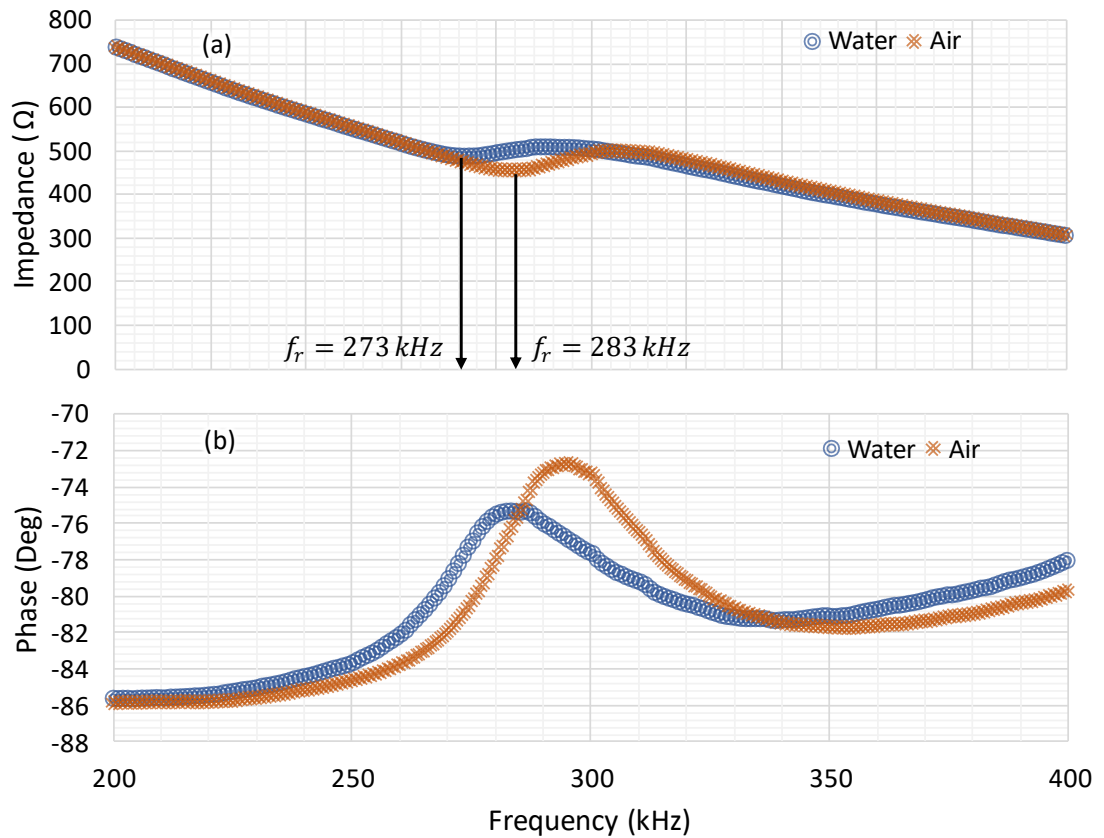


**Figure 4-6: (a) Encapsulated transducer impedance magnitude behaviour versus frequency in air and water; (b) Encapsulated transducer phase response versus frequency in air and water.**

### 4.3 Transducer Calibration

Before starting with any experimental setup for the data communication telemetry, the transducer calibration is necessary due to two major reasons:

1. It is crucial for validating the pressure amount and obtaining an initial estimate of the transducer performance.
2. Transducer calibration can be used to perform frequency sweep which is utilised to detect the practical resonance frequency that is defined as the actual frequency, on which, the transducer operates in its maximum amplitude voltage.

### 4.3.1 Calibration set-up

The transducer was tested in a water tank with dimensions of  $(3 \times 2 \times 2) m$ , the tank walls are coated with anechoic absorbers to provide acoustic isolation and prevent any undesirable ultrasonic reflection, the transducer calibration can only carry out accurately in a free field environment. Therefore, the experiments took place in the SEA lab, this lab provides the required testing equipment and mediums for experiments on acoustic and electromagnetic transmissions. Figure 4-7 presents the calibration setup, and show the devices used in this experiment. A waveform generator Agilent (33500B) was used to generate 5 cycles burst of sine waves with  $20 V_{pp}$ . Then, the generated signal was applied directly to the transmitter transducer. At the receiver side, a calibrated hydrophone (TC4014) from Teledyne was used. It incorporates a preamplifier of 26 dB gain. Moreover, it provides a wide frequency range (15 – 480) Hz and has excellent omnidirectional characteristics. The hydrophone was connected to the input module RESON EC6073 from Teledyne and the signal was filtered using a bandpass filter with (200 – 500) kHz lower and upper cut-off frequencies, respectively. After that, the signal was conditioned using an amplifier with a 40 dB amplification. Finally, the received signal was captured and displayed using Tektronix TDS2024B oscilloscope.

The frequency response of the designed transducer was examined by applying a sinusoidal burst with a frequency ranging between (260 to 350 kHz). Although the *PZT* crystal of the designed transducer has a resonance frequency of 300 kHz, the measured resonance frequency that provides maximum output voltage was at 320 kHz. The frequency difference between the calculated and measured value is due to the manufacturer resonance frequency tolerance of the *PZT* crystal and the impact of the encapsulation of the *PZT* crystal.

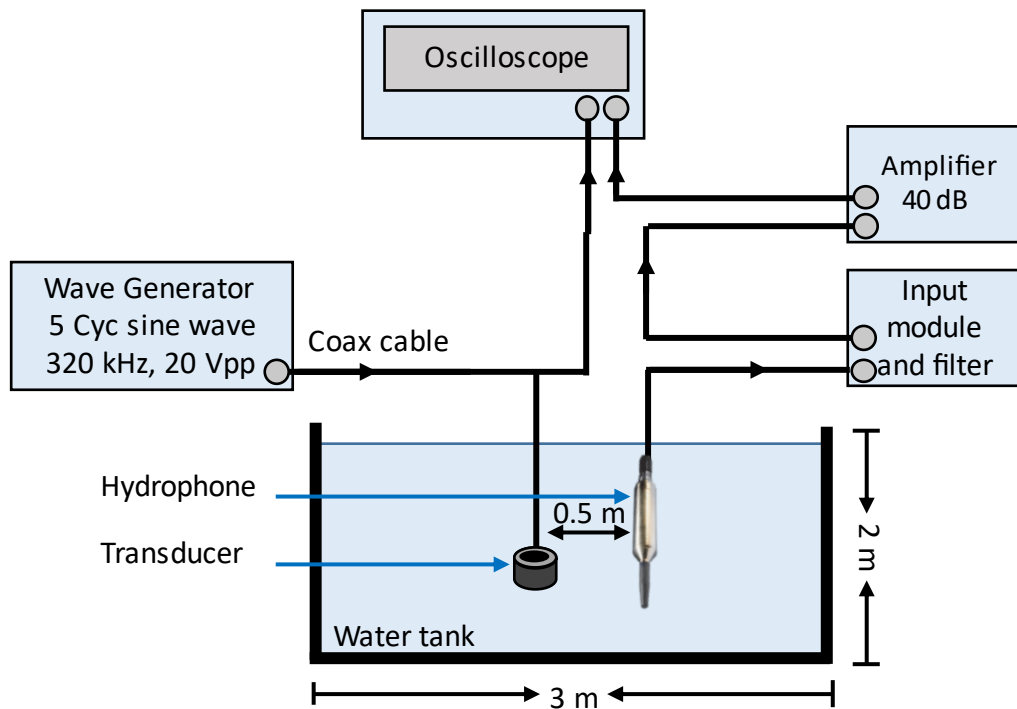


**Figure 4-7: Calibration setup for the designed ultrasound transducer. The transducer and the hydrophone were immersed in a water tank with a 0.5 m distance in between. Signal conditioning was used for the hydrophone received signal to reduce the outside of the desired frequency range.**

#### 4.3.1 Calibration Results

To estimate the designed ultrasound transducer performance, sonar equations have been employed to calculate the pressure level in the water. Figure 4-8 shows the received hydrophone conditioned signal that has amplitude  $V_{pp} = 2.7 V$  ( $0.95 V_{RMS}$ ) which is equivalent to  $Rx_{signal} = -0.42 dB$  based on the Decibel voltage level ( $dBV$ ) following equation:

$$dBV = 20 \log_{10} \left( \frac{V_{rms}}{V_{ref}} \right) \quad 4-2$$

Where  $V_{rms}$ : is the *RMS* voltage and  $V_{ref}$  is the reference voltage, which is 1 V.

The effective sensitivity ( $S_{eff}$ ) at the receiver was determined using the following equation:

$$S_{eff} = R_s + G_{RX} \quad 4-3$$

Where  $R_s$  is the receiving sensitivity of the hydrophone which is  $-187.5 \text{ dB re } 1 \text{ V}/\mu\text{Pa}$  at  $320 \text{ kHz}$ , and  $G_{RX}$  is the gain of the amplifier at the receiver, which is  $40 \text{ dB}$ . By substituting the aforementioned values, the  $S_{eff} = -147.5 \text{ dB re } 1 \text{ V}/\mu\text{Pa}$ .

Hence, the received signal level ( $RL$ ) can be calculated by:

$$RL = Rx_{signal} - S_{eff} \quad 4-4$$

Yielding the is  $RL = 147.08 \text{ dB re } 1\mu\text{Pa}$ , which represents the pressure level in water.

Since the distance between the tested transducer and the hydrophone was not  $1 \text{ m}$ , the spherical spreading range ( $R$ ) need to be calculated and the measured pressure was modified  $-6 \text{ dB}$  by using the following equation:

$$R = 20\log_{10}D \quad 4-5$$

Where  $D$  is the distance between the transducer and the hydrophone  $0.5 \text{ m}$ .

The Transmitting Voltage Response ( $TVR$ ) was calculated by the following equation:

$$TVR = RL - Tx_{signal} - R \quad 4-6$$

Where  $Tx_{signal}$  is the transmitted voltage in dB, since the  $V_{pp} = 20 \text{ V}$ , by using equation 4-2 the  $Tx_{signal} = 17 \text{ dB}$ .

After substituting the values, the  $TVR = 124 \text{ dB re } 1\mu\frac{\text{Pa}}{1\text{V}}$  at  $1\text{m}$ , which is a promising result for such a miniaturised transducer. The actual pressure ( $P$ ) =  $1.58 \text{ P}$  level at  $1 \text{ V}$  was calculated by the following equation:

$$P = P_{ref} * 10^{\frac{TVR}{20}} \quad 4-7$$

Where  $P_{ref}$  is the reference pressure level  $P_{ref} = 1\mu\text{P}$ .

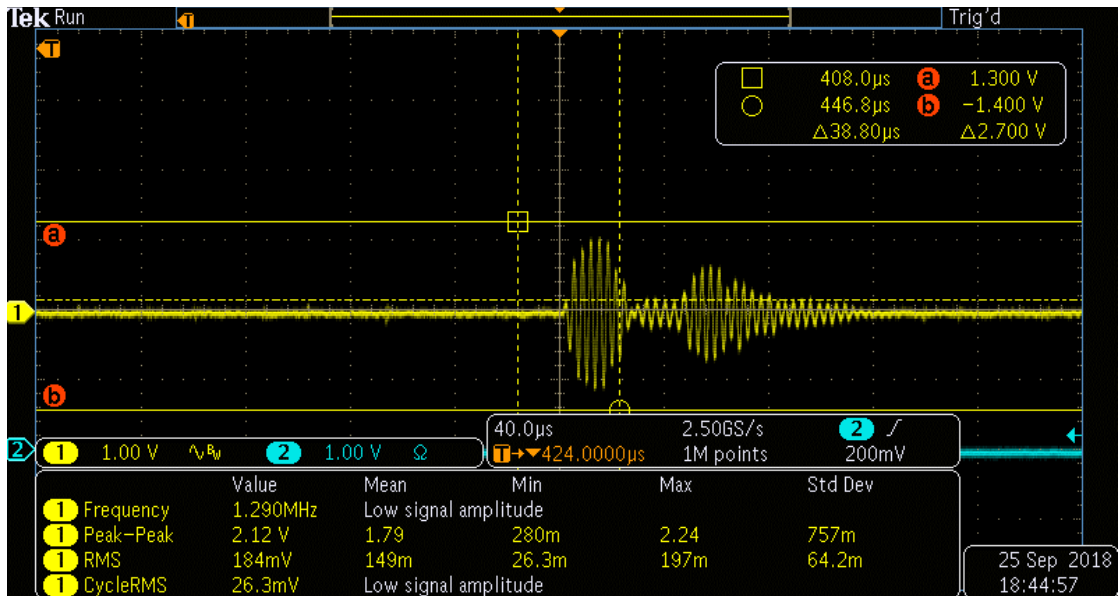


**Figure 4-8: The conditioned hydrophone received signal, the signal has 2.7 V amplitude and the result show the first path signal then followed by the multipath ‘echoes’.**

The frequency response of the received signal in Figure 4-8 was post-processed using Matlab. 1 M data points were processed over 424  $\mu$ s, before further processing the data points were adjusted to include the data points of interest of the received signal. Then the sampling frequency- 24 MHz was calculated based on the number of samples per sampling duration of the signal area of interest. Figure 4-9 shows the frequency response of the received hydrophone signal after applying fast Fourier transform (FFT), it can be seen the damp transient response peaks around the operating frequency high peak.

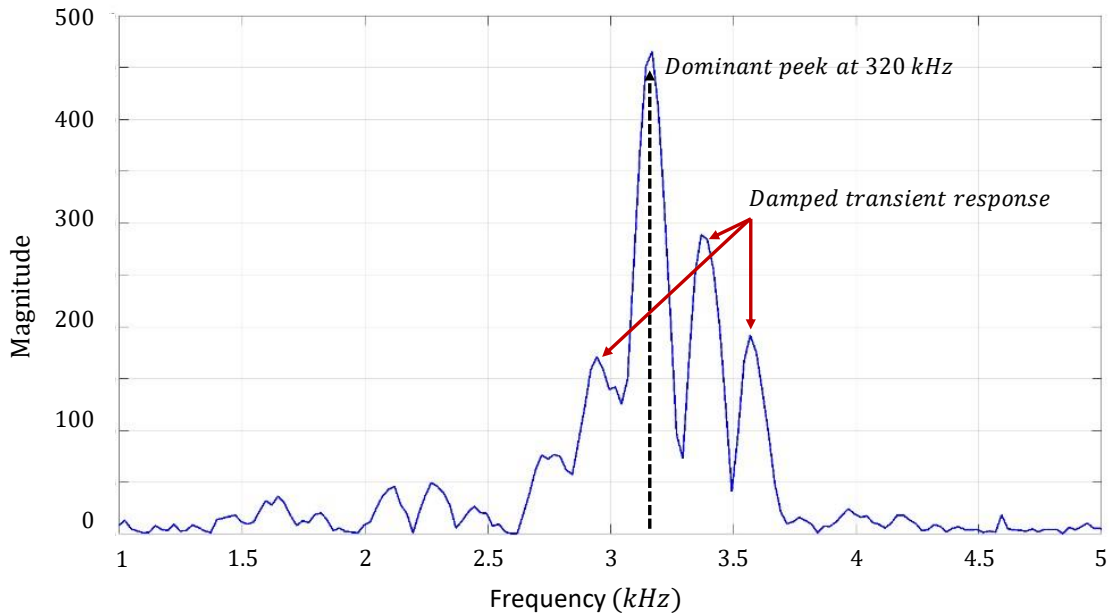


**Figure 4-9: Frequency spectrum of the hydrophone received signal. It can be seen that the maximum frequency peak at 320 kHz, the spectrum shows the damped transient parts around the resonance frequency.**

#### 4.4 Analog Front End

On the receiver side, amplifier circuitry is required to increase the signal sufficiently to be detected by a threshold detector on the microcontroller. This is achieved by utilising the *AFE* as shown in Figure 4-10 and Table 4-1 which depicts its circuit schematic and the value of the components. The *AFE* design is a tradeoffs between the high quality filtering, stability and the circuit complexity, as the unnecessary high Q filtering requires more filtration stages and more complex circuit design. The *AFE* consists of an operation amplifier (*Op – Amp*) and bandpass filters which are designed to achieve the following specifications:

1. **High order filter:** It must provide a tight filter around the transducer resonance frequency, 320 kHz transmission band, to maximise the *SNR*. This issue is crucial due to the severe weakness of the acoustic signal, typically in the  $\mu V$  as measured by past literature [155] and our measurements.

2. **Amplification:** An amplifier system is therefore required with a gain of 35–40 *dB* to match a threshold detector. Doing so requires a minimum of 23 *mV* roots mean square (*RMS*) on the embedded control unit.
3. **Stability:** The selected filter topology should have the capability of achieving a high *Q* factor and gain at the same time maintain stability.
4. **Power:** The selected *Op – Amp* should achieve the required gain and has low power consumption.

To ensure maximum signal to noise performance, a broadband bandpass filter with high gain has been developed, preceded by a 4<sup>th</sup> order cascaded multiple feedback bandpass filters. These filters are designed precisely to achieve the required gain at the operation frequency.

The process of *AFE* linear filter design is achieved by the following three steps:

1. Utilising a mathematical approach to obtain an approximation function in the filter design.
2. Design simulation and tuning seeking for a satisfactory response.
3. Implementation of *PCB* design.

All the above-mentioned steps are presented in the following subsections.

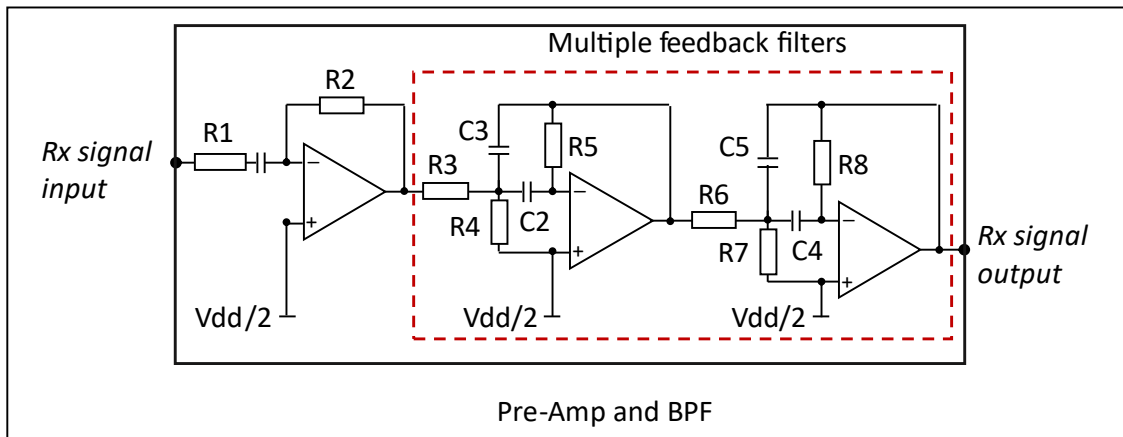


**Figure 4-10:** The designed *AFE* circuit schematic that required at the receiver side, the transducer in the receiving operation driven by three stages filters and amplifier, the first stage is broadband bandpass filter and the second and third stages are multiple feedback filters designed to achieve the required gain at the given centre frequency.

**Table 4-1:** The tuned resistors and capacitors values of the *AFE*.

Components	Value
<i>R1</i>	1 kΩ
<i>R2</i>	12 kΩ
<i>R3</i>	2 kΩ
<i>R4</i>	800 Ω
<i>R5</i>	15 kΩ
<i>R6</i>	3 kΩ
<i>R7</i>	600 Ω
<i>R8</i>	20 kΩ
<i>C1</i>	470 pf
<i>C2 and C3</i>	120 pf
<i>C4 and C5</i>	100 pf

#### 4.4.1 Broad Bandpass Filter Design (First Stage)

The broadband filter stage designed at 320 kHz centre frequency and it has a wide passband bandwidth and a roll-off gain of 20 dB/Decade. The goal of this stage was to provide the highest possible gain that is limited by the selected Op-Amp magnitude response at the desired frequency.

#### 4.4.2 Multiple Feedback Filter Design (Second and Third Stages)

The multiple feedback bandpass filter topology was selected as it is capable of achieving a high  $Q$  factor and high gain at the same time maintain stability. However, it provides a small amount of bandwidth. As per Figure 4-10, the circuit diagram of the multiple feedback filters includes two feedback paths:

1. The first one provides a low pass filter response represented by  $R3$  and  $C3$  in the first stage and  $R6$  and  $C5$  in the second stage.
2. The second path provides a high pass response represented by  $C2$  and  $R5$  in the first stage and  $C4$  and  $R8$  in the second stage.

Both multiple feedback bandpass filter stages designed using staggered tuning technique, each stage is tuned in frequency slightly different from the 320 kHz centre frequency. The first stage has a centre frequency of  $f_{c1} = 310$  kHz which is lower than the desired centre frequency, the second stage has a centre frequency of  $f_{c2} = 338$  kHz which is higher than the desired centre frequency. The first stage was designed by assuming the capacitors  $C2$  and  $C3$  have the same value  $C = 120$  pf. Then accordingly, the value of  $R5$  and the input resistors  $R3$  and  $R4$  were determined from the following design equation:

$$R5 = \frac{Q}{2\pi f_{c1} C} \quad 4-8$$

$$R3 = \frac{Q}{2\pi f_{c1} CG} \quad 4-9$$

$$R4 = \frac{Q}{2\pi f_{c1} C(2Q^2 - G)} \quad 4-10$$

Where:

$Q$  : is the quality factor that its value is adjusted between 4 – 5 based on the audio application design requirements [156, 157].

$G$  : is the gain which is determined using equation 4-11.

$f_{c1}$  : is the cutoff frequency of the first stage and was calculated based on equation 4-12:

$$G = R5/2R3 \quad 4-11$$

$$f_{c1} = \frac{1}{2\pi C} \sqrt{\frac{R3 + R4}{R3R4R5}} \quad 4-12$$

On the other hand, the parameters of the second stage were designed and calculated similarly by letting  $C4$  and  $C5$  have the same value  $C = 100 \text{ pf}$ .

#### 4.5 AFE Simulation Design

In order to check the design performance and tune the calculated values, the circuit was simulated using LTspice from Analog Devices. The design performance of the cascaded filters depends primarily on the selected Op-Amp specifications. In this design, the LTC6255 single Op-Amps have been utilised from Linear Technology, Table 4-2 presents the key specifications of the Op-Amps. Given that the gain-bandwidth product ( $GBWP$ ) of the Op-Amp, the maximum gain that can be achieved for each stage is up to  $20 \text{ dB}$  at  $320 \text{ kHz}$  frequency [158]. In addition, the capacitor's values were tuned to reduce the potential effect of stray capacitors on the circuit design.

**Table 4-2: Op-Amp key specification employed for the AFE design.**

Specification	Value
$GBWP$ (MHz)	6.5
Slew rate ( $V/\mu s$ )	1.8
Supply voltage ( $V$ )	1.8 – 5.25
Quiescent Current ( $\mu A$ )	65
Operating temperature ( $^{\circ}C$ )	-40 to 125

Thereafter, both the  $AC$  magnitude and phase responses of the broad bandpass filter were determined as depicted in Figure 4-12. The first stage was designed to achieve a gain of  $19 \text{ dB}$  and a passband bandwidth of  $590 \text{ kHz}$ , considering that, the lower cut-

off frequency ( $f_L$ ) and the higher cut-off frequency ( $f_H$ ) are  $140\text{ kHz}$  and  $730\text{ kHz}$  respectively. In addition, the low pass capacitor is neglected as it has a small value. Furthermore, the applied input signal was a sine wave with  $V_{rms} = 7\ \mu\text{V}$  voltage and  $320\text{ kHz}$  frequency.

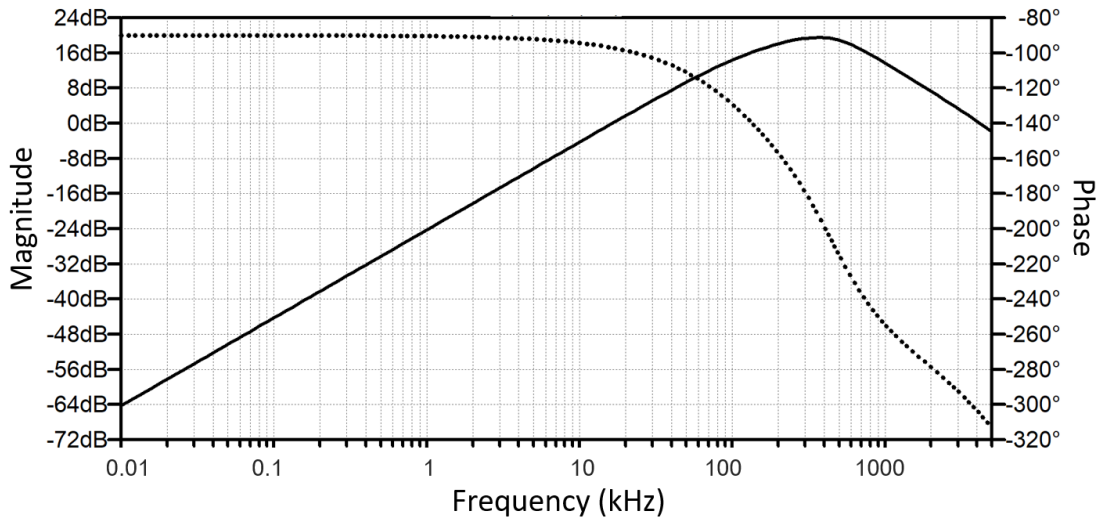


**Figure 4-11: Simulated magnitude and phase responses of the first stage bandpass filter, the achieved gain was 19 dB and the passband was 590 kHz.**

The simulation  $AC$  response of the multiple feedback filters (second and third stages), presented in Figure 4-12. From the results, it is obvious that the second stage response at  $f_{c1} = 310\text{ kHz}$  centre frequency provides a gain of  $11\text{ dB}$ . In addition, the third stage magnitude response at  $f_{c2} = 338\text{ kHz}$  centre frequency provides  $16.6\text{ dB}$  gain. The results were achieved by employing frequency tuning using a bank of capacitors.

The transient response has been examined for the first and second stages by using the following procedure: An input signal with a differential amplitude  $V_{pp} = 20\ \mu\text{V}$  was applied. As expected, the amplitude of the output signal was  $V_{pp} = 61\ \mu\text{V}$  which is corresponding to the first amplification stage gain of  $11\text{ dB}$ . Similarly, the same input was applied to the second stage. The amplitude of the output was recorded to be  $V_{pp} = 123\ \mu\text{V}$  which is corresponding to the second amplification stage gain of  $16.6\text{ dB}$ .

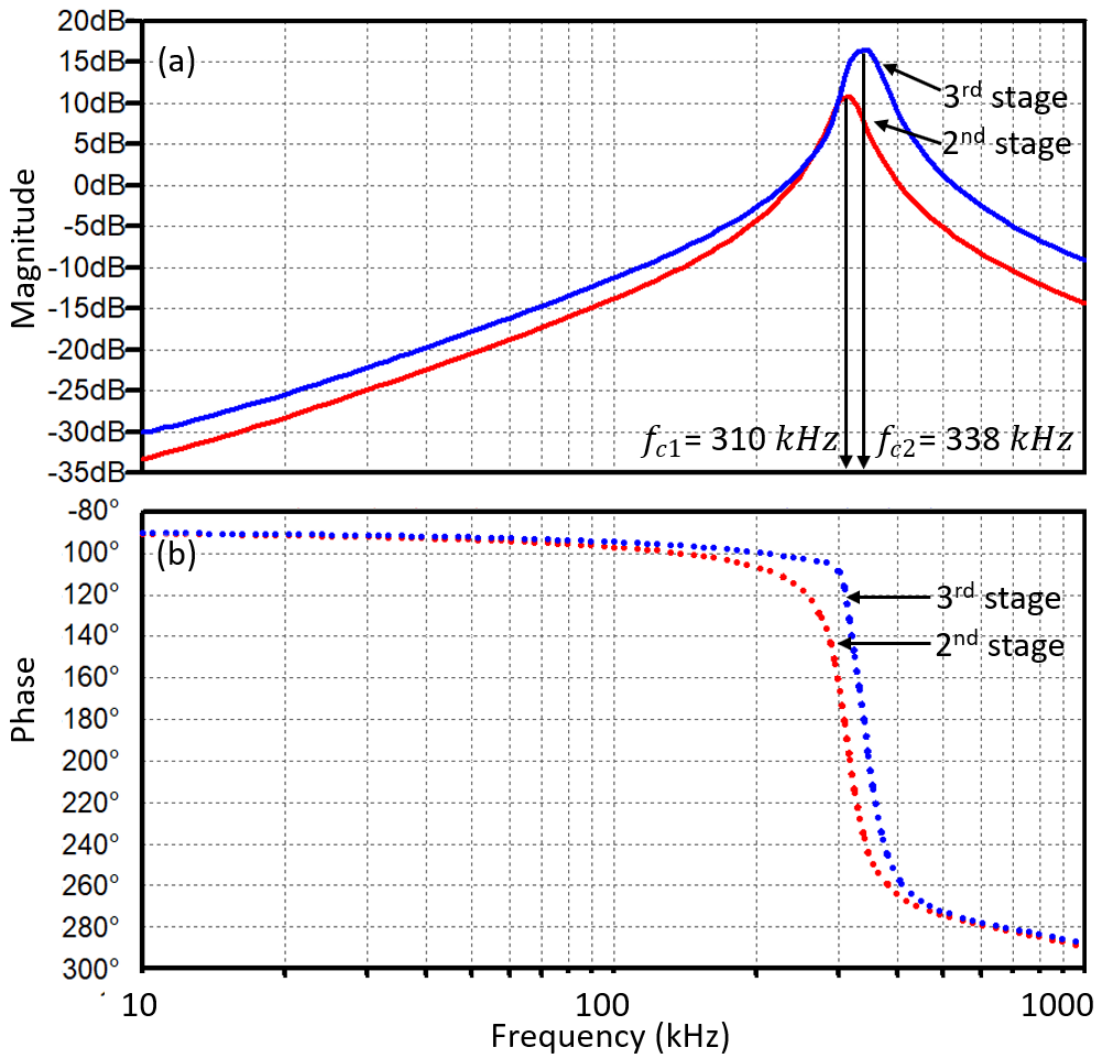


**Figure 4-12: AC response simulation results of the multiple feedback filters: (a) the magnitude response of the two bandpass filters, Stagger tuned technique has been employed to achieve the required centre frequency and gain; (b) Phase response of the bandpass filters.**

#### 4.5.1 Simulation Results the Three Stages Filtration and Amplification

As explained earlier, the receiver analog circuitry requires a precise amplification and filtration design. This circuit has the capability of improving the *SNR* performance and filtering out the band noise. Doing so, reduce the complexity of the signal recovering at the receiver. Figure 4-13 illustrates the frequency response of the designed circuit. Table 4-1 shows the final tuned selected values of the resistors shown in Figure 4-10 at 320 kHz centre frequency. The gain of the simulated results of the three stages which are connected in series was 40 dB. However, it is noticeable that the total gain of the circuit is less than the designed gain of each separated stage. This happens due to the

former stage provides current to the later stage that is not available when they are not connected altogether.

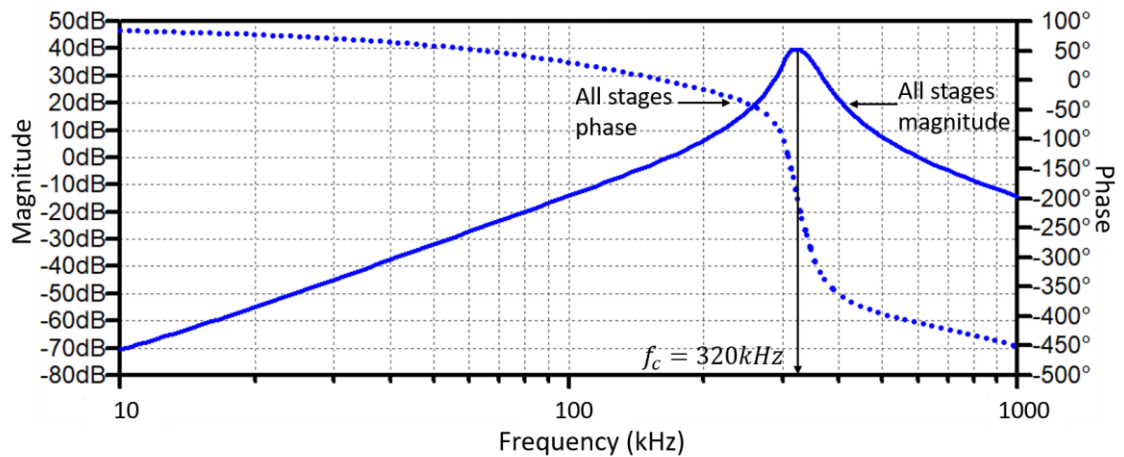


**Figure 4-13: Frequency response simulation of the three stages amplification and filtration, the achieved gain is 40 dB at frequency of 320 kHz and 50 kHz bandwidth.**

#### 4.6 Embedded Control Unit

This unit developed by others in the lab. But the systems design integration developed by me. The embedded control unit includes three main parts as shown in Figure 4-14 which presents the block diagram of the control unit. The three main parts are listed as shown below:

1. **The embedded control system:** which includes *MK22FN512VLH12* Microcontroller Unit (*MCU*) that based on the processor 120 MHz ARM Cortex-M4 from *NXP*, the *MCU* includes 512 KB flash memory with 128 KB RAM in a 64 pin Low Profile Quad Flat Pack (*LQFP*) package. In addition, the *MCU* provided with a Digital Signal Processing (*DSP*) function block and multiple communication interfaces. Therefore, it has the ability to be employed for high computational functions and low processing efficiency applications. The *MCU* can be programmed externally with a Multilink FX programmer, via a *JTAG* connector. Additionally, the system includes a UART port that provides a connection with the computer for real-time debugging.

2. **Power management circuit (PMC):** is the second main part that is customized for managing the power of the system. The *PMC* is responsible for creating the voltage levels required by the system and delivering the power provided by a 3.7 V and 165 mAh lithium-polymer (*Li – Po*) battery. The 3.7 V is initially regulated down to 3.3 V by a low dropout regulator (*LDO*)–*TLV70233DBVR* capable of supplying up to 300 mA. In order to maintain the stability of the output voltage, a 1  $\mu$ F capacitor has been added to both the input and output of the device. The value of this capacitor is selected based on the manufacturer suggestion in the datasheet of the *LDO*.
3. **Recording chip:** The recording commercial chip *RHA2116* from Intan technology, *RHA2000* family series, is the last part of the embedded control unit, the device includes 16 amplifiers that have a bandwidth suitable for different types of neural recording signals (e.g. *EEG* and *EKG*), the output of the desired amplifier is routed out of the chip using analog multiplexer (Mux-out), the output signal is fed to the *MCU* analog to digital converter (*ADC*) for further analysis. The dimensions of the board are 10 mm x 10 mm, with 8 pins for recordings. The chip supply voltage is 3.3 V which compatible with the embedded control unit.

For further information on the embedded control unit design can be found in [159]. It should be noted that the embedded control unit is employed to explore the optimal communication protocol. I would envisage most of the components being implemented onto a custom *ASIC* in tandem with a microcontroller die in a future implantable system.

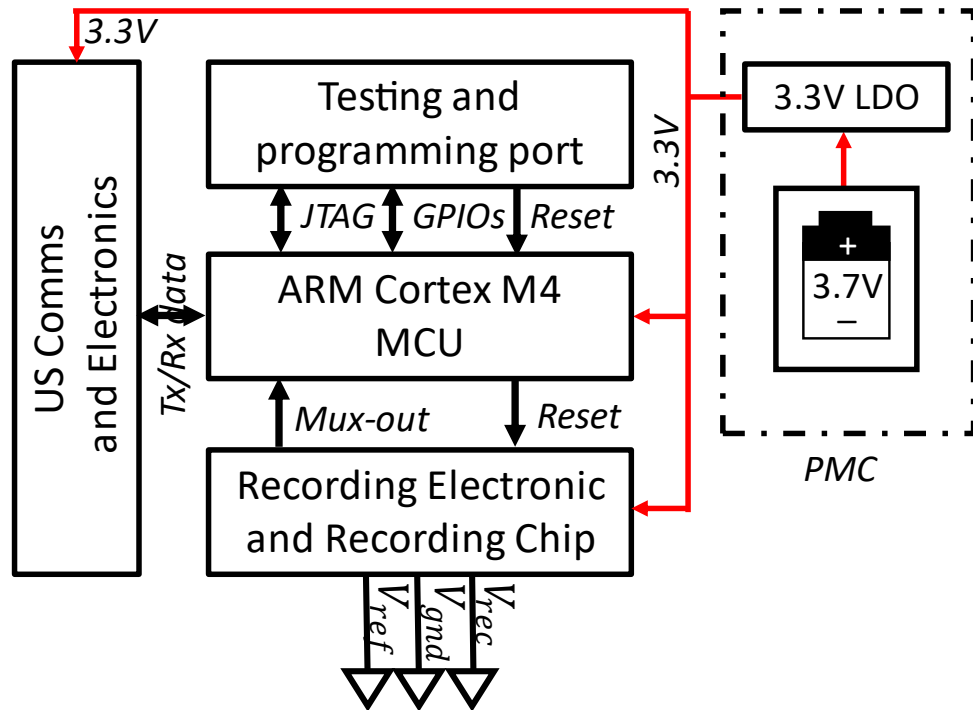


**Figure 4-14: Block diagram of the whole system focusing on the embedded control unit which can collect the recorded neural data from the recording chip, then digitizes and process the data for the ultrasound communication link. The *PMC* supplies the system with the requires power using 3.7 V rechargeable battery.**

## 4.7 Physical Implementation

### 4.7.1 Ultrasound AFE PCB Design

At first, the *AFE* circuit was designed on sperate *PCB* in order to examine the channel characteristics, frequency and transient responses of the filters and amplifiers. Figure 4-15 shows the *PCB* design of the ultrasound *AFE*. The *AFE PCB* has  $(11 \times 30 \times 1.5)$  mm dimensions and consists of two layers with two dual Op-Amps LTC6256 from Linear Technology, the last stage of the Op-Amp used as a unity gain isolation buffer. The *PCB* consist of two layers:

1. The top layer hosts 25 total components.
2. The bottom layer is placed with polygon (ground plane) to provide both electrical and magnetic shielding.

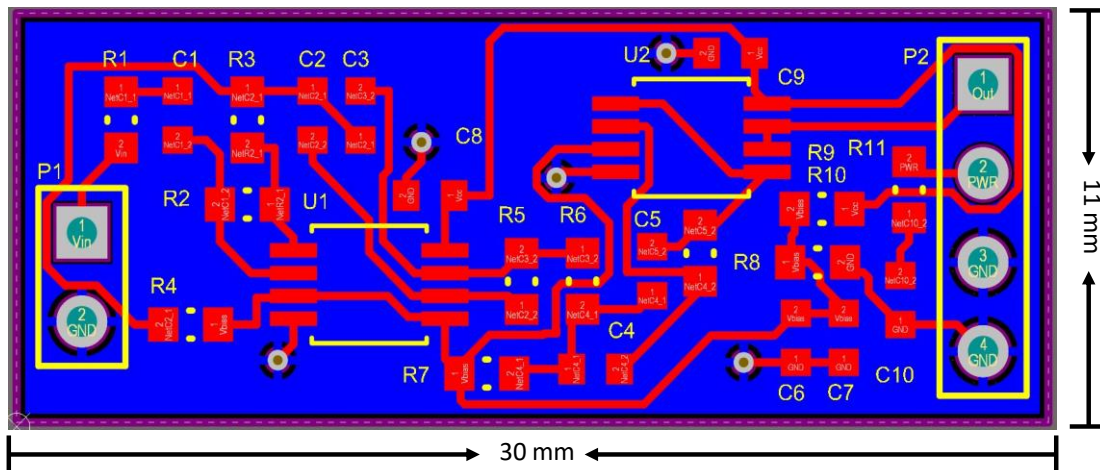


**Figure 4-15: Ultrasonic *AFE* PCB design with an area of  $351.67 \text{ mm}^2$ , the PCB implemented for examining the AC and transient response of the filter and amplifiers and to examine the channel characteristics.**

#### 4.7.2 System Prototype PCB Design

The test system prototype has been implemented to evaluate an initial basic analysis for the system and examine its performance. The ultrasound *AFE* was integrated with the embedded control unit on one PCB board as shown in Figure 4-16 the board includes 4 layers with dimensions of  $(40 \times 50 \times 1.55) \text{ mm}$ . The PCB was designed in this specific shape to encapsulate the ultrasound *AFE* only and prepare it for In-Vitro experimental testing. In addition, this allows a real-time debugging of the control unit using Multilink FX programmer, via a *JTAG* connector. Finally, employ the *UART* port to provide a connection with the computer.

Figure 4-17 (a) shows the designed system prototype for experimental testing, the wire bonding and encapsulations of the ultrasound *AFE*. As per Figure 4-17 (b), it is noticeable that *PU* encapsulation material provides more protection for the board from the surrounded environment, as mentioned in 4.2.3.

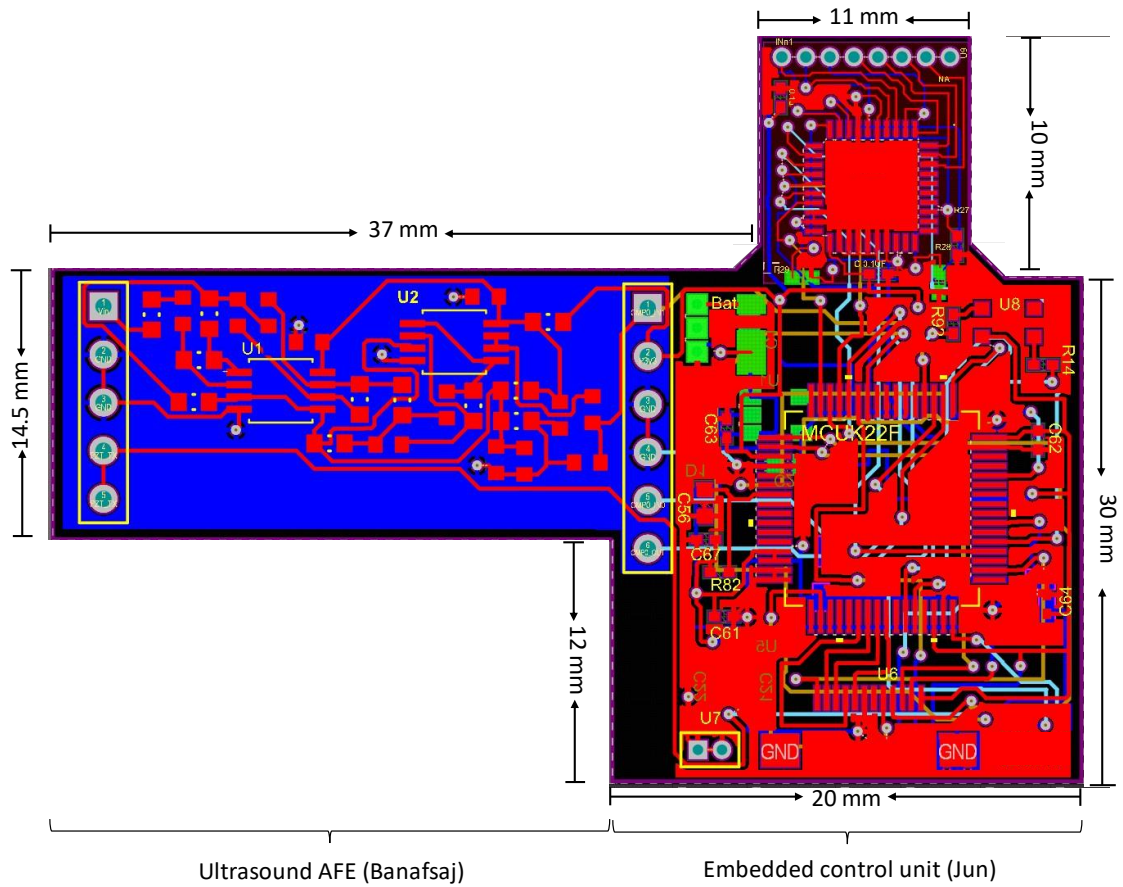


Figure 4-16: The designed *PCB* for the overall system with  $(40 \times 50 \times 1.55) \text{ mm}$  dimensions, the system prototype has been designed to examine the system performance in terms of ultrasound communication, energy and channel effect.

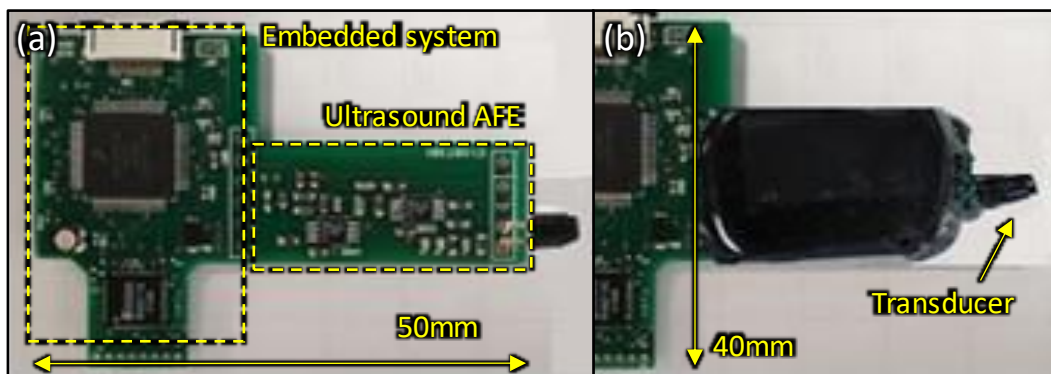
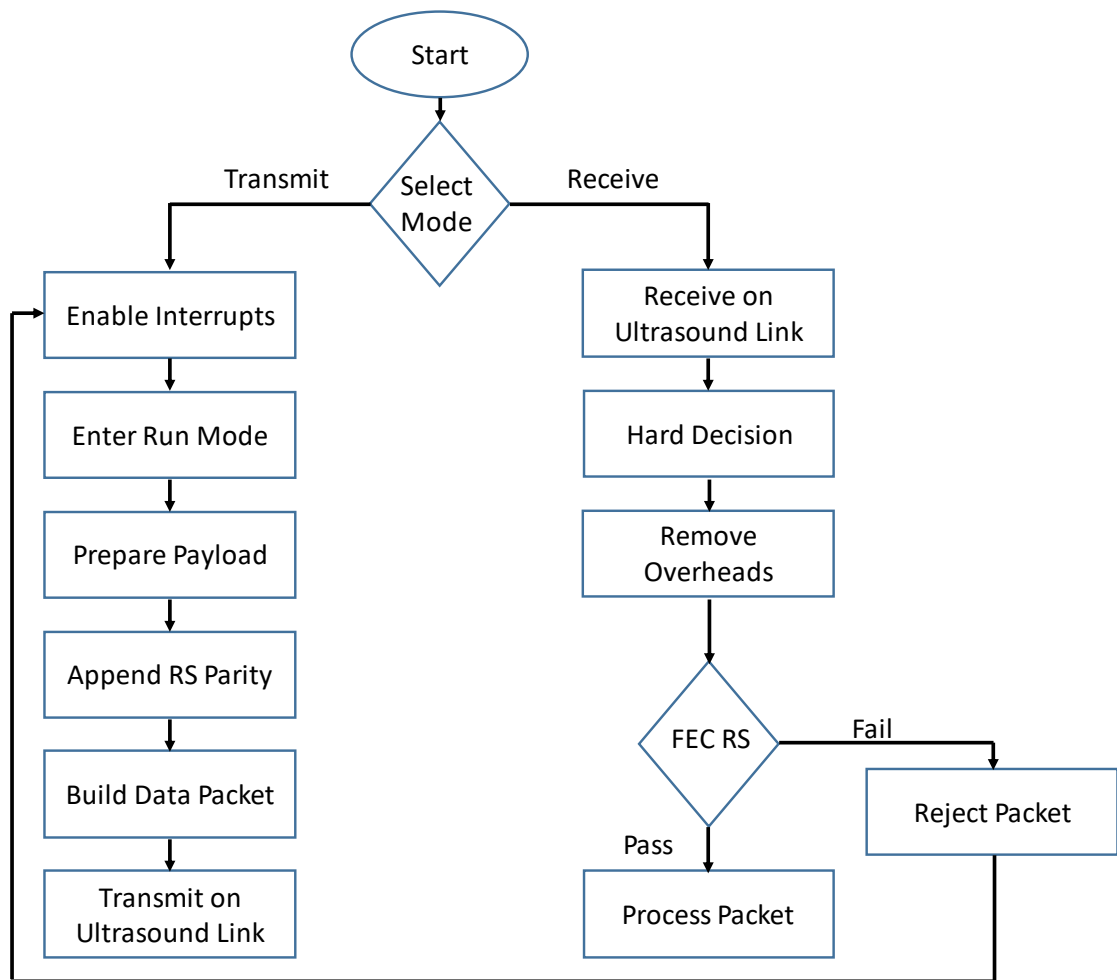


Figure 4-17: (a) and (b) The designed *PCB* for the overall system with  $(50 \times 40) \text{ mm}$  dimensions. The ultrasound transducer wire bonding shown in (a) and encapsulations of the ultrasound *AFE* shown in (b).

## 4.8 Software Architecture

The main communication software algorithm of the ultrasound communication link is presented in Figure 4-18, there are two different modes of operation:

1. **Transmit mode:** this mode is used when the implant device (*BeNs* or the central unit) needs to transmit data, the microcontroller wakes up, by switching from the standby mode to the run mode, as a response to the internal interrupt source. The packet is set by appending the overheads and *RS* parity bits, by calling the *RS* initiates and *RS* encode functions, to build the packet before the transmission via the ultrasound transducer. The packet includes three main parts: header, payload, and the *RS* parity bits as presented in Figure 3-19. The implant switches from the run (full operation mode) to the listening mode.
2. **Receive mode:** this mode receives the incoming data packet (bit by bit). The received data bits are passed through the comparator (hard decision) to decide if bit "1" or "0" is transmitted. The comparator compares the incoming signal amplitude with the reference signal amplitude which is set to be 1.804 V. The data integrity is verified by feeding the received bits to the *RS* code, the *RS* decode function is called after initialising the function, the verified data will be processed otherwise the packet will be rejected. All the above processes are run in the full operation run mode after finishing the data processing the microcontroller switches to the standby mode. The guard interval period to overcome the multipath effect is considered in the software algorithm by turning off the data receiving for 800  $\mu$ s then turned on again to be ready for the next data bit. During the guard interval period, the microcontroller supposed to switch to the standby mode to save power.



**Figure 4-18: Ultrasound communication software algorithm for both the transmitter and receiver.**



## Chapter 5. System Level Testing

### 5.1 Introduction

This chapter presents the system calibration and testing of reliable and efficient ultrasonic communication telemetry using omnidirectional transducers to implement intra-body communication inside the human body tissue phantom. The system specifications were presented in Table 5-1. The prototype was implemented to evaluate the system performance first in saline and up to 30 *cm* distance between the transmitter and receiver. Short pulses sequences with guard intervals were employed to minimize the multipath effect. A *RS* error correction coding scheme has been employed to achieve reliable communication at low *SNR* (at longer distances). Energy per bit and current consumption for the transmitter and receiver main parts were presented and discussed in terms of battery life.

**Table 5-1: System prototype main specifications.**

Parameters	Description
Prototype dimensions (mm)	(40 × 50 × 1.5)
Operating frequency (kHz)	320
US active element shape	Soft PZT tube
Active element dimensions (mm)	(3.5 × 2.5 × 3)
Encapsulation material	Polyurethane
Operation mode	Radial
Clock frequency	100 <i>MHz</i>
Application	Deep implantable bioelectronic sensors

### 5.2 Tissue Phantom Experimental Setup

A test system was developed to provide an initial analysis of our system. This consisted of a tank of dimensions: (50 × 30 × 25) *cm* to mimic a simplified human body. The transducer and *AFE* were encapsulated in order to be safely immersed in saline. Two tests setup were used:

1. **The transmitted signal generated by waveform generator:** the wave generator was employed to transmits a signal with three different amplitude voltages

(1.8, 3.3 and 20) V. In addition, to investigate the communication through the channel, a sinusoidal waveform was employed first.

2. **The transmitted signal generated by the microcontroller:** this setup was used to test and evaluate the final designed system prototype, square pulses were generated by the microcontroller and transmitted through the tissue phantom medium.

### 5.2.1 AFE Frequency Response Results and Discussion

As explained earlier, the receiver analog circuitry requires a precise amplification and filtration design. The *AFE* capable of improving the *SNR* performance and filter out the band noise, which makes the signal recovering at the receiver less complicated. Figure 5-1 illustrates the frequency response of the designed circuit and compared with the simulation result, the bandwidth of the measured result was 50 *kHz* and the achieved quality factor was 6.4 at 320 *kHz* cutoff frequency. However, the simulated circuit frequency response shows a higher gain from the measured circuit due to the component tolerance a 4 *dB* gain difference between the simulated and measured results. The designed *AFE* circuit consumes 250  $\mu A$  current when supplied 3.3 *V* and consumes 70  $\mu A$  when supplied with 1.8 *V* voltage.

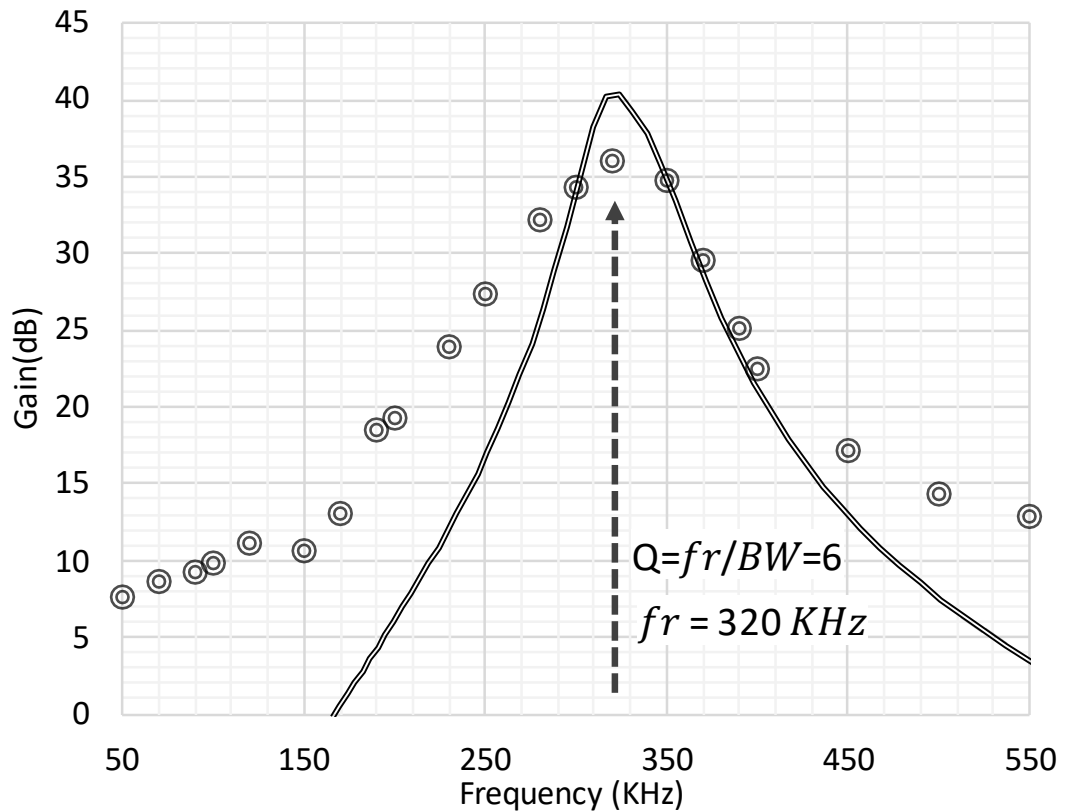


**Figure 5-1: Simulated and measured frequency response of the designed amplifier and multiple feedback bandpass filter, the gain is 36 dB at 320 kHz and the bandwidth is 50 kHz.**

### 5.2.2 Channel Impulse Response

The channel impulse response was investigated by sending a short burst sine wave signal of five cycles at 320 kHz that launched every 5 ms, the signal was generated using waveform generator Agilent (33500B) and applied directly to the transmitter transducer, the ultrasound waves will travel through the channel to the receiver transducer. The received signal was captured by the receiver transducer and pass through the AFE then displayed using a digital oscilloscope Agilent (DSO-X 3034A).

Figure 5-2 represents the impulse response of the channel at 6 cm distance between the transmitter and receiver. The first arrived signal is the primary signal, and the subsequent signals represent the multipath spread caused by the reflection and scattering of the transmitted wave. From this figure, the time  $T_1$  which represents the

consumed time of the signal to travel through the channel can be measured. Furthermore, this time depends on two factors: first the distance between the transmitter and receiver. Second the speed of sound in water. The time  $T_2$  represents the primary signal plus the multipath spread. This time indicates the waiting time between each consecutive two pulses. Sending another pulse of data before the end of  $T_2$  will cause data loss and interference. In order to differentiate between the received signal and its multipath, a threshold voltage ( $V_{th}$ ) was set as the minimum amplitude that needed to be set at the receiver to detect the primary signal. For such a multipath channel, continuous wave data transmission is not suitable to be adopted. Therefore, the most promising solution is the data burst transmission; however, on the price of the data transmission rate.

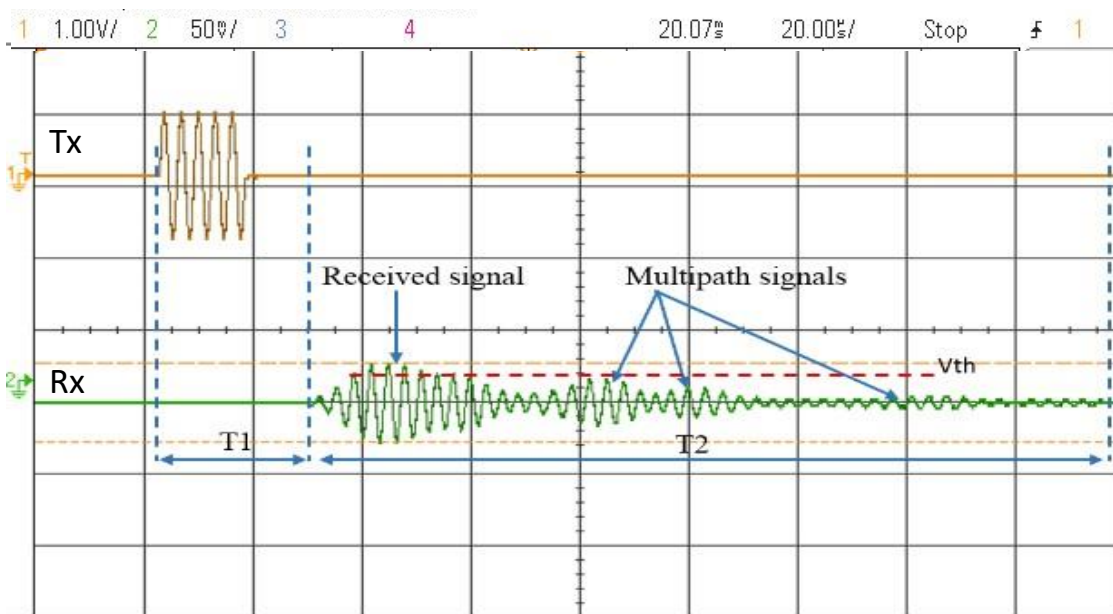


**Figure 5-2: Channel impulse response of the experiment setup.** The first channel shows the transmitted signal of  $320\text{ kHz}$  frequency and  $1.8\text{ V}$  amplitude. The second channel shows the received acoustic signal and the multipath, the results were captured with the aid of averaging.

### 5.2.3 Signal to Noise Ratio Measurements

The  $SNR$  was measured for three different transmission voltages ( $1.8, 3.3$  and  $20\text{ V}$ ) and over a distance ranging from ( $1 - 38$ )  $cm$ . A short burst sine wave signal of five cycles was generated at  $320\text{ kHz}$  frequency and launched every  $5\text{ ms}$ , the signal was generated using waveform generator Agilent (33500B). The transmitter was fixed in

front of the receiver and the latter is moved apart gradually. The  $SNR$  was calculated using equation 3-14. Figure 5-3 presents the  $SNR$  versus distance for three different input voltages. Three different measurements of the signal amplitude and noise values have taken to show the spread of data around the mean value. It can be seen a gradual decay in the  $SNR$  as the distance increases. It is obvious that the lowest  $SNR$  is obtained at 1.8 V transmission voltage whereas the highest at 20 V.

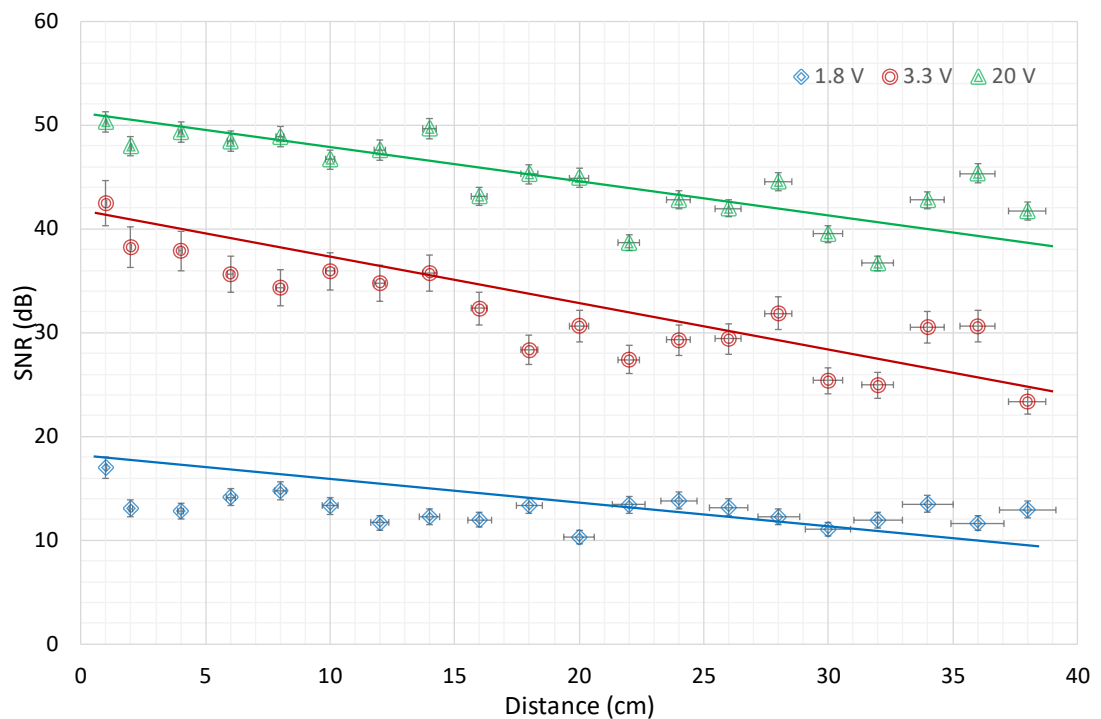


**Figure 5-3: Signal to noise ratio against the distance for different transmission voltages (1.8, 3.3 and 20 V). It can be seen that a slight decaying in the  $SNR$  as the distance increases.**

### 5.2.4 Latency Versus Distance

The latency of the signal was measured by the oscilloscope for different input voltages and over a distance range (1 – 36) cm. The latency represents the  $T1$  period (as shown in Figure 5-2) when the signal was generated by the function generator and after processed by the  $AFE$ . The latency of the primary signal as a function of distance was demonstrated in Figure 5-4, It can be seen a linear relationship between them, as the distance increases the time consumed for the primary signal to arrive increases. The recorded results were similar for the three transmission voltages. The reason behind this delay is generally due to the low speed of sound in water, this delay needs to be

considered in the receiver side to recover the received signal properly. The key point is that latency does not affect transmission data rate. But latency does slow down handshaking between devices considerably.

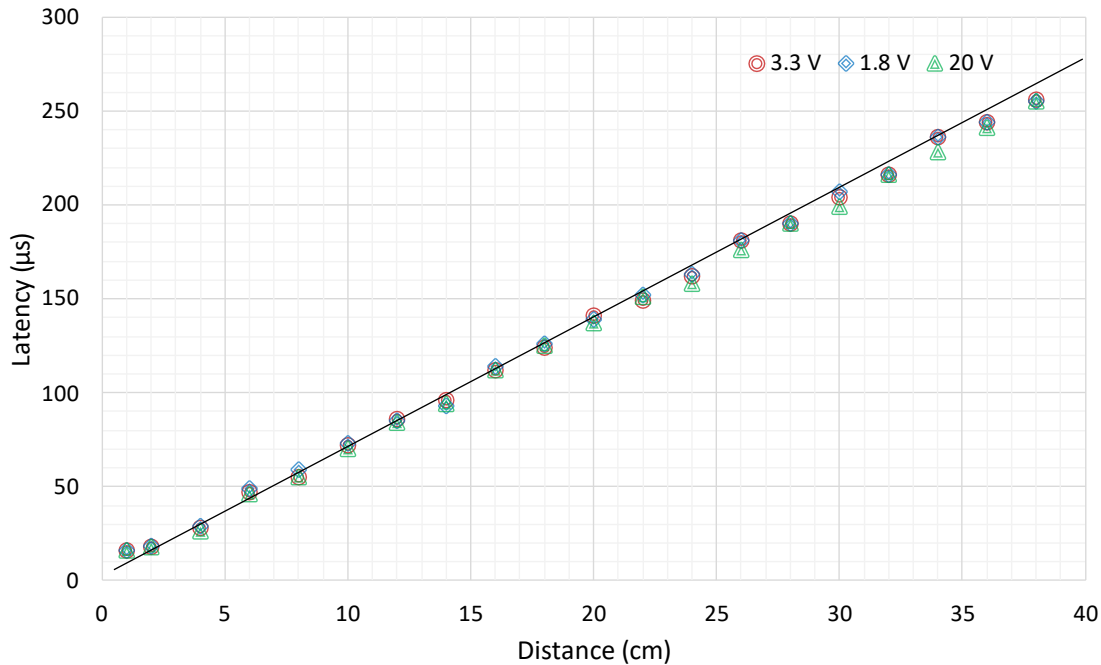


**Figure 5-4: The time consumed for the 5 cycles transmitted burst to arrive at the receiver as a function of distance. It can be seen that for different transmission voltages (1.8, 3.3 and 20) V the time for the transmitted signal is similar. The time consumed for the signal to travel to the receiver increases as the distance increases.**

### 5.2.5 Transmission Loss Versus Distance

The transmission loss of the signal during travelling from the transmitter to the receiver was determined as a function of distance. The transmission loss was calculated by subtracting the receiving power (output power) from the transmitting power (input power), the receive and transmitted power were calculated by measuring the voltage drop across a load resistor. The power loss of the transmitted waves during travelling through the channel is illustrated in Figure 5-5. The result was calculated for 3.3 V transmission voltage. It can be observed as the distance increases the power loss increases slightly, unlike the electromagnetic signal, which dramatically changed as the depth of the implant increases. At a distance of 20 cm the loss is increased by 150 dB.

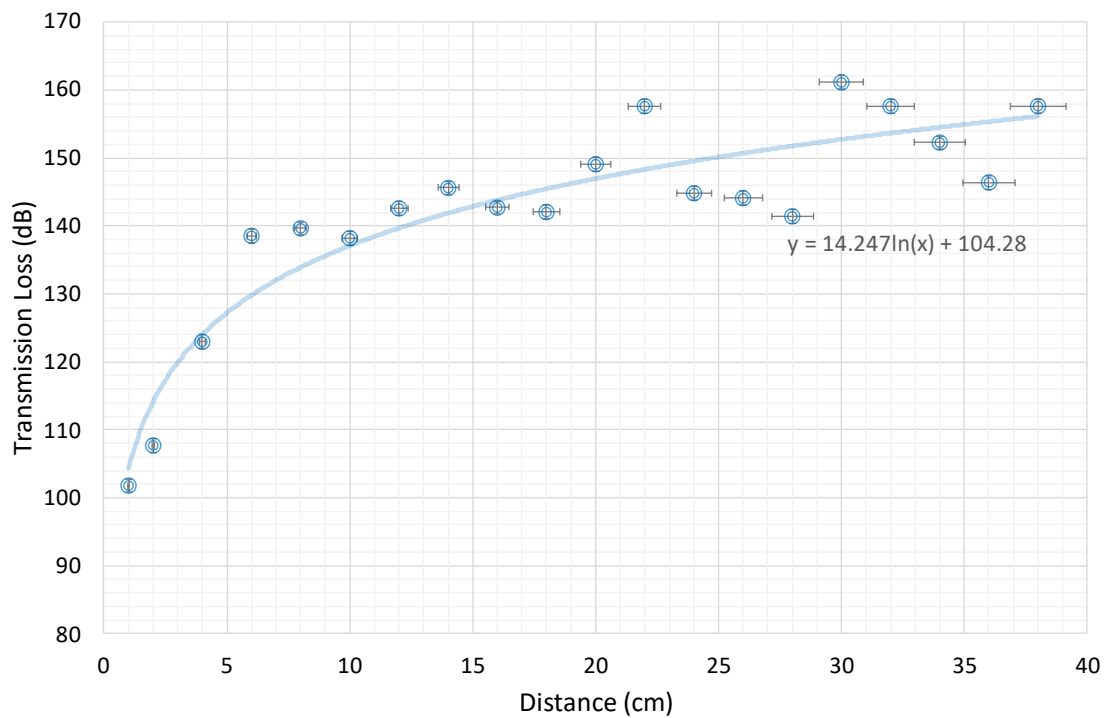


**Figure 5-5: Transmission loss through the channel during the transmission as a function of the distance between Tx and Rx, it can be seen that the power loss increases as the distance between the transmitter and receiver increases.**

## 5.2.6 Electromagnetic Crosstalk

Ultrasound communication crosstalk appears as a relatively small amplitude signal arriving before the primary ultrasound signal at the receiver in Figure 5-6. Typically, this crosstalk electromagnetic signal appears concurrently in time with the transmitted ultrasound signal. Crosstalk can be appeared due to lack in the setup of the experiment in terms of sealing the components and improper grounding which creates an undesirable electromagnetic path between the transmitter and receiver. Both the transmitter and receiver were grounded with the saline to prevent electromagnetic crosstalk.

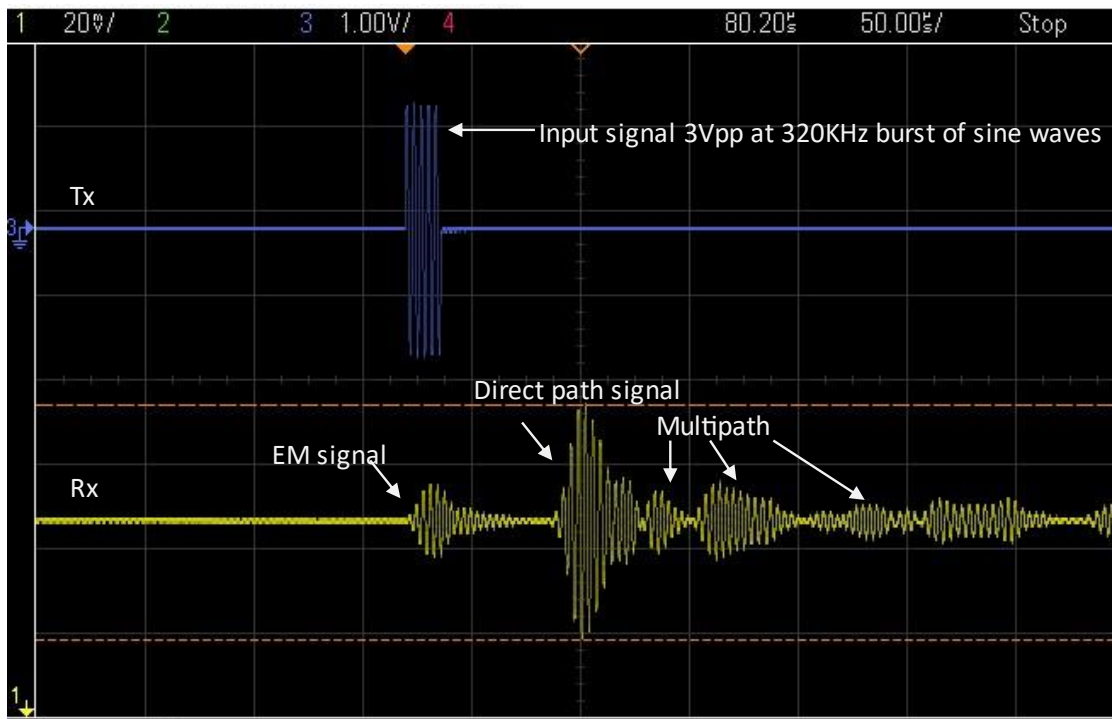


**Figure 5-6: Transient response of the first experiment setup in saline, 5 cycles of sine wave burst are transmitted at 320 kHz and 3.3 V amplitude, the received signal shows the electromagnetic crosstalk that appeared exactly in the same time of the transmission, then followed by the ultrasound trains of signals. Signal captured with the help of averaging.**

### 5.3 Communication System Evaluation in the Tissue Phantom

System evaluation was carried out at room temperature ( $23^{\circ}\text{C}$ ) by placing the transmitter and receiver in the saline bath model as described in Section 5.2. Both transducers were fully submerged throughout the experiments. The receiver was fixed in the saline bath and grounded with saline, the transmitter was mounted in such a way to be able to move forward and backwards in front of the receiver and also grounded with saline. Figure 5-7 demonstrates the experimental setup of the system. At the transmitter (right side), the data was generated, encoded and the packet applied to the transmitter transducer. In the receiver (left side), the packet received by the transducer and fed to the *AFE*, then decoded at the control unit. Both the transmitter and receiver signals were observed by the digital oscilloscope Agilent (DSO-X 3034A) and the controlling, processing and debugging were performed using the Kinetis Design Studio (*KDS*) development software environment that used for Kinetis *MCUs*.

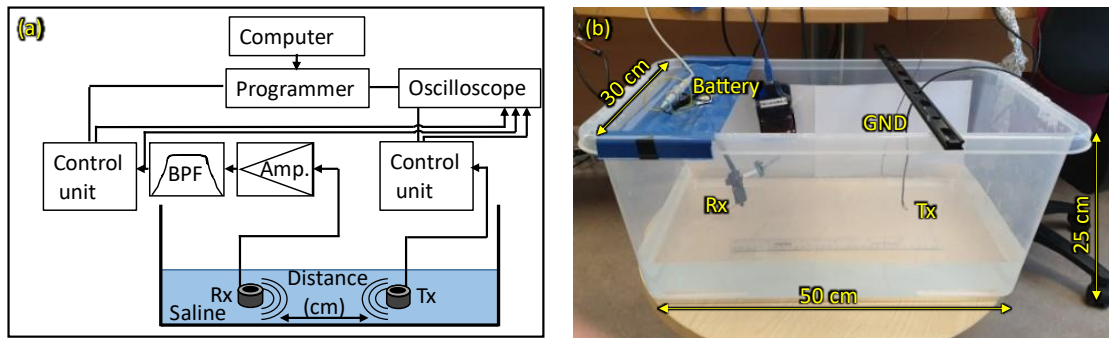


**Figure 5-7: (a) Block diagram of the experimental set-up for the ultrasound communication link, measured results were recorded as a function of the distance between the Tx and Rx; (b) The experimental set-up of the communication link and the tank of dimensions (50 x 30 x 25) cm was utilised for mimicking the human tissue environment. Both the transmitter and receiver were grounded with the saline in order to prevent any chance of the electromagnetic crosstalk.**

### 5.3.1 Timing and Multipath Analysis

Figure 5-8 illustrates the transient response of the proposed system two bytes of binary data pulsed out from the transmitter transducer at 320 kHz frequency considering the minimum delay between each consecutive pulse (guard interval = 1 ms) to avoid the surface reflected and the multipath effect signals at the receiver. *OOK* technique was employed to encode the binary data.

It can be seen in Figure 5-8 (a) the Rx-A that represents the received signal after filtration and amplification, each pulse has the primary signal (direct path) and the echo signal (multipath) that have lower amplitude from the primary signal, the multipath amplitude can be exploited to set the reference voltage input of the comparator. Figure 5-8 (a) Rx-I signal represents the output of the comparator after comparing the received signal with the reference voltage to decide bit “1” or “0” is transmitted.

The results from Figure 5-8 (a and b) show that there is a significant multipath effect (i.e., long propagation delay spread), As such a finite delay is required between each pulse which will limit the data rate. Furthermore, all systems will have a noise profile which will cause errors. As such, a communication scheme is required to ensure reliable communications.

The primary consideration from the impulse response analysis is the multipath effect and the need to provide a threshold to determine the bit-state of the signal at a specified time. There are a variety of possible modulation schemes. However, *OOK* modulation scheme was utilised because of its simplicity, and robustness to the variability of different body conditions and dimensions when implanted.

In the employed *OOK* scheme the binary “1” was represented by the presence of the carrier and binary “0” was represented by the absence of the carrier signal. It can, therefore, be scalable to simple electronic hardware in future bioelectronic nodes. However, only one binary bit can be transmitted per symbol, which limits the data throughput that can be achieved in this modulation scheme.

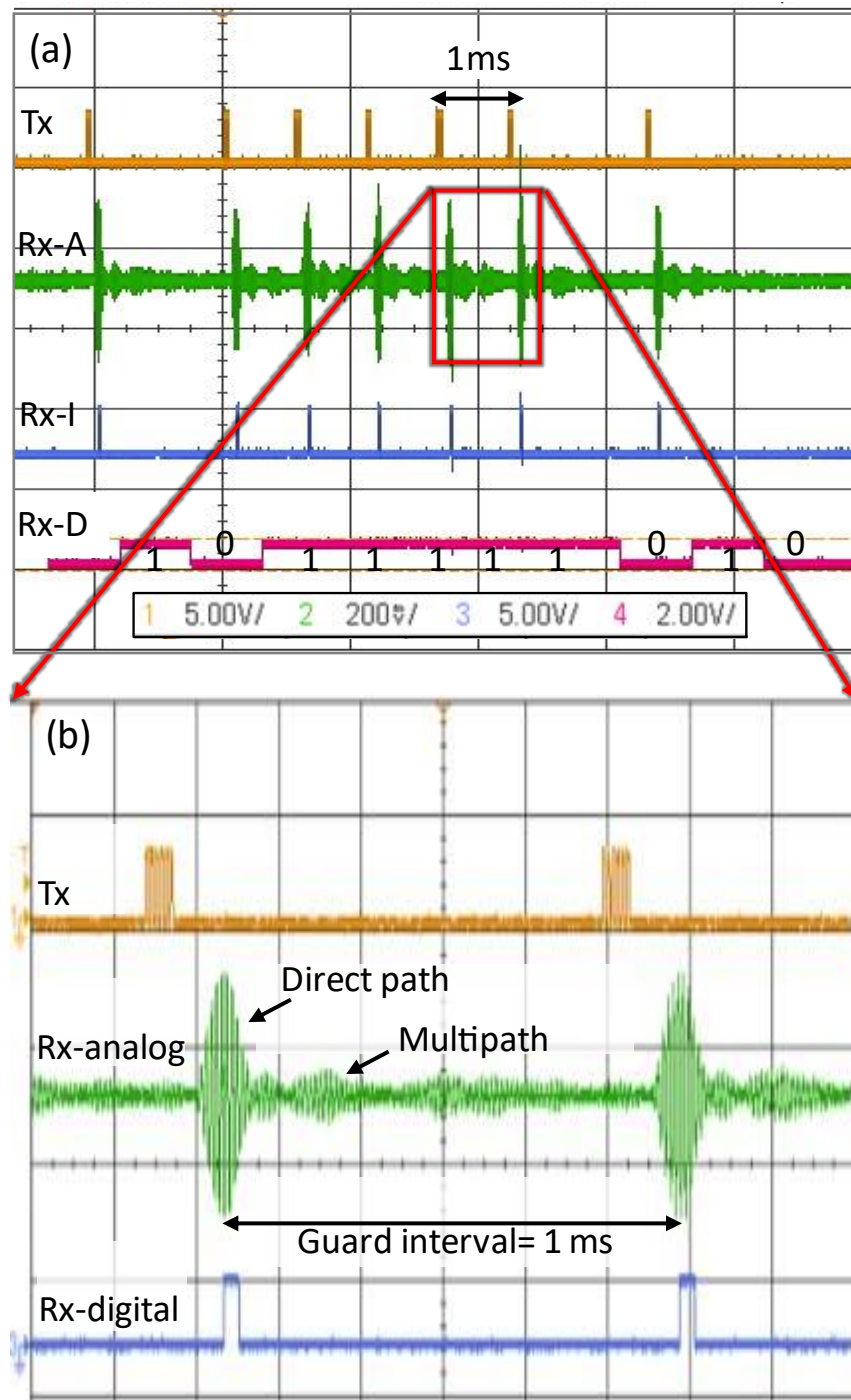
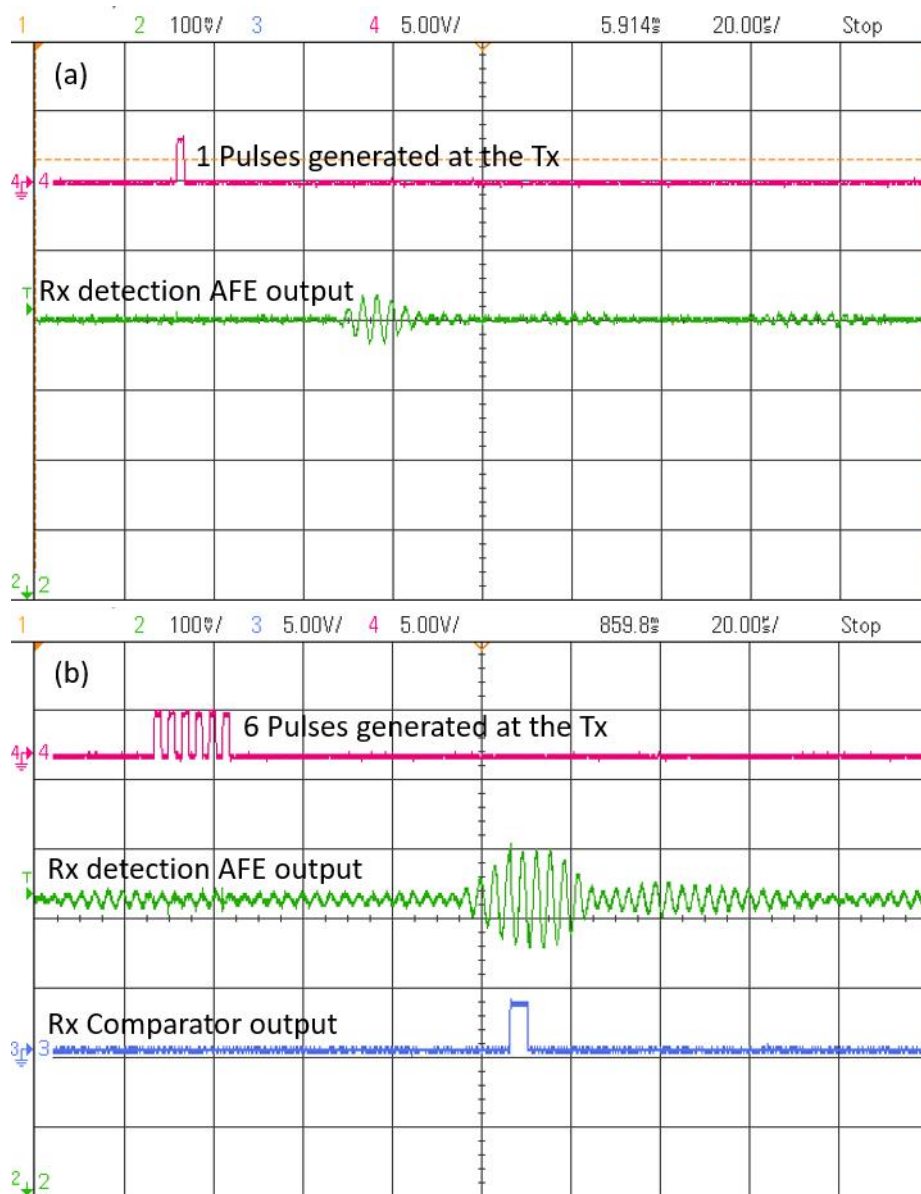


Figure 5-8: (a) Operation transient results of the proposed system, trace 1 represents the transmitted pulses at  $320\text{ kHz}$ , trace 2 is the received signal after filtering the out of operation band noise and amplification and shows the multipath effect, trace 3 is the output of the comparator and the trace 4 shows the received 16 bits; (b) presents the direct path and multipath signals, a guard interval of  $1\text{ ms}$  inserted at the receiver to mitigate the multipath effect.

### 5.3.2 Bandwidth and Received Signal Amplitude

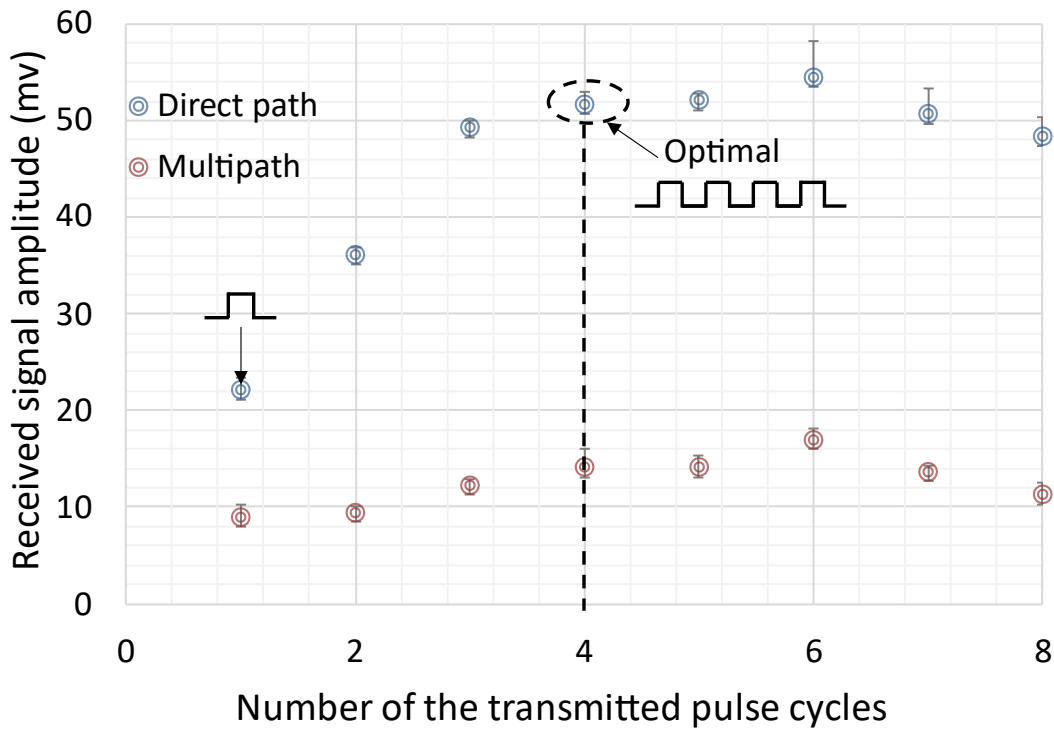
From the early characterization shown in Figure 5-8, the minimum pulse width, representing bit "1" was limited by the system bandwidth, which was showed to be  $50\text{ kHz}$ . Therefore, to achieve the maximum amplitude of the received signal, the received signal amplitude was measured for each number of cycles of the transmitted pulses ranging from one cycle and up to eight pulse cycles. Figure 5-9 shows two different scenarios for the transmitted cycles when only one pulse cycle was transmitted the signal amplitude was low around  $68\text{ mV}_{p-p}$ . When six pulse cycles were transmitted the amplitude increases and detected at the receiver side.

Figure 5-10 presents the received signal amplitude for the primary path and multipath as a function of the transmitted number of cycles. The optimal transmitted pulse cycles were four since the received signal amplitude was  $52\text{ mV}$  and it is around this value when the transmitted pulse cycles were 5, 6 and 7. Since six cycles pulse achieves higher amplitude, a signal of six pulse cycles was generated at  $320\text{ kHz}$ . Pulse amplitude modulation-*OOK* was employed in this design, a data burst of  $320\text{ kHz}$  was generated from the transmitter, each burst includes 16 bytes payload, a bit "1" represented by six cycles (on level) and in a bit "0" no pulse transmitted for the same previous period (off level). The multipath effect was allowed to decay prior to the transmission of subsequent bits by inserting a guard interval period of  $1\text{ ms}$ .



**Figure 5-9: Ultrasound signal transmission exemplar through tissue phantom for two different transmission pulses; (a) One pulse generated at the transmitter; (b) Six pulses transmitted through the channel. It can be seen that the signal amplitude higher when six pulses were transmitted.**

The data packet with 3.3 V amplitude is generated from the microcontroller and applied directly to the transmitter transducer to be transmitted through the channel. The receiver implant transducer receives the transmitted signal. The received signal is fed to the *AFE* to be filtered and amplified and then applied to the threshold-based peak comparator, the reference voltage of the comparator is selected in such a way to prevent the false detection of noise then extract the digital bits.



**Figure 5-10: Maximum amplitude at the receiver for the primary path and the first multipath signals as a function of number of pulse cycles at the transmitter. Six pulse cycles were employed in the transmitter as it achieves high amplitude at the receiver.**

### 5.3.3 Forward Error Correction Code

A light version of the system *FEC* code was adapted to negate transmission errors. For this task, *RS* code was utilised for two reasons:

1. *RS* is capable of correcting burst errors since the correction occurs at the symbol level regardless of whether a signal bit or multiple bits in the symbol are in error. The symbol consists of several bits. For simplicity, in this system, the symbol represents one byte.
2. *RS* can be efficiently implemented in software on a microcontroller which saves the need for any additional hardware (i.e., low complexity). In addition, *RS* is a hard decision decoder being suitable for a low power processor, its ability to operate with non-binary symbols and it has no error floor effect, so it eliminates the need for an additional *CRC* for error checking.

As explained earlier in section 3.14, *RS* code is characterised by three main parameters  $n$ ,  $k$  and  $t$ , for this system,  $t$  equals 4 which means the *RS* code capable of correcting up to 4 bytes or symbols. The symbol size limits the codeword length ( $n$ ), for the *RS* code  $n = 2^{m-1}$ , where  $m$  is the number of bits per symbol. For 8 bits per symbol ( $m = 8$ ), the maximum codeword length is 255 bytes. The payload size can be adjusted by truncating the data symbol with zero paddings but only transmitting the payload and parity bytes, and at the receiver reinserting them before passing to the decoder.

### 5.3.4 SNR, Latency and Data Throughput

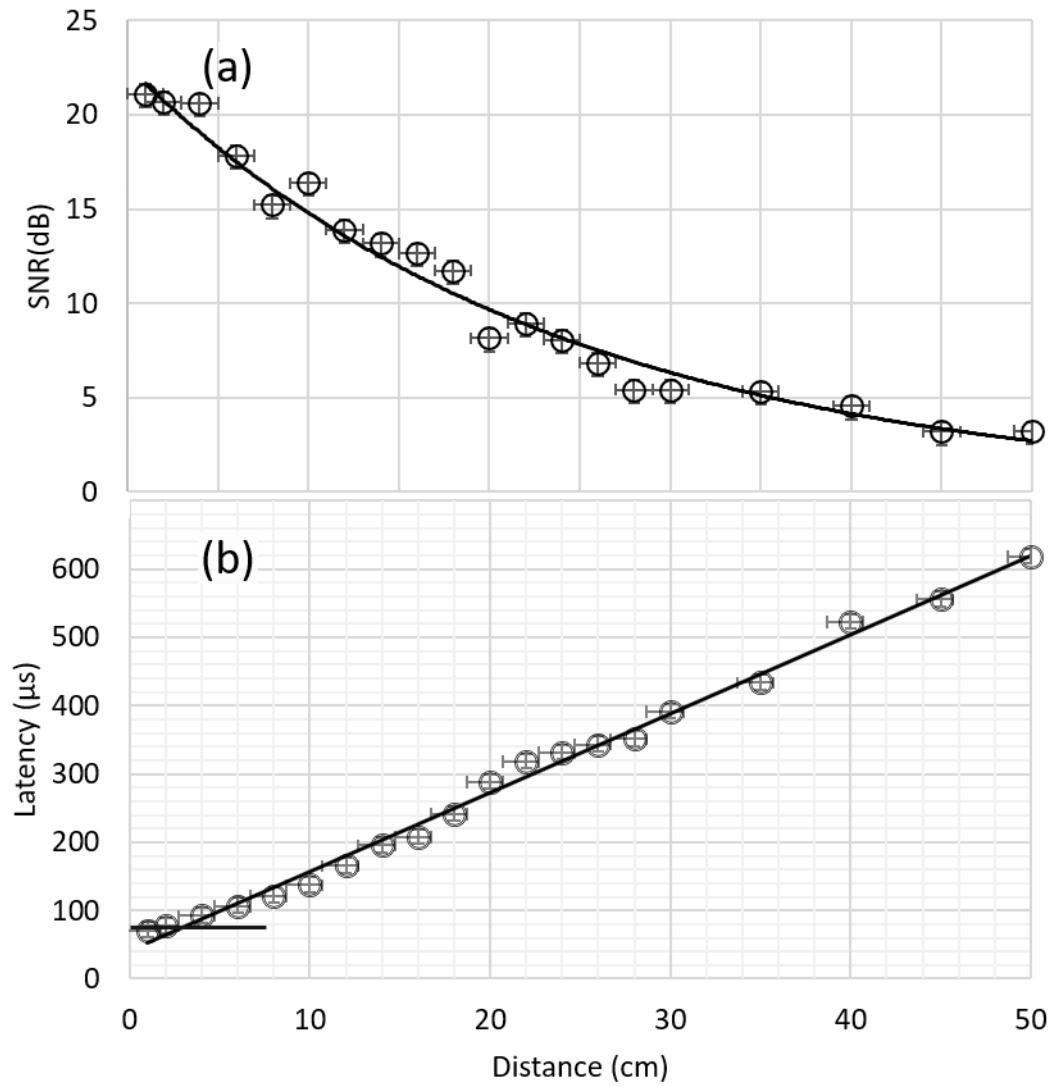
In order to examine the quality of the communication link, *SNR* test was established to measure and evaluate the *SNR* per pulse as a function of distance. Similar to the previously explained set-up that was employed for the experiment, the *RMS* voltage of the received signal was measured. In order to measure the noise power, no transmission through the channel was established and the *AC RMS* value of the noise was measured using a digital oscilloscope Agilent (DSO-X 3034A). *SNR* was calculated in decibels by Equation 3-14, from 1 *cm* distance up to 30 *cm*.

Figure 5-11 (a) presents the *SNR* as a function of distance, it can be seen a nonlinear decay in the *SNR* with distance. This can be easily explained in terms of the sonic wavefront expanding like a sphere over 3*D* space, with a spherical surface area of  $(4\pi r)^2$ . As such, the *SNR* can be expected to decrease with  $1 / r^n$ . In the free space,  $n$  is equal to 2. However, with multiple echoes  $n$  is less than 2 which is good for the signal strength but in practice results in multipath effects. There will be additional multipath effects, but these will be temporally separated from the primary signal amplitude (which will come first). The recorded *SNR* = 21 *dB* at 1 *cm* distance and this value decays to 5 *dB* at a distance of 40 *cm*—approximately the distance from the chest to the bladder.

The latency test was established to measure the time consumed of the ultrasound pulse train when generated at the transmitter and travel through the channel till output by

the receiver. The test is performed for 1 *cm* distance up to 30 *cm* at each distance the latency is measured.

Figure 5-11 (b) shows the latency of the ultrasound signal when generated at the transmitter until output by the receiver as a function of distance. It can be seen that the latency increases linearly as the distance between the implants increase, to reach 500  $\mu\text{s}$  at a distance of 40 *cm*. This result is expected and can be calculated from the speed of sound in saline = 1540 *m/s*. It is nevertheless an important consideration in setting the synchronization timing between sender and receiver nodes.



**Figure 5-11: (a) SNR as a function of distance, a gradual decrease in SNR performance can be noticed as the distance between the Tx and Rx increases; (b) Latency of the ultrasound signal when generated by the Tx and after it received by the Rx through the channel as a function of distance.**

The data throughput was measured and evaluated while varying the distance for different payload sizes. The data throughput is accredited to the rate of the error-free received a packet at the receiver and calculated based on the following equation [148] from 1 cm distance up to 30 cm:

$$Data\ throughput = \frac{P_L(1 - PER)}{T_p} \quad 5-1$$

Where  $P_L$  is the payload length per packet and  $T_p$  is the time consumed data to be received at the receiver.

Figure 5-12 illustrates data throughput as a function of distance. The highest achieved throughput is 612 *bps* then this value decreases as the distance increases. The ultimate limit to the data rate is determined by the guard interval (1 *ms*) required to negate the multipath effect. Together with overhead from headers and error correction code, this leads to a data rate of less than 1 *kbit/s*.

Once the *SNR* drops below 10 (distance 20 *cm* based on the measurements), errors start to present, increasing the packet error rate and thus decreasing the data rate.

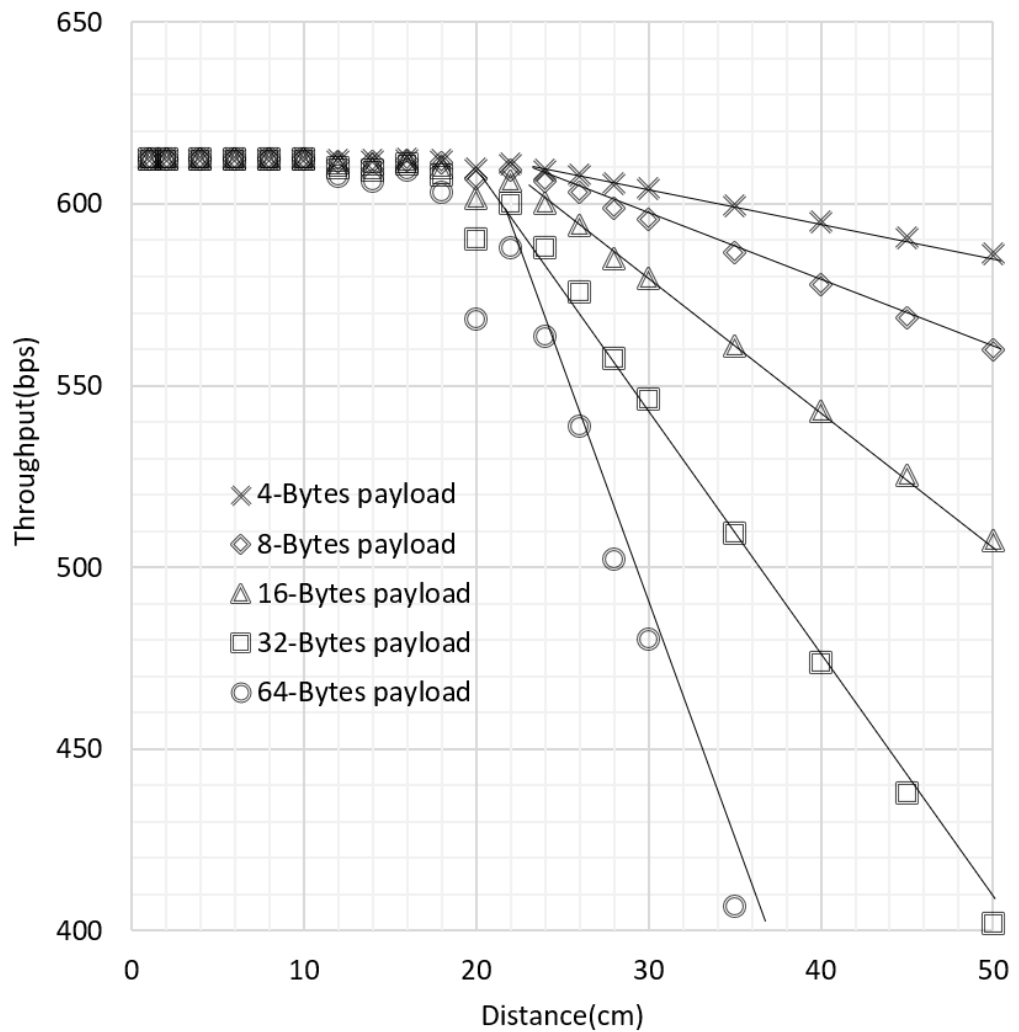


**Figure 5-12: Data throughput versus the distance between the transmitter and receiver for different payload bytes size.**

### 5.3.5 BER and PER

Based on the literature in chapter two the accepted *BER* range for the implanted devices is around  $10^{-4}$ , however, they did not mention at what *SNR* value this *BER* value was achieved. *BER* performance and *PER* were demonstrated in order to examine the performance of data transmission of the implemented system. The *BER* was calculated by dividing the number of erroneous bits by the total number of the transmitted bits, the *BER* presented as a function of the *SNR* with *FEC* and without *FEC*. The transmitted block includes 200 bits (1-byte header +16-byte payload +8-byte

parity). The received payload was compared with the reference data (bit by bit) at the receiver, the *BER* test was run for 1000 iteration in order to achieve accurate results.

Figure 5-13 (a) demonstrates the *BER* performance of the ultrasound communication link without and with the *RS* code. It can be seen that a significant *BER* performance improvement in the presence of the *RS* code at low *SNR*. For instance, at 12 *dB SNR* the *BER* was  $10^{-1}$  without the *FEC*. On the other hand, at the same *SNR* with the *FEC* the *BER* improved to be  $10^{-3}$ . This clearly demonstrates that accurate information transmission can only be achieved with error correction schemes. It is worth to highlight that this is highly important as commands to bioelectronics nodes need to be interpreted correctly for safe operation. Similarly, closed-loop activity needs accurate data from which to determine interventions.

Similarly, the *PER* was calculated with and without the *FEC* by dividing the inappropriately received packets by the total number of the received packets. Inappropriately received packet represents the packets that the decoder can detect but cannot correct.

Figure 5-13 (b) presents the *PER* performance as a function of *SNR* and distance, it can be seen a significant enhancement of the *PER* at low *SNR* and larger distance when using *FEC*. For instance, at 6 *dB SNR* there is no way to receive an error-free packet without the *FEC*, whereas, for the same *SNR* in the presence of the *FEC* only 1 packet out of 100 might be received with an error. It is worth mentioning that *RS* code is error correction and detection which mean even if the decoded data have more than the error-correcting capability, in our case 4 bytes errors, the decoder will detect that, in this case, the packet can be rejected and the receiver can ask to resend the data again. The achieved *PER* with no *FEC* is  $10^{-3}$  at 21 *dB SNR*. Whereas the same *PER* can be achieved at lower *SNR* using the *FEC*.

Figure 5-14 (a) and (b) present the *BER* and *PER* as a function of the normalised *SNR*  $E_b/N_0$ , the  $E_b/N_0$  calculated based on equation 3-15, both *BER* and *PER* were shifted by 1.8 *dB*. The achieved coding gain was 5.3 *dB* with the channel coding.

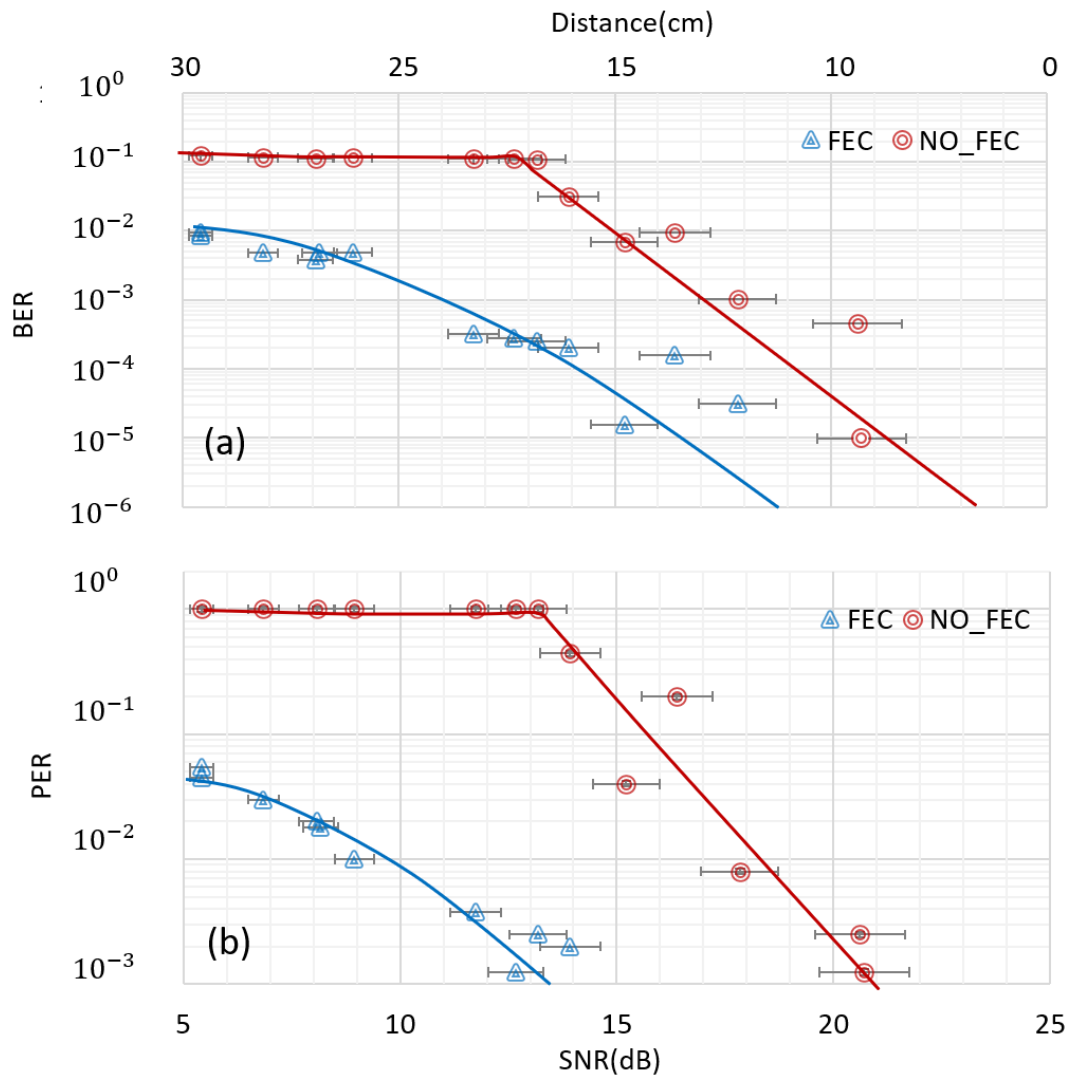
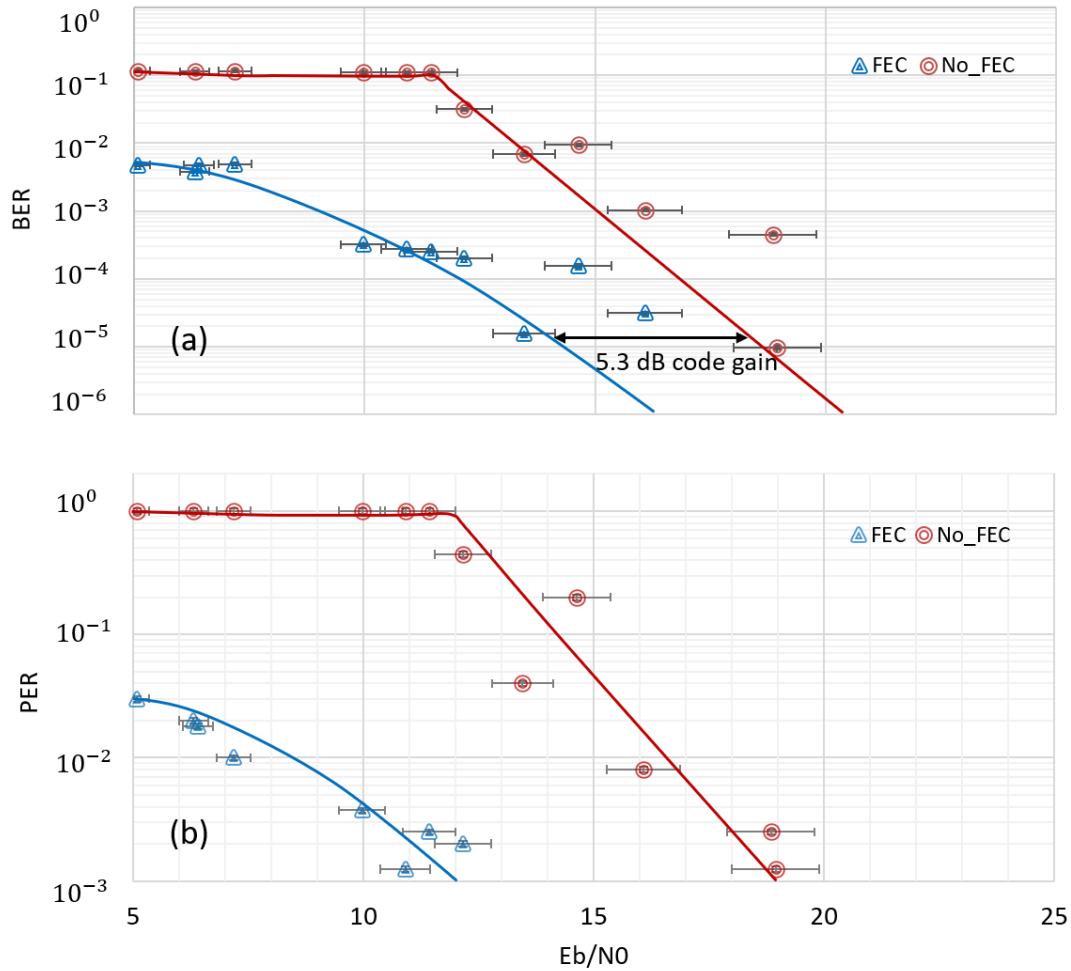


Figure 5-13: (a) Measured *BER* performance of the ultrasound communication link versus the *SNR* for up to 30 cm distance in multipath channel, results presented with and without *RS* code; (b) Measured *PER* versus the *SNR* for up to 30 cm distance in multipath channel, results presented with and without *RS* code.



**Figure 5-14: (a) Measured  $BER$  performance of the ultrasound communication link versus the normalised  $E_b/N_0$  in multipath channel, results presented with and without  $RS$  code; (b) Measured  $PER$  versus the normalised  $E_b/N_0$  in multipath channel, results presented with and without  $RS$  code.**

### 5.3.6 Current Consumption and Energy Per Bit

energy per bit for the microcontroller, transducer, and ultrasound electronics were calculated. The current consumption also measured for each main part of the system.

Figure 5-15 (a) shows the current consumption for the overall system in (mA). The current consumption of the system for the main parts includes the microcontroller in three different power cycling modes (standby, listen and run), ultrasound electronics and the *PMC*. The power management consumes  $35 \mu A$  in both transmitter and receiver.

The ultrasound *AFE* consume  $250\ \mu A$ , primarily to amplify the received ultrasound signal at the receiver. However, it should be noted that: (i) this power is only consumed in the periods when a signal is expected and thus the electronics are on. (ii) The ultrasound electronics were designed and implemented from off the shelf components. In a final system, the circuit current consumption and size can be significantly reduced to a few  $\mu A$  if implemented and integrated as an *ASIC* chip.

From Figure 5-15 (a) the Cortex-M4 microcontroller that was used in the system consumes (15, 0.5, 0.0035) *mA* in (full, listen, standby) modes, respectively. As a general rule, microcontroller units operate most efficiently when utilised at higher speeds, followed by sleep cycling. In the designed system, as it operates with a timed *OOK* protocol, the unit can wake up, receive data, and implement any action as a result, before going back to sleep. Furthermore, the microcontroller will generate the pulses when receiving and transmitting bit “1” only then it will enter into the standby mode during bit “0” and the guard interval. Those modes of operation are important and reflect the proposed communication protocol explained previously in section 3.15. Table 5-2 shows the microcontroller current consumption for three different modes. It should be noted that the microcontroller MK22FN512VLH12 was employed in the system design since it has been used previously in rodent animal systems in the Neuroprosthesis lab. However, there are lower power microcontrollers that can reduce the quiescent operating current requirement significantly.

**Table 5-2: Microcontroller current consumption in three operation modes.**

Operation Mode	Current Consumption ( <i>mA</i> )
Full operation	15
Standby	0.0035
Listen	0.5

Since the transmission of data is highly influenced by the energy consumption in the system electronics, processing of the signal and transmission antenna. This relation can

be addressed by capturing the energy efficiency metric that measured in Joule per bit. Figure 5-15 (b) presents the energy per bit for the  $Tx$  and  $Rx$  microcontrollers,  $Tx$  transducers and  $Rx$  ultrasound  $AFE$ . It can be seen that reasonable energy can be achieved in the system during communication and processing. This result was expected for the system since it implemented with less complex receiver electronics and modulation schemes.

It was found that the transmission power consumption is equal to  $18\text{ mW}$  and  $49\text{ mW}$  for the ultrasound transmitter and the microcontroller in the run mode respectively as shown in Figure 5-15 (a), Consequently, the energy required to transmit one bit  $E_b$  can be easily calculated as:  $E_b = P \times \tau$  where:  $\tau$  is the duration required to send one bit. The required energy cost is  $642\text{ nJ}$  per bit data packet.

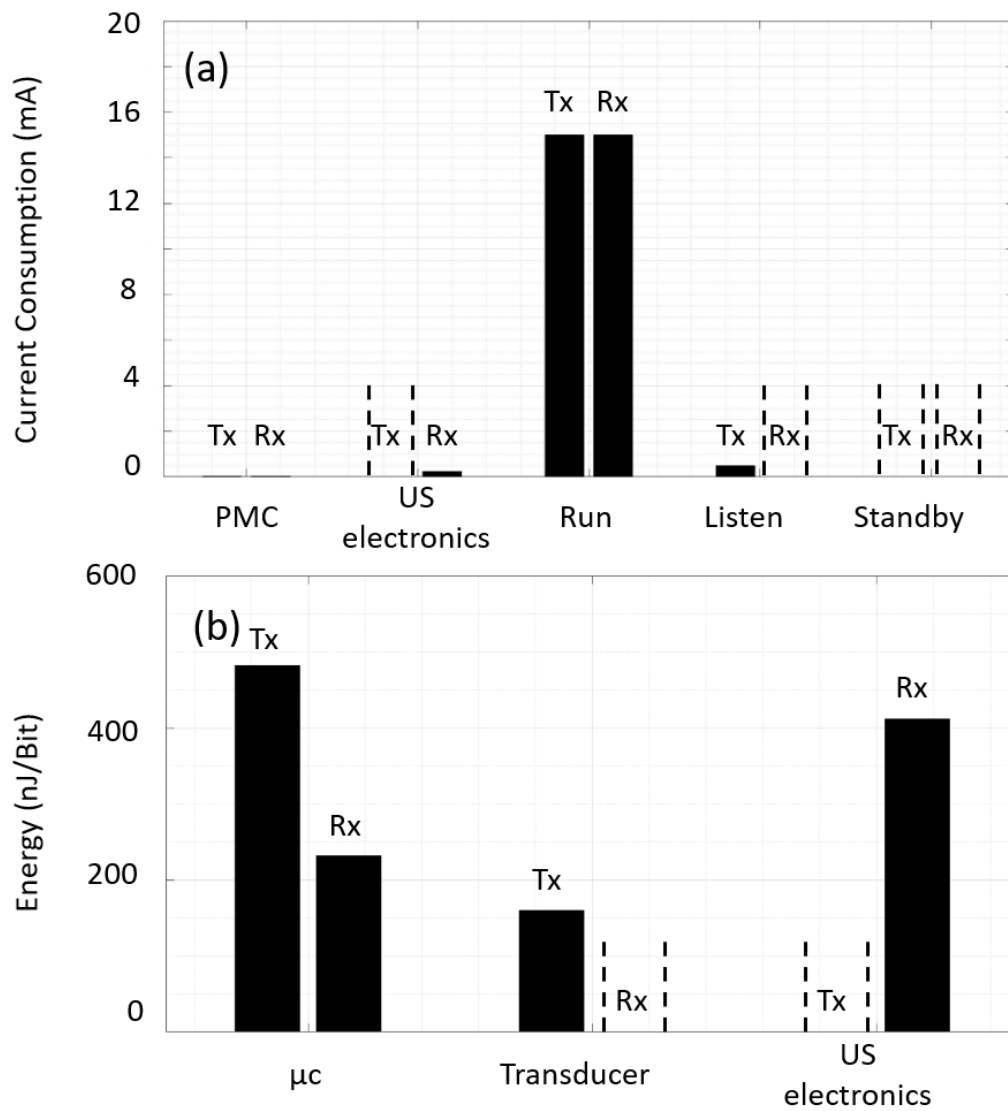


**Figure 5-15: (a) Current consumption of both the transmitter and receiver, the ASIC unit consumes  $35 \mu A$ , the US electronics at the receiver only consume  $250 \mu A$ , the microcontroller operates in three power modes to save the energy it consumes  $15 mA$ ,  $500 \mu A$  in Tx only and  $3.5 \mu A$  for the run, listen and standby modes respectively; (b) Energy per bit for the transmitter and receiver, the microcontroller consumes ( $482$  and  $232$ )  $nJ$  per bit as a transmitter and receiver respectively, the transducer energy is  $160 nJ$  per bit and finally the receiver US electronics energy per bit  $412 nJ$ .**



## Chapter 6. Conclusion and Future work

### 6.1 Conclusion

In this thesis, a design and testing of reliable and efficient ultrasonic communication telemetry have been presented, omnidirectional transducers that vibrate at 320 *kHz* radial resonance frequency have been employed to implement in the future intra body communication inside the human body. A prototype has been implemented to evaluate the system performance in a tissue phantom at up to 30 *cm* distance between the transmitter and receiver. Short pulses sequences with guard intervals have been employed to minimize the multipath effect.

Error-free data is a significant requirement for medical devices. In particular, although errors can be acceptable in collected data such as physiological data which may be inherently noisy – even at the neural signal level and specific data, the transmission of intervention protocols and commands needs to be accurate (error-free) – e.g. whether to release or not release a drug or the stimulus intensity. As such, error detection and correction low-overhead *RS* code has been implemented onto the microcontroller to achieve reliable communication even at low *SNR* which is likely the case over longer distances.

Results have been shown that for transmission within the body: ultrasound has a unique capability to transmit over tens of *cm* between implantable nodes with a very small energy budget. This is not realistically achievable with optical or RF transmission.

Although the proposed prototype device is relatively large, it is scalable to much smaller dimensions which will be explained in the next section.

### 6.2 Personal View on The Impact of this Work in The Bioelectronic Medicines Field

I believe that bioelectronic medicines will have a promising future in the treatment of chronic conditions such as diabetes, inflammatory bowel disease, lupus etc. In the last few years, Galvani Bioelectronics (GSK) in the UK and SetPoint Medical in the US have

been developing new therapies for chronic diseases. Bioelectronic therapies' next generation can be used as a personalised treatment for each patient's need. Hence it requires significant data collection from within the body and transmission to/ from the external wearable unit. Based on the designed prototype, ultrasound communication can be an effective and promising method to be employed for those scenarios.

### 6.3 Personal Work Criticism

The presented system in this thesis provides reliable and efficient ultrasonic communication telemetry. However, there are still some parts of the system that can be explored and improved further. Therefore, the main parts that can be improved will be listed in the following points, and the improvements will be discussed in more details in the next section.

- 1- **Transducer encapsulation:** PU was used in the current system prototype. Although, this material has already been used in one of Medtronic pacemaker leads. More biocompatible silicon based materials can be used as they are already used for the implanted devices and some of them have good acoustic properties.
- 2- **Microcontroller type:** the currently used microcontroller is based on Arm Cortex-M4 and includes a high *DSP* computation function. This microcontroller with the DSP module is quite powerful and lots of modules not used by the designed system. Therefore, given the receiver energy budget and size constraints, it can be replaced by low power and small size microcontroller that can fulfil the requirements.

### 6.4 Future Work

The research work presented in this thesis establishes a substantial advancement over the previously reported systems for the intra body communication application. However, there are still some interesting research areas that can be explored further. The author's ideas are explained in this section, the designed system developments are divided into hardware and software developments, each part is explained in detail.

As per Figure 4-16, the purpose was to implement a robust and optimal communication link, so these have been implemented using discrete components. Furthermore, the microcontroller and sensor electronics are also discrete as per Figure 4-17 (a) and (b). In a future/final micro-system, I would envisage much of the electronics to compress to a single *ASIC* for sensing and communications and perhaps a separate microcontroller chip for processing. Furthermore, a custom ceramic base can be used instead which would be more suitable for implantable devices compared to a *PCB* base. A concept final configuration can be seen in Figure 6-1 that shows 3D model of the final configuration of the system before the passivation.

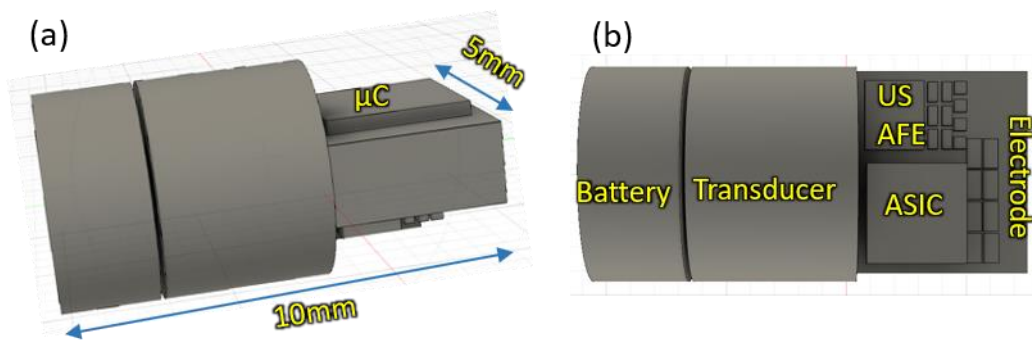


**Figure 6-1: (a) Side view with mm dimensions of the miniaturised system; (b) Top view 3D model of the system before the passivation that shows the main utilised components and how it can be miniaturized to be injectable.**

#### 6.4.1 Hardware Improvement and Further Development

##### 1. Wire material

In this work an ultrafine copper wire has been used for the *PZT* crystal wire bonding, this copper wire has a diameter of 0.13 *mm*. Although it provides a good electrical conductivity, it can defect and susceptible to corrosion over long term operation. Therefore, for the future device, the gold wires are a good replacement since the gold wires are corrosion resistant and provide adequate electrical and mechanical properties.

## 2. *PZT* transducer material

It is worth pointing out that any device would be encapsulated and thus would be safe at least for short periods and is thus suitable for in-vivo research, which would need to be performed before any clinical translation. Nevertheless, further into the future, the toxicity of *PZT* will mean that (lead/heavy metal free) alternatives such as potassium sodium niobate [160] will need to be explored.

## 3. Transducer encapsulation

In this work, *PU* was utilised as a coating material for the transducer since it has an acoustic impedance that is close to the tissue impedance and it can achieve good mechanical robustness, provide excellent water resistance and reduce the possible interface reflections. Furthermore, *PU* has already been used in the pacemaker leads from a Medtronic model P1501DR [113], indicating biocompatibility. However, an alternative coating material can be explored and employed for the transducer encapsulation Table 6-1 provides a range of encapsulation materials that widely used in biomedical implanted devices and their acoustic impedance. The closest impedance of the encapsulation material to the medium impedance (Table 3-1) will result in less reflection and loss of signal power.

**Table 6-1: Encapsulation materials and their acoustic impedance.**

Polydimethylsiloxane (PDMS)	
Material name	Acoustic impedance ( $10^6 \text{ kg m}^{-2} \text{ s}^{-1}$ )
Sylgard 170	1.37
Sylgard® 160	1.5
GE® RTV-615	1.1
Sylgard 184	1

## 4. *AFE* design

The ultrasound *AFE* was designed and implemented from off the shelf components, the current consumption of this design was  $250 \mu\text{A}$ . In the future system, the circuit current consumption and size can be significantly reduced

into a few  $\mu A$  if implemented and integrated as an *ASIC* chip to be more compatible for an injectable *BeNs*.

## 5. Microcontroller type

In this work, the microcontroller MK22FN512VLH12 was employed in the system design since it already been used widely in rodent animal systems by the Neuroprosthesis lab team. This microcontroller is based on Arm Cortex-M4 and includes a high *DSP* computation function. Since in the designed system floating point or a complex *DSP* function are not used, there are two methods to reduce the unnecessary background power consumption. First, the *DSP* of the microcontroller can be turned off when unused. However, this method can be useful for periodic computation tasks that can be compressed in time. *BeNs* devices are assumed to spend most of their time in deep sleep and then wake up for periods of communication activity (as explained in section 5.3.6). However, during these periods when the devices are awake for communication activity, they spend most of their time in a moderately low energy “listening” mode where they are waiting for the arrival of a data packet. Likewise, when a packet arrives the processing of the data packet can only happen in real time (it is an event of fixed duration) and cannot be compressed into a shorter time period by upping the clock frequency. Therefore, the second method can be explored by choosing a processor that has just enough computational resources/memory to do the required amount of computation spread over the period of communication. There are lower power microcontrollers that can reduce the operating current requirement significantly. An example of other microcontrollers is MKL02Z32VFK4 microcontroller with 24 pin-QFN packages, the core processor based on Arm Cortex-M0+ which provide ultra-low power operation, the package dimensions are (4 × 4 × 1) mm.

## 6.4.2 Communication Software Further Development

### 1. Modulation type

In the designed system, *OOK* modulation technique has been used since it requires a less complex receiver in terms of hardware and processing. Another modulation approach is *ppm* where the binary data bits are encoded by varying

intervals between pulses of equal duration. This can be very power efficient, multipath tolerant and can be detected with a very simple receiver, like the designed receiver, using minimal energy (which is what needed for *BeNs*). In a multipath channel such as the human body, it is desirable always to send the shortest duration pulse that the channel bandwidth will support to minimise fading, longer pulse duration will cause the superposition of the multipath to a complete cancellation by destructive interference.

In this work, the *PPM* and Differential Pulse Position Modulation (*DPPM*) have been explored. The concept results are presented in the coming sections and the remaining experiments should be considered as an open area of future research.

### ***PPM and DPPM***

In the *PPM*, the binary data bits are encoded by varying the position of pulses of equal duration, hence the transmission power is constant for all the transmitted data. The *DPPM* is a modification for the *PPM* that encode the binary data bits by varying intervals between pulses of equal duration. *DPPM* add several advantages over the *PPM* such as synchronisation pulse is not necessary for the *DPPM* (unlike the *PPM*), less bandwidth and less average power are required for *DPPM* and *DPPM* is less complex to implement. Figure 6-2 shows the difference between the *PPM* and *DPPM*.

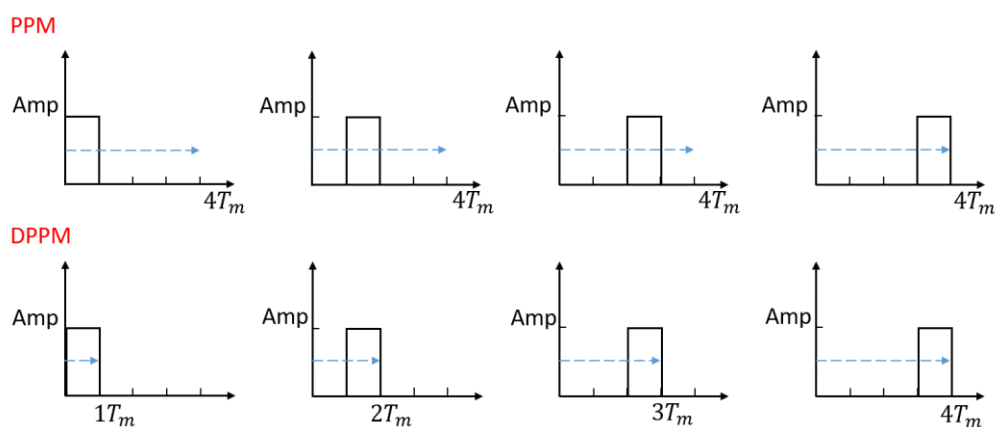


**Figure 6-2: The key difference between the *PPM* and *DPPM*, it can be seen the *DPPM* remove the off period that followed after the on the pulse.  $T_m$  represents the mapping duration.**

### **Data Encoding and Decoding using DPPM**

Using the same experimental setup of the *OOK* modulation, the binary bits were encoded using the *DPPM*, the key target of the *DPPM* is to improve the data rate, therefore, two bits per symbol are encoded, unlike the *OOK* (transmit only one bit per symbol). Table 6-2 shows the time interval assigned for each two bits combination, each pulse encoded based on the previous pulse. Two pulses of 2 ms time interval are inserted as a synchronisation pulse after that the data will be received. At the receiver, the difference between each consecutive pulsed will be measured to decode the binary bits. Out of the period, interval was added to return to standby mode in case the receiver missed the packet.

**Table 6-2: 2-DPPM bit mapping.**

<b>Bit Combination</b>	<b>DPPM time delay (ms)</b>
Synch pulse	2
00	0.8
01	0.85
10	0.9
11	1
Out of period	1.2

Figure Shows the transmitted data using the 2 – *DPPM* bit mapping, and the received data in the ultrasound *AFE* then the data detection by the embedded control unit. It can be seen that the data symbols have variable durations based on the 2 – *DPPM* bit mapping. Further *PER* performance for *DPPM* needs to be examined and compare it with the *OOK* in terms of data rate and energy efficiency.

Finally, more sophisticated modulation schemes with *PSK/QAM, OFDM* etc. can be employed but such schemes require more complicated hardware, software and the receiver energy budget is equally as important as the transmit energy budget for implantable devices. Hence further development is needed on low power implementation with dedicated integrated circuit designs or programmable logic devices. In the case of an implant transmitting out to a receiver on the skin surface

(where a higher energy receiver could be used), more bandwidth efficient modulation schemes can be considered to achieve higher data rates if required.

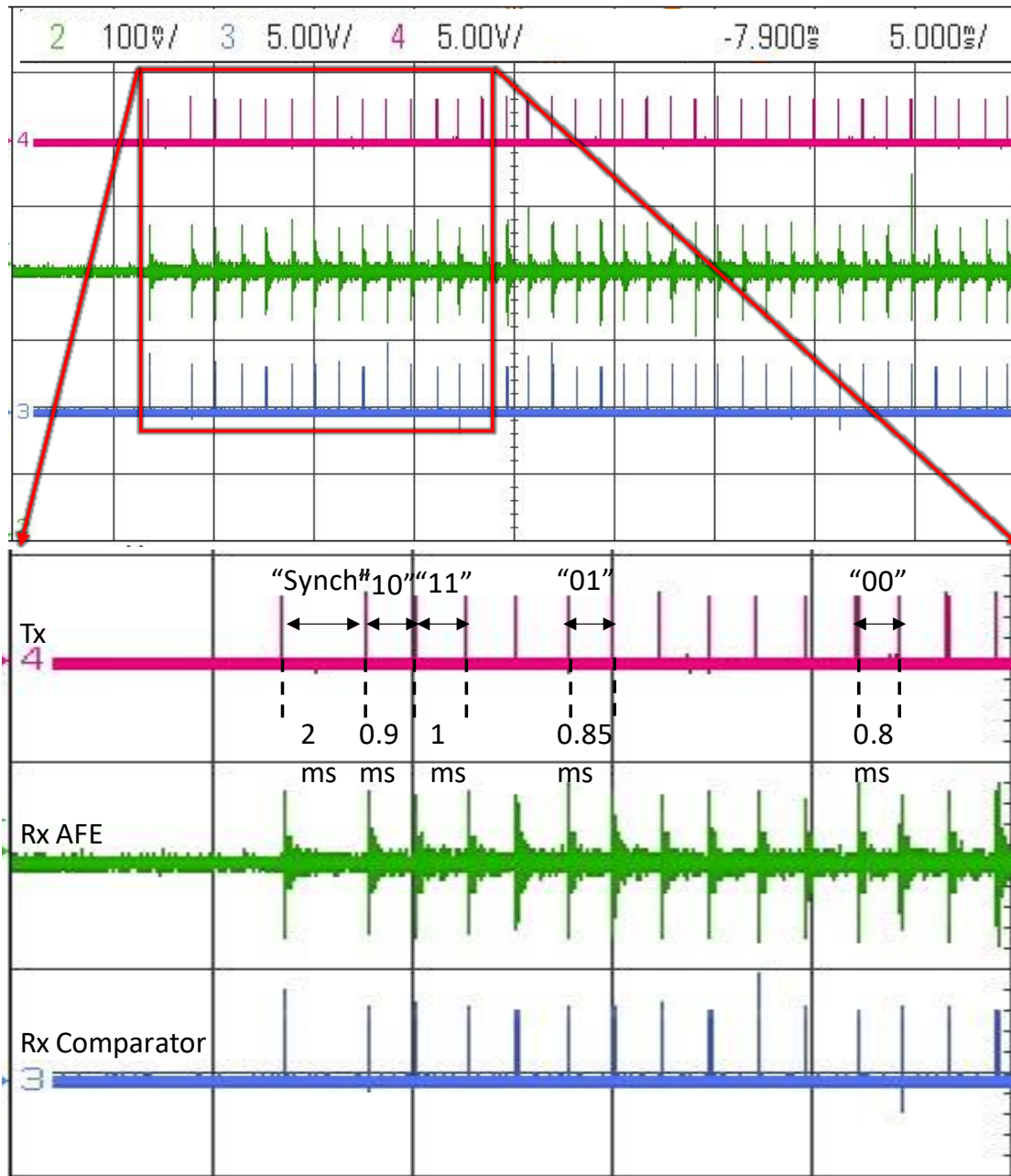


Figure 6-3: Bit encoding of the *DPPM*, trace 1 shows the transmitter pulses started by the synch period, trace 2 shows the receiver *AFE* and trace 3 shows the detected pulses at the receiver.

## 2. Power cycling

Switching the microcontroller between run mode and low power modes can help energy saving and extend the implant lifetime. Since the *BeNs* have a constrained energy budget, it is important to meet the energy required for appropriate operation without compromise the performance. As presented previously, Transmission can be achieved at an energy cost of 642 *nJ* per bit data packet using on/off power cycling in the electronics.

The current consumption can be reduced significantly when replacing MK22FN512VLH12 based on Arm Cortex-M4 with MKL02Z32VFK4 based on Arm Cortex- M0+ core. For the future implementation of the *BeNs*, the microcontroller MKL02Z32VFK4 have been explored in terms of the current consumption and the switching between power modes. Table 6-3 shows the measured current consumption of the MKL02Z32VFK4 microcontroller for four different power modes: normal run, very low power run (*VLPR*), Stop and very low power stop (*VLPS*).

**Table 6-3: Measured Current consumption of the MKL02Z32VFK4 microcontroller.**

Core (MHz)	Speed (MHz)	Bus/Flash Speed (MHz)	Supply Voltage (V)	Current Consumption (mA)
<b>Run</b>				
48		24	3.3	5.7
4		2	3.3	1.42
4		2	1.8	1.63
<b>VLPR</b>				
4		1	3.3	0.321
4		1	1.8	1.56
<b>Stop</b>				
48		24	3.3	0.27
4		2	3.3	0.25
48		24	1.8	0.26
<b>VLPS</b>				
48		24	3.3	0.0028
4		4	3.3	0.0024
4		4	1.8	0.00215

### **6.4.3 Experimental Testing and Investigation**

#### **1. In Vivo experiment**

At the current time, there are no clinical systems that utilise ultrasound as a communication method. However, it is widely used for in-body imaging, and in some forms of therapeutic intervention such as kidney stone removal. Its physiological effects are well understood, and thus clinical utilisation has no inherent regulatory barriers. Therefore, the designed system can be tested In Vivo on the human body safely. Both that transmitter and receiver can be placed on the surface of the skin with the aid of coupling gel on each side of the human abdomen area and test the communication through the body. The experiment can be repeated for different distances such as chest-abdomen, neck-abdomen, and arm.

#### **2. Acoustic noise investigation**

The acoustic noise, that can appear when communicating inside the body, in the low operating frequency range (i.e. hundreds of *kHz* range) is poorly understood at present and should be considered as an open area of research. Measurement of transmission loss versus distance in tissue at a low operating frequency can also be investigated.

## Chapter 7. Appendix A

The appendix data provides some additional data to support data analysis of the previous research work in chapter two. In particular, full summary tables for the following tables provide comparative data for transducers of different form factors: disc (Table A-1), directional plate (Table A-2), directional cube (Table A-3), directional PMUT (Table A-4), omnidirectional sonomicrometry (Table A-5) and omnidirectional Tube (Table A-6). It is worth highlighting some definitions that used in the aforementioned tables:

Backscattering modulation: Detection of backscattered analog signal level from the device.

Transmission distance: The distance between the Tx and Rx in the medium of transmission.

Benchtop device: The device was implemented as a benchtop system with transducer and external benchtop electronics.

PCB device: The device was implemented on a printed circuit board and encapsulated.

ASIC device: The device electronics were implemented on an application specific integrated circuit chip.

**Table A-1: Summary of all reported devices using a directional disc transducer form factor.**

Ref.	Diameter size (mm)	Application	Resonance frequency (MHz)	Modulation	Data rate(kbps)	Medium	Distance (mm)	BER	Device
[85]	6	Comms/Power	1	ASK, FSK and PSK	25	Tissue phantom	50	$10^{-6}$	PCB
[74]	9.5	Comms	1	OOK-FDM	120	Saline	30	-	Benchtop
[75]	15	Comms	0.5	FSK	0.5	Water	10	-	Benchtop
[84]	19	Comms	5	QAM	5000-30000	Beef liver	50	-	Benchtop
[83]	19	comms	5	64 QAM	30000	Pork loin and beef liver	58.6	$10^{-4}$	Benchtop
[70]	9.5	Comms	5	16 QAM	1300	Human kidney phantom	100	$10^{-4}$	Benchtop
[78]	1.1	Comms/Power	1	OOK	75	Water	37.5	-	PCB
[80]	9.5	Comms	5	PPM + time hopping and spread spectrum	700, 70	Human kidney phantom	100	$10^{-6}$	Benchtop

[81]	9.5	Comms	0.7	<i>PPM</i>	90	thoracic phantom	180	$10^{-6}$	Benchtop
[76]	6	Comms	1	<i>OOK-PM</i>	25	Animal	50	-	<i>ASIC</i>
[77]	13	Comms	1	Backscattering	-	Water	50	-	<i>PCB</i>
[79]	15	Comms/Power	0.765	<i>ASK/Backscattering</i>	0.110, 1.2	Water	150	-	Benchtop

**Table A-2: Summary of all reported devices using a directional plate transducer form factor. The reported transducers of plate shape are a trade-off between the transducer size and resonance frequency.**

Ref.	Dimensions ( <i>mm</i> )	Application	Resonance frequency ( <i>MHz</i> )	Modulation	Data rate ( <i>kbps</i> )	Medium	Distance ( <i>mm</i> )	<i>BER</i>	Device
[69]	(1 x 1 x 1.4)	Comms/Power	1	-	-	Chicken meat	30	-	<i>PCB</i>
[68]	(0.55 x 0.55 x 0.4)	Comms/Power	Tx 2.5 and Rx 1	<i>OOK</i>	Tx 100 and Rx 25	Animal tissue and Castor oil	60 and 85	$10^{-4}$ in castor oil	Fully packaged
[86]	(1.08 x 1.08 x 1.44)	Comms	1	<i>QPSK</i>	250	Mineral oil	50	$10^{-4}$	<i>PCB</i>

**Table A-3: Summary of all reported devices using a directional cube transducer form factor.**

Ref.	Size ( $mm^3$ )	Application	Resonance frequency ( $MHz$ )	Modulation	Data rate ( $kbps$ )	Medium	Distance ( $mm$ )	<i>BER</i>	Device
[87]	1.44	Comms/ Power	1	<i>OOK</i>	-	Castor oil	60	-	-
[71]	0.75	Comm/ Power	1.78	Backscatter	50 (average)	Oil	50	-	Fully packaged
[82]	0.75	Comm/ Power	1.85	Backscatter	500	Rat	8.9	-	Fully packaged
[90]	0.8	Comm/ Power	1.6	Backscatter	-	Oil	20	-	Benchtop

**Table A-4: Summary of all reported devices using a PMUT transducer form factor.**

Ref.	Dimensions ( $mm$ )	Applicatio n	Resonance frequency ( $MHz$ )	Modulatio n	Data rate ( $kbps$ )	Medium	Distance ( $mm$ )	<i>BER</i>	Device
[72]	(3 × 3 × 0.5) $mm$	Comms	0.6	<i>BPSK</i> and <i>QPSK</i>	298 ( <i>BPSK</i> ) and 596 ( <i>QPSK</i> )	Tissue phantom	50	$10^{-6}$ ( <i>BPSK</i> ) and $10^{-5}$ ( <i>QPSK</i> )	<i>PCB</i> + Benchtop

**Table A-5: Summary of all reported devices using an omnidirectional sonomicrometry transducer form factor. With more sophisticated modulation scheme the bit error rate performance improved for the communication application experiments.**

Ref.	Size ( <i>mm</i> ) (diameter)	Application	Resonance frequency ( <i>MHz</i> )	Modulation	Data rate ( <i>kbps</i> )	Medium	Distance ( <i>mm</i> )	BER	Device
[97]	1	Imaging	1.3	<i>OOK</i>	1000	Chicken meat	30	$10^{-2}$	Benchtop
[67]	2	Comms	1.2	4 <i>QAM</i>	200	Gelatine bone phantom	80	$10^{-4}$	<i>PCB</i>
[66]	2	Comms	1.2	<i>OFDM</i>	340	Beef liver	100	$10^{-4}$	<i>PCB</i>
[88]	2	Comms	1.1	<i>QAM</i>	3200	Rabbit abdomen	22	$10^{-5}$	Benchtop

**Table A-6: Summary of all reported devices using a tube transducer form factor.**

Ref.	Dimension ( <i>mm</i> )	Application	Resonance frequency ( <i>MHz</i> )	Modulation	Data rate ( <i>kbps</i> )	Medium	Distance ( <i>mm</i> )	BER	Device
[42]	(3 x 3.5 x 2.5)	Comms	0.32	<i>OOK</i>	1	Saline	Up to 300	$10^{-5}$	<i>PCB</i>
[73]	(3 x 3.5 x 2.5)	Comms	0.32	-	70	Saline	Up to 360	-	Benchtop



## References

- [1] S. Packer, N. Mercado, and A. Haridat, "Bioelectronic medicine—ethical concerns," *Cold Spring Harbor perspectives in medicine*, vol. 9, no. 10, p. 034363, 2019.
- [2] G. Shaw, D. Claremont, and J. Pickup, "In vitro testing of a simply constructed, highly stable glucose sensor suitable for implantation in diabetic patients," *Biosensors and Bioelectronics*, vol. 6, no. 5, pp. 401-406, 1991.
- [3] B. Bonaz, "Is-there a place for vagus nerve stimulation in inflammatory bowel diseases?," *Bioelectronic Medicine*, vol. 4, no. 1, p. 4, 2018.
- [4] O. Bloom, K. F. Cheng, M. He, A. Papatheodorou, B. T. Volpe, B. Diamond, and Y. Al-Abed, "Generation of a unique small molecule peptidomimetic that neutralizes lupus autoantibody activity," *Proceedings of the National Academy of Sciences*, vol. 108, no. 25, pp. 10255-10259, 2011.
- [5] L. Spel and F. Martinon, "Inflammasomes contributing to inflammation in arthritis," *Immunological reviews*, vol. 294, no. 1, pp. 48-62, 2020.
- [6] N. Yessad, M. Omar, A. Tari, and A. Bouabdallah, "QoS-based routing in Wireless Body Area Networks: A survey and taxonomy," *Computing*, vol. 100, no. 3, pp. 245-275, 2018.
- [7] P. Angelidis, "Mobile telemonitoring insights," in *Medical informatics: Concepts, methodologies, tools, and applications*: IGI Global, 2009, pp. 107-112.
- [8] P. A. Angelidis, "Personalised physical exercise regime for chronic patients through a wearable ICT platform," *International journal of electronic healthcare*, vol. 5, no. 4, pp. 355-370, 2010.
- [9] B. K. Rivera, S. K. Naidu, K. Subramanian, M. Joseph, H. Hou, N. Khan, H. M. Swartz, and P. Kuppusamy, "Real-time, in vivo determination of dynamic changes in lung and heart tissue oxygenation using EPR oximetry," in *Oxygen Transport to Tissue XXXVI*: Springer, 2014, pp. 81-86.
- [10] A. Yakovlev, S. Kim, and A. Poon, "Implantable biomedical devices: Wireless powering and communication," *IEEE Communications Magazine*, vol. 50, no. 4, pp. 152-159, 2012.
- [11] D. S. Elterman, "The novel Axonics® rechargeable sacral neuromodulation system: Procedural and technical impressions from an initial North American experience," *Neurourology and urodynamics*, vol. 37, no. S2, pp. S1-S8, 2018.
- [12] B. Jaafar, J. A. Neasham, and P. Degenaar, "What Ultrasound Can and Cannot Do in Implantable Medical Device Communications," *IEEE Reviews in Biomedical Engineering*, 2021.
- [13] V. A. Sironi, "Origin and evolution of deep brain stimulation," *Frontiers in integrative neuroscience*, vol. 5, p. 42, 2011.
- [14] A. M. Lozano, N. Lipsman, H. Bergman, P. Brown, S. Chabardes, J. W. Chang, K. Matthews, C. C. McIntyre, T. E. Schlaepfer, and M. Schulder, "Deep brain stimulation: current challenges and future directions," *Nature Reviews Neurology*, vol. 15, no. 3, pp. 148-160, 2019.
- [15] A. Fasano, V. S. Fung, L. Lopiano, B. Elibol, I. G. Smolentseva, K. Seppi, A. Takáts, K. Onuk, J. C. Parra, and L. Bergmann, "Characterizing advanced Parkinson's

- disease: OBSERVE-PD observational study results of 2615 patients," *BMC neurology*, vol. 19, no. 1, p. 50, 2019.
- [16] F. B. Rodrigues, G. S. Duarte, D. Prescott, J. Ferreira, and J. Costa, "Deep brain stimulation for dystonia," *Cochrane Database of Systematic Reviews*, no. 1, 2019.
- [17] V. Salanova, "Deep brain stimulation for epilepsy," *Epilepsy & Behavior*, vol. 88, pp. 21-24, 2018.
- [18] F. V. Tjong and V. Y. Reddy, "Permanent leadless cardiac pacemaker therapy: a comprehensive review," *Circulation*, vol. 135, no. 15, pp. 1458-1470, 2017.
- [19] "THE ERA OF IMPLANTABLE INSULIN PUMP THERAPY FOR DIABETES PATIENTS BEGINS!" Implantable Insulin Pump. <https://theiipump.com/index.php/history-chapter-two/> (accessed 24/11, 2020).
- [20] C. L. Jones, J. R. Fischer, and S. L. Hernandez, "Sacral neuromodulation for the treatment of persistent genital arousal disorder," *Obstetrics & Gynecology*, vol. 128, no. 2, pp. 321-323, 2016.
- [21] L. Greenemeier, "FDA approves first retinal implant," *Nature*, vol. 15, p. 2013, 2013.
- [22] G. Clark, "Cochlear Implants. In: Speech Processing in the Auditory System," *Springer Handbook of Auditory Research*, vol. 18, 2004.
- [23] S. Ogbonnaya and C. Kaliaperumal, "Vagal nerve stimulator: evolving trends," *Journal of natural science, biology, and medicine*, vol. 4, no. 1, p. 8, 2013.
- [24] K. J. Burchiel and A. M. Raslan, *Functional Neurosurgery and Neuromodulation*. Elsevier Health Sciences, 2018.
- [25] A. Soltan, J. M. Barrett, P. Maaskant, N. Armstrong, W. Al-Atabany, L. Chaudet, M. Neil, E. Sernagor, and P. Degenaar, "A head mounted device stimulator for optogenetic retinal prosthesis," *Journal of neural engineering*, vol. 15, no. 6, p. 065002, 2018.
- [26] S. D. Sharma, S. L. Cushing, B. C. Papsin, and K. A. Gordon, "Hearing and speech benefits of cochlear implantation in children: A review of the literature," *International Journal of Pediatric Otorhinolaryngology*, p. 109984, 2020.
- [27] B. R. Southwell, "Electro-Neuromodulation for Colonic Disorders—Review of Meta-Analyses, Systematic Reviews, and RCTs," *Neuromodulation: Technology at the Neural Interface*, 2020.
- [28] G. P. Thomas and B. C. Jobst, "Critical review of the responsive neurostimulator system for epilepsy," *Medical Devices (Auckland, NZ)*, vol. 8, p. 405, 2015.
- [29] K. Mathieson, J. Loudin, G. Goetz, P. Huie, L. Wang, T. I. Kamins, L. Galambos, R. Smith, J. S. Harris, and A. Sher, "Photovoltaic retinal prosthesis with high pixel density," *Nature photonics*, vol. 6, no. 6, pp. 391-397, 2012.
- [30] A. PARK. "Why It's Time to Take Electrified Medicine Seriously." Time. <https://time.com/5709245/bioelectronic-medicine-treatments/> (accessed 05/09, 2020).
- [31] A. Kanashiro, G. S. Bassi, F. d. Queiróz Cunha, and L. Ulloa, "From neuroimmunomodulation to bioelectronic treatment of rheumatoid arthritis," *Bioelectronics in medicine*, vol. 1, no. 2, pp. 151-165, 2018.
- [32] A. N. Khan, A. Ermakov, G. Sukhorukov, and Y. Hao, "Radio frequency controlled wireless drug delivery devices," *Applied Physics Reviews*, vol. 6, no. 4, p. 041301, 2019.
- [33] L. Connectivity. "Laird Connect." <https://connectivity-staging.s3.us-east-2.amazonaws.com/2019-07/062019%20-%20White%20Paper%20-%20Medical.pdf> (accessed 05/10, 2020).

- [34] C. Camara, P. Peris-Lopez, and J. E. Tapiador, "Security and privacy issues in implantable medical devices: A comprehensive survey," *Journal of biomedical informatics*, vol. 55, pp. 272-289, 2015.
- [35] J. K. Mattingly, N. T. Greene, H. A. Jenkins, D. J. Tollin, J. R. Easter, and S. P. Cass, "Effects of skin thickness on cochlear input signal using transcutaneous bone conduction implants," *Otology & neurotology: official publication of the American Otological Society, American Neurotology Society [and] European Academy of Otology and Neurotology*, vol. 36, no. 8, p. 1403, 2015.
- [36] F.-G. Zeng, S. Rebscher, W. Harrison, X. Sun, and H. Feng, "Cochlear implants: system design, integration, and evaluation," *IEEE reviews in biomedical engineering*, vol. 1, pp. 115-142, 2008.
- [37] D. D. Zhou and E. S. Greenbaum, *Implantable neural prostheses*. Springer, 2009.
- [38] P. Verrills and M. Russo, "Peripheral nerve stimulation for back pain," in *Stimulation of the Peripheral Nervous System*, vol. 29: Karger Publishers, 2016, pp. 127-138.
- [39] N. S. ÖZYALÇIN, "A different option for neuromodulation procedures: sacral nerve stimulation," *TURKIYE FIZIKSEL TIP VE REHABILITASYON DERGISI-TURKISH JOURNAL OF PHYSICAL MEDICINE AND REHABILITATION*, vol. 61, no. 2, pp. 155-165, 2015.
- [40] H. R. Sharif and Y. S. Kavian, *Technological breakthroughs in modern wireless sensor applications*. IGI Global, 2015.
- [41] A. D. Rush and P. R. Troyk, "A power and data link for a wireless-implanted neural recording system," *IEEE Transactions on Biomedical Engineering*, vol. 59, no. 11, pp. 3255-3262, 2012.
- [42] B. Jaafar, J. Luo, D. Firfilionis, A. Soltan, J. Neasham, and P. Degenaar, "Ultrasound Intra Body Multi Node Communication System for Bioelectronic Medicine," *Sensors*, vol. 20, no. 1, p. 31, 2020.
- [43] J. Wiskin, B. Malik, R. Natesan, D. Borup, N. Pirshafiey, M. Lenox, and J. Klock, "Full Wave 3D Inverse Scattering Transmission Ultrasound Tomography: Breast and Whole Body Imaging," in *2019 IEEE International Ultrasonics Symposium (IUS)*, 2019: IEEE, pp. 951-958.
- [44] L. Drukker, R. Droste, P. Chatelain, J. A. Noble, and A. T. Papageorghiou, "Safety indices of ultrasound: adherence to recommendations and awareness during routine obstetric ultrasound scanning," *Ultraschall in der Medizin-European Journal of Ultrasound*, vol. 41, no. 02, pp. 138-145, 2020.
- [45] J. C. Simon, A. D. Maxwell, and M. R. Bailey, "Some work on the diagnosis and management of kidney stones with ultrasound," *Acoustics today*, vol. 13, no. 4, p. 52, 2017.
- [46] S. Morrissey. (2007) Are Microchip Tags Safe? *Time*. Available: <http://content.time.com/time/health/article/0,8599,1672865,00.html>
- [47] DNY3D, *shutter stock*. [Online]. Available: <https://www.shutterstock.com/image-illustration/3d-rfid-chip-implant-animal-id-377871181>.
- [48] K. N. Bocan and E. Sejdić, "Adaptive transcutaneous power transfer to implantable devices: A state of the art review," *Sensors*, vol. 16, no. 3, p. 393, 2016.
- [49] C. P. Conran, "Antenna Designs for Wireless Medical Implants," M.S. thesis 2013.
- [50] K. Shahzad and B. Oelmann, "A comparative study of in-sensor processing vs. raw data transmission using ZigBee, BLE and Wi-Fi for data intensive monitoring

- applications," in *2014 11th International Symposium on Wireless Communications Systems (ISWCS)*, 2014: IEEE, pp. 519-524.
- [51] NFC. "near field communication." <http://nearfieldcommunication.org/far-field.html> (accessed 09/09, 2020).
- [52] O. C. Laboratory. "Electromagnetic Radiation: Field Memo." [https://www.osha.gov/SLTC/radiofrequencyradiation/electromagnetic\\_fieldmemo/electromagnetic.html](https://www.osha.gov/SLTC/radiofrequencyradiation/electromagnetic_fieldmemo/electromagnetic.html) (accessed 09/09, 2020).
- [53] M. Catrysse, B. Hermans, and R. Puers, "An inductive power system with integrated bi-directional data-transmission," *Sensors and Actuators A: Physical*, vol. 115, no. 2-3, pp. 221-229, 2004.
- [54] D. Jiang, D. Cirmirakis, M. Schormans, T. A. Perkins, N. Donaldson, and A. Demosthenous, "An integrated passive phase-shift keying modulator for biomedical implants with power telemetry over a single inductive link," *IEEE transactions on biomedical circuits and systems*, vol. 11, no. 1, pp. 64-77, 2016.
- [55] M. Kiani and M. Ghovanloo, "A 13.56-Mbps pulse delay modulation based transceiver for simultaneous near-field data and power transmission," *IEEE transactions on biomedical circuits and systems*, vol. 9, no. 1, pp. 1-11, 2014.
- [56] A. S. Poon, S. O'Driscoll, and T. H. Meng, "Optimal operating frequency in wireless power transmission for implantable devices," in *2007 29th Annual International Conference of the IEEE Engineering in Medicine and Biology Society*, 2007: IEEE, pp. 5673-5678.
- [57] A. Yakovlev, J. H. Jang, and D. Pivonka, "An 11micro Watt Sub-pJ/bit Reconfigurable Transceiver for mm-Sized Wireless Implants," *IEEE transactions on biomedical circuits and systems*, vol. 10, no. 1, pp. 175-185, 2015.
- [58] J. S. Ho, A. J. Yeh, E. Neofytou, S. Kim, Y. Tanabe, B. Patlolla, R. E. Beygui, and A. S. Poon, "Wireless power transfer to deep-tissue microimplants," *Proceedings of the National Academy of Sciences*, vol. 111, no. 22, pp. 7974-7979, 2014.
- [59] R. Nazempour, Q. Zhang, R. Fu, and X. Sheng, "Biocompatible and implantable optical fibers and waveguides for biomedicine," *Materials*, vol. 11, no. 8, p. 1283, 2018.
- [60] T. Liu, U. Bihl, S. M. Anis, and M. Ortmanns, "Optical transcutaneous link for low power, high data rate telemetry," in *2012 Annual International Conference of the IEEE Engineering in Medicine and Biology Society*, 2012: IEEE, pp. 3535-3538.
- [61] C. f. D. a. R. Health. "Marketing Clearance of Diagnostic Ultrasound Systems and Transducers." FDA. <https://www.fda.gov/media/71100/download> (accessed 09/09, 2020).
- [62] H.-J. Kim, H. Hirayama, S. Kim, K. J. Han, R. Zhang, and J.-W. Choi, "Review of near-field wireless power and communication for biomedical applications," *IEEE Access*, vol. 5, pp. 21264-21285, 2017.
- [63] W. W. Au and M. C. Hastings, *Principles of marine bioacoustics*. Springer, 2008.
- [64] M. J. Griffin, Howarth, H.V.C., Pitts, P.M., Fischer, S., Kaulbars, U., Donati, P.M. and Bereton, P.F. , "Guide To Good Practice on Whole-Body Vibration. Non-binding guide to good practice with a view to implementation of Directive 2002/44/EC on the minimum health and safety requirements regarding the exposure of workers to the risks arising from physical agents (vibrations)," *Human Sciences Group*, 2006.
- [65] H. N. Schwerdt, W. Xu, S. Shekhar, A. Abbaspour-Tamijani, B. C. Towe, F. A. Miranda, and J. Chae, "A fully passive wireless microsystem for recording of

- neuropotentials using RF backscattering methods," *Journal of Microelectromechanical Systems*, vol. 20, no. 5, pp. 1119-1130, 2011.
- [66] T. Bos, W. Dehaene, and M. Verhelst, "Ultrasound In-Body Communication with OFDM through Multipath Realistic Channels," in *2019 IEEE Biomedical Circuits and Systems Conference (BioCAS)*, 2019: IEEE, pp. 1-4.
- [67] T. Bos, W. Jiang, J. D'hooge, M. Verhelst, and W. Dehaene, "Enabling ultrasound in-body communication: FIR channel models and QAM experiments," *IEEE transactions on biomedical circuits and systems*, vol. 13, no. 1, pp. 135-144, 2018.
- [68] T. C. Chang, M. L. Wang, J. Charthad, M. J. Weber, and A. Arbabian, "27.7 A 30.5 mm 3 fully packaged implantable device with duplex ultrasonic data and power links achieving 95kb/s with < 10<sup>-4</sup> BER at 8.5 cm depth," in *2017 IEEE International Solid-State Circuits Conference (ISSCC)*, 2017: IEEE, pp. 460-461.
- [69] J. Charthad, M. J. Weber, T. C. Chang, and A. Arbabian, "A mm-sized implantable medical device (IMD) with ultrasonic power transfer and a hybrid bi-directional data link," *IEEE Journal of solid-state circuits*, vol. 50, no. 8, pp. 1741-1753, 2015.
- [70] E. Demirors, G. Alba, G. E. Santagati, and T. Melodia, "High data rate ultrasonic communications for wireless intra-body networks," in *2016 IEEE International Symposium on Local and Metropolitan Area Networks (LANMAN)*, 2016: IEEE, pp. 1-6.
- [71] M. M. Ghanbari, D. K. Piech, K. Shen, S. F. Alamouti, C. Yalcin, B. C. Johnson, J. M. Carmena, M. M. Maharbiz, and R. Muller, "A Sub-mm 3 Ultrasonic Free-Floating Implant for Multi-Mote Neural Recording," *IEEE Journal of Solid-State Circuits*, vol. 54, no. 11, pp. 3017-3030, 2019.
- [72] B. Herrera, E. Demirors, G. Chen, R. Guida, F. Pop, N. Dave, C. Cassella, T. Melodia, and M. Rinaldi, "Pmut-based high data rate ultrasonic wireless communication link for intra-body networks."
- [73] B. Jaafar, A. Soltan, J. Neasham, and P. Degenaar, "Wireless Ultrasonic Communication for Biomedical Injectible Implantable Device," in *2019 41st Annual International Conference of the IEEE Engineering in Medicine and Biology Society (EMBC)*, 2019: IEEE, pp. 4024-4027.
- [74] K. Keramatzadeh and A. M. Sodagar, "Design and implementation of an ultrasonic link for concurrent telemetry of multiple data streams to implantable biomedical microsystems," in *2018 IEEE 61st International Midwest Symposium on Circuits and Systems (MWSCAS)*, 2018: IEEE, pp. 1090-1093.
- [75] M. Li and Y. T. Kim, "Feasibility Analysis on the Use of Ultrasonic Communications for Body Sensor Networks," *Sensors*, vol. 18, no. 12, p. 4496, 2018.
- [76] Y.-S. Luo, J.-R. Wang, W.-J. Huang, J.-Y. Tsai, Y.-F. Liao, W.-T. Tseng, C.-T. Yen, P.-C. Li, and S.-I. Liu, "Ultrasonic power/data telemetry and neural stimulator with OOK-PM signaling," *IEEE Transactions on Circuits and Systems II: Express Briefs*, vol. 60, no. 12, pp. 827-831, 2013.
- [77] F. Mazzilli, M. Peisino, R. Mitouassiou, B. Cotté, P. Thoppay, C. Lafon, P. Favre, E. Meurville, and C. Dehollain, "In-vitro platform to study ultrasound as source for wireless energy transfer and communication for implanted medical devices," in *2010 Annual International Conference of the IEEE Engineering in Medicine and Biology*, 2010: IEEE, pp. 3751-3754.
- [78] M. Meng and M. Kiani, "Gastric seed: Toward distributed ultrasonically interrogated millimeter-sized implants for large-scale gastric electrical-wave recording," *IEEE Transactions on Circuits and Systems II: Express Briefs*, vol. 66, no. 5, pp. 783-787, 2019.

- [79] S. Ozeri and D. Shmilovitz, "Simultaneous backward data transmission and power harvesting in an ultrasonic transcutaneous energy transfer link employing acoustically dependent electric impedance modulation," *Ultrasonics*, vol. 54, no. 7, pp. 1929-1937, 2014.
- [80] G. E. Santagati and T. Melodia, "Experimental evaluation of impulsive ultrasonic intra-body communications for implantable biomedical devices," *IEEE Transactions on Mobile Computing*, vol. 16, no. 2, pp. 367-380, 2016.
- [81] G. E. Santagati and T. Melodia, "An implantable low-power ultrasonic platform for the Internet of Medical Things," in *IEEE INFOCOM 2017-IEEE Conference on Computer Communications*, 2017: IEEE, pp. 1-9.
- [82] D. Seo, R. M. Neely, K. Shen, U. Singhal, E. Alon, J. M. Rabaey, J. M. Carmena, and M. M. Maharbiz, "Wireless recording in the peripheral nervous system with ultrasonic neural dust," *Neuron*, vol. 91, no. 3, pp. 529-539, 2016.
- [83] A. Singer, M. Oelze, and A. Podkowa, "Mbps experimental acoustic through-tissue communications: MEAT-COMMS," in *2016 IEEE 17th International Workshop on Signal Processing Advances in Wireless Communications (SPAWC)*, 2016: IEEE, pp. 1-4.
- [84] A. C. Singer, M. Oelze, and A. Podkowa, "Experimental ultrasonic communications through tissues at Mbps data rates," in *2016 IEEE International Ultrasonics Symposium (IUS)*, 2016: IEEE, pp. 1-4.
- [85] J.-Y. Tsai, K.-H. Huang, J.-R. Wang, S.-I. Liu, and P.-C. Li, "Ultrasonic wireless power and data communication for neural stimulation," in *2011 IEEE International Ultrasonics Symposium*, 2011: IEEE, pp. 1052-1055.
- [86] M. L. Wang and A. Arbabian, "Exploiting spatial degrees of freedom for high data rate ultrasound communication with implantable devices," *Applied Physics Letters*, vol. 111, no. 13, p. 133503, 2017.
- [87] M. L. Wang, T. C. Chang, T. Teisberg, M. J. Weber, J. Charthad, and A. Arbabian, "Closed-loop ultrasonic power and communication with multiple miniaturized active implantable medical devices," in *2017 IEEE International Ultrasonics Symposium (IUS)*, 2017: IEEE, pp. 1-4.
- [88] G. Tabak, S. Yang, R. J. Miller, M. L. Oelze, and A. C. Singer, "Video-Capable Ultrasonic Wireless Communications through Biological Tissues," *IEEE transactions on ultrasonics, ferroelectrics, and frequency control*, vol. 68, no. 3, pp. 664-674, 2020.
- [89] J. Oevermann, P. Weber, and S. H. Tretbar, "Encapsulation of Capacitive Micromachined Ultrasonic Transducers (CMUTs) for the Acoustic Communication between Medical Implants," *Sensors*, vol. 21, no. 2, p. 421, 2021.
- [90] M. M. Ghanbari and R. Muller, "Optimizing Volumetric Efficiency and Backscatter Communication in Biosensing Ultrasonic Implants," *IEEE Transactions on Biomedical Circuits and Systems*, vol. 14, no. 6, pp. 1381-1392, 2020.
- [91] T. Akin, K. Najafi, and R. M. Bradley, "A wireless implantable multichannel digital neural recording system for a micromachined sieve electrode," *IEEE Journal of solid-state circuits*, vol. 33, no. 1, pp. 109-118, 1998.
- [92] A. D. Dehennis and K. D. Wise, "A wireless microsystem for the remote sensing of pressure, temperature, and relative humidity," *Journal of Microelectromechanical Systems*, vol. 14, no. 1, pp. 12-22, 2005.
- [93] Y. Hu and M. Sawan, "A fully integrated low-power BPSK demodulator for implantable medical devices," *IEEE Transactions on Circuits and Systems I: Regular Papers*, vol. 52, no. 12, pp. 2552-2562, 2005.

- [94] M. Piedade, J. Gerald, L. A. Sousa, G. Tavares, and P. Tomás, "Visual neuroprosthesis: A non invasive system for stimulating the cortex," *IEEE Transactions on Circuits and Systems I: Regular Papers*, vol. 52, no. 12, pp. 2648-2662, 2005.
- [95] G. J. Suaning and N. H. Lovell, "CMOS neurostimulation ASIC with 100 channels, scaleable output, and bidirectional radio-frequency telemetry," *IEEE Transactions on Biomedical Engineering*, vol. 48, no. 2, pp. 248-260, 2001.
- [96] H. Yu and K. Najafi, "Low-power interface circuits for bio-implantable microsystems," in *2003 IEEE International Solid-State Circuits Conference, 2003. Digest of Technical Papers. ISSCC.*, 2003: IEEE, pp. 194-487.
- [97] S. H. Kondapalli, Y. Alazzawi, M. Malinowski, T. Timek, and S. Chakrabartty, "Multiaccess in vivo biotelemetry using sonomicrometry and M-scan ultrasound imaging," *IEEE Transactions on Biomedical Engineering*, vol. 65, no. 1, pp. 149-158, 2017.
- [98] M. L. Oelze, T. Riedl, and A. Singer, "Method and apparatus for ultra high bandwidth acoustic communication and power transfer," ed: Google Patents, 2018.
- [99] T. Melodia, R. Guida, and G. E. Santagati, "Reconfigurable Implantable Medical System For Ultrasonic Power Control And Telemetry," ed: Google Patents, 2019.
- [100] T. Melodia and G. E. Santagati, "Software-Defined Implantable Ultrasonic Device for Use in the Internet of Medical Things," ed: Google Patents, 2018.
- [101] S. Campbell, "A short history of sonography in obstetrics and gynaecology," *Facts, views & vision in ObGyn*, vol. 5, no. 3, p. 213, 2013.
- [102] M. Postema, *Fundamentals of medical ultrasonics*. CRC Press, 2011.
- [103] W. R. Hendee and E. R. Ritenour, *Medical imaging physics*. John Wiley & Sons, 2003.
- [104] C. Gao, G. Zhao, and H. Fourati, *Cooperative Localization and Navigation: Theory, Research, and Practice*. CRC Press, 2019.
- [105] W. D. O'Brien Jr, "Ultrasound–biophysics mechanisms," *Progress in biophysics and molecular biology*, vol. 93, no. 1-3, pp. 212-255, 2007.
- [106] L. APC International, *Piezoelectric ceramics: principles and applications*. APC International, 2002.
- [107] Steminc, "PIEZO CYLINDER." [Online]. Available: <https://www.steminc.com/PZT/en/piezo-ceramic-tube-90-khz>.
- [108] STEMINC. [Online]. Available: [www.steminc.com/PZT/en/piezo-ceramic-block-5x5x66mm-200-khz](http://www.steminc.com/PZT/en/piezo-ceramic-block-5x5x66mm-200-khz).
- [109] piceramic, "piezo-technology." [Online]. Available: [www.piceramic.com/en/piezo-technology/properties-piezo-actuators/displacement-modes/](http://www.piceramic.com/en/piezo-technology/properties-piezo-actuators/displacement-modes/).
- [110] K. K. Sappati and S. Bhadra, "Piezoelectric polymer and paper substrates: a review," *Sensors*, vol. 18, no. 11, p. 3605, 2018.
- [111] M. Acosta, N. Novak, V. Rojas, S. Patel, R. Vaish, J. Koruza, G. Rossetti Jr, and J. Rödel, "BaTiO<sub>3</sub>-based piezoelectrics: Fundamentals, current status, and perspectives," *Applied Physics Reviews*, vol. 4, no. 4, p. 041305, 2017.
- [112] Z.-P. Cao, C.-M. Wang, T.-L. Zhao, S.-L. Yu, H.-Z. Wu, Y.-M. Wang, Q. Wang, Y. Liang, Y.-N. Wei, and Y. Zhang, "Piezoelectric properties and thermal stabilities of strontium bismuth titanate (SrBi<sub>4</sub>Ti<sub>4</sub>O<sub>15</sub>)," *Ceramics International*, vol. 41, no. 10, pp. 13974-13982, 2015.

- [113] A. J. Teo, A. Mishra, I. Park, Y.-J. Kim, W.-T. Park, and Y.-J. Yoon, "Polymeric biomaterials for medical implants and devices," *ACS Biomaterials Science & Engineering*, vol. 2, no. 4, pp. 454-472, 2016.
- [114] V. R. Amin, "Ultrasonic attenuation estimation for tissue characterization," 1989.
- [115] U. o. N. Dame, "acoustics of the body," 2003. [Online]. Available: [www3.nd.edu/~nsl/Lectures/mphysics/](http://www3.nd.edu/~nsl/Lectures/mphysics/).
- [116] C.-M. Chen and B. Choubey, "Ultrasound Transducer Quality Factor Control Using Coupled External Electrical Resonator," in *2018 IEEE SENSORS*, 2018: IEEE, pp. 1-4.
- [117] K. G. Baker, V. J. Robertson, and F. A. Duck, "A review of therapeutic ultrasound: Biophysical effects," *Journal of Women's Health Physical Therapy*, vol. 34, no. 3, pp. 111-118, 2010.
- [118] A. A. Saber and A. Saber, "Therapeutic ultrasound: Physiological Role, clinical applications and precautions," *Journal of Surgery*, vol. 5, no. 3-1, pp. 61-69, 2017.
- [119] C. K. Holland, C. X. Deng, R. E. Apfel, J. L. Alderman, L. A. Fernandez, and K. J. Taylor, "Direct evidence of cavitation in vivo from diagnostic ultrasound," *Ultrasound in medicine & biology*, vol. 22, no. 7, pp. 917-925, 1996.
- [120] D. Dalecki, C. H. Raeman, S. Z. Child, and E. L. Carstensen, "Intestinal hemorrhage from exposure to pulsed ultrasound," *Ultrasound in medicine & biology*, vol. 21, no. 8, pp. 1067-1072, 1995.
- [121] H.-C. Yang, *Introduction to Digital Wireless Communications*. IET, 2017.
- [122] S. R. Bullock, *Transceiver and System Design for Digital Communications*. SciTech Publishing, 2000.
- [123] Y. S. Cho, J. Kim, W. Y. Yang, and C. G. Kang, *MIMO-OFDM wireless communications with MATLAB*. John Wiley & Sons, 2010.
- [124] J. Bates, "Abdominal ultrasound: how, why and when," *How, Why and When*. Edinburgh, Churchill Livingstone, 2004.
- [125] S. O. Agbo and M. N. Sadiku, *Principles of Modern Communication Systems*. Cambridge University Press, 2017.
- [126] U. Madhow, *Fundamentals of digital communication*. Cambridge University Press, 2008.
- [127] M. Tomlinson, C. Jung Tjhai, M. A. Ambroze, M. Ahmed, and M. Jibril, *Error-Correction Coding and Decoding: Bounds, Codes, Decoders, Analysis and Applications*. Springer Nature, 2017.
- [128] Z. Yang, *Neural computation, neural devices, and neural prosthesis*. Springer, 2014.
- [129] K. technologies, "Agilent technologies educator's corner." [Online]. Available: <http://www.educatorscorner.com>.
- [130] B. Ziaie, S. C. Rose, M. D. Nardin, and K. Najafi, "A self-oscillating detuning-insensitive class-E transmitter for implantable microsystems," *IEEE transactions on biomedical engineering*, vol. 48, no. 3, pp. 397-400, 2001.
- [131] N. Chitkara, N. Chandoke, and S. Deb, "Comparative Study of Different Switch Implementations for Ook Modulator," in *2014 International Conference on Devices, Circuits and Communications (ICDCCom)*, 2014: IEEE, pp. 1-4.
- [132] G. John, *Digital communications*. Mc-Graw-Hill, 2001.
- [133] G. Smillie, *Analogue and digital communication techniques*. Elsevier, 1999.
- [134] K. J. Opieliński, M. Celmer, and R. Bolejko, "Crosstalk effect in medical ultrasound tomography imaging," in *2018 Joint Conference-Acoustics*, 2018: IEEE, pp. 1-6.

- [135] Q. Meng, F. Yao, and Y. Wu, "Review of crosstalk elimination methods for ultrasonic range systems in mobile robots," in *2006 IEEE/RSJ International Conference on Intelligent Robots and Systems*, 2006: IEEE, pp. 1164-1169.
- [136] S. Shin, M.-H. Kim, and S. B. Choi, "Ultrasonic distance measurement method with crosstalk rejection at high measurement rate," *IEEE Transactions on Instrumentation and Measurement*, vol. 68, no. 4, pp. 972-979, 2018.
- [137] K. Nguyen, L. H. Le, M. D. Sacchi, L. Huynh, and E. Lou, "Adaptive Noise Cancellation in the Intercept Time-Slowness Domain for Eliminating Ultrasonic Crosstalk in a Transducer Array," in *5th International Conference on Biomedical Engineering in Vietnam*, 2015: Springer, pp. 32-35.
- [138] R. K. Crane, *Propagation handbook for wireless communication system design*. CRC press, 2003.
- [139] D. Adamy, *Practical communication theory*. Scitech Pub Inc, 2014.
- [140] G. Breed, "Summit Technical Media," *High Frequency Electronics*. [Online]. Available: <http://www.highfrequencyelectronics.com/Archives/Archives2002-2003.shtml>.
- [141] M. Schiff, *Introduction to Communication systems simulation*. Artech House, 2006.
- [142] A. Mahmood and R. Jäntti, "Packet error rate analysis of uncoded schemes in block-fading channels using extreme value theory," *IEEE Communications Letters*, vol. 21, no. 1, pp. 208-211, 2016.
- [143] I. Glover and P. M. Grant, *Digital communications*. Pearson Education, 2010.
- [144] J. C. Moreira and P. G. Farrell, *Essentials of error-control coding*. John Wiley & Sons, 2006.
- [145] A. Neubauer, J. Freudenberger, and V. Kuhn, *Coding theory: algorithms, architectures and applications*. John Wiley & Sons, 2007.
- [146] R. Johannesson and K. S. Zigangirov, *Fundamentals of convolutional coding*. John Wiley & Sons, 2015.
- [147] T. K. Moon, *Error correction coding: mathematical methods and algorithms*. John Wiley & Sons, 2005.
- [148] K. D. Rao, *Channel coding techniques for wireless communications*. Springer, 2015.
- [149] A. Erdogan, E. Cayirci, and V. Coskun, "Sectoral sweepers for sensor node management and location estimation in adhoc sensor networks," in *IEEE Military Communications Conference, 2003. MILCOM 2003.*, 2003, vol. 1: IEEE, pp. 555-560.
- [150] T. D. Lagkas, *Wireless Network Traffic and Quality of Service Support: Trends and Standards: Trends and Standards*. IGI Global, 2010.
- [151] H. S. Gougheri, A. Dangi, S.-R. Kothapalli, and M. Kiani, "A comprehensive study of ultrasound transducer characteristics in microscopic ultrasound neuromodulation," *IEEE transactions on biomedical circuits and systems*, vol. 13, no. 5, pp. 835-847, 2019.
- [152] C. Sun, S. Jiang, and Y. Liu, "Numerical study and optimisation of a novel single-element dual-frequency ultrasound transducer," *Sensors*, vol. 18, no. 3, p. 703, 2018.
- [153] S. Lin, Z. Fu, X. Zhang, Y. Wang, and J. Hu, "Radially sandwiched cylindrical piezoelectric transducer," *Smart materials and structures*, vol. 22, no. 1, p. 015005, 2012.

- [154] A. Sanni, A. Vilches, and C. Toumazou, "Inductive and ultrasonic multi-tier interface for low-power, deeply implantable medical devices," *IEEE Transactions on Biomedical Circuits and Systems*, vol. 6, no. 4, pp. 297-308, 2012.
- [155] A. V. Craciun, "Low noise, low power variable gain amplifier for ultrasounds," in *2017 International Conference on Optimization of Electrical and Electronic Equipment (OPTIM) & 2017 Intl Aegean Conference on Electrical Machines and Power Electronics (ACEMP)*, 2017: IEEE, pp. 845-850.
- [156] D. Lancaster, *Active filter cookbook*. Elsevier, 1996.
- [157] W. G. Jung, "IC op-amp. cookbook. Howard W. Sams & Co," *Inc., Indianapolis, Ind*, 1980.
- [158] L. Technology. <https://www.analog.com/media/en/technical-documentation/data-sheets/625567fd.pdf> (accessed 15/07, 2020).
- [159] J. Luo, D. Firfilionis, M. Turnbull, W. Xu, D. Walsh, A. Soltan, R. Ramezani, Y. Liu, R. Bailey, and A. S. Idil, "The Neural Engine: A Reprogrammable Low Power Platform for Closed-loop Optogenetics," *IEEE Transactions on Biomedical Engineering*, 2020.
- [160] Y. Saito, H. Takao, T. Tani, T. Nonoyama, K. Takatori, T. Homma, T. Nagaya, and M. Nakamura, "Lead-free piezoceramics," *Nature*, vol. 432, no. 7013, pp. 84-87, 2004.